A time sensitive modelling of the two extreme BL Lacertae objects 1ES 1218+304 and 1ES 0229+200

Pedro Ivo Silva Batista

DISSERTATION

zur Erlangung des akademischen Grades
doctor rerum naturalium
(Dr. rer. nat.)
in der Wissenschaftsdisziplin ”Astroteilchenphysik”

eingereicht an der
Mathematisch-Naturwissenschaftliche Fakultät
der Universität Potsdam

Gutachter: 1. Dr. Elisa Pueschel
2. Prof. Dr. Martin Pohl
3. Prof. Dr. Markus Böttcher

Tag der mündlichen Prüfung: 03.12.2024

Published online on the
Publication Server of the University of Potsdam:
https://doi.org/10.25932/publishup-67336
https://nbn-resolving.org/urn:nbn:de:kobv:517-opus4-673364

Abstract

In this thesis, the broadband spectral energy distribution (SED) of the sources 1ES 1218+304 and 1ES 0229+200 is studied. 1ES 1218+304 and 1ES 0229+200 are two well-known extreme high-frequency-peaked BL Lac objects (EHBLs), a type of blazar. Blazars are in turn a type of active galactic nuclei (AGN) with the presence of a jet of relativistic charged particles where, by random chance, the jet points towards Earth.

Data taken by the ultraviolet/optical telescope UVOT, and the X-ray telescope XRT, on board the Neils Gehrels *Swift* Observatory satellite, are used. The ultraviolet/optical and X-ray data are analysed together with gamma-ray data in the 30 MeV to 300 GeV range taken by the *Fermi*-LAT detector and in the 50 GeV to 30 TeV range, provided by the VERITAS Collaboration. The light curves of each energy band were built and analysed with a Bayesian blocks algorithm. The intrinsic spectral indices in the VHE range were found to be $\Gamma_{VHE} \gtrsim 2$, except during the quietest period of 1ES 0229+200, from 57419 MJD to 58017 MJD, where the intrinsic spectral index was found to be $\Gamma_{VHE} = 1.2 \pm 0.4$. Evidence of non-stationary extreme states was found, after analysis of the frequencies and luminosities of the synchrotron peak relative to the TeV slope $S = 2 - \Gamma_{VHE}$.

The Bayesian blocks were used to select four periods of data from each source, and SEDs were constructed from the combined data from these periods. A one-zone leptonic synchrotron self-Compton (SSC) emission scenario is used to describe the broadband SEDs. We used a Monte Carlo Markov chain (MCMC) to sample the parameter space of the SSC model and obtain the median and asymmetric 1-sigma standard deviations. The values of the minimum Lorentz factors of electrons are found to be compatible with 1, while the values of the Doppler factor δ_D vary between 10 and 90. The estimated values of the equipartition parameter k_{eq} (the ratio between the electrons energy density and the magnetic field energy density) have a maximum of 10^4 and a minimum of 2, where the latter is not observed in the literature.

Zusammenfassung

In dieser Arbeit wird die breitbandige spektrale Energieverteilung (SED) der Quellen 1ES 1218+304 und 1ES 0229+200 untersucht. 1ES 1218+304 und 1ES 0229+200 sind zwei bekannte, extrem hochfrequente BL Lac-Objekte (EHBLs), welche zu den Blazaren gehören. Blazare wiederum sind aktive galaktische Kerne (AGN) mit einem Jet aus relativistisch geladenen Teilchen, der zufällig auf die Erde gerichtet ist.

Es werden Daten des ultravioletten/optischen Teleskops UVOT und des Röntgenteleskops XRT an Bord des Neils Gehrels *Swift* Observatoriumssatelliten, werden verwendet. Die ultravioletten/optischen und Röntgendaten werden zusammen mit Gammastrahlendaten im 30 MeV bis 300 GeV Bereich, die vom *Fermi*-LAT -Detektor aufgenommen wurden, und im 50 GeV bis 30 TeV Bereich, die von der VERITAS-Kollaboration bereitgestellt wurden, analysiert. Die Lichtkurven jedes Energiebandes wurden erstellt und mit einem Bayesian Block-Algorithmus analysiert. Die intrinsischen spektralen Indizes im VHE-Bereich ergaben sich zu $\Gamma_{VHE} \gtrsim 2$, außer während der ruhigsten Periode von 1ES 0229+200, von 57419 MJD bis 58017 MJD, wo der intrinsische Spektralindex $\Gamma_{VHE} = 1.2 \pm 0.4$ betrug.

Bei einer Analyse der Frequenzen und Helligkeiten des Synchrotron-Peaks relativ zur TeV-Steigung $S = 2 - \Gamma_{VHE}$ wurden Hinweise auf nicht-stationäre Extremzustände gefunden. Die Bayes'schen Blöcke wurden verwendet, um vier Datenperioden von jeder Quelle auszuwählen, und SEDs wurden aus den kombinierten Daten dieser Perioden konstruiert. Ein Ein-Zonen-Synchrotron-Selbst-Compton (SSC)-Emissionsszenario wird verwendet, um die Breitband-SEDs zu beschreiben. Wir verwendeten eine Monte-Carlo-Markov-Kette (MCMC), um den Parameterraum des SSC-Modells abzutasten und den Median und die asymmetrischen 1-Sigma-Standardabweichungen zu erhalten. Die Werte der minimalen Lorentz-Faktoren der Elektronen sind mit 1 kompatibel, während die Werte des Dopplerfaktors δ_D zwischen 10 und 90 variieren. Die geschätzten Werte des Äquipartitionsparameters k_{eq} (das Verhältnis zwischen der Energiedichte der Elektronen und der Energiedichte des Magnetfeldes) haben ein Maximum von $\sim 10^4$ und ein Minimum von 2, letzteres wurde in der Literatur noch nicht beobachtet.

Declaration of authorship

I, Pedro Ivo Silva Batista, declare that this thesis titled, 'A time sensitive modelling of the two extreme BL Lacertae objects 1ES 1218+304 and 1ES 0229+200' and the work presented in it are my own in collaboration with my supervisor, Elisa Pueschel. I confirm that:

* No part of this work was or will be submitted for any degree or diploma or certificate or other qualification at this University or elsewhere.
* Unless otherwise stated, this thesis is the result of my own work.
* Any quotations mentioned in the thesis have been accurately cited.

Acknowledgements

As I was finishing this thesis, I thought about not making a big deal out of the acknowledgements and go with the average “I thank my supervisor, and thank this person, and that other person, and this funding agency...” and etc... But, the truth is that my morbidly over-dramatic persona would never allow such a thing.

So, brace yourselves.

I do believe that every person who has ever asked me or talked to me about my PhD, heard me saying “I’m so lucky to have Elisa as supervisor”, because, that is simply true. Through moving to a (very) different country to start the PhD, facing COVID ages two months after, and finishing the PhD with very little in person contact, plus the normal difficulties of a PhD, she has never once transpired an ounce of doubt in me. All the trust and support Elisa provided through the course of the PhD was essential to reach the position I am today.
So, thank you Elisa.

To trust in a thin-moustached-physicist dude and hop onto a flight to a different continent, with no more than two candies and a napkin in their pockets, can only mean one of two things: insanity, or a deep sense of loyalty. Well, I guess in this case, it could actually be both. Because, for one, after many years now, not for a second I could ever question the loyalty. But also, don’t people say ‘love makes you do crazy things’? So it was both... I think that deep down we knew, that no matter what, we could trust each other. And trusted we did. And loved.
Thank you, Ana.

Trust has been a recurring theme by now. And, if ‘to trust’ was a competition, there would be no shot against my family. Simply put, they trust me the longest. To the unaware reader, I’m the eldest of five: after me, came two of the kindest women I know (together I might add, they’re twins). And after them, came two of the kindest men I know (together I might add, they’re also twins... (yes, you read that right, two pairs of twins)). The very-hard-working parents always provided what the big family needed. And trusted. I was once the first child to leave the home, to study in another city, to study abroad, but eventually, all children made through, and are becoming beautiful, thoughtful, kind, special people.
So, thanks Dad, thanks Mom, thanks Julia, thanks Laura, thanks João, and thanks Marco. Also thanks to both my grandmas. I love you all.

We’re getting to the friends section, and luckily for me, this would be a huge section. But I’m probably running out of allowed characters in an acknowledgement before the reviewers fall sleep, so I will try to be more concise, but no promises. I have the tough-love kind, the let-me-comfort you kind, the we-haven’t-spoken-in-a-year-but-this-feels-normal kind, and many others kinds of friends, and I would like to thanks all of them. But, I also have the ‘family’ kind of friends. Those that are there, no matter what. Hell, they even move to the same country as you (or continent at least) to make your life easier! The ones that share and shape your interests, and lend you money, and a bed and a room for a weekend, maybe two weeks, sometimes two months... These kind you know? I hope you have them, because I do, and I don’t know what I would be without them.
Thanks Rodrigo, Caio, Rebeca, André and Raul. And through them, thanks AdS and MLGuaratuba people.
Thanks to my ‘friends from before’, Victor and Maria.

To my fellow scientists and friends from DESY, in particular to the VERITAS group, Arkadipta, Donggeun, Sonal and all the others, and from the friends in the VERITAS collaboration, in particular to Ste O’Brien, Collin Adams, Olivier Hervet, Amy Furniss, Lucy Fortson and all others, and to Gernot, that dedicated a lot of time tutoring and advising me, my warmest thank you.

Finally, this work was funded by the Helmholtz Association in Germany. VERITAS is supported by grants from the U.S. Department of Energy Office of Science, the U.S. National Science Foundation and the Smithsonian Institution, and by NSERC in Canada. I would also like to acknowledge the excellent work of the technical support staff at the Fred Lawrence Whipple Observatory and at the collaborating institutions in the construction and operation of the instrument.

"...
What is now false of what we said:
Some or all?
Whom do we still count on? Are we just left over, thrown out
Of the living stream? Shall we remain behind
Understanding no one and understood by none?
Have we got to be lucky?
This you ask. Expect
No other answer than your own."
– To a Waverer, Bertolt Brecht

Contents

List of Figures

List of Tables

Introduction 1

The history of humanity is the history of astronomy. Humans have always used their eyes to capture visible light for astronomical observations, and as time passed, we learnt that there is much more than the eye can see. With the discovery of ionizing radiation from outside the Earth's atmosphere by Victor Francis Hess between 1911 and 1913, we have also learnt that not only light can be used to study the cosmos. The puzzling creation of this ionizing radiation throughout the universe pushed the boundaries of astronomy. In recent years, astronomy has relied more and more on multi-messengers to understand the universe. Light, cosmic rays (charged particles accelerated to relativistic velocities), neutrinos, and gravitational waves serve to form the picture of the universe as a whole.

The emission of light by astrophysical objects - galaxies, stars, giant gaseous clouds, etc. - provides insight towards the origin of such objects and also towards physical interactions between matter. The electromagnetic spectrum spans from the slowest radio frequencies to very high-frequency gamma rays.

1.1 Active galactic nuclei

One type of such *astrophysical light-emitting objects* that are of great interest to the astrophysical community is the **active galactic nucleus (AGN)**.

AGNs are systems composed of a super massive black hole (SMBH), with masses in the range of 10^4 - 10^{10} $M_\odot$, which by accreting surrounding matter produces radiation and particle ejection. Surrounding the SMBH there is matter in the form of an accretion disk, a dusty torus, and scattered ionized gas clouds known as the broad-line region (BLR), closer to the SMBH, and the narrow-line region (NLR), farther to the SMBH. The defining characteristic of an AGN is that the radiation produced by its central engine outshines its host galaxy, therefore being considered **active**.

1.1.1 AGN classification

AGNs are classified according to their observational properties, as shown in Figure 1.1. According to the presence or absence of a relativistic particle jet expelled from its central engine, AGNs are historically classified as

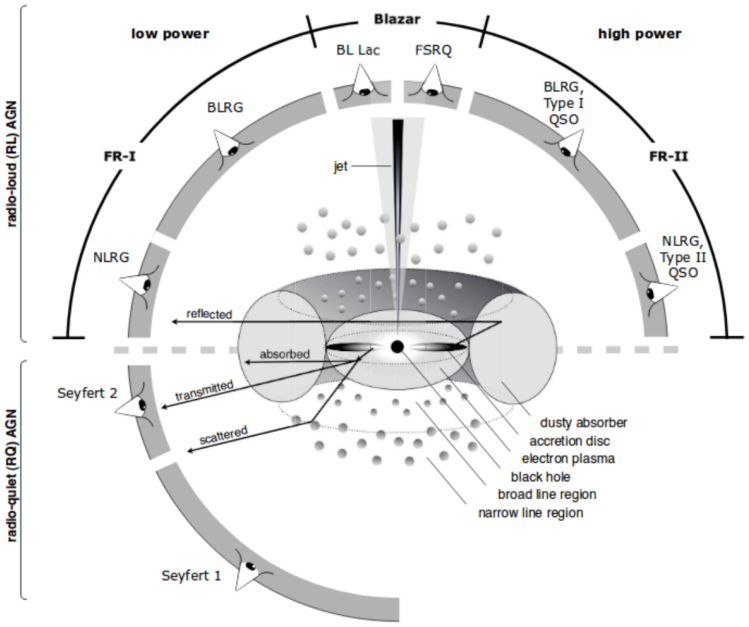

Figure 1.1: The unified AGN scheme as understood today. Taken from [1].

radio loud or radio quiet, respectively [1]. If a jetted AGN has its jet orientation aligned with our line of sight it is called a blazar, and if not, as a radio galaxy. It can also be classified according to the spectral signature of the highly ionised matter at the central engine by the presence and width of such spectral emission lines; whether X-ray light produced in the AGN is highly absorbed or not. For a complete overview of the AGN classification, please refer to [2].

[1]: Beckmann et al. (2013), *The AGN phenomenon*

[2]: Beckmann et al. (2012), *Active galactic nuclei*

1.1.2 The AGN electromagnetic spectrum

Electromagnetic emission of AGN is detected in a wide range of energies, from radio frequencies ($\sim 10^9$ Hz) to gamma rays ($\sim 10^{21}$ Hz). Different types of AGN present different spectral energy distributions (SEDs), energy per area per time. An example is provided in Figure 1.2. In the different energy ranges, we have:

Infrared (IR) selected AGNs provide a probe into obscuring material and dust around the central engine.

Ultraviolet/optical selected AGNs offer a view into the emission from the accretion disk.

X-ray selected AGNs emission traces back to the corona.

Gamma-ray and radio selected AGNs strong non-thermal emission is associated with jet physics.

We refer to [3] for a review of research with different energy bands of AGN emission.

[3]: Padovani et al. (2017), "Active galactic nuclei: what's in a name?"

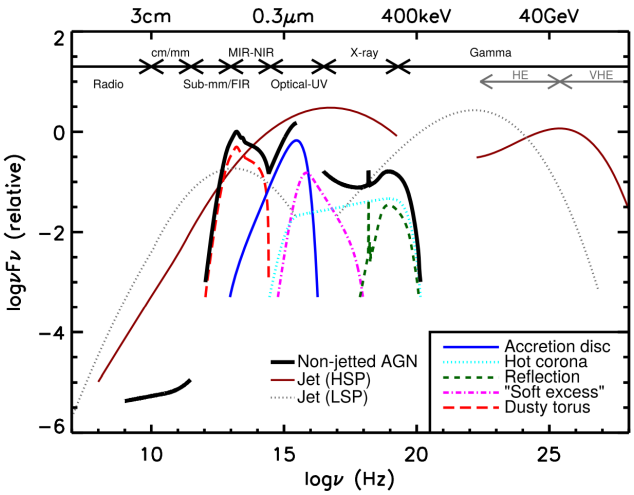

Figure 1.2: Examples of SEDs from non-jetted AGN (black), low-frequency-peaked BL Lac objects (dotted) and high-frequency-peaked BL Lac objects (brown), as well as the contributions from thermal emission from blazars components. Extracted from [3]. Image credit: C. M. Harrison.

1.2 Layout of the thesis

In this thesis, we will look to a selected gamma-ray AGN sample, consisting of two blazar sources, 1ES 1218+304 and 1ES 0229+200, using archival multiwavelength (MWL) gamma-ray, X-ray, and ultraviolet/optical data. In Chapter 2, we will introduce the blazar class of AGNs and, in particular, why a particular type of blazar, the BL Lac objects, are of interest for gamma-ray astronomy. In Chapter 3, we will introduce the radiative processes by which light can be emitted by BL Lac objects and how we model such emission. From the source to Earth, we arrive at the way in which we detect light. In Chapter 4, we explain the methods used to detect light at the wavelengths used in this thesis. The data reduction and reconstruction are explained for gamma-ray measurements with imaging Cherenkov array telescopes (IACTs) and space-based measurements; X-ray and ultraviolet/optical measurements by satellite detectors. Next, in Chapter 6 we introduce the statistical concepts used to analyse the acquired data. With all the concepts introduced, we present the results of our work in Chapter 7, Chapter 8, and Chapter 9, and we discuss our results and prospects in Chapter 10.

Blazars 2

The blazar is one amongst the many flavours of AGN, a galaxy where the radiation produced by its central engine outshines the radiation of its host galaxy. Blazars are jetted AGN, i.e. an AGN that exhibits a highly-collimated jet of relativistic charged particles. But a Blazar's distinguishing feature is that its jet orientation is closely aligned with Earth's line of sight to the Blazar, at an angle $\theta \lesssim 10^{\circ}$.

2.1 Types of blazar

Blazars can be classified as flat-spectrum radio quasars (FSRQs) or BL Lacs according to emission lines originating from the BLR. The BLR gases at typical velocities of ~ 1000 km s^{-1} emit broad ionization lines (or Balmer lines), mainly hydrogen's Hα (6563 Å), Hβ (4861 Å) and Hγ (4340 Å) lines [2]. A Blazar that exhibits these Balmer lines on top of a non-thermal optical continuum is classified as an FSRQ. When such optical lines are faint or non-dominant over the non-thermal optical spectrum, this source is classified as a BL Lac object. Quantitatively, the equivalent width (EW) of these lines is used as a criterion to distinguish between BL Lac and FSRQs. The EW of an emission line is defined as

[2]: Beckmann et al. (2012), *Active galactic nuclei*

$$EW = \int d\lambda \frac{F_s(\lambda) - F_c(\lambda)}{F_c(\lambda)}, \tag{2.1}$$

where $F_s(\lambda)$ is the intensity of the emission line (energy per wavelength per time per solid angle) and $F_c(\lambda)$ is the intensity of the optical continuum. An object is classified as a BL Lac when its emission lines $EW < 5$ Å.

2.1.1 Redshift ditributions

BL Lacs and FSRQs are detected on average at very different redshifts. Shown in Figure 2.1 are the redshift distributions of BL Lacs and FSRQs from the multifrequency Roma-*BZCAT* blazar catalogue [4]. BL Lacs have an average redshift of $\langle z \rangle \approx 0.3$, while FSRQs are located, on average, on a larger redshift of $\langle z \rangle \approx 1.4$. However, since BL Lacs do not have distinct optical features, their redshift is not so easily determined. For example, approximately 40% of the BL Lac sources in the *BZCAT* catalogue do not have a measurement of their redshift. Still, even at closer distances when compared to FSRQs, BL Lacs objects provide great opportunities

[4]: Massaro et al. (2009), "Roma-BZCAT"

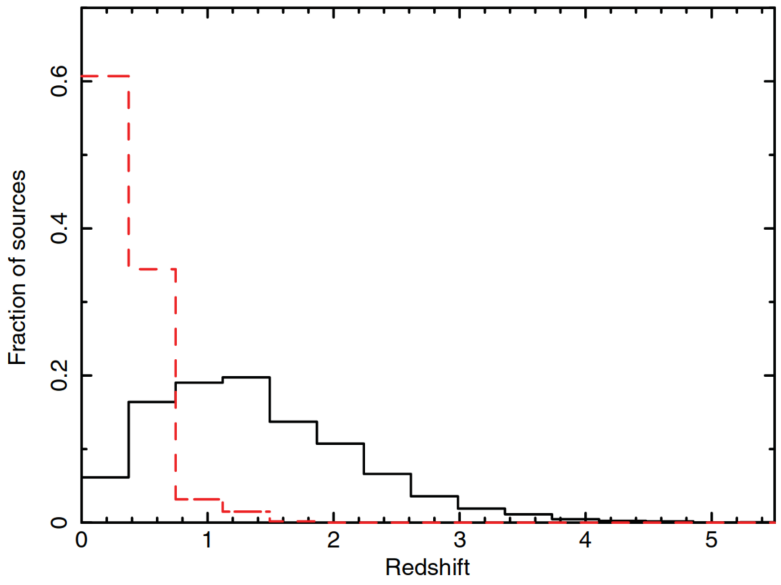

Figure 2.1: Redshift distributions of FSRQs (black solid line) and BL Lac objects (red dashed line) from the blazar catalogue *BZCAT* [4]. Taken from [6].

for studies of photon propagation through the intergalactic medium (see, e.g., [5]).

[5]: Biteau et al. (2022), "Gamma-ray cosmology and tests of fundamental physics"

2.2 Gamma-ray blazars

In the context of gamma-ray astronomy, blazars are one of the most detected types of source. To put this into perspective, we examine the number of detected sources in the Very-High Energy (VHE) gamma-ray range - electromagnetic radiation with energies higher than ~ 50 GeV up to ~ 50 TeV - in the TeVCat catalogue* [7]. Of the 252 sources listed in TeVCat, 96 are extragalatic sources. Of the extragalatic sources, 86 are AGN. Illustrated in Figure 2.2, we see that of the 86 AGNs listed, 80 are identified as blazars, around 93%. Then, out of the 80 Blazars, 67 are, in fact, BL Lac objects, while only 9 (~ 10% of all listed AGN) are FSRQs.

[7]: Wakely et al. (2008), "TeVCat: An online catalog for very high energy gamma-ray astronomy"

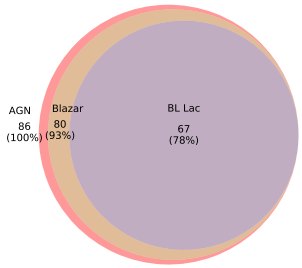

Figure 2.2: Venn diagram created from AGN, Blazars and BL Lac objects on the TeVCat catalogue.

In Figure 2.3, a map of the third AGN catalogue by *Fermi*-LAT [8], together with a map of the sources listed in TeVCat, is shown. The Large Area Telescope (LAT) is a gamma-ray detector on board the *Fermi* Gamma-ray Space Telescope (*Fermi*) [9]. *Fermi*-LAT operates in what is known as the high energy gamma-ray range (HE), from 30 MeV up to ~ 1 TeV. By way of comparison, the *Fermi*-LAT map in Figure 2.3 includes 1563 high Galactic latitude sources (at least 10° distant from the galactic plane), of which 415 are FSRQs (~ 26%), 657 are BL Lacs (~ 42%) and 402 (~ 25%) are unidentified blazar sources.

[8]: Ackermann et al. (2015), "The third catalog of active galactic nuclei detected by the Fermi large area telescope"

[9]: Atwood et al. (2009), "The large area telescope on the Fermi gamma-ray space telescope mission"

To begin to understand why blazars are one of the most frequently detected sources in gamma-ray astronomy, we can look at another blazar characteristic: Blazars generally have a double "hump" Spectral Energy

* `http://tevcat2.uchicago.edu/`

Distribution (SED), as shown in Figure 2.4. The first peak is believed to be caused by the synchrotron radiation emitted by relativistic leptons (electrons and positrons) or hadrons (mostly protons) within the jet when interacting with the magnetic fields permeating the medium. This radiation peaks in the radio - X-ray range, forming the low-energy synchrotron hump. The second peak could be caused either by inverse Compton (IC) processes, when low-energy photons can be scattered to gamma-ray energies by the relativistic particles within the jet, or by hadronic reactions through pion decay. In the IC case, if the photons being accelerated are the very same synchrotron photons emitted by the particles in the jet, we have a Synchotron Self-Compton (SSC) emission scenario. If the to-be-accelerated low-energy photons originate from thermal emission of the matter surrounding the black hole (the BLR, the disk, etc.), we have an External Compton (EC) scenario. The IC emission peaks mostly in the gamma-ray range. Radiative processes and emission scenarios will be discussed in more detail in Chapter 3.

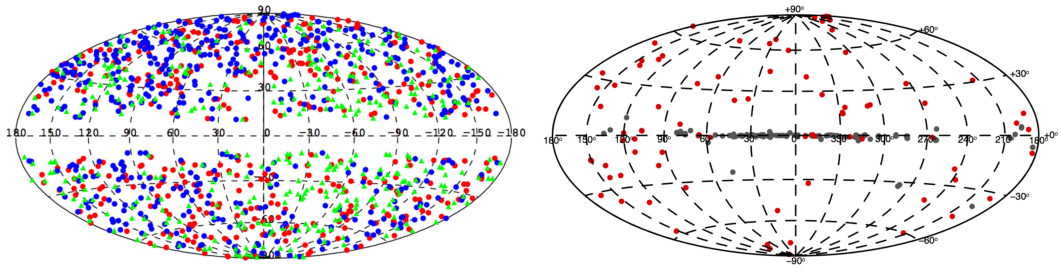

Figure 2.3: Maps of gamma-ray sources in the HE and VHE range. Taken from [3].

2.2.1 The blazar sequence

In Figure 2.4 it is shown the so-called *Blazar sequence*. The authors of [10] have divided the blazars detected by *Fermi*-LAT at the time and grouped them according to their IC luminosity $\nu L_{\nu,IC}$, complementing the work of [11] which had previously grouped the sources according to their synchrotron luminosity $\nu L_{\nu,s}$.

[10]: Ghisellini et al. (2017), "The Fermi blazar sequence"

[11]: Fossati et al. (1998), "A unifying view of the spectral energy distributions of blazars"

The Blazar sequence seems to support the classification of BL Lac objects: BL Lacs are classified according to their synchrotron peak frequency and luminosity, ν_s and $\nu L_{\nu,s}$, and the IC peak frequency and luminosity, ν_{IC} and $\nu L_{\nu,IC}$. Low-frequency peaked BL Lac objects (LBLs) have $\nu_s < 10^{14}$ Hz, intermediate-frequency peaked BL Lac objects (IBLs) have $10^{14} < \nu_s < 10^{15}$ Hz, while high-frequency peaked BL Lac objects (HBLs) typically have $\nu_s > 10^{15}$ Hz.

From Figure 2.4, we observe a smooth transition in the energy of the synchrotron peaks. FSRQs and LBLs peak at lower energies (also known as Low Synchrotron Peaked or LSP), IBLs at intermediate energies, and

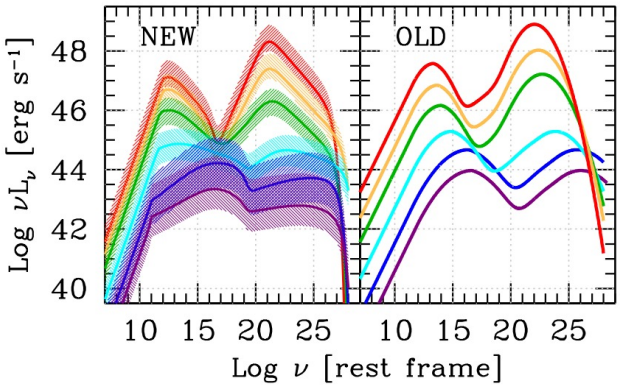

Figure 2.4: The new and old Blazar sequence from [10] and [11] respectively. The old sequence (right) binned blazar data in radio luminosity bins, while the new one (left) used bins of gamma-ray luminosity.

HBLs at higher energies. We also notice a transition from a Compton-dominated emission - where the bolometric energy carried by IC photons is larger than the energy carried by synchrotron photons as seen in the SED - to a slightly synchrotron-dominated emission. We discussed in Subsection 1.1.2 about gamma-ray selected AGNs. HBLs have significantly higher emission in the VHE energy range, which is consistent with the dominance of HBLs in the VHE range discussed in the last section. We also notice the peak energy of the first hump near the UV/X-ray range, whereas for LBLs the synchrotron peak frequency is located around sub-mm/FIR (far infrared) energies. Optical contributions from the accretion disc, the hot corona, dusty torus, etc., are not usually observed in HBL SEDs.

Blazar sequence interpretations

The origins of the Blazar sequence are still under debate. There are efforts to understand blazars in the context of a unified AGN theory. In [12], the authors propose that FSRQs evolve into LBLs and later into HBLs. As surrounding matter gets accreted into the AGN's core, there is fewer thermal radiation from the surrounding matter to be potentially up-scattered via IC processes. This scenario supports the interpretation provided in [10], where the shift from a Compton-dominated emission and the shift to higher peak frequencies is likely due to a change from an EC scenario, where the observed IC is dominated by thermal photons from the BLR and torus that were upscattered to gamma-ray energies, to an SSC emission. In the EC scenario, the cooling rate of particles in the jet is energy independent and depends only on the jet power, whereas the cooling rate in an SSC scenario strongly depends on the observed synchrotron luminosity. An increased synchrotron luminosity also means an increased synchrotron self-absorption rate, leading to a higher Compton dominance (see, e.g., [13]). An expansion of this interpretation was provided in [14], where IBLs would be in fact misaligned HBL objects.

On the other side of the discussion, some authors propose that the Blazar sequence could actually be the result of a selection bias. This bias would

[12]: Böttcher et al. (2002), "An evolutionary scenario for blazar unification"

[13]: Dermer et al. (2009), *High energy radiation from black holes: gamma rays, cosmic rays, and neutrinos*

[14]: Meyer et al. (2011), "From the blazar sequence to the blazar envelope"

be caused by the difficulty in determining the redshift of BL Lac objects [6]. That would induce the selection towards nearby objects with a high synchrotron peak frequency.

[6]: Giommi et al. (2012), "A simplified view of blazars"

2.2.2 Flux variability of blazars

Blazars exhibit strong variability across the electromagnetic spectrum [15], which means that their brightness can change rapidly and dramatically over timescales ranging from minutes to years. Minute-scale variability was first observed in the VHE energy range in HBL objects (e.g. [16, 17]).

[15]: Ulrich et al. (1997), "Variability of active galactic nuclei"

[16]: Aharonian et al. (2007), "An exceptional very high energy gamma-ray flare of PKS 2155–304"

[17]: Albert et al. (2007), "Variable very high energy γ-ray emission from Markarian 501"

The variability of Blazars can be attributed to several factors, including inhomogeneities in the jet flow (e.g., [18]), turbulence within the jet (e.g., [19]) and others.

[18]: Böttcher et al. (2010), "Timing signatures of the internal-shock model for blazars"

[19]: Guo et al. (2016), "Efficient production of high-energy nonthermal particles during magnetic reconnection in a magnetically dominated ion-electron plasma"

2.3 The extreme HBL puzzle

2.3.1 A historical overview

As detection technology has improved, more and more BL Lac objects have been detected across the electromagnetic spectrum. Mrk 501 was detected by the X-ray telescope on board the *BeppoSAX* satellite [20], showing "unprecedented syncrothron activity" [21] where the X-ray spectrum (0.2 - 200 keV) was modelled with a power law ($\propto E^{-\alpha}$) and exhibited a spectral index $\alpha < 1$ suggesting that synchrotron emission would peak above $\sim$ 100 keV $\sim 10^{19}$ Hz, around four orders of magnitude above the usual HBL classification. In [22], more X-ray measurements of a selected sample of "extreme" synchrotron-peaked blazars were presented. The authors pointed to variations in the spectral indices and the energy of the synchrotron peak relative to previous observations. Such variations were not observed in FSRQ and LBL populations.

[20]: Boella, G. et al. (1997), "BeppoSAX, the wide band mission for X-ray astronomy"

[21]: Pian et al. (1997), "BeppoSAX observations of unprecedented synchrotron activity in the BL Lacertae object Markarian 501"

[22]: Costamante, L. et al. (2001), "Extreme synchrotron BL Lac objects - Stretching the blazar sequence"

In the gamma-ray realm, interest peaked: the strong synchrotron activity coming out of these extreme blazars indicated electrons with sufficiently high energy to boost photons to TeV energies. Several studies attempted to find and select the best blazar candidates for TeV detection (e.g., [23]). In the VHE range, the second generation of imaging atmospheric Cherenkov telescopes (IACTs), composed by the Very Energetic Radiation Imaging Telescope Array System (VERITAS) [24], the High Energy Stereoscopic System (H.E.S.S.) [25] and the Major Atmospheric Gamma Imaging Cherenkov Telescopes (MAGIC) [26] collaborations, have now enough sensitivity to detect these EHBLs in the TeV range (energies > 100 GeV). Data from radio to gamma-ray frequencies have provided further insight into the nature of EHBLs.

[23]: Costamante, L. et al. (2002), "TeV candidate BL Lac objects"

[24]: Weekes et al. (2002), "VERITAS: the very energetic radiation imaging telescope array system"

[25]: Benbow et al. (2005), "The status and performance of H.E.S.S."

[26]: Lorenz (2004), "Status of the 17 m ∅ MAGIC telescope"

Several surveys were conducted to identify this source population. The 3HSP catalogue [27] expands the 1WHSP [28] and 2WHSP [29] catalogues to identify HBL and EHBL candidates with comprehensive multiwavelength (MWL) measurements from radio up to VHE gamma rays. As summarised in [30], EHBLs show three distinct behaviours:

[27]: Chang, Y.-L. et al. (2019), "The 3HSP catalogue of extreme and high-synchrotron peaked blazars"

[28]: Arsioli, B. et al. (2015), "1WHSP: An IR-based sample of 1000 VHE blazar candidates"

[29]: Chang, Y.-L. et al. (2017), "2WHSP: A multi-frequency selected catalogue of high energy and very high energy blazars and blazar candidates"

[30]: Biteau et al. (2020), "Progress in unveiling extreme particle acceleration in persistent astrophysical jets"

1. During large flares, blazars may temporarily exhibit extreme behaviour, characterised by a shift in energy peaks to higher values. This behaviour is temporary, and the objects eventually return to their typical state as a HBL.
2. Some blazars display a constant hard synchrotron spectrum up to 10-100 keV, with spectral indices of $\alpha > 2$, without a consistent hard spectrum in the TeV range.
3. Other blazars exhibit a persistent hard gamma-ray spectrum with a peak above several TeV, which remains largely unchanged despite variations in flux. The synchrotron spectrum of these objects typically peaks in the X-ray range.

In Figure 2.5 we see three examples of the behaviours listed above. (1) Mkn 501 is an HBL that shows an increase in the energy of the synchrotron and IC peaks in comparison to long quiescent states, i.e. periods of constant flux without flaring events. (2) 1ES 1426+428 an HBL with a synchrotron peak persistently shifted toward higher energies. (3) 1ES 0229+200, with persistent synchrotron and IC peaks above the usual HBL classification ($\nu_s > 10^{15}$).

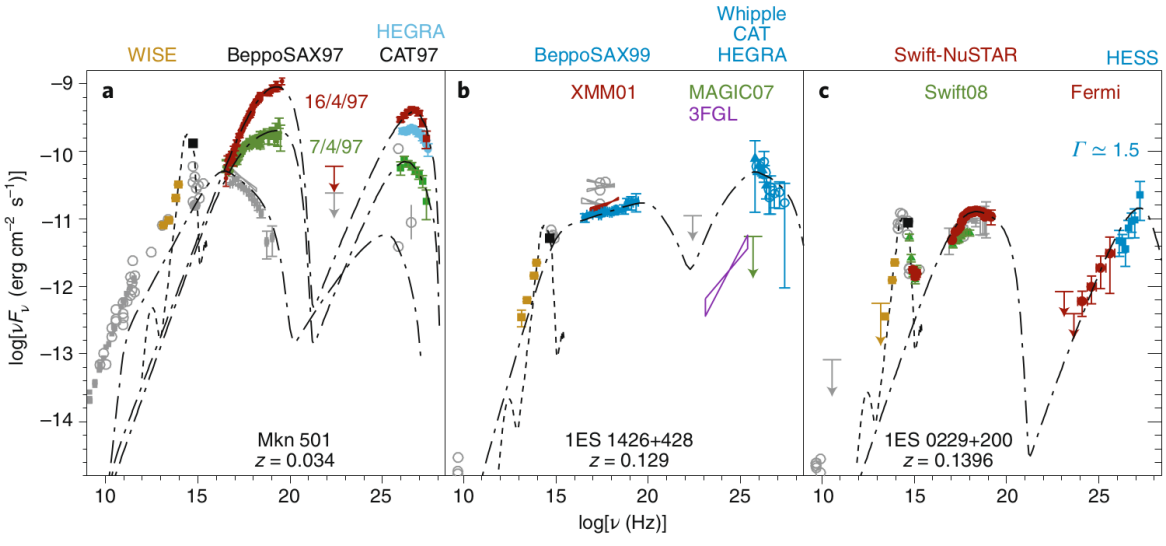

Figure 2.5: EHBL SEDs that demonstrate three different extreme behaviours. SSC guideline models are depicted as dashed-dotted lines. Extracted from [30] (see for further references)

2.3.2 EHBLs emission

Historically, the SED of BL Lac objects have been described using a one-zone leptonic SSC model (e.g. [31]): A population of electrons and positrons, propagating in a relativistic compact spherical region, interacts with magnetic fields and emits synchrotron radiation. These synchrotron photons are upscattered to higher gamma-ray energies via IC processes by these same electrons and positrons.

[31]: Maraschi et al. (1992), "A jet model for the gamma-ray–emitting Blazar 3C 279"

One-zone SSC models fail to fully describe EHBL emission data without requiring non-physical conditions, such as a very high minimum energy of the electron population in the emission region [32]. Other scenarios have been proposed in an attempt to explain the SED of EHBLs, for instance, EC scenarios with photons from the accretion disk [33], the BLR [34], and/or the dusty torus (DT) [35]. We discuss more about the challenges of modelling EHBLs and provide insight, based on the findings of this work, in Chapter 9 and Chapter 10.

[32]: Tavecchio et al. (2009), "The hard TeV spectrum of 1ES 0229+200: new clues from Swift"
[33]: Dermer et al. (1993), "Model for the high-energy emission from blazars"
[34]: Sikora et al. (1994), "Comptonization of diffuse ambient radiation by a relativistic jet: The source of gamma rays from blazars?"
[35]: Błażejowski et al. (2000), "Comptonization of infrared radiation from hot dust by relativistic jets in quasars"

Other scenarios considered proton-induced synchrotron emission and photon-hadron interactions [36, 37], where, a hadronic population exists in the emission region and contributes to the overall emission of the source, i.e., in addition to the usual leptonic scenarios. These models have been used to describe EHBL emission data at the expense of including more degrees of freedom in the models.

[36]: Böttcher et al. (2013), "Leptonic and hadronic modeling of Fermi-detected blazars"
[37]: Prosekin et al. (2012), "Time structure of gamma-ray signals generated in line-of-sight interactions of cosmic rays from distant blazars"

In [38], the authors analysed MWL data from a sample of EHBLs in which they state that the SSC model can reproduce the extreme properties of EHBL SEDs, however, it requires a very high minimum energy of the electron population in the emission region, and conditions orders out of equipartition ($\gg 1$) that can be estimated from the ratio between the energy density of the electron population and the energy density of the magnetic fields in the emission region.

[38]: Costamante et al. (2018), "The NuSTAR view on hard-TeV BL Lacs"

Due to the limited sensitivity - the minimum energy flux (commonly in erg per cm^2 per second) that a given instrument can detect within a certain amount of time - of current instruments, especially in the gamma-ray range, studies are usually limited to either flare events or long observation periods. Therefore, time evolution plays an important role in the analysis of EHBL data.

2.4 VERITAS observations of EHBLs

Two sources appear across EHBLs studies, the objects 1ES 0229+200 and 1ES 1218+304. 1ES 0229+200 first detected by the H.E.S.S. Collaboration [39] and 1ES 1218+304 first detected by the MAGIC Collaboration [40] are two EHBLs that fall into the third category of EHBLs, with persistent

[39]: Aharonian, F. et al. (2007), "New constraints on the mid-IR EBL from the HESS discovery of VHE gamma rays from 1ES0229+200"
[40]: Albert et al. (2006), "Discovery of very high energy gamma rays from 1ES 1218+30.4"

hard spectrum, and a gamma ray spectrum that peaks above several TeV. **These two objects will be the focus of this work.**

The *Very Energetic Radiation Imaging Telescope Array System* [41] (VERITAS) is in its 16th year of service since it was first commissioned in 2007 [42], at the time of writing this thesis. VERITAS dedicates two-thirds of its observation time to extragalactic observations composed mainly of Blazar observations. The VERITAS Collaboration reported its first spectral measurements of 1ES 0229+200 in 2014 [43] and the detection of 1ES 1218+304 in 2009 [44]. In [43] and [45], the authors used a one-zone SSC model to model the MWL SED, including VHE gamma-ray data collected between the periods of 2009 and 2012 for 1ES 0229+200 and a period of one month in 2009 for 1ES 1218+304. In these works, the one-zone SSC model was able to reproduce the SED of these sources, but again at the expense of having unexpected conditions, as mentioned in Section 2.3. At the time of writing this thesis, the VERITAS Collaboration had collected $\sim$ 180 h of data on 1ES 0229+200 and 1ES 1218+304 each. In this work, we will present the results of a long-term study that accounts for source variability across different wavelengths to further probe the behaviour of the EHBLs 1ES 0229+200 and 1ES 1218+304. We will introduce the VERITAS detector in more detail in Subsection 4.1.3.

[41]: Holder (2011), "VERITAS: Status and highlights"

[42]: Holder et al. (2006), "The first VERITAS telescope"

[43]: Aliu et al. (2014), "A three-year multi-wavelength study of the very-high-energy gamma-ray blazar 1ES 0229+200"

[44]: Acciari et al. (2009), "VERITAS observations of the BL Lac object 1ES 1218+304"

[45]: Archambault et al. (2014), "Test of models of the cosmic infrared background with the multiwavelength of the blazar 1ES 1218+30.4 in 2009"

2.5 Why EHBLs?

EHBLs are among the most energetic sources in the known universe. Charged particles can be accelerated to relativistic energies in EHBL jets, leading to radiation emission through various processes (see Chapter 3). The radiation emitted by these objects is then tied to the particle acceleration processes, which, in turn, are closely related to their matter content and distribution. Therefore, a better understanding of radiation emission expands our understanding of the mechanisms of particle acceleration that drive these powerful sources. However, the emission modelling of EHBLs has proved challenging. The energy output of EHBLs radiation extends beyond 10 TeV and the hard TeV spectra (e.g. [39]), combined with the cosmological distances these sources are found at ($z \gtrsim 0.1$), makes the emission from these sources not only a probe to particle acceleration, but also to the propagation of photons through the interstellar medium[5, 30, 46]. The main interactions that a gamma ray can undergo during its propagation are illustrated in Figure 2.6:

Extragalactic Background Light (EBL) The center-of-mass energy threshold of a photon-photon interaction favours the interaction of > 100 GeV gamma rays with low energy cosmic background radiation [47, 48], the EBL. VHE photons interact with infrared/optical EBL photons, generating a pair electron/positron, thus attenuating the observed VHE spectrum on Earth. The measured VHE gamma-ray

[5]: Biteau et al. (2022), "Gamma-ray cosmology and tests of fundamental physics"

[30]: Biteau et al. (2020), "Progress in unveiling extreme particle acceleration in persistent astrophysical jets"

[46]: Pueschel et al. (2021), *Cosmology with very-high-energy gamma rays*

[47]: Gould et al. (1967), "Opacity of the universe to high-energy photons"

[48]: Hill et al. (2018), "The Spectrum of the Universe"

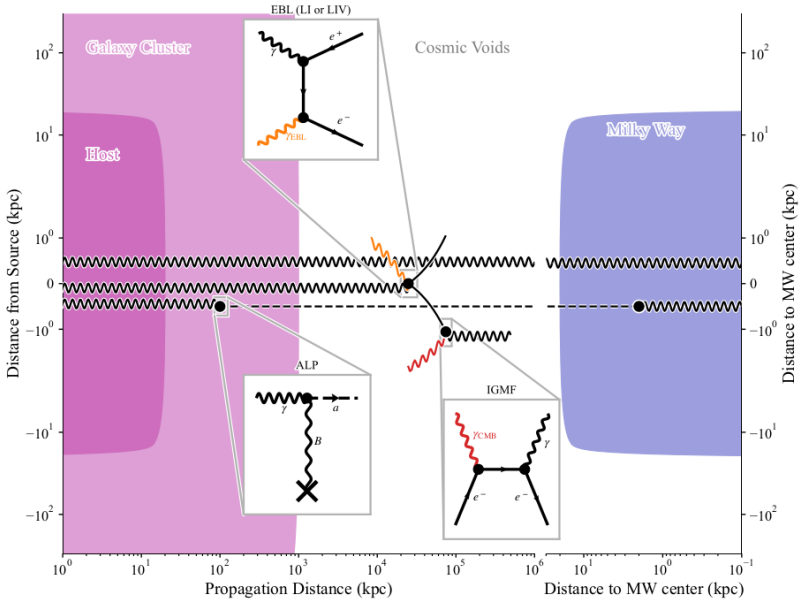

Figure 2.6: Schematic from possible interactions between a gamma-ray and the intergalactic medium. As a gamma-ray photon is emitted from its host galaxy it can interact an EBL photon and annihilate into an electron/positron pair before reaching the Milky Way. Following these EBL interactions, the pair electron/positron can have their trajectories bent by the IGMF, and interact with a CMB photon, creating a secondary lower-energy gamma ray. The gamma ray can hypothetically oscillate into an ALP during its propagation and oscillate back to a gamma-ray photon before reaching Earth. Adapted from [5]

flux can then be used to measure the EBL spectrum [13]. The EBL attenuation factor will depend on the energies of the interaction and the distance between the gamma-ray sources and Earth. Therefore, for higher gamma-ray energies and higher redshifts, the attenuation by the EBL will be stronger, making EHBLs excellent candidates for EBL studies (e.g. [49]).

Intergalactic Magnetic Field (IGMF) The universe is permeated with magnetic fields [50]. Pairs of electron-positrons, generated by the interaction of gamma rays with the EBL photons, can deviate from their initial trajectory in the presence of the IGMF. The electron/-positron pair can upscatter photons from local photon fields, such as the Cosmic Microwave Background (CMB) [51], via IC process up to gamma-ray energies, generating an apparent extended gamma-ray emission. A potential measure of the apparent extension of the gamma-ray emission from an EHBL can constrain the strength of the magnetic fields (e.g., [52]).

Physics beyond the standard model EHBLs are prime candidates for studies of physics beyond our current understanding of the standard model. Lorentz Invariance Violation (LIV) tests are commonly performed by searching for modified EBL attenuation effects [53, 54]. In LIV studies, gamma-ray data beyond the tenths of TeV are used to compare assumptions of an energy regime where Lorentz invariance would be no longer valid as opposed to the usual LI theory. Other theoretical scenarios include the oscillation of gamma rays into axion-like particles (ALPs), which could modify the observed gamma-ray spectrum at Earth [55, 56].

[50]: Durrer et al. (2013), "Cosmological magnetic fields: their generation, evolution and observation"

[51]: Jelley (1966), "High-Energy γ-Ray Absorption in Space by a 3.5°K Microwave Field"

[52]: Ackermann et al. (2018), "The Search for Spatial Extension in High-latitude Sources Detected by the Fermi Large Area Telescope"

[53]: Abdalla et al. (2021), "Sensitivity of the Cherenkov telescope array for probing cosmology and fundamental physics with gamma-ray propagation"

[54]: Lang et al. (2019), "Improved limits on Lorentz invariance violation from astrophysical gamma-ray sources"

[55]: De Angelis et al. (2011), "Relevance of axionlike particles for very-high-energy astrophysics"

[56]: Mirizzi et al. (2007), "Signatures of axionlike particles in the spectra of TeV gamma-ray sources"

Radiative processes and emission from blazars

3

The emission from blazars/EHBLs is observed across the electromagnetic spectrum, spanning from radio emission ($< 3 \times 10^9$ Hz $\sim 1 \times 10^{-5}$ eV) up to gamma rays ($> 3 \times 10^{19}$ Hz $\sim 1 \times 10^5$ eV).

Charged particles travel at relativistic speeds along a Blazar jet. In this work, we assume that these particles are electrons and positrons. These relativistic electrons and positrons interact with the magnetic fields present in the medium and emit photons via synchrotron radiation. Now, these synchrotron photons have a chance of being scattered by a higher-energy electron/positron to higher energies via Inverse Compton (IC) processes. These photons are beamed in the direction of propagation of the electrons because of relativistic effects. While propagating through the interstellar medium, photons at the highest energies photons, the IC-scattered photons, have a chance to interact with the low-energy photons of the extragalactic background light (EBL), thus being converted into pairs of electrons and positrons. The interaction with the EBL then attenuates the observed flux of the highest-energy photons that reach Earth.

In this chapter, we will introduce the aforementioned phenomena and how they are used to describe the emission from blazars as seen from Earth. The free parameters of the model, the analysis techniques and physical insights are presented and discussed in Chapter 9 and Chapter 10.

3.1 Acceleration processes

In this work, we leave the particle acceleration scenario unspecified; One of the most well-accepted hypotheses of particle acceleration to relativistic energies is via diffusive shock acceleration. First proposed by Enrico Fermi [57], it consists of an average positive energy gain of charged particles by stochastically scattering with randomly distributed magnetic clouds (or magnetic centres), known as second-order Fermi acceleration (SOFA). The net average energy gain in SOFA processes is on the order of $\sim \beta^2$ [58], where *beta* is the normalised velocity of the particle in the observer frame. The idea was later revised to the idea of particles scattering with relativistic magnetic shock fronts (e.g., [59]), known as first-order Fermi acceleration. In the case of FOFA, the net average energy gain is of the order of $\sim \beta$, where β in this case is the normalised velocity of the shock front. The net average energy gain of FOFA allows efficient particle acceleration, where the resulting particle

[57]: Fermi (1949), "On the origin of the cosmic radiation"

[58]: Morlino (2017), "High-energy cosmic rays from supernovae"

[59]: Blandford et al. (1978), "Particle acceleration by astrophysical shocks."

spectrum is given by a power law in energy, $dN/dE \propto E^{-\alpha}$, with $\alpha \sim 2$. It is also worth mentioning other acceleration scenarios that are proposed in the literature:

Shear acceleration Relativistic outflow (in a Blazar jet) with shears in the velocity of the background flow could induce particle acceleration similar to SOFA [60]. A spine-sheath structure within the jet could produce these conditions[61].

[60]: Rieger et al. (2004), "Shear acceleration in relativistic astrophysical jets"

[61]: Sikora et al. (2016), "A spine–sheath model for strong-line blazars"

Magnetic reconnection Fast variability times could be explained by the reconnection of magnetic lines in plasma in jetted emission from AGN. A jet-within-jet approach would explain co-spatial acceleration of smaller structures when combined with an enveloped emission from schock acceleration [62]. Magnetic structures in the jet are prone to instabilities that can release energy upon reconnection, thus accelerating particles [63, 64].

[62]: Shukla et al. (2020), "Gamma-ray flares from relativistic magnetic reconnection in the jet of the quasar 3C 279"

[63]: Chiuderi et al. (1989), "Extragalactic jets as current-carrying systems. I. Equilibrium and stability"

[64]: Giannios, D. et al. (2006), "The role of kink instability in Poynting-flux dominated jets"

3.2 Relativistic effects

The observed flux of photons on Earth is affected by special relativity effects. That is, the flux observed at Earth is beamed (Subsection 3.2.1) and boosted by relativistic Doppler effects (Subsection 3.2.3). In this section, we introduce these concepts.

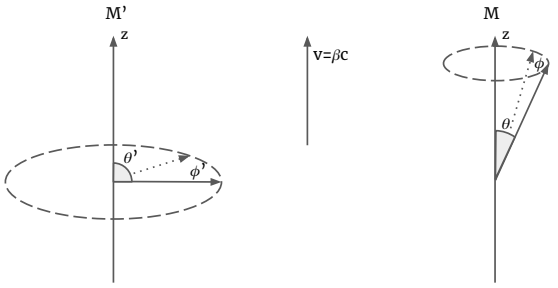

Figure 3.1: Relativistic angles transformations between two inertial reference frames, M and M' with relative velocity v.

Let us consider two inertial reference frames, M and M', where M' is the rest frame of a photon emitting region that moves with a velocity $v = \beta c$ with respect to the observer frame, M. From now on, we define all primed quantities (e.g. θ') as measured in the emission region frame M' and the unprimed quantities as measured in the stationary observer's frame M.

The bulk Lorentz factor of the co-moving frame M', Γ, is given by

$$\Gamma = \frac{1}{\sqrt{1-\beta^2}}. \tag{3.1}$$

The angles θ, ϕ, θ', and ϕ' are defined as shown in Figure 3.1. Lorentz transformations impose

$$\mu' = \frac{\mu - \beta}{1 - \beta\mu}, \tag{3.2}$$

$$\mu = \frac{\mu' + \beta}{1 + \beta\mu'}, \tag{3.3}$$

$$\phi' = \phi, \tag{3.4}$$

where $\mu = \cos\theta$.

A photon with energy ε' in the co-moving frame M', will have an energy ε observed in frame M given by [13]

[13]: Dermer et al. (2009), *High energy radiation from black holes: gamma rays, cosmic rays, and neutrinos*

$$\varepsilon = \frac{\varepsilon'}{\Gamma(1 - \beta\mu)}, \tag{3.5}$$

where we define the **Doppler factor**

$$\delta_D \equiv \frac{\varepsilon}{\varepsilon'} = \frac{1}{\Gamma(1 - \beta\mu)}. \tag{3.6}$$

3.2.1 Relativistic beaming

From Equation 3.3, it is possible to notice that for an angle $0 \leq \theta' \leq \pi/2$, and noting that $0 \leq \beta < 1$, we have

$$\mu = \mu' \frac{1 + \beta/\mu'}{1 + \beta\mu'} \implies \mu \geq \mu' \implies \theta < \theta' \text{ for } 0 \leq \theta' \leq \pi/2.$$

Now consider a photon emitted at an angle $\theta' = \pi/2$ in the co-moving frame M'. Therefore, from Equation 3.3 we have $\mu = \beta$. From Equation 3.1, we find

$$\beta = \sqrt{1 - \frac{1}{\Gamma^2}} = \mu = \cos\theta.$$

If $\Gamma \gg 1$, we can approximate

$$\sqrt{1 - \frac{1}{\Gamma^2}} \approx 1 - \frac{1}{2\Gamma^2},$$
$$\cos\theta \approx 1 - \frac{\theta^2}{2},$$

By comparing the two equations above, we can verify that for highly relativistic motions ($\Gamma \gg 1$), photons will be beamed into an angle θ_{beam} given by

$$\theta_{beam} = \frac{1}{\Gamma}. \tag{3.7}$$

3.2.2 Relativistic Doppler effect

We defined in Equation 3.5 and Equation 3.6 how the energy of a photon emitted in frame M', ε', is observed in frame M. Recalling the relation between a photon energy, ε, and its frequency, ν

$$\varepsilon = h\nu, \tag{3.8}$$

where h is the Planck constant, we have

$$\frac{\nu}{\nu'} = \delta_D. \tag{3.9}$$

Let us now consider that the photon is emitted at an angle $\theta' = 0$, where $\mu = \mu' = 1$. Using Equation 3.6, we can then calculate $\delta_{D,forward}$ as

$$\delta_{D,forward} = \frac{1}{\Gamma(1-\beta)} = \frac{(1+\beta)}{\Gamma(1-\beta^2)} = (1+\beta)\Gamma \approx 2\Gamma, \tag{3.10}$$

where we consider the relativistic case of $\beta \to 1$. We can repeat this exercise with a photon being emitted at an angle $\theta' = \pi$, that is, moving away from the observer. In this case, $\mu = \mu' = -1$. We can then calculate $\delta_{D,backward}$, with $\beta \to 1$,

$$\delta_{D,backward} = \frac{1}{\Gamma(1+\beta)} \approx \frac{1}{2\Gamma}. \tag{3.11}$$

Noting that $\Gamma \geq 1$, we can see that the photons emitted "forward" will have their frequencies increased while the photons emitted "backward" will have their frequencies decreased.

3.2.3 Doppler boosting

The spectral flux density of photons in a frequency interval $[\nu, \nu + d\nu]$, F_ν, is given by

$$F_\nu \equiv \frac{dE}{dtdAd\nu} = \frac{h\nu dN}{dtdAd\nu}, \tag{3.12}$$

where dN is the number of photons. The unit area interval dA can be written as $dA = d_L^2 d\Omega$, where d_L^2 is the distance between the source region and the observer (also known as the "luminosity distance") and $d\Omega$ is the solid angle unit interval, as

$$d\Omega = \sin\theta d\theta d\phi = -d\cos\theta d\phi = -d\mu d\phi. \tag{3.13}$$

If we take the ratio between the observed spectral flux density, F_ν and the emitted spectral flux density (also known as intrinsic emission), $F'_{\nu'}$, we obtain the following:

$$\frac{F_\nu}{F'_{\nu'}} = \frac{\frac{h\nu dN}{dtdAd\nu}}{\frac{h\nu' dN'}{dt' dA' d\nu'}} = \frac{\nu}{\nu'}\frac{d\nu'}{d\nu}\frac{dN}{dN'}\frac{dt'}{dt}\frac{d\Omega'}{d\Omega}. \tag{3.14}$$

Since dN is the number of photons, an integer number, it does not change between the two reference frames. Therefore

$$dN = dN' \tag{3.15}$$

Noting that frequency is defined as the number of cycles undergone during one unit of time interval,

$$\nu = \frac{1}{\Delta t} = \frac{1}{dt}, \tag{3.16}$$

combined with Equation 3.9, we have

$$\frac{\nu}{\nu'} = \frac{d\nu}{d\nu'} = \frac{dt'}{dt} = \delta_D. \tag{3.17}$$

Lastly, from Equation 3.4, Equation 3.2 and Equation 3.1, we get

$$d\phi' = d\phi, \tag{3.18}$$

$$d\mu' = \frac{d\mu(1-\beta\mu) + (\mu-\beta)\beta d\mu}{(1-\beta\mu)^2} = \frac{d\mu}{\Gamma^2(1-\beta\mu)^2} = \delta_D^2 d\mu, \tag{3.19}$$

implying,

$$d\Omega' = \delta_D^2 d\Omega. \tag{3.20}$$

Finally, plugging in Equation 3.15, Equation 3.17, and Equation 3.20 into Equation 3.14, we get

$$F_\nu = \delta_D^3 F'_{\nu'}. \tag{3.21}$$

This effect is known as *Doppler boosting*. It implies that intrinsic emission at the source is observed to be amplified by a factor of δ_D^3. It can be interpreted as a "focussing" of particles (due to a decreased solid angle) and also a shift towards higher frequencies. The energy flux density $F \equiv \int F_\nu d\nu$ is also boosted by a factor δ_D^4:

$$F \equiv \int F_\nu d\nu = \delta_D^4 \int F'_{\nu'} d\nu' = \delta_D^4 F'. \tag{3.22}$$

3.3 Synchrotron radiation

A relativistic charged particle will emit synchrotron radiation when accelerated in the presence of a magnetic field. A particle with charge Q and velocity $\vec{v}$ travelling through a magnetic field $\vec{B}$, will have acceleration $\vec{a} \equiv d\vec{v}/dt$ given by

$$\vec{F} = \frac{d}{dt}(\gamma m \vec{v}) = Q\left(\vec{E} + \frac{1}{c}\vec{v} \times \vec{B}\right) \implies$$
$$\implies \frac{d\vec{v}}{dt} = Q\frac{\vec{v} \times \vec{B}}{\gamma mc} \equiv \omega_L \left(\vec{v} \times \frac{\vec{B}}{B}\right),$$

where γ is the Lorentz factor of the particle*, and we assume that no electric field is present ($\vec{E} = 0$). The Larmor angular frequency ω_L is defined:

$$\omega_L \equiv \frac{QB}{\gamma mc}. \tag{3.23}$$

The accelerated particle loses energy to the emitted synchrotron radiation at a rate $\left(\frac{dE}{dt}\right)_{\rm syn}(\psi)$ given by [13]:

$$\left(\frac{dE}{dt}\right)_{\rm syn}(\psi) = -\frac{16\pi c}{3}\left(\frac{Q^2}{mc^2}\right)^2 \left(\frac{B^2}{8\pi}\right)\beta_{\rm par}^2 \gamma^2 \sin^2\psi, \tag{3.24}$$

where $\beta_{\rm par} = \left|\vec{\beta_{\rm par}}\right| = |\vec{v}|/c$ is the normalised particle's velocity, and ψ is the pitch angle between the particle's velocity and the magnetic field orientation in such a way that $\vec{\beta_{\rm par}}.\vec{B} = \beta_{\rm par} B \cos\psi$. Particles are expected to be randomly distributed over pitch angles due to random, faster than the energy loss rate, scattering [13, 65]. We can look then at the energy-

[13]: Dermer et al. (2009), *High energy radiation from black holes: gamma rays, cosmic rays, and neutrinos*
[65]: Boettcher et al. (2012), *Relativistic jets from active galactic nuclei*

* Important to note the distinction between the bulk Lorentz factor of the co-moving frame/acceleration region Γ

loss rate for an average over the pitch angle given by

$$\left(\frac{dE}{dt}\right)_{\rm syn} = \frac{1}{4\pi}\int_{4\pi}\left(\frac{dE}{dt}\right)_{\rm syn}(\psi)d\Omega =$$

$$= -\frac{1}{4\pi}\frac{16\pi c}{3}\left(\frac{Q^2}{mc^2}\right)^2\left(\frac{B^2}{8\pi}\right)\beta_{\rm par}^2\gamma^2\frac{1}{2}\int_{-1}^{1}\sin^2\psi d\cos\psi =$$

$$-\frac{4}{3}\frac{8\pi c}{3}\left(\frac{Q^2}{mc^2}\right)^2 U_B\beta_{\rm par}^2\gamma^2, \quad (3.25)$$

where $U_B = B^2/8\pi$ is the magnetic field energy density. We can express Equation 3.25 in terms of the particle's Lorentz factor γ, recalling the relation $E = \gamma mc^2$, and taking the electron's charge ($Q = e$) and mass ($m = m_e$), we have

$$-\left(\frac{d\gamma}{dt}\right)_{\rm syn} = -\dot{\gamma}_{\rm syn} = \frac{4}{3}c\sigma_T u_B\beta_{\rm par}^2\gamma^2 \quad (3.26)$$

where we introduce the Thomson cross section:

$$\sigma_T = \frac{8\pi}{3}\left(\frac{e^2}{m_e c^2}\right)^2, \quad (3.27)$$

where the magnetic field energy density U_B per electron is given by

$$u_B = \frac{B^2}{8\pi m_e c^2}. \quad (3.28)$$

For a highly relativistic electron ($\gamma \gg 1$), Equation 3.26 becomes

$$-\dot{\gamma}_{\rm syn} = \frac{4}{3}c\sigma_T u_B\gamma^2. \quad (3.29)$$

Then, the typical synchrotron cooling timescale for a single electron is given by

$$\tau_{\rm syn} = \frac{\gamma}{|\dot{\gamma}_{\rm syn}|} = \frac{3}{4c\sigma_T u_B\gamma}. \quad (3.30)$$

The observed peak frequency of synchrotron radiation produced by a single electron can be described by the following relation:

$$\nu_{\rm pk}^{\rm syn} \cong \frac{eB}{2\pi m_e c}\gamma^2. \quad (3.31)$$

In Figure 3.2, we compare the observed peak frequency of synchrotron radiation given in Equation 3.31 for different values of the magnetic field

B as a function of the Lorentz factor of the particle, γ. As mentioned in Section 2.3, the values of $\nu_{\rm pk}^{\rm syn}$ are observed up to frequencies of $> 10^{15}$ Hz in HBLs and up to $\sim 10^{19}$ Hz in EHBLs. In Figure 3.2 the dashed lines represent the frequencies converted to energy, of 0.3 keV, 100 keV, and 300 MeV (Equation 3.8). With this, we can derive some typical values of the magnetic field B in EHBLs - low values such as 1μG require large electron Lorentz factors, while strong magnetic fields of 100 G result in synchrotron radiation up to HE gamma-ray energies. Very low magnetisation values ($\sim$ 1 mG) have been observed in EHBLs (e.g., [38]).

[38]: Costamante et al. (2018), "The NuSTAR view on hard-TeV BL Lacs"

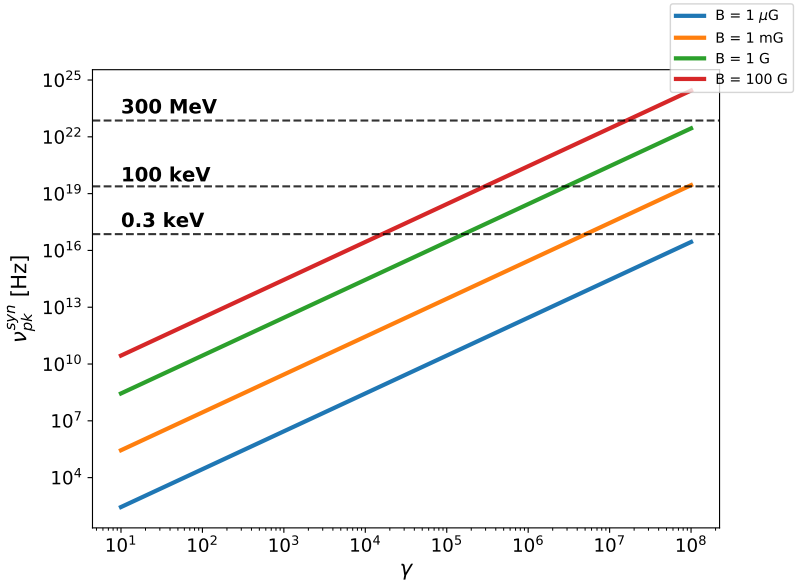

Figure 3.2: The synchrotron peak frequency from a single electron as a function of the electron's Lorentz factor γ, for different magnetic field strengths. The dashed lines represent the corresponding equivalent energies from $E = h\nu$, of 0.3 keV, 100 keV and 300 MeV.

The complete derivation of the synchrotron radiation flux of a single electron is covered extensively in several references (e.g. [66–68]). The power $P_{\rm syn}$ emitted by an electron with a pitch angle $\psi = \pi/2$ in a magnetic field with strength B, at a frequency ν is given by

[66]: Blumenthal et al. (1970), "Bremsstrahlung, synchrotron radiation, and Compton scattering of high-energy electrons traversing dilute gases"
[67]: Rybicki et al. (1979), *Radiative processes in astrophysics*
[68]: Longair (2011), *High energy astrophysics*

$$P_{\rm syn}(\nu) = \frac{dE}{dtd\nu} = \frac{\sqrt{3}e^3 B}{h} F_{syn}(x), \tag{3.32}$$

where $x = \nu/\nu_c$, and

$$\nu_c = \frac{3}{2}\frac{eB}{2\pi m_e c}\gamma^2. \tag{3.33}$$

$F_{syn}(x)$ is the elementary synchrotron flux, defined as

$$F_{syn}(x) \equiv x \int_x^\infty d\xi K_{5/3}(\xi), \tag{3.34}$$

[69]: MacDonald (1898), "Zeroes of the Bessel functions"

where $K_{5/3}$ is the Modified Bessel function of the second kind [69] given by

$$K_{5/3}(\xi) = \frac{\Gamma\left(\frac{1}{2}\right)\left(\frac{\xi}{2}\right)^{5/3}}{\Gamma\left(\frac{13}{6}\right)} \int_1^\infty dt e^{-\xi t}\left(t^2-1\right)^{7/6}, \tag{3.35}$$

with ξ as the integration variable and $\Gamma(n)$ is the Gamma function.

Figure 3.3 shows the synchrotron spectrum of a single electron computed from Equation 3.34.

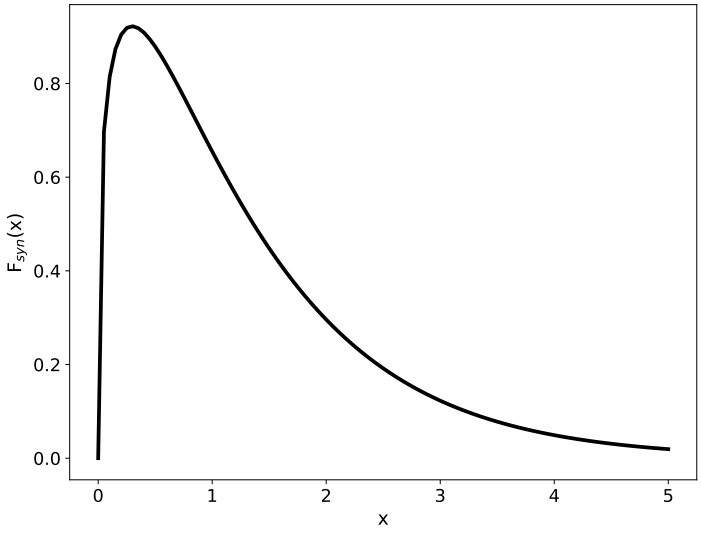

Figure 3.3: Elementary synchrotron radiation flux as a function of $x = \nu/\nu_c$. ν_c is the resonance frequency, defined in Equation 3.33, where γ is the electron Lorentz factor, and B is magnetic field strength.

So far we have only described the properties of synchrotron radiation emitted by a single particle, and more specifically, a single electron. More generally, the synchrotron radiation produced in a Blazar is expected to be emitted by a population of charged particles, usually electrons and positrons, that are accelerated in a relativistic region within the Blazar jet.

The synchrotron flux from a relativistic region with electron distribution $N_e(\gamma)$ is given by [70]:

[70]: Finke et al. (2008), "Synchrotron self-Compton analysis of TeV X-ray-selected BL Lacertae objects"

$$\nu F_\nu^{\text{syn}} = f_\varepsilon^{\text{syn}} = \frac{\sqrt{3}\delta_D^4 \nu' e^3 B}{4 d_L^2} \int_1^\infty d\gamma' N_e'(\gamma') R(x), \tag{3.36}$$

where $R(x)$ is given by:

$$R(x) = \frac{x}{2} \int_0^\pi d\theta \sin\theta \int_{\nu/\nu_c}^\infty d\xi K_{5/3}(\xi). \tag{3.37}$$

3.4 Compton (and Inverse Compton) scattering

The Compton effect is the scattering between a photon and an electron at rest, where the photon transfers some energy and momentum to the electron. The Inverse Compton (IC) scattering is when a relativistic high-energy electron transfers energy and momentum to a low-energy photon.

A scattering between a photon of energy $\varepsilon' = h\nu'$ and an electron, in the electron rest frame (ERF), is illustrated in Figure 3.4. Here we keep the notation of primed quantities referring to the ERF and non-primed quantities referring to the observers frame. The energy and momentum conservation of the system implies the following:

$$h\nu' + m_e c^2 = h\nu'_s + \gamma'_e m_e c^2 \tag{3.38}$$

$$x: \quad \frac{h\nu'}{c} = \frac{h\nu'_s}{c}\cos\chi' + \gamma'_e v'_e \cos\theta'_e \tag{3.39}$$

$$y: \quad \frac{h\nu'_s}{c}\sin\chi' = \gamma'_e v_e \sin\theta'_e, \tag{3.40}$$

where χ' and θ'_e are the scattered angles of the electron and photon, respectively (Figure 3.4). Here we used the relativistic momentum of the photon $p = \varepsilon/c$. If we introduce the dimensionless energy of the photon,

$$\epsilon = \frac{h\nu}{m_e c^2}, \tag{3.41}$$

Equations Equation 3.38, Equation 3.39 and Equation 3.40 become

$$\epsilon' + m_e c^2 = \epsilon'_s + \gamma'_e \tag{3.42}$$

$$x: \quad \epsilon' = \epsilon'_s \cos\chi' + \gamma'_e \beta'_e \cos\theta'_e \tag{3.43}$$

$$y: \quad \epsilon'_s \sin\chi' = \gamma'_e \beta'_e \sin\theta_e, \tag{3.44}$$

and $\beta'_e = v'_e/c$.

Solving Equations Equation 3.42, Equation 3.43 and Equation 3.44, we get that the energy ϵ'_s of the scattered photon is given by

$$\epsilon'_s = \frac{\epsilon'}{1 + \epsilon'(1 - cos\chi')}, \tag{3.45}$$

and with χ' ranging between $-1 < \chi' < 1$, we see that $\epsilon'/(1+2\epsilon') < \epsilon_s' < \epsilon'$.

The differential cross section for Compton scattering between an electron and a photon in the ERF is given by [13, 65]:

$$\frac{d\sigma_C}{d\epsilon_s' d\Omega_s'} = \frac{3}{16\pi}\sigma_T\left(\frac{\epsilon_s'}{\epsilon'}\right)^2\left(\frac{\epsilon_s'}{\epsilon'} + \frac{\epsilon'}{\epsilon_s'} - 1 + \cos^2\chi'\right)\times \\ \times\,\delta\left(\epsilon_s' - \frac{\epsilon'}{1+\epsilon'(1-cos\chi')}\right), \quad (3.46)$$

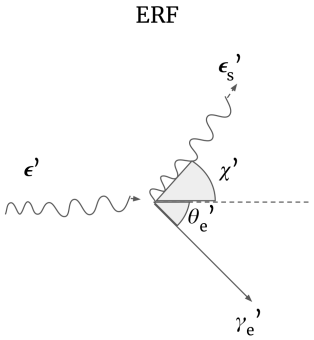

Figure 3.4: Geometry of the Compton scattering in the ERF.

where σ_T is defined in Equation 3.27 and $d\Omega_s' = d\phi_s' d\cos\chi'$. The total Compton cross section, also known as Klein-Nishina cross section, is then

$$\sigma_C(\epsilon') = \int_0^\infty d\epsilon_s' \oint d\Omega_s' \frac{d\sigma_C}{d\epsilon_s' d\Omega_s'} = \\ = \frac{3\sigma_T}{8\epsilon'^2}\left[4 + \frac{2\epsilon'^2(1+\epsilon')}{(1+2\epsilon')^2} + \frac{\epsilon'^2 - 2\epsilon' - 2}{\epsilon'}\ln(1+2\epsilon')\right]. \quad (3.47)$$

We can study the asymptotic behaviour of $\sigma_C(\epsilon')$ when $\epsilon' \ll 1$ and $\epsilon' \gg 1$. In such regimes, $\sigma_C(\epsilon')$ can be approximated to

$$\sigma_C(\epsilon') \to \begin{cases} \sigma_T\left[1 - 2\epsilon' + \frac{26}{5}\epsilon'^2 + \mathcal{O}(\epsilon'^3)\right], \epsilon' \ll 1, \\ \\ \frac{\pi r_e^2}{\epsilon'}\left[ln(2\epsilon') + 1/2 + \mathcal{O}(\epsilon'^{-1})\right], \epsilon \gg 1, \end{cases} \quad (3.48)$$

where $r_e = e^2/m_e c^2$ is the classical electron radius. These regimes are called Thomson ($\epsilon' \ll 1$) and Klein-Nishina regimes ($\epsilon' \gg 1$). We notice that at first order, in the Thomson regime, the Compton cross section approximates to the Thomson cross section (Equation 3.27), while as the energy increases the cross section decreases exponentially, as shown in Figure 3.5.

The general equation of the energy loss rate of an electron in the observer frame, where the electron has a Lorentz factor γ and a normalised velocity β, undergoing Compton scattering with a photon distribution $n_{ph}(\epsilon, \Omega_{ph})$ is written as

$$-\left(\frac{d\gamma}{dt}\right)_C = c\oint d\Omega_{ph}\int_0^\infty d\epsilon n_{ph}(\epsilon,\Omega_{ph})(1-\beta\mu)\times \\ \times \oint d\Omega_s \int_0^\infty d\epsilon_s(\epsilon_s - \epsilon)\frac{d\sigma_C(\epsilon')}{d\epsilon_s d\Omega_s}, \quad (3.49)$$

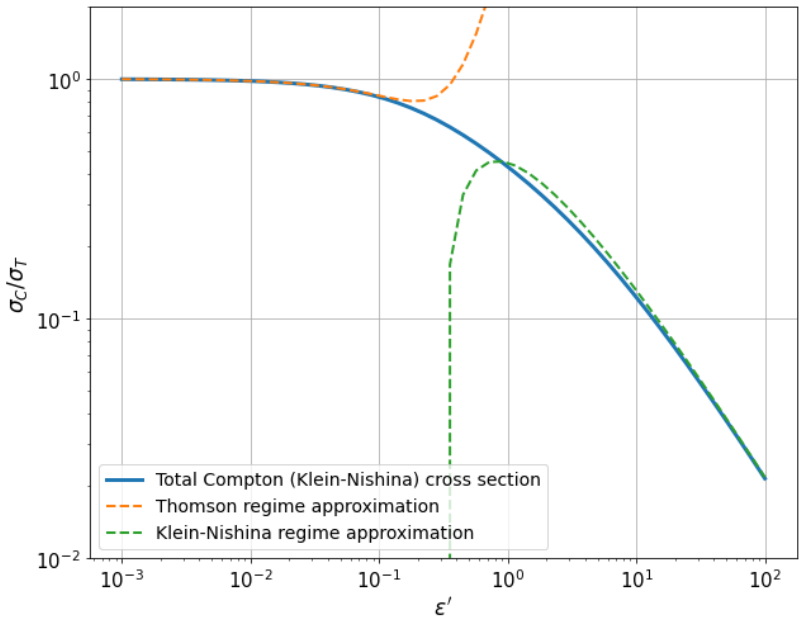

Figure 3.5: The normalized Compton cross section (solid blue) from Equation 3.47, and the asymptotic cases, the Thomson regime (dashed orange) and Klein-Nishina regime (dashed green), as obtained in Equation 3.48

where $d\Omega_{ph,s} = d\mu_{ph,s} d\phi_{ph,s}$, and $\mu_{ph,s} = \cos\theta_{ph,s}$ and $\theta_{ph,s}$ are the angles between the incoming/scattered photon and the initial direction of the electron's velocity (i.e., $\hat{\beta}$). In the observers frame, the differential cross section can be derived from Equation 3.46:

$$\frac{d\sigma_C}{d\epsilon_s d\Omega_s} = \frac{\epsilon_s}{\epsilon_s'} \frac{d\sigma_C}{d\epsilon_s' d\Omega_s'}, \tag{3.50}$$

and using the transformations from Equations 3.5 and 3.2 apply between the pairs (ϵ, ϵ_s) and (ϵ', ϵ_s'), and (μ, μ_s) and (μ', μ_s').

3.4.1 Synchrotron Self-Compton

A non-thermal electron population can scatter via IC, synchrotron photons emitted by this same population of electrons. This process is known as Synchrotron Self-Compton (SSC). Assuming an isotropic radiation field of synchrotron photons, the energy-loss rate of an electron undergoing SSC scattering will be given by

$$-\left(\frac{d\gamma}{dt}\right)_{\rm SSC} = -\dot{\gamma}_{\rm SSC} = \frac{4}{3} c\sigma_T \int_0^\infty d\epsilon \frac{n_{ph,syn}(\epsilon)}{\epsilon} G(\gamma\epsilon), \tag{3.51}$$

where $n_{ph,syn}(\epsilon)$ is the distribution of synchrotron photons and $G(E)$ [13] is

$$G(E) = \ln(1+4E)\left(1+\frac{3}{E}+\frac{3}{E}\frac{1}{E^2}+\frac{\ln(1+4E)}{2E}-\frac{\ln(4E)}{E}\right)- \\ -\frac{5}{2E}-\frac{4E}{1+4E}\left(\frac{2}{3}+\frac{1}{2E}+\frac{1}{8E^2}\right)+\frac{8}{3}E\frac{1+5E}{(1+4E^2)}+ \\ +\frac{1}{E}\sum_{n=1}^{\infty}\frac{(1+4E)^{-n}}{n^2}-\frac{\pi^2}{6E}-2. \quad (3.52)$$

If the synchrotron-emitting electrons are distributed in a spherical region with radius R_B (commonly referred to as "blob"), moving at a normalised velocity β relative to the observer - therefore, with a Doppler factor δ_D given by Equation 3.6 assuming $\mu \to 0$ - and the source is located at a distance d_L from the observer, the quantity $n_{ph,syn}(\epsilon)$ can be calculated with [70]:

$$n_{ph,syn}(\epsilon) = \frac{3d_L^2 f_\epsilon^{\rm syn}}{cR_B^2\delta_D^4\epsilon}, \quad (3.53)$$

where $f_\epsilon^{\rm syn}$ is given by Equation 3.36. Therefore, we can fully calculate the energy loss rate Equation 3.51 for a single electron.

The observed SSC flux from a relativistic blob with radius equal to R_B containing a population $N_e'(\gamma')$ of non-thermal electrons, can be fully calculated with [70]:

$$f_{\epsilon_s}^{\rm SSC} = \frac{9}{16}\frac{\sigma_T\epsilon_s'^2}{\pi R_B^2}\int_0^\infty d\epsilon' \frac{f_\epsilon^{\rm syn}}{\epsilon'^3}\int d\gamma' \frac{N_e'(\gamma')}{\gamma'^2}F_C(q,\Gamma), \quad (3.54)$$

where $F_C(q,\Gamma)$ is

$$F_C(q,\Gamma) = \left[2q+(1+2q)(1-q)+\frac{1}{2}\frac{(\Gamma q)^2}{1+\Gamma q}(1-q)\right]\times \\ \times H\left(q;\frac{1}{4\gamma'^2},1\right), \quad (3.55)$$

where H is the Heaviside function and

$$q \equiv \frac{\epsilon_s'/\gamma'}{\Gamma(1-\epsilon_s'/\gamma')},\ \Gamma = 4\epsilon'\gamma' \quad (3.56)$$

SSC energy loss rate in the Thomson regime

Expanding Equation 3.52 for $E \ll 1$, the lowest-order expansion yields $G(E) \approx \frac{32}{9}E^2$, which approximates Equation 3.51 to

$$-\dot{\gamma}_{\mathrm{SSC,\,T}} \approx \frac{4}{3} c\sigma_T \gamma^2 \int_0^\infty d\epsilon \epsilon n_{ph,syn}(\epsilon) = \frac{4}{3} c\sigma_T \frac{u_{ph}}{m_e c^2} \gamma^2, \tag{3.57}$$

where we introduce the energy density of the photon radiation field $u_{ph} = m_e c^2 \int_0^\infty d\epsilon \epsilon n_{ph,syn}(\epsilon)$. $-\dot{\gamma}_{\mathrm{SSC,\,T}}$ is the energy loss rate in the Thomson regime, where $E = \gamma\epsilon \ll 1$. By comparing Equation 3.24 and Equation 3.57, we observe that in the Thomson regime we have

$$\frac{\dot{\gamma}_{\mathrm{SSC,\,T}}}{\dot{\gamma}_{\mathrm{syn}}} = \frac{\tau_{\mathrm{syn}}}{\tau_{\mathrm{SSC,\,T}}} = \frac{u_{ph}}{u_B}, \tag{3.58}$$

where τ_{syn} is defined in Equation 3.30 and the SSC cooling timescale, τ_{SSC}, follows the same definition.

3.5 Flux attenuation by the Extragalactic Background Light

While Blazar radiation emission is collimated and localised, the Universe is permeated with background radiation. One of the components of this background radiation is the Extragalactic Background Light (EBL).

The intrinsic emission described above is not what is observed at Earth. Due to the typical values of Blazars' redshifts, their intrinsic emission at the highest energies is impacted by the EBL. The EBL extends from wavelengths 0.1 to 1000 μm ($\sim 10^{-3}$ eV - 10 eV), ranging from ultraviolet (UV) through optical and infrared (IR) light, as shown in Figure 3.6 [71]. The EBL spectral energy distribution in the wavelength range of $\sim$ 0.1 μm to $\sim$ 300μm stellar emission [48]. The optical range from $\sim$ 300 μm to $\sim$ 3000 μm is dominated by to infrared emission by galaxies with high redshifts [72]. Several works were conducted to measure and model the EBL (e.g. [73–75]), and to estimate and better understand the universe's opacity to the propagation of gamma rays.

[71]: Saldana-Lopez et al. (2021), "An observational determination of the evolving extragalactic background light from the multiwavelength HST/CANDELS survey in the Fermi and CTA era"
[48]: Hill et al. (2018), "The Spectrum of the Universe"
[72]: Lagache et al. (2005), "Dusty Infrared Galaxies"
[73]: Domínguez et al. (2011), "Extragalactic background light inferred from AEGIS galaxy-SED-type fractions"
[74]: Finke et al. (2010), "Modeling the extragalactic background light from starts and dust"
[75]: Franceschini, A. et al. (2008), "Extragalactic optical-infrared background radiation, its time evolution and the cosmic photon-photon opacity"

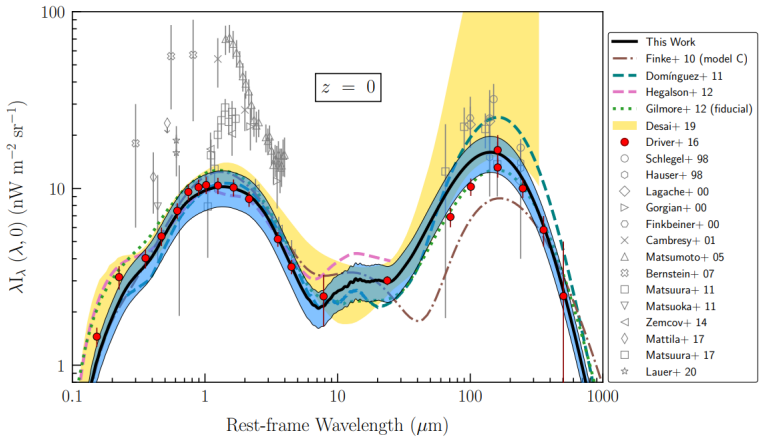

Figure 3.6: Spectral energy distribution of the EBL at $z = 0$ as measured in [71]. See [71] and references therein.

A photon-photon interaction can occur if the energy of the centre of mass is at least twice the mass of the electron. A photon of energy ε_1 interacts with a photon of energy ε_2 colliding at an angle Ψ with $\cos\Psi = \kappa$, produces a pair electron/positron. The pair will have in the centre-of-momentum frame (cm) - the frame where the sum of the momenta is equal to zero - a normalised velocity β_{cm} of

$$\beta_{cm} = \sqrt{1 - \frac{2}{\varepsilon_1 \varepsilon_2 (1-\kappa)}}. \tag{3.59}$$

Equation 3.59 then implies that

$$\varepsilon_1 \geq \frac{2}{\varepsilon_2 (1-\kappa)}, \tag{3.60}$$

so that for a head-on collision ($\kappa = -1$), the threshold condition is

$$\varepsilon_{1,th} = \frac{1}{\varepsilon_2}. \tag{3.61}$$

For a 1 TeV photon propagating through the Universe, Equation 3.61 yields $\varepsilon_{\gamma,th} = 1$ eV. In general, the threshold of the interaction of a VHE photon energy ε_γ(TeV), emitted from a far source with redshift z, interacting with an EBL photon of energy ε_{EBL}(eV), accounting for the expansion of the Universe is [74].

$$\varepsilon_\gamma(\text{TeV}) = \frac{0.26}{(1+z)\varepsilon_{EBL}(\text{eV})}. \tag{3.62}$$

The cross section for this interaction ($\gamma\gamma$ refers to a two-photon interaction) is given by [76]

[76]: Gould (2006), *Electromagnetic processes*

$$\sigma_{\gamma\gamma}(\beta_{cm}) = \frac{3}{16}\sigma_T(1-\beta_{cm}^2)\left[(3-\beta_{cm}^4)\ln\left(\frac{1+\beta_{cm}}{1-\beta_{cm}}\right) - 2\beta_{cm}(2-\beta_{cm}^2)\right], \tag{3.63}$$

such that the opacity for a gamma ray with energy ε_γ propagating through a field of EBL photons with a distribution $n_{EBL}(\varepsilon, \Omega; x)$ over a distance of length l is [65]

$$\tau_{\gamma\gamma} = \int_0^l dx \int_{4\pi} d\Omega(1-\kappa) \int_{\frac{2}{\varepsilon_\gamma(1-\kappa)}}^{\infty} d\varepsilon n_{EBL}(\varepsilon, \Omega; x)\sigma_{\gamma\gamma}(\varepsilon_\gamma, \varepsilon, \kappa), \tag{3.64}$$

where Ω is the solid angle.

Effectively, the TeV photon flux observed at Earth F_{obs} is then the intrinsic flux emitted by the source, F_{int}, attenuated by a factor $e^{-\tau_{\gamma\gamma}}$

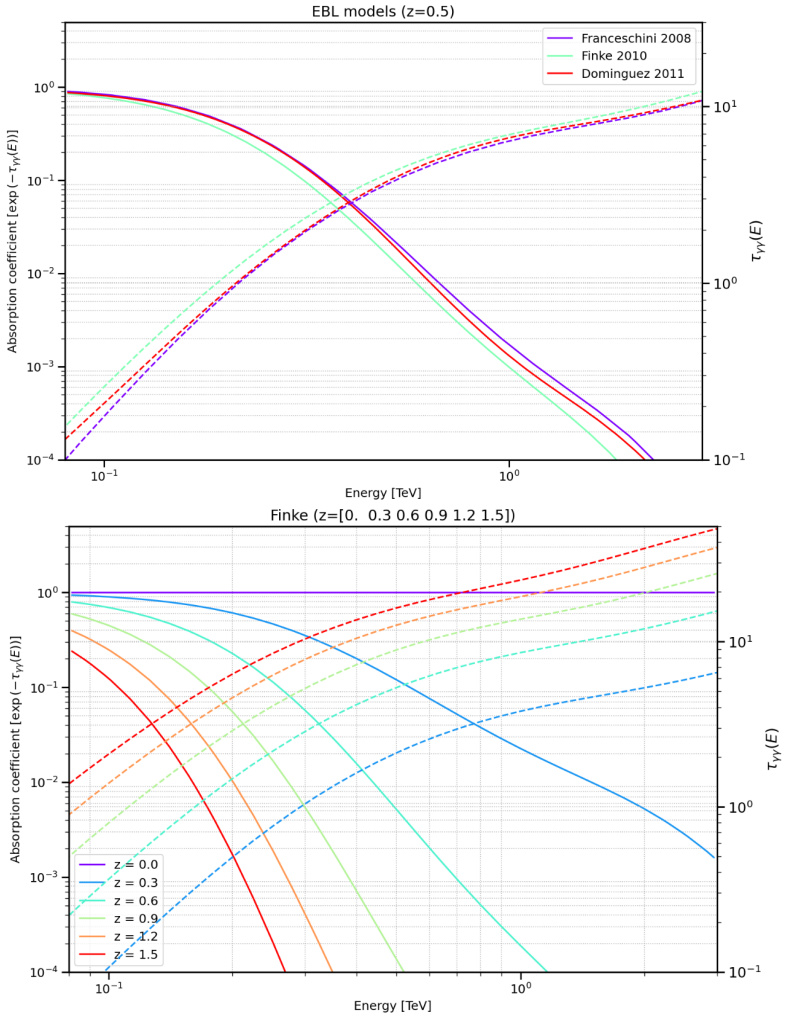

Figure 3.7: EBL attenuation and opacity for different models (top, at $z = 0.5$) and redshifts (bottom), as calculated with the model from [74]. The solid lines are the absorption coefficient $e^{-\tau_{\gamma\gamma}(\varepsilon)}$ (left-side axis), and the dashed lines are the optical depths $\tau_{\gamma\gamma}(\varepsilon)$ (right-side axis).

$$F_{obs}(\varepsilon) = F_{int}(\varepsilon)e^{-\tau_{\gamma\gamma}(\varepsilon)}. \tag{3.65}$$

In Figure 3.7, we show the different attenuation factors and opacity for the models presented in [73–75] and the redshift dependency due to increased line of sight length.

Instrumentation 4

In this chapter, we will introduce the methods used to gather data for this work. The X-ray through gamma-ray emission from Blazars roughly follows a power law $dN/dE \sim E^{-\Gamma}$ with $\Gamma \sim 2-3$, meaning that fewer photons are emitted as the energy increases. Earth's atmosphere is opaque to ultraviolet (UV) light, X-rays, and gamma rays (as shown in Figure 4.1). Different techniques and technologies are used for different wavelengths: VERITAS, a ground-based gamma-ray detector, provides photon data for energies $\gtrsim 100$ GeV up to a few dozens TeV, the so-called very high energy range (VHE). For energies between ~ 100 MeV and up to a few hundreds GeV, called the high-energy range (HE), we used public data from the Large Area Telescope (LAT), which is on board of the Fermi Gamma-ray Space Telescope. The UV/optical and X-ray data are provided by the X-Ray Telescope (XRT) and the Ultraviolet/Optical Telescope (UVOT), which are on board the space-based Neils Gehrels *Swift* Observatory. We will cover the detection techniques and telescope specifications.

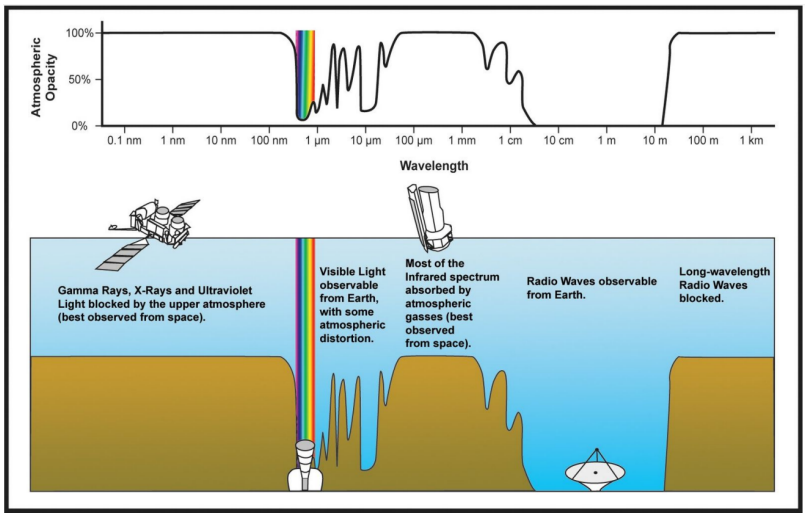

Figure 4.1: Earth's atmospheric opacity over the electromagnetic spectrum. Credits: NASA

Useful definitions

Sensitivity The minimum energy density (commonly expressed in erg per cm^2 per second) that an instrument can detect within a certain amount of time. Estimated from simulations.

Energy dispersion The probability of reconstructing the photon at a given energy, as a function of the photon's true energy. Estimated from simulations.

Energy resolution The energy-dependent uncertainty on the photon energy measured by an instrument. Commonly defined as the one standard deviation in each energy bin of the energy

dispersion. Estimated from simulations.

Angular resolution The energy-dependent uncertainty in the reconstructed arrival direction of the photon for a given instrument. Commonly defined as the 68% containment radius in each energy bin. Estimated from simulations.

Effective area The energy-dependent area of a detector that can detect photons (usually in m^2). Estimated from simulations.

Field of View The portion of the sky in deg^2 that a detector can observe.

Duty cycle The amount of time during a year that a detector is active and observing, usually expressed as percentages.

4.1 VHE gamma-rays

At energies > 1 TeV, the Crab Nebula, the brightest steady gamma-ray emitter known to these days, has a flux of

$$\Phi_\gamma^{Crab}(> 1\text{TeV}) = \\ = (2.1 \pm 0.1) \times 10^{-11} \text{photons cm}^{-2}\ \text{s}^{-1}$$

which yields approximately 1 photon per m^2 per year [77]. A space-based gamma-ray detector would have to be unreasonably large to reach adequate statistics for physical studies in the VHE regime. Also, VHE gamma-rays cannot be detected directly from the ground. In order to measure the properties of VHE gamma-rays, one has to rely on the fact that when gamma rays reach Earth, they interact with the atmosphere and initiate a chain of particle reactions producing a so-called Extensive Air Shower (EAS). The gamma-ray photon interacts with a virtual photon from an atmospheric nuclei's Coulomb field, generating an electron-positron pair:

[77]: Sciascio (2019), "Ground-based gamma-ray astronomy: An introduction"

$$\gamma + \gamma \rightarrow e^- + e^+.$$

Then each electron and positron can emit a photon via Brehmsstrahlung with a radiation length X_0 *. In air, the radiation length is $X_0 \approx 37$ g cm^{-2} [78]. This process cascades, propagating downwards until the particles in the shower reach an average critical energy $E_c \simeq 86$ MeV (in air), where ionisation losses start to dominate. That corresponds to around 27 radiation lengths in the atmosphere (~ 1000 g cm^{-2}). Therefore, the shower altitude where the particle production is maximum can be estimated to ~ 10 km. After this altitude, the shower starts to lose strength as more particles fall below the energy required for further particle production.

[78]: Grieder (2010), *Extensive air showers: High energy phenomena and astrophysical aspects - A tutorial, reference manual and data book*

* The length that a particle will travel on average before losing $(1/e)$-th of its energy to Bremsstrahlung radiation, in g cm^{-2}

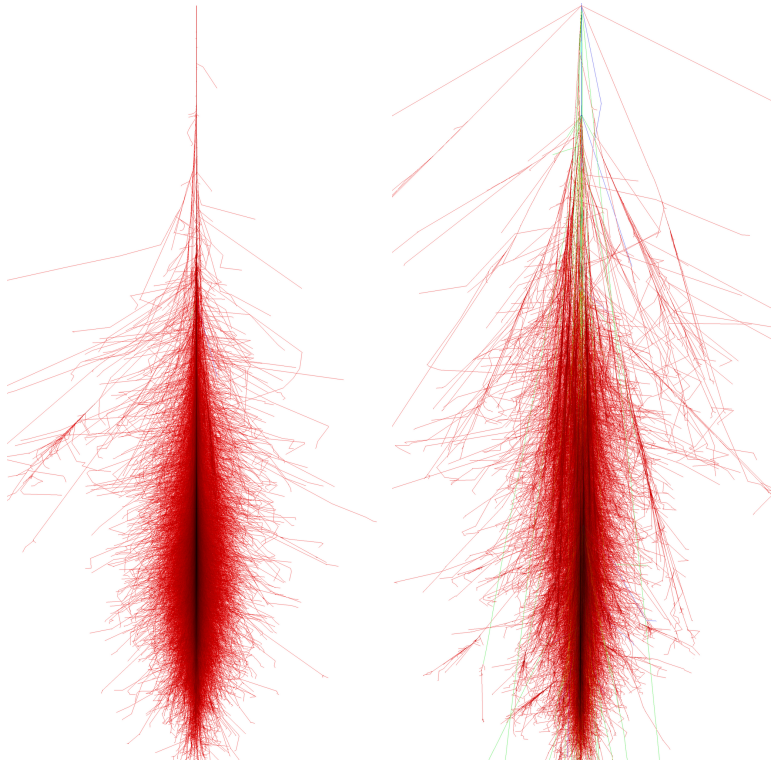

Figure 4.2: Simulation of a photon EAS (left) and a proton EAS (left) at 1 TeV. Taken from `https://www.iap.kit.edu/corsika/`, compiled by Fabian Schmidt

Together with gamma rays, cosmic rays (CRs)[†], interact with Earth's atmosphere and generate EAS. CRs reaching the top of the atmosphere, with energies of ~ 1 TeV, are composed mainly of protons (~ 90%), helium (~ 9%) and heavier nuclei (~ 1%) [79]. CR-induced EASs contain a variety of particles created through nucleon-nucleon interactions, including pions, neutrinos, muons, and photons.

[79]: Battiston (2020), "High precision cosmic ray physics with AMS-02 on the International Space Station"

$$p + N \rightarrow \pi^{\pm}; \pi^{0}; \mu^{\pm}; \nu_{\mu}; \overline{\nu_{\mu}}; e^{\pm}; \gamma ...$$

The photons in the showers can further generate an electron-positron pair and initiate a sub-electromagnetic shower, similar to that of a gamma-ray-initiated shower. However, the development of a proton-initiated EAS is more complex than that of a gamma-ray-induced EAS because of the higher multiplicity of particles produced in each step and momentum conservation. This is evident in the lateral distribution of particles in the shower, with proton-induced EAS being broader and more asymmetrical than gamma-ray-induced showers.

EAS detection involves both direct and indirect methods. As discussed above, EASs stop producing particles at some point in their evolution. Therefore, direct detection techniques revolve arrays of particle detectors at high altitudes, such as the High Altitude Water Cherenkov Gamma-ray Observatory (HAWC)[80], the future Southern Wide field-of-view Gamma-ray Observatory (SWGO)[81], and the Large High Altitude Air

[80]: Abeysekara et al. (2017), "Observation of the Crab nebula with the HAWC gamma-ray observatory"

[81]: Schoorlemmer (2019), "A next-generation ground-based wide field-of-view gamma-ray observatory in the southern hemisphere"

[†] Relativistic charged nuclei accelerated at astrophysical sources

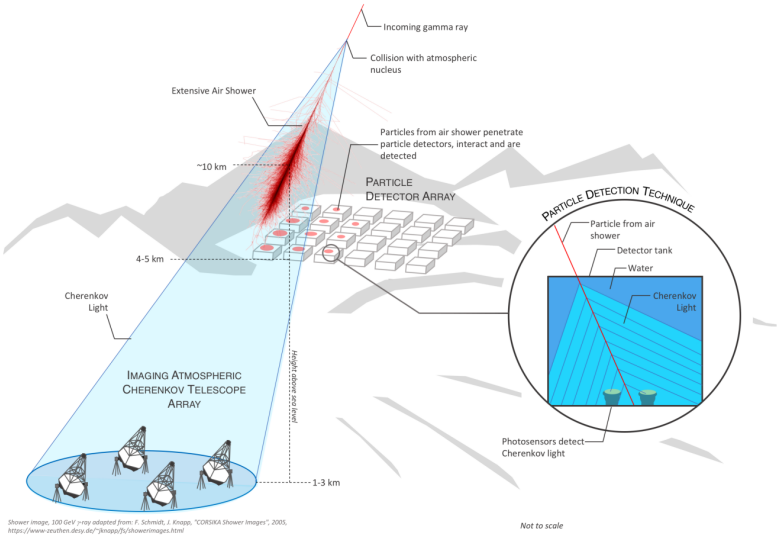

Figure 4.3: An schematic of the detection of an EAS via IACTs and particle detectors. Taken from [81]

Shower Observatory (LHAASO)[82].

[82]: Cao et al. (2019), "The large high altitude air shower observatory (LHAASO) science book (2021 Edition)"

Indirect detection consists mostly in imaging atmospheric Cherenkov techniques (IACTs), which uses the Cherenkov radiation produced during the propagation of shower particles. Charged particles propagating faster than light in a dielectric medium will cause the production of Cherenkov radiation [83]. A schematic representation of IACT and direct detection can be seen in Figure 4.2.

[83]: Jelley (1955), "Cerenkov radiation and its applications"

It should be noted that direct detection methods also make use of Cherenkov radiation, but in this case the radiation is produced inside water tanks instead of air.

4.1.1 Cherenkov radiation

When a charged particle travels in a dielectric medium with a refractive index n at a speed v faster than the speed of light in the medium (c/n),

$$v > \frac{c}{n} \Leftrightarrow \beta n > 1 \tag{4.1}$$

where $\beta = v/c$, the medium emits light with UV/optical frequencies. A schematic of a three-telescope IACT detection of a gamma-ray EAS is shown in Figure 4.7. This process is known as Cherenkov radiation. Following the work in [83], we can observe from Equation 4.1 that this condition imposes a threshold on the energy of the particle. We can calculate the threshold energy E_{min} recalling the relativistic kinetic energy of a particle of rest mass m, $E = \gamma mc^2 - mc^2$, where γ is the Lorentz factor of the particle, $\gamma = 1/\sqrt{(1-\beta^2)}$, finding

[83]: Jelley (1955), "Cerenkov radiation and its applications"

$$E_{min} = mc^2 \left[\frac{n}{\sqrt{(n^2-1)}} - 1 \right]. \tag{4.2}$$

For an electron travelling at sea level ($n = 1.00029$), the threshold energy is $E_{min} \sim 21$ MeV [78].

[78]: Grieder (2010), *Extensive air showers: High energy phenomena and astrophysical aspects - A tutorial, reference manual and data book*

The Cherenkov radiation is emitted in a cone around the direction of the emitting particle velocity at an angle θ following the relation:

$$\cos\theta = \frac{1}{\beta n} \tag{4.3}$$

As shown in Figure 4.4, the particle travels along the medium in a time Δt at a speed v, while spherical wavelets are emitted radially and propagate at a speed c/n and thus accumulate (by coherent interference) forming a wave front that results in a cone of light (Figure 4.5) with an opening angle of θ.

An important effect of Cherenkov emission from EAS is what is called the light "pool": as the shower penetrates further down, the refractive index increases, and according to Equation 4.3, the angle θ increases. That means that particles higher up in the shower will have emit Cherenkov radiation at a smaller opening angle, while towards the end of the shower this angle increases, however, particles travel less. Cherenkov photons will then accumulate in a pool of radius $\sim$ 130 m on the ground. In Figure 4.6, we can see on the left panel the density of Cherenkov photons as a function of the distance to the shower for several energies of a primary gamma-ray and the photon density on the ground for a 300 GeV gamma-ray initiated shower.

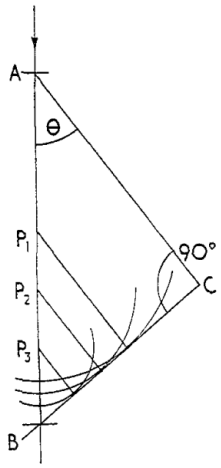

Figure 4.4: The formation of wave fronts due to Cherenkov radiation from a single particle. Taken from [83]

4.1.2 Imaging Atmospheric Cherenkov Technique

The Imaging Atmospheric Cherenkov Technique (IACT) measures Cherenkov light from EASs to determine the direction and energy of the primary

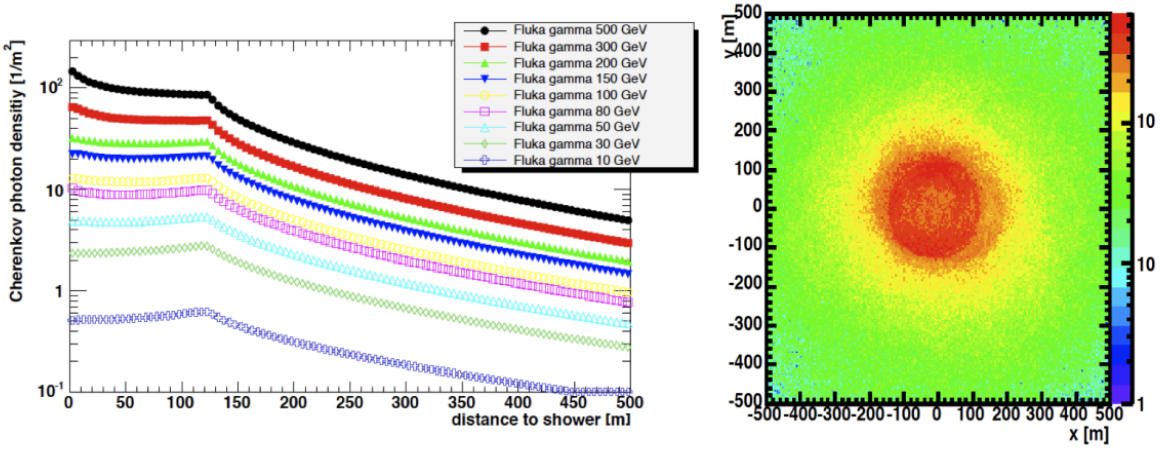

Figure 4.6: Cherenkov photons density as a function of the distance to the shower axis. Taken from [84]. Credits: G. Maier

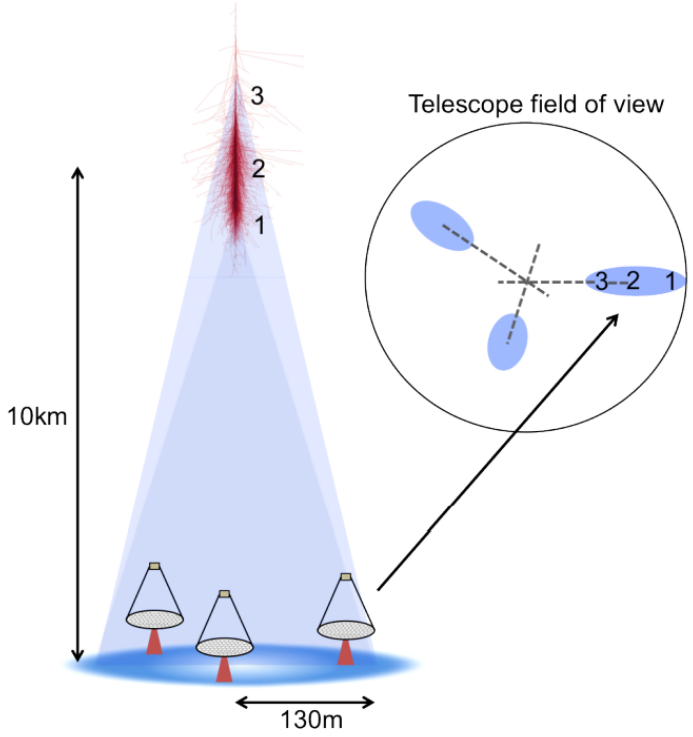

Figure 4.7: Schematic of an EAS detection with an IACT. Taken from [84]

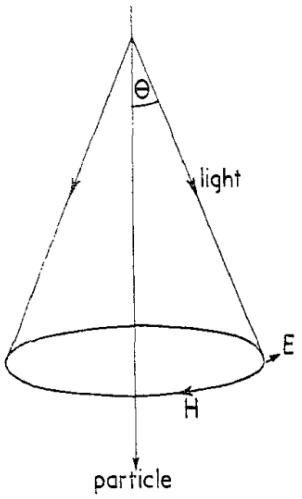

Figure 4.5: The Cherenkov cone from a single particle. Taken from [83]

particle and its type (gamma-ray or hadron). IACT telescopes use a large mirror dish to collect light and focus it onto a camera, usually made of photomultiplier tubes (PMTs). The PMTs convert Cherenkov photons into electrons through the photoelectric effect. The electronic information from each PMT, including the time at which a Cherenkov signal is recorded, is used to reconstruct information about the primary particle. An example of a typical pulse - in this case, digital counts per second - is shown on the inset figure in Figure 4.9. Typically, IACT detectors consist of two or more telescopes for stereoscopic detection. Combining information from multiple images improves the reconstruction of the primary particle properties, which is also important for distinguishing between signal and background events.

4.1.3 The VERITAS telescope

VERITAS [24] is an array of four atmospheric Cherenkov telescopes, located at the Fred Lawrence Whipple Observatory in Arizona, USA (31°40′N 110°57′W, 1.268 m a.s.l.). The first VERITAS telescope [42] has been operating since 2005. The complete array was commissioned in 2007 and continues to operate to the present day. The array passed through two major upgrades throughout the years: the relocation of "Telescope 1"‡ in 2009 which improved the sensitivity of the array by 30% [85] and the camera upgrade in 2012, which replaced the camera's PMTs with

[24]: Weekes et al. (2002), "VERITAS: the very energetic radiation imaging telescope array system"

[42]: Holder et al. (2006), "The first VERITAS telescope"

[85]: Perkins et al. (2009), "VERITAS telescope 1 relocation: Details and improvements"

‡ VERITAS' four telescopes are called Telescope 1, Telescope 2, Telescope 3 and Telescope 4

Figure 4.8: The VERITAS telescope' site after Telescope 1 relocation.

PMTs with higher quantum efficiency[§] which improved the Cherenkov photon collection efficiency by 50%[86]. Between the monsoon season and bright moonlight nights, VERITAS collects roughly around 1000 h of data per year.

[86]: Kieda (2013), "The gamma ray detection sensitivity of the upgraded VERITAS observatory"

VERITAS lifetime into three different periods:

V4 The period before the relocation of Telescope 1, from Sep. 1, 2007 to Aug. 31, 2009

V5 The period before the camera upgrade, from Sep. 1 2009 to Aug. 31, 2012

V6 The period after the camera upgrade up to present days, from Sep. 1, 2012 forwards

The VERITAS array was built to detect gamma rays in the energy range of ~ 100 GeV to ~ 30 TeV, and can detect a source with 1% of the Crab Nebula flux and a similar spectral slope in ~ 25 h [41]. VERITAS reported an energy-dependent angular and energy resolutions of 0.1° and 15% - 20% for gamma rays at 1 TeV [87]. Data from the VERITAS telescopes were used in this thesis.

[41]: Holder (2011), "VERITAS: Status and highlights"

[87]: Park (2016), "Performance of the VERITAS experiment"

We describe the VERITAS telescope structure, cameras, and trigger and data acquisition systems.

[§] The ratio of detected electrons to incident photons

Telescope structure The VERITAS telescopes feature the Davies-Cotton design [88]. Each telescope's primary mirror or "dish" is composed of 345 identically shaped facets. The focal ratio[¶] of the system is f/1, with a focal length of 12 metres. The hexagonal facets, made of a single piece of glass with sides measuring approximately 61 cm [89], have a radius of curvature of approximately 24 metres. The aluminium coating increases durability and achieves a reflectivity of 92% at 320 nm. Each telescope has a total collection area of ~ 100 m^2. Illustrated in Figure 4.9, a schematic of the VERITAS array telescopes and their relative positions to each other. The telescopes are roughly 80 to 130 m apart from each other.

[88]: Davies et al. (1957), "Design of the quartermaster solar furnace"

[89]: Roache et al. (2008), "Mirror facets for the VERITAS telescopes"

Cameras The cameras composed of 499 pixel high-quantum efficiency Hamamatsu R10560 PMTs [90], are positioned at the focal plane. Each PMT has a FoV of 0.15° and is fitted with a Winston cone [91], a device that limits light collection gaps and reduces the intensity of background light by limiting the acceptance angle. The total FoV of the telescopes is 3.5°.

[90]: Nepomuk Otte (2011), "The upgrade of VERITAS with high efficiency photo-multipliers"

[91]: Winston (1974), "Principles of solar concentrators of a novel design"

Trigger System VERITAS uses a three-level trigger system. The first, L1, works on the pixel level. A constant fraction discriminator [92] checks if the pulse amplitude recorded by the PMT is above a certain threshold. All triggered pixels are then passed to the second level trigger, L2. The L2 trigger [93] is a pattern recognition trigger that searches for at least three adjacent L1 triggered pixels within a time window of ~ 6 ns. The L2 trigger mostly selects against random fluctuations from the NSB. The final level trigger, L3, requires an L2 trigger from two or more telescopes within a time window of ~ 50 ns.

[92]: Hall et al. (2003), "Veritas CFDs"

[93]: Zitzer et al. (2013), "The VERITAS upgraded telescope-level trigger systems: Technical details and performance characterization"

Data Acquisition System The VERITAS Data Acquisition System (DAQ) [94] works on both the telescope and the array levels. It consists of two components: VME Data Acquisition (VDAQ) and the Event Builder. Each telescope has custom-built flash analogue-to-digital converters [95] (FADCs) to read signals from pixels, digitising them at a rate of 500 Msamples per second (2 ns per sample). The FADCs are housed in VME crates and connected to the VDAQ system. The VDAQ reads FADC data and sends event numbers, event types[‖], and other information to the *Event Builder*, which combines events from individual telescopes to create a telescope-level event. The array-level *Harvester* receives the telescope-level event and creates an array-level event. The events from a single observation run (typically 15-30 min) are stored in a custom format, the VERITAS Bank File (VBF), containing event data and metadata, and saved locally and on two external servers.

[94]: Hays et al. (2007), "VERITAS data acquisition"

[95]: Rebillot et al. (2003), "The VERITAS flash ADC electronics system"

[¶] The ratio between the focal length of the optical system and its aperture

[‖] Events could be of the "Pedestal" type used later in the analysis. See Subsection 5.1.2.

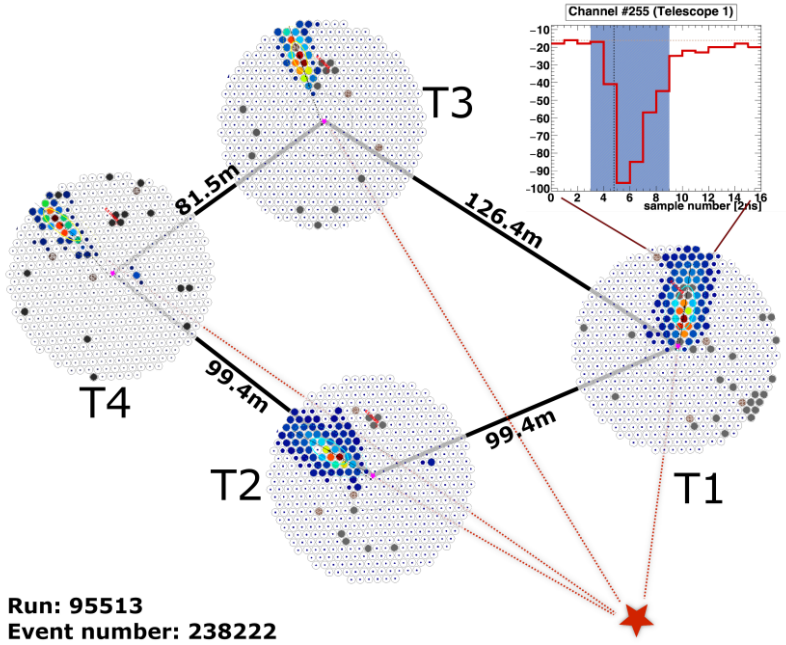

Figure 4.9: Example of the images on the VERITAS cameras, the estimated direction of the detected shower and the approximated distances between the telescopes. The inset shows a characteristic signal from one of the camera's PMTs. Taken from [96].

4.2 HE gamma-rays

At energies ranging from a few MeV to ~ 100 GeV, gamma-ray photons are unable to produce a sufficiently large EAS so that IACTs can properly reconstruct its energy and arrival direction (see Section 4.1). The detection techniques used in gamma-ray telescopes have roots in particle-physics detectors. Depending on the primary photon's energy, one of three processes can occur: the photoelectric effect, the Compton effect, or pair-creation effect. While the photoelectric effect dominates at low energies, around 1 MeV the Compton effect becomes the primary process. Above a few tens MeV, the main interaction process guiding gamma-ray detection is electron-positron pair production. Pair-conversion techniques consist of measuring electron energy via interaction with a medium.

We will focus on energies in the high-energy range of ~ 100 MeV to ~ 100 GeV. *Fermi* was launched in June 2008 and its operational ever since. Only data from the LAT detector is used in this thesis. We will discuss the *Fermi*-LAT instrument and its specifications.

4.2.1 *Fermi*-LAT

Fermi-LAT is a gamma-ray telescope that detects gamma rays in the energy range of ~20 MeV to more than 300 GeV. With an FoV of 2.4 sr, *Fermi*-LAT surveys the entire sky about every 3 h and had 55,992 complete orbits at the 10 yr mark [97]. It uses the pair production process to detect incoming gamma rays and measure their energy and trajectory. An incoming gamma ray interacts with the detector (tungsten foils and

[97]: Ajello et al. (2021), "Fermi farge area telescope performance after 10 years of operation"

scintillation crystals described below), forming an electron-positron pair. The energy of the gamma ray is distributed to the pair. This also generates an electromagnetic shower (the same phenomenon discussed in Section 4.1). The energy and trajectory of the particles in the shower are then measured via a combination of tracking and calorimetry, allowing for the reconstruction of the energy and direction of the primary gamma ray. As in the IACT case, the biggest background source is CRs, where an anticoincidence shield is employed to reject such events. The diffuse emission of gamma rays is another source of unwanted events. The diffuse emission is then modelled and taken into account during the analysis (see Subsection 7.2.2).

An image of the Fermi-LAT detector can be seen in Figure 4.10. Fermi-LAT has three components for gamma-ray photon identification:

The Anticoincidence Detector (ACD) A layer of plastic scintillators with a low atomic number (Z) on the outer side of the spacecraft. The goal of the ACD is to reject the incoming CRs. Charged particles interact with the ACD, producing a light signal. A signal from the ACD scintillators indicates that the particle is a charged particle and not a gamma ray, allowing the event to be vetoed. The purpose of the low atomic number of the material is to reduce the attenuation effect on gamma rays while still rejecting most of the CR background.

The Tracker (TKR) 16 modules containing 18 layers of silicon strip detectors (SSDs) and tungsten foil layers that record the hits' positions of electron-positron pairs created by the gamma ray passing through the tungsten foil. The tungsten is chosen for its high Z value, increasing the probability of pair production. The SSD measures the trajectory of electron-positron pairs in the TKR. These measurements are used to reconstruct the direction of incidence of the gamma ray.

The Calorimeter (CAL) To determine the energy of incoming gamma rays, Fermi-LAT uses a 3D imaging calorimeter (CAL) made of CsI(Tl) scintillation crystals. The CAL measures the energy deposited and provides 3D imaging of the electromagnetic shower development, allowing for an estimate of the initial photon trajectory.

4.2.2 Trigger system

[97]: Ajello et al. (2021), "Fermi farge area telescope performance after 10 years of operation"
[98]: Ackermann et al. (2012), "The Fermi large area telescope on orbit"

The LAT's trigger system is described in [97, 98]. Each detector component - ACD, TKR, and CAL - can issue a trigger request. The majority of LAT trigger requests are generated in the TKR, where a trigger request is issued when three consecutive TKR planes are hit ("three-in-a-row"). The hit threshold in the TKRs occurs when the charge deposited during

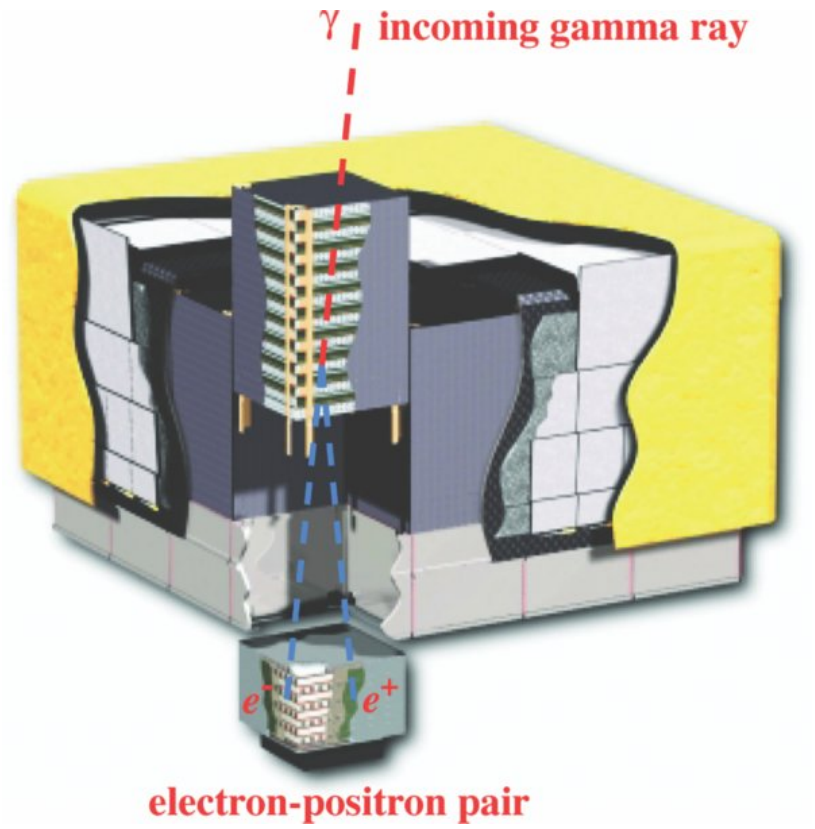

Figure 4.10: A side view of the *Fermi*-LAT detector showing the ACD, one of the TKR and CAL modules. Taken from [9]

the interaction is at least one-fourth of the charge deposited by a single minimum ionizing particle (MIP) or larger. Each CAL crystal is equipped with two fast analog trigger discriminators: the Fast Low Energy (FLE), which issues triggers for deposited energies above 100 MeV, and a Fast High Energy (FHE) for energies above 1000 MeV. For the ACD, two trigger requests can be issued: one for ionizing particles passing through the ACD, used as a veto, and a second one that indicates a heavily ionizing particle. The ACD signal issued by heavy ions can be used to calibrate the non-linearity of the response of the scintillation crystals in the highest energies achieved by LAT (further details in [99]).

Once a trigger is issued, a *time coincidence window* is open for 700 ns, which allows for the collection of other trigger requests. Due to different cabling lengths, the trigger signals from the TKR, CAL and ACD have to be synchronized. Another system, the *Fast Trigger Delay*, applies a delay for each subsystem, synchronizing them.

The combination of ACD, TKR, and CAL allows determination of the trajectory and energy of the event and discriminates charged-particle events. At the analysis level (see Chapter 5), *Fermi*-LAT shows an energy resolution of $8\% - 9\%$ in the 1 GeV-10 GeV range and an angular resolution of 0.6° at 1 GeV. For energies above 100 MeV, *Fermi*-LAT shows a point source integral sensitivity** of 3×10^{-9} photons per cm^2 per second [9].

[9]: Atwood et al. (2009), "The large area telescope on the Fermi gamma-ray space telescope mission"

** For a one-year sky survey period.

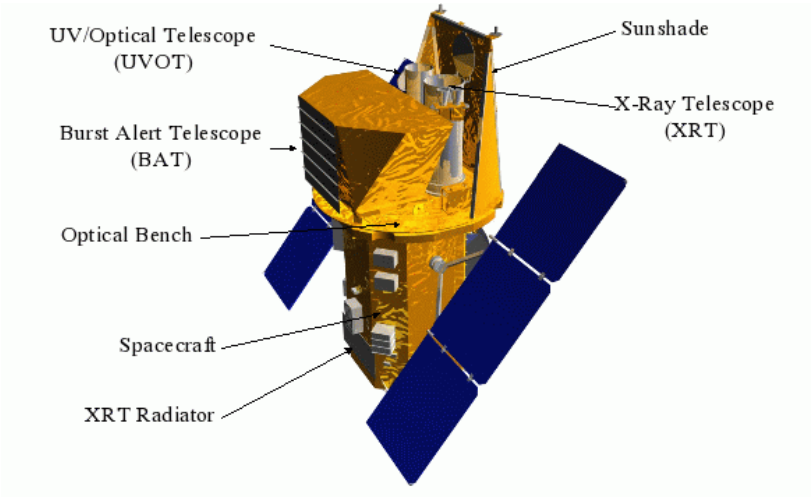

Figure 4.11: Image of the *Swift* space craft highlighting several components' positions. Reproduced from `https://www.swift.ac.uk/about/instruments.php`

4.3 X-rays and Ultraviolet/Optical light: the *Swift* mission

The ultraviolet/optical through X-ray range spans from ~ 2 eV up to ~ 10 keV. The Neils Gehrels *Swift* Observatory [100], is a multi-wavelength observatory launched in November 2004. It was placed in a low-earth circular orbit with the primary scientific objective of studying gamma-ray bursts (GRBs)[††]. *Swift* consists of three instruments: the Burst Alert Telescope (BAT) [101], the X-Ray Telescope (XRT) [102], and the Ultraviolet/Optical Telescope (UVOT) [103], shown in Figure 4.11. The BAT detects X-ray emissions in the 15-150 keV range from GRBs and determines their location with arcminute accuracy. The XRT is designed to perform X-ray imaging and spectroscopy of astronomical sources, including gamma-ray burst afterglows, active galactic nuclei, and other objects. The UVOT is an optical-UV telescope originally designed to study the early light from GRBs, but it is also widely used to study UV/optical light from astronomical objects. UVOT provides subarcsecond localisation power and photometric redshift measurements.

[100]: Gehrels et al. (2004), "The Swift gamma-ray burst mission"

[101]: Barthelmy et al. (2005), "The burst alert telescope (BAT) on the SWIFT Midex mission"

[102]: Burrows et al. (2005), "The Swift X-Ray Telescope"

[103]: Roming et al. (2005), "The Swift ultra-violet/optical telescope"

Data from XRT and UVOT are used in this thesis. In the next sections, we will describe XRT and UVOT specifications.

4.3.1 *Swift*-XRT

One of the most used techniques for the detection of astrophysical X-rays is the use of Wolter I type telescope designs [104]: X-rays are reflected at shallow angles by a paraboloid surface onto a second hyperboloid surface, focussing the light. It allows the nesting of several reflecting surfaces in

[104]: Wolter (1952), "Spiegelsysteme streifenden Einfalls als abbildende Optiken für Röntgenstrahlen"

[††] GRBs are extremely energetic, temporary outbursts of gamma rays, that can last from milliseconds to hours.

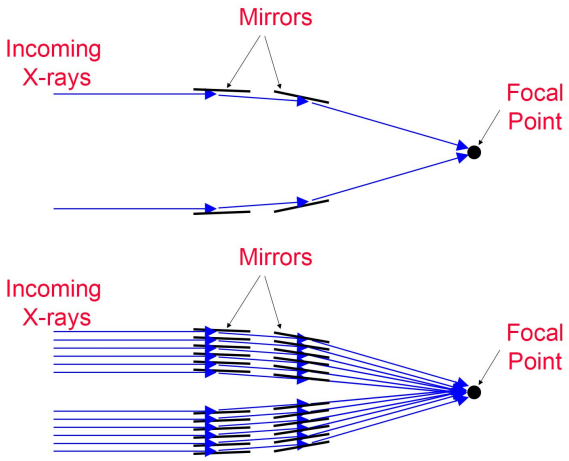

Figure 4.12: An schematic of a grazing incidence in a Wolter I type telescope (top), and the nesting of several reflecting surfaces for increased light collecting area (bottom). Credit: NASA's Imagine the Universe

order to increase the total light collection area, as illustrated in Figure 4.12[‡‡].

Swift-XRT is an X-ray telescope with a Wolter I grazing incidence optical design [104]. It operates in the 0.2-10 keV range and has a FoV of about $23' \times 23'$. The mirror system of the telescope consists of 12 Ni shells with gold coating, arranged concentrically. Each shell is 600mm in length and has diameters ranging from 191 mm to 300 mm, resulting in a focal length of 3.5 metres. The light is focused onto a charged-coupled device (CCD) detector for imaging and a microchannel plate for high-speed timing. XRT has an effective area around 125 cm^2 at energies of 1.5 keV with an integral sensitivity of 2×10^{-14} erg per cm^2 per second in 10^4 seconds. XRT has an energy resolution of 260 eV at 5.9 keV photon energies[§§] and an angular resolution of 18".

4.3.2 *Swift*-UVOT

The Ultra-Violet/Optical Telescope (UVOT) on board the Swift Gamma-ray Observatory was designed to capture early (within 1 minute of the burst) UV light from GRBs. UVOT also performs optical follow-up observations from the GRBs' afterglows in the 170-600 nm range (around 2-7 eV). UVOT uses a combination of UV and optical broadband filters and grisms.

Figure 4.13 shows an schematic of UVOT main detection system. *Swift*-UVOT uses a modified Ritchey-Chrétien optical configuration, with a 30 cm primary mirror and a 7.2 cm secondary mirror, resulting in a focal ratio of f/12.7 and a FoV of $17'$. Incoming light is reflected by the two mirrors onto a third, at a 45 degree angle, redirecting the light onto the filter wheel. The filter wheel has optical filters for the U, V, and B ranges,

[‡‡] Reproduced from `https://imagine.gsfc.nasa.gov/observatories/technology/xray_-telescopes1.html`

[§§] From `https://www.swift.ac.uk/analysis/xrt/modes.php`. This is a more recent estimate of the energy resolution, compared to the resolution at launch of 140 eV at 5.9 keV [102].

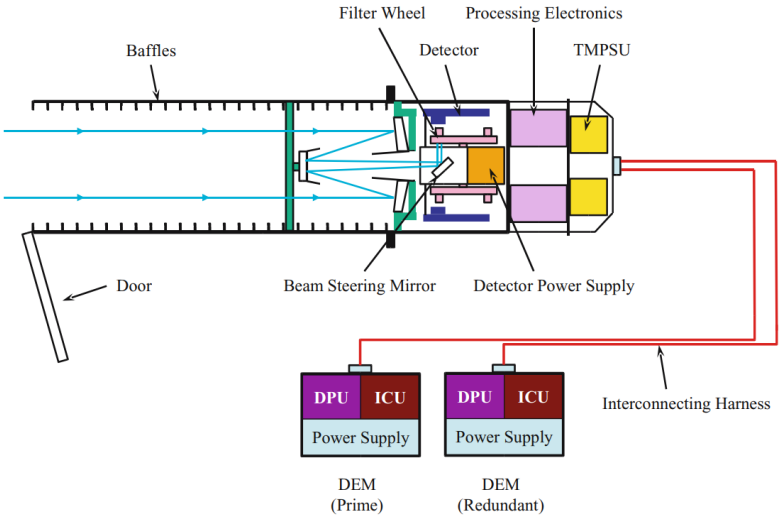

Figure 4.13: Schematic of *Swift*-UVOT and its several components. Taken from [103]

and ultraviolet filters W1, M2, W2 plus a white-light filter. After passing through the filters, light is detected on a CCD device with an imaging area of 256 × 256 pixels, where each pixel covers a 4 × 4 arcsec area of the sky, resulting in the FoV aforementioned. The effective areas of the filters are shown in Figure 4.14 and the corresponding central frequencies of each filter, alongside their respective full-width half-maximum (FWHM) values are listed in Table Table 4.1.

The photons strike a photocatode that produces an electron discharge, which is then amplified by a sequence of microchannel plates (MCPs), producing an electron cloud. The electron cloud arrives at a phosphor screen, which scintillates, producing more photons that are then directed through fiber to the CCD. The integrated CCD image is readout every 11 ms. The readout photons create a so-called "splash" in the CCD pixels.

Table 4.1: UVOT filters. Filters names on the left column. Central wavelengths in the middle column. Full-width-half-max values on the right column. Adapted from [103]

Filter	λ_C (nm)	FWHM (nm)
V	544	75.0
B	439	98.0
U	345	87.5
UVW1	251	70.0
UVM2	217	51.0
UVW2	188	76.0
White	385	260.0

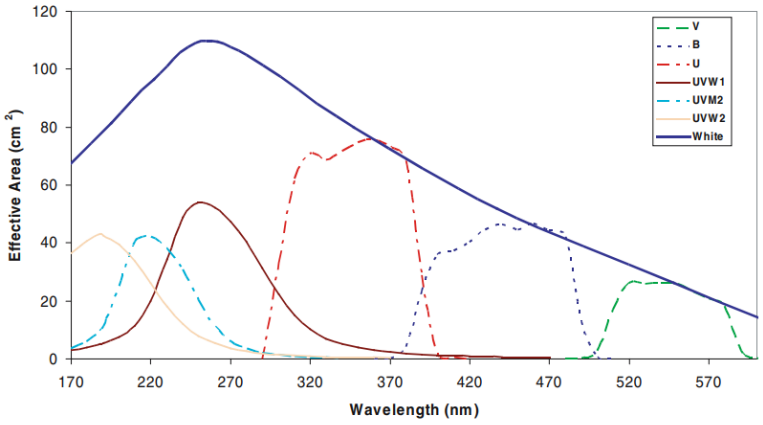

Figure 4.14: Effective area per type of filter in UVOT. Taken from [103]

4.4 Overview

In this chapter, we describe the instruments that provide the data that are fundamental to this thesis. These are state-of-the-art instruments in their own energy range and techniques. It is worth mentioning that for future work, data from other instruments could be used, such as *Swift*-BAT [101] and the Nuclear Spectroscope Telescope Array (NuSTAR) [105] for X-ray data beyond 10 keV up to 150 keV. Another honorable mention is the future Cherenkov Telescope Array (CTA) [106], a future-generation IACT that is expected to have a sensitivity about two orders of magnitude better than current IACTs over an even wider range of energies [107].

[101]: Barthelmy et al. (2005), "The burst alert telescope (BAT) on the SWIFT Midex mission"

[105]: Harrison et al. (2013), "The nuclear spectroscopic telescope array (NuSTAR) high-energy X-ray mission"

[106]: Acharya et al. (2013), "Introducing the CTA concept"

[107]: Zanin et al. (2021), "CTA – the World's largest ground-based gamma-ray observatory"

Low-level reconstruction 5

Different instruments use different techniques of photon data collection and different reconstruction methods and algorithms should be used in order to accommodate the specifics of each instrument.

A general overview of the event reconstruction and low-level reconstruction is:

1. Photons and background particles reach (or hit) the detector and interact with it
2. Some of the particles (including photons) are rejected due to either anti-background shielding, or a previously set threshold on some of the particle's properties (e.g., minimum energy)
3. The surviving particles will interact with the detector's hardware, producing electronic signals
4. These electronic signals are then pre-processed internally by the detector's software to generate data that will be further analysed
5. The pre-processed data are transferred and stored in databases
6. The data are analyzed by specialized software to produce events lists of the surviving particles containing the particle's energy, direction of arrival, whether the particle is a photon or a background particle, etc.

In this chapter, we describe these techniques and reconstruction methods used in this thesis for the VERITAS, *Fermi*-LAT and *Swift* XRT and UVOT instruments (described in Chapter 4).

5.1 VERITAS analysis

An introduction to the IACT technique and the VERITAS instrument was provided in Subsection 4.1.2 and Subsection 4.1.3. To analyse the data collected by the VERITAS instrument, we use the software `Eventdisplay` [108, 109], which is a C/C++ software, based around the `ROOT` [110] framework. It comprises an analysis based on the "Hillas" parameterization method [111] of the images formed in the telescope cameras. The Cherenkov light is measured in each PMT pixel, and its signal is integrated. From now on, we will refer to PMT pixels as just pixels. The cameras are calibrated each night of observation for any delays in signal reading and signal "gain" (more details later in Subsection 5.1.1). The images are cleaned of environmental and electronic background noise and then parametrized following the Hillas method. Once the images are cleaned and parametrized, a stereo reconstruction is performed to reconstruct the primary particle's

[108]: Maier et al. (2017), "Eventdisplay: An Analysis and Reconstruction Package for Ground-based Gamma-ray Astronomy"

[109]: Maier et al. (2022), *VERITAS-Observatory/EventDisplay_v4: Eventdisplay - version v487e*

[110]: Brun et al. (1997), "ROOT — An object oriented data analysis framework"

[111]: Hillas (1985), "Cerenkov light images of EAS produced by primary gamma rays and by nuclei"

energy, direction of arrival, distance to the telescopes on the ground, etc. The particles are then classified into gamma-ray or background hadrons (mostly protons). We then use the package `V2DL3` [112] to generate a list of events following the **Gamma Astro Data Formats** (GADF) [113]. In the next sections, we describe these steps in more detail.

[112]: Bird et al. (2023), *V2DL3 - VERITAS (VEGAS and Eventdisplay) to DL3 converter.*
[113]: Nigro et al. (2021), "Evolution of data formats in very-high-energy gamma-ray astronomy"

5.1.1 Calibration

The VERITAS cameras' PMTs convert the incoming Cherenkov photons into electrons via the photoelectric effect. The amount of electrons converted in each PMT that was hit by photons is known as photoelectrons (PE). In the PMTs, a gain amplifies the PE signal. The FADCs (see Subsection 4.1.3) then convert the "gained" PE signal to digital counts (DC) *. The DC signal of each pixel is registered by the DAQ. To compensate for the difference in gain levels from each pixel, a calibration run is taken at the beginning of each night. A LED flasher is set up to evenly illuminate the whole camera for 2 minutes at an adjustable rate. The camera is forced to trigger at the same time and rate as the flasher, and since the brightness of the flasher is known, we can estimate the difference in gain between pixels. This technique also enables the timing calibration of the signal obtained in each pixel, where differences can be caused by different cable lengths between the camera and the DAQ. This type of run is known as the "Flasher run" and its data are used during the analysis to account for the issues mentioned above.

The throughput calibration

In 2021, an extensive investigation was conducted on the impacts of the ageing of the VERITAS detectors [96]. The objective was to quantify the effects of age on total light throughput. Using measurements of the electronic system gain and mirror dishes reflectivity, the throughput over the years was estimated. The throughput is defined as the product of the mirror reflectivity and the corresponding gain factor of each telescope (see [96] for further details). Once the throughput factors were available, *a posteriori* corrections are applied during the analysis, mainly to the detector's response. The technique was validated against Crab Nebula's data, showing effective calibration of the data and correct energy reconstruction.

[96]: Adams, C. B. et al. (2022), "The throughput calibration of the VERITAS telescopes"

* There are two types of gain: a low gain and a high gain. Both gains are applied to the signal, and if the high-gain signal saturates the FADC channels, the low-gain signal is converted and registered by the DAQ, otherwise the high-gain signal is chosen.

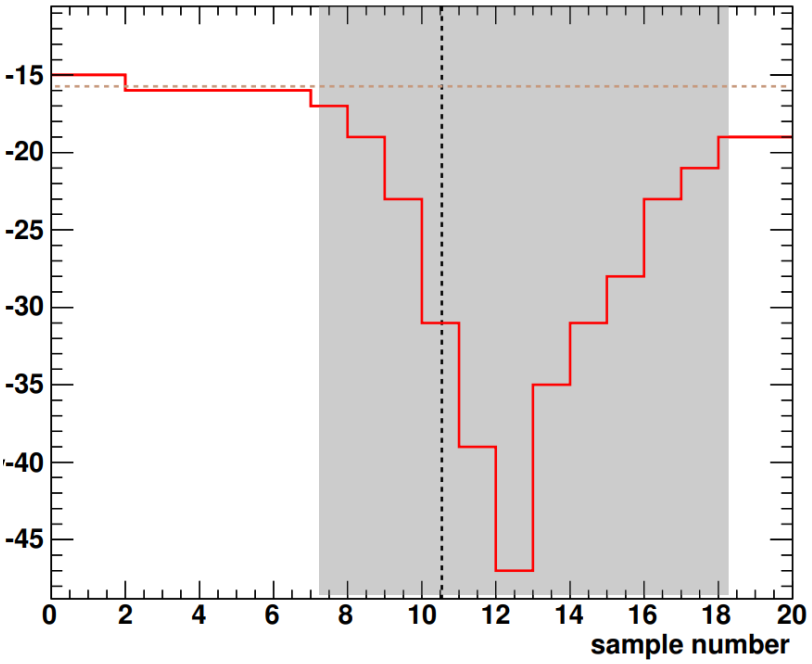

Figure 5.1: `Eventdisplay` example of a Cherenkov photon's trace. The shaded region corresponds to the first window pass. Credits: Gernot Maier

5.1.2 Pedestal determination

The DAQ records the DC signal of each pixel in every camera for a window of 32 ns (Subsection 4.1.3). The typical duration of a Cherenkov pulse produced by an EAS is ~ 10 ns [78]. The result is the **trace** of a pixel: the DC number as a function of time (binned as the number of samples), as shown in Figure 5.1. The trace is the elementary data of an event, and when combining the trace information from all pixels in each camera, we can fully reconstruct the main properties of the event. The FADC trace is manually offset by a known value. An artificial triggering of the pixels at a known rate (3 Hz) is forced when there is no presence of Cherenkov light. The mean of the distribution of the integrated number of DC per trace yields the offset value, defined as the pedestal level. The pedestal standard deviation yields a measure of the noise produced by electronics noise and the night sky background (NSB).

[78]: Grieder (2010), *Extensive air showers: High energy phenomena and astrophysical aspects - A tutorial, reference manual and data book*

5.1.3 Signal timing

The next step on the analysis is to determine the arrival time of the Cherenkov photons on each pixel. We use a two-pass method [24]: an integration of each FADC trace is performed with a fixed wide integration time window (~ 20 ns). The first estimation of the arrival time T_0 is provided as the time in which the pulse reaches 50% of its maximum DC number. The charge in each pixel is integrated and the image is cleaned and parametrized with the methods described in Subsection 5.1.4 and Subsection 5.1.5. The position of each remaining pixel along the major axis of the parametrized image is determined and used in the fit described

[24]: Weekes et al. (2002), "VERITAS: the very energetic radiation imaging telescope array system"

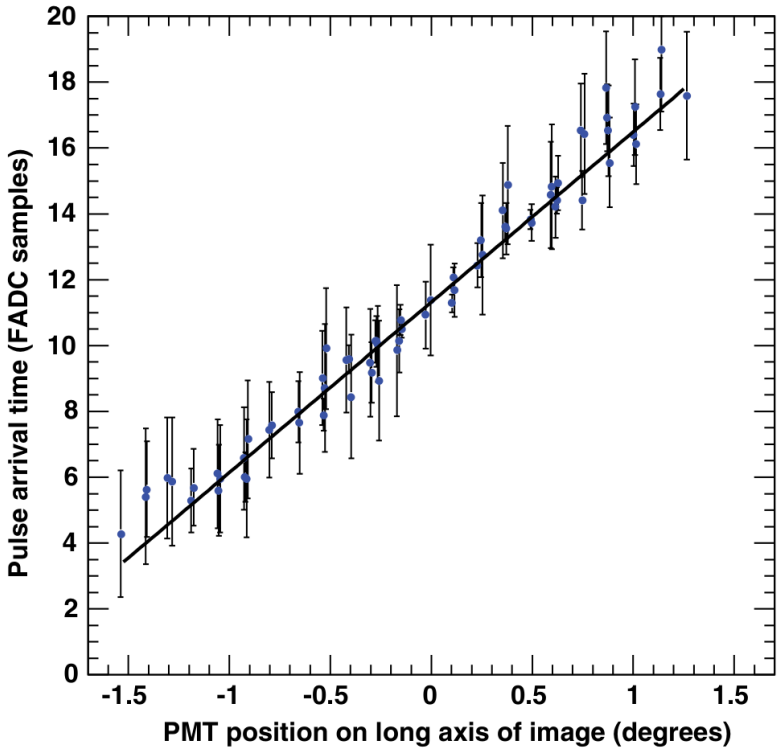

Figure 5.2: Example of pulse arrival time distribution across image axis. Taken from [24]

below. The pulse arrival time at each remaining pixel as a function of its position is fitted with a first-order degree polynomial function, as shown in Figure 5.2. The slope of the function provides the time gradient across the image. The process is repeated in the second pass, but now the arrival time T_0 of each pixel is calculated from the fitted function. A shorter non-fixed time window ($\sim$ 10 ns) with the new T_0 as the lower boundary. This window will be used for the new FADC traces integrations. Finally, the images are cleaned up and parameterized again and the process is finished.

5.1.4 Image cleaning

[114]: Bond et al. (2003), "An island method of image cleaning for near threshold events from atmospheric Čerenkov telescopes"

We apply the method of *pixel island finding*, proposed in [114]. Having determined the pedestal levels and their standard deviation (also known as *pedvar*) as described in Subsection 5.1.2, the method finds the relevant pixels that contain Cherenkov light. A pixel that is five times higher than its *pedvar* value is defined as a signal pixel. Adjacent pixels (neighbours) to the signal pixel must contain an integrated signal 2.5 times higher than their *pedvar*. This refers to a signal-to-noise ratio of 5/2.5, the standard values in the `Eventdisplay` analysis of the VERITAS data. These thresholds can be manually changed in the analysis if required.

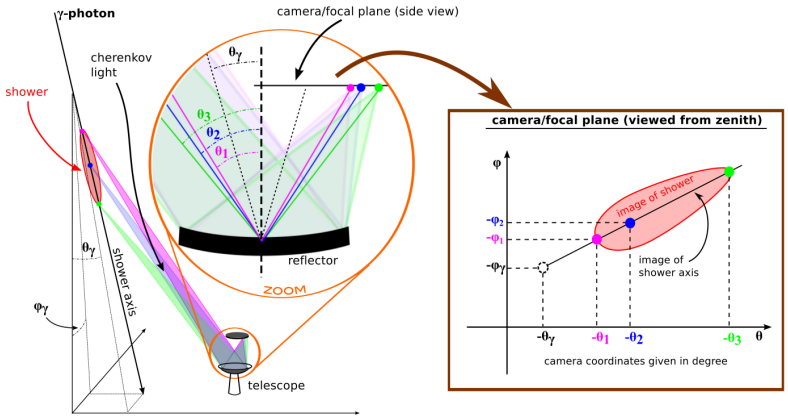

Figure 5.3: Shower image as seen by the camera. Credits: Christian Skole [115]

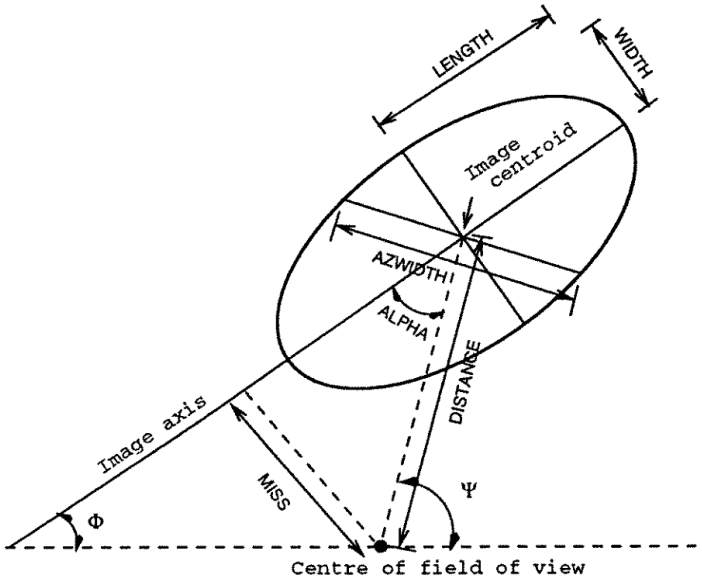

Figure 5.4: Sketch of parametrized camera image. Taken from [117]

5.1.5 Image parametrization

The surviving pixels after cleaning form a 2-dimensional image of the EAS Cherenkov light cone as seen by each camera. Gamma-ray-initiated EAS usually has an ellipsoidal form, as seen in Figure 5.3. As the shower develops, Cherenkov beams emitted at different points in the development of the shower are reflected on the camera at different positions, reflecting the development of the shower.

In [111, 116] a parameterization method was proposed that consists of a moment analysis of the projection distributions of the pixels' charge (or DC) and position onto the x and y coordinates. A detailed description of this method is provided in [117]. A representation of the method can be seen in Figure 5.4

In the `Eventdisplay` analysis, the parameters used are:

size The integrated charge of all signal PMTs in the image.
centroid The image's centre of gravity coordinates.

[111]: Hillas (1985), "Cerenkov light images of EAS produced by primary gamma rays and by nuclei"
[116]: Cawley et al. (1983), "Application of two dimensional imaging of atmospheric Cerenkov light to very high energy gamma ray astronomy"
[117]: Fegan (1997), "γ/hadron separation at TeV energies"

Table 5.1: Selection cuts used in the analysis for the pre-selection of events to be reconstructed

Name	Description	Threshold
mintubes	Minimum number of surviving pixels in the image	5
minsize	Minimum image size	100
maxloss	Maximum loss percentage	20%
nTels	Minimum required number of telescopes	2

dist The distance between the image *centroid* and the center of the camera's FoV.

phi The angle between the image's major axis and the x axis in camera coordinates.

length The RMS spread of light parallel to the image's major axis.

width The RMS spread of light perpendicular to the image's major axis.

asymmetry A measure of the image's asymmetry.

[111]: Hillas (1985), "Cerenkov light images of EAS produced by primary gamma rays and by nuclei"

Besides the parameters proposed in [111], we make use of other image's properties such as:

loss The fraction of the image's *size* contained in pixels at the edge of the camera. Especially used in selecting/rejecting truncated images at the camera's border.

t_grad The image's time gradient along the major axis

FUI Fraction under image or FUI is the fraction of pixels that are contained within the parametrized ellipsis. Especially useful for distinguishing between gamma-ray and hadron images.

[117]: Fegan (1997), "γ/hadron separation at TeV energies"

The mathematical description of the Hillas parameters can be seen in [117].

5.1.6 Shower localization

Once the images of all four cameras have been parametrized, we can start the stereoscopic reconstruction of the event. We start with the reconstruction of particle's direction of arrival and the position of the shower's core; the core of the shower is the position in which the shower axis hits the ground. The events and event images are pre-selected based on selection cuts, where events that do not meet the requirements are discarded. These requirements are shown in Table 5.1.

[118]: Hofmann et al. (1999), "Comparison of techniques to reconstruct VHE gamma-ray showers from multiple stereoscopic Cherenkov images"

The direction of arrival of the EAS is reconstructed as the 2D weighted average position of the interceptions between each pair of camera images [118], as shown in Figure 5.5.

The source position $\vec{r}$ is calculated as

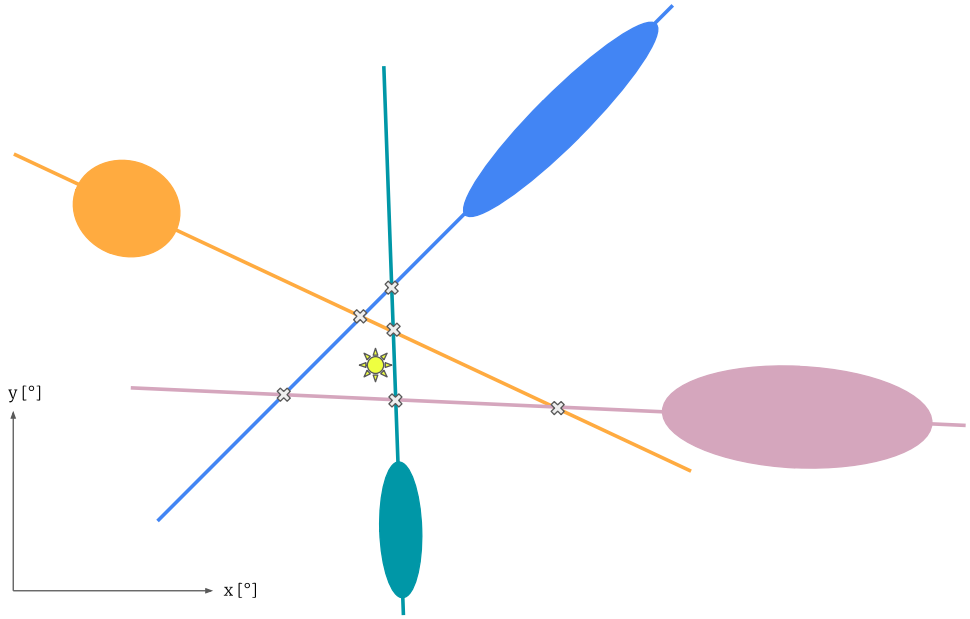

Figure 5.5: Sketch of stereo reconstruction.

$$\vec{r} = \frac{\sum_i \sum_{j \neq i} w_{ij} \vec{r}_{ij}}{\sum_i \sum_{j \neq i} w_{ij}}, \tag{5.1}$$

where $\vec{r}_{ij}$ is the interception between the image axes of telescopes i and j. The weight w_{ij} is calculated as follows:

$$w_{ij} = \left(\frac{1}{size_i} + \frac{1}{size_j} \right)^{-1} \times \left(\frac{width_i}{length_i} + \frac{width_j}{length_j} \right)^{-1} \times \sin(\theta_{ij}). \tag{5.2}$$

The source position $\vec{r}$ is given in camera coordinates (°×°). This is then transformed to sky coordinates for each detected event. To obtain the core position, we apply a similar method, this time using the interception of the image axes in "ground" coordinates. Once the core position is known, we can calculate the so-called impact parameter R_i, i.e., the distance between the core position and the i-th telescope.

5.1.7 Energy, emission height and mean scaled parameters

The next step in the analysis is to estimate the **emission height**, i.e., the height at which the maximum of the shower occurs, the **energy** of the primary particle and the mean *width* and *length*, scaled by the images sizes

and impact parameter. These quantities are used later in the analysis to discriminate between gamma-ray and hadron events (Subsection 5.1.8).

Emission height

Proton showers will start developing deeper in the atmosphere compared to gamma-ray showers, making emission height a useful parameter for discriminating between protons and gamma rays. The emission height (*EH*) can be estimated, per pair of telescopes, and then weighted averaged as follows [119]:

[119]: Aharonian et al. (1997), "The potential of ground based arrays of imaging atmospheric Cherenkov telescopes. I. Determination of shower parameters"

$$EH_{ij} = \frac{|\vec{T}_i - \vec{T}_j|}{|\vec{centroid}_i - \vec{centroid}_j|} \implies$$

$$\implies EH = \frac{\sum_i \sum_{j \neq i} w_{ij} EH_{ij}}{\sum_i \sum_{j \neq i} w_{ij}}, \quad (5.3)$$

where $\vec{T}_i$ is the position of the i-th telescope.

Energy

EAS produced at different energies have different properties when observed by different telescopes. Showers produced at higher energies will emit more Cherenkov light; therefore, more electrons will be produced by the PMTs when detecting such showers, resulting in larger *size* values. However, Cherenkov light of showers falling at greater distances (R) from the telescopes is less likely to be detected than that of those falling closer to the telescopes. The current method of energy estimation relies on the so-called **lookup tables** (see Figure 5.6): gamma-ray and proton-induced showers are simulated under varied conditions that cover the extent of VERITAS observations, such as different zenith angles, observation modes, and different NSB levels. The tables are filled with 2D histograms of *size* in DC versus R (the impact parameter) in metres, with the median values of the true energy from the MC simulations, and a second table is filled with the 90% containment width of the energy distribution. Then, the estimated energy of a shower is estimated as:

$$E = \frac{\sum_i^N E_i(R_i, size_i)/\sigma^2_{E,i}(R_i, size_i)}{\sum_i^N 1/\sigma^2_{E,i}(R_i, size_i)}, \quad (5.4)$$

where E is the reconstructed energy of the event. $E_i(R_i, S_i)$ and $\sigma^2_{E,i}(R_i, S_i)$ are the simulated median energy and 90% width as a function of the

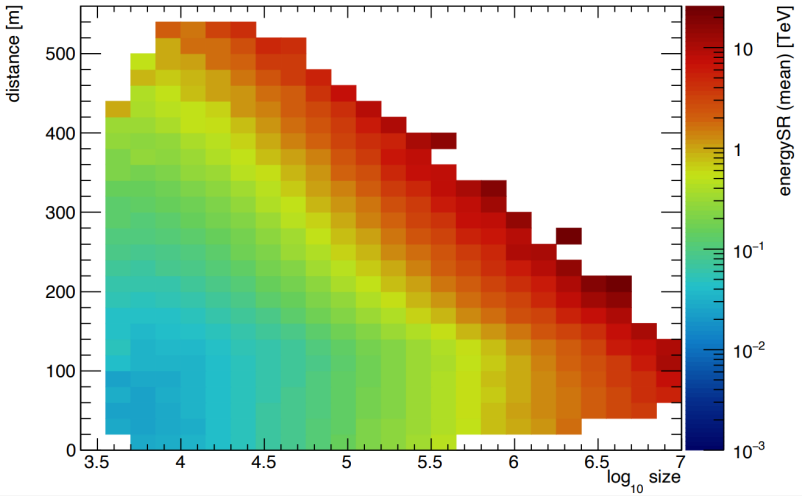

Figure 5.6: Energy lookup table: a 2-D histogram of the reconstructed energy (z-axis, colorcoded) as a function of the $log_{10}(size)$ of the image (x-axis) and the distance of the shower to the telescope (y-axis). Credits: Gernot Maier

impact parameter R_i and $size_i$ of the i-th image. N is the total number of reconstructed images (triggered and surviving the cuts). The energy E is then assigned to the event and is used later in the analysis to estimate higher-level products, such as spectra and light curves.

Mean reduced scaled parameters

The lookup table procedure is also used to define what are known as the mean reduced scaled length ($MRSL$) and mean reduced scaled width ($MRSW$) of an event.

$MRSL$ and $MRSW$ are defined similarly to Equation 5.4, as follows:

$$MRSL = \frac{1}{N}\sum_{i}^{N}\left(\frac{length_i - length(R_i, size_i)}{\sigma_{length}(R_i, size_i)}\right).\left(\frac{length(R_i, size_i)}{\sigma_{length}(R_i, size_i)}\right)^2, \quad (5.5)$$

$$MRSW = \frac{1}{N}\sum_{i}^{N}\left(\frac{width_i - width(R_i, size_i)}{\sigma_{width}(R_i, size_i)}\right).\left(\frac{width(R_i, size_i)}{\sigma_{width}(R_i, size_i)}\right)^2, \quad (5.6)$$

where $length/width_i$ are the results of the parametrization described in Subsection 5.1.5. $length/width(R_i, size_i)$ and $\sigma_{length/width}(R_i, size_i)$ are the median and the 90%-containment values at R_i and $size_i$, from the search table. Once again, the sum is performed over the N number of reconstructed telescope images. The values of $MRSL$ and $MRSW$ are a particularly powerful discriminator between gamma-ray and hadronic showers [120].

[120]: Krawczynski et al. (2006), "Gamma–hadron separation methods for the VERITAS array of four imaging atmospheric Cherenkov telescopes"

5.1.8 Gamma/hadron separation

With the detected events fully reconstructed, we now want to discriminate which events are produced by gamma rays and which ones are produced by background cosmic rays, such as proton and helium. As mentioned previously, gamma-ray-initiated EAS presents morphological differences from hadronic EAS. A Boosted Decision Trees (BDT) algorithm [121, 122] provided by the Toolkit for Multivariate Data Analysis (TMVA) [123] is used. A machine learning (ML) multivariate technique, such as BDTs, will combine the information on the morphology of the events provided by the reconstructed parameters and yield a value that indicates the probability of a random event being a gamma ray or a background hadron. As described in [124], BDTs need to be trained using a controlled sample of signal and background events known as *test sample*. The test sample is constructed from MC simulations of gamma-ray EAS as the signal training sample, and the background training sample is composed of data from VERITAS observations of point sources taken regions free of gamma-ray sources. To reduce the contamination of gamma-ray events in the background data, only observations with just one known gamma-ray source present in the FOV are considered. Furthermore, the OFF region from which the data are extracted must be at least 0.22° from the location of the source.

[121]: Breiman (2017), *Classification and regression trees*

[122]: Freund et al. (1999), "A short introduction to boosting"

[123]: Hoecker et al. (2009), *TMVA - toolkit for multivariate data analysis*

[124]: Krause et al. (2017), "Improved γ/hadron separation for the detection of faint γ-ray sources using boosted decision trees"

A set of training parameters is defined on the basis of its discrimination power, i.e., its capability to distinguish a gamma-ray event from a background event. The parameters used are: *MRSL* (Equation 5.5), *MRSW* (Equation 5.6), the emission height *EH* (Equation 5.3), the *size* of the second largest image *Size2Max*, and the logarithm of the χ^2 values calculated at the energy E and emission height, $\log_{10}[\chi^2(E)]$ and $\log_{10}[\chi^2(EH)]$. The definition of $\chi^2(E)$ and $\chi^2(EH)$ are as follows:

$$\chi^2(E) = \sum_i^N \frac{(E - E_i(R_i, size_i))^2}{\sigma^2_{E,i}(R_i, size_i)}, \tag{5.7}$$

and

$$\chi^2(EH) = \sum_i \sum_{j \neq i} \left(EH - EH_{ij}\right)^2, \tag{5.8}$$

Figure 5.7 shows the distributions of the training parameters for the signal and background training samples. From Figure 5.7, we can notice the difference in the distribution of the training parameters between signal and background samples, due to the different aspects of the EAS produced.

In order to take into account the energy and zenith angle dependencies, the BDTs are trained for different combinations of energy bins and the

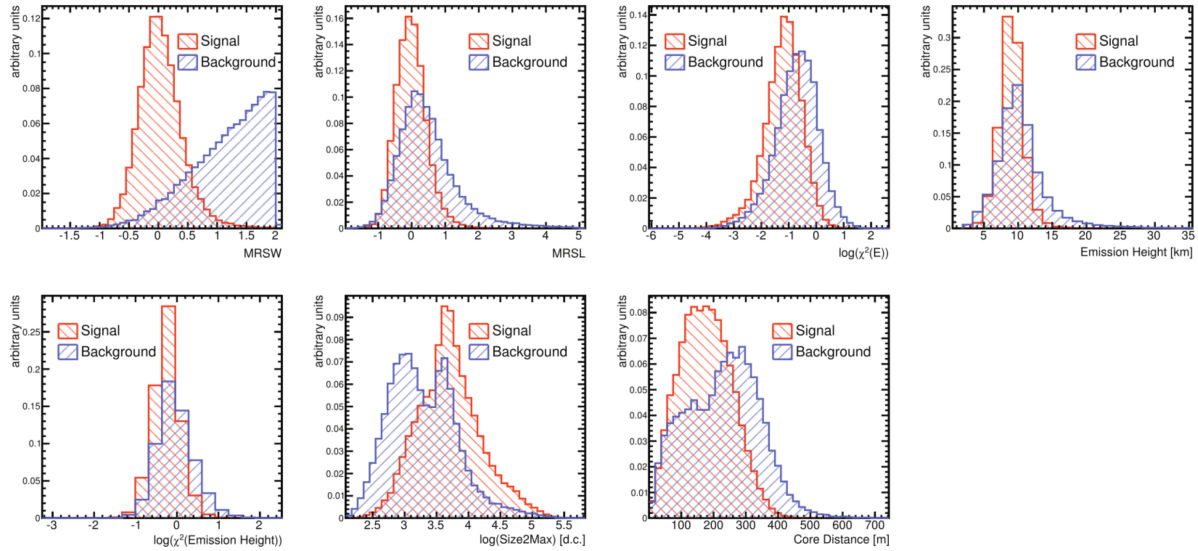

Figure 5.7: Parameters utilized in the BDT training for both signal and background input samples. The distributions correspond to events with energies > 1 TeV and zenith observation angles ranging from 0° to 22.5°. Taken from [124]

observation zenith angle, as shown in Table 5.2.

Energy bins (TeV)	Zenith angle (deg)
0.08-0.32	0.-22.5
0.32-0.50	22.5-32.5
0.50-1.00	32.5-42.5
>1.00	>42.5

Table 5.2: Energy and zenith angle bins used in the training of the BDTs.

Name	Spectral index
Soft	$\Gamma \lesssim -3.5$
Moderate	$-2.5 \gtrsim \Gamma \gtrsim -3.5$
Hard	$\Gamma \gtrsim -2.5$

Table 5.3: The different spectral index regimes used during the BDT training and its nomenclature.

The BDT training is performed for each energy and zenith angle bin, assuming three spectral index ranges of a random source shown in Table 5.3, with at least 10 signal events per bin. For further details on the technique and optimization, see [124].

Pre-selection cuts and application to data

When used for data analysis, previous cuts are imposed to eliminate trivially classifiable background events and misreconstructed events, further increasing the quality of the sample. To eliminate obvious background events, cuts are made on the values of $MRSW$ ($-2.0 < MRSW < 2.0$) and $MRSW$ ($-2.0 < MRSW < 5.0$). And after the events are classified by the BDTs, a final cut is imposed on the reconstructed direction of arrival of the event, where the squared angular distance between the reconstructed direction of arrival of the event and the estimated source position cannot

be larger than 0.008 $^{\circ 2}$. This is known as the θ^2-cut. The value of θ^2 is determined using simulations.

5.2 *Fermi*-LAT analysis

The main components of the *Fermi*-LAT detector were introduced in Subsection 4.2.1. Gamma ray detection by the *Fermi*-LAT detector is based on the conversion of incoming gamma rays into electron/positron pairs when interacting with the detector. Spatial, temporal, and energetic information on the particles produced during this interaction is recorded and used to reconstruct the direction and energy of the original gamma ray, as well as to reject background that can be caused by CRs or gamma rays entering the detector from the opposite direction.

LAT sends around 15 GB of raw data daily to NASA's Goddard Space Flight Center (GFSC), which are delivered to the SLAC National Accelerator Laboratory (SLAC), where the data is processed and the events are reconstructed [97]. The raw and processed data are constantly monitored by the LAT Data Quality Monitoring (DQM) System to ensure the quality of the data [97]. High-level photon data (fully reconstructed and selected event list) are made publicly available at NASA's Fermi Science Support Center (FSSC)[†] as Flexible Image Transportation System (FITS) [125] files.

[97]: Ajello et al. (2021), "Fermi farge area telescope performance after 10 years of operation"

[125]: Hanisch et al. (2001), "Definition of the Flexible Image Transport System (FITS)"

We use the latest data *Fermi*-LAT release, *Pass 8* [126], released in 2015 succeeding *Pass 7* [98], and later receiving an update in 2018 [127]. In this section, we will provide a brief description of the *Pass 8* method of event reconstruction and selection.

[126]: Atwood et al. (2013), *Pass 8*

[98]: Ackermann et al. (2012), "The Fermi large area telescope on orbit"

[127]: Bruel et al. (2018), *Fermi-LAT improved Pass~8 event selection*

5.2.1 Event reconstruction

Readout events are downlinked to the GFSC to be processed and reconstructed. *Pass 8* reconstruction takes a global approach: ACD, TKR, and CAL information is combined to minimize uncertainties and improve reconstruction precision.

At the TKR, gamma rays are converted into electron/positron pairs, which can initiate an electromagnetic shower. The tracks of particles travelling through the TKR are recorded. Once the particles reach the CAL, the deposited energy forms a 3D image of the shower as clusters.

With the electrons and positrons tracks, vertexing is performed to reconstruct the gamma ray's direction. Then, energetic and directional information from the CAL clusters is extracted by fitting the profiles of the individual shower clusters.

[†] `https://fermi.gsfc.nasa.gov/ssc/data`

Finally, the directional information of the particle is used to trace the energy deposition at the ACD in an event-by-event fashion, assisting in the background rejection.

5.2.2 Event selection

The final step in *Fermi*-LAT low-level reconstruction is the selection of events that will be used for the high-level analysis, based on the reconstructed outputs, namely energy, direction, and particle type. *Pass 8* event selection continues to use the so-called *event classes* and *event types* analysis from the previous *Pass 7* iteration [99]. Event selection is based on a classification tree method (CT), implemented with the TMVA toolkit [123]. Each event is classified according to a *class* and a *type* [‡]. The *event classes* refer to the expected background rate within the data sample, where the main ones are the `SOURCE`, `CLEAN` and `ULTRACLEAN` event classes with progressively lower background rates. Two extra classes are provided with an additional veto provided if charge is deposited onto an ACD tile that is spatially correlated with the direction of the incoming particle, namely `SOURCEVETO` and `ULTRACLEANVETO`, the latter being the most restrictive class, where a low CR contamination is required for analysis. Each class is then partitioned into *event types*, namely `FRONT/BACK`, `EDISP` and `PSF`. The event types `FRONT` and `BACK` indicate whether the conversion process occurred in the front section of the TKR - the first 12 layers - or in the last 4 thicker layers, respectively. `BACK` type events can be caused due to diffuse emission, including stray light from Earth's atmosphere, and are often a source of background. The types `EDISP` and `PSF` are divided into 4 subtypes (`EDISP0` through `EDISP3` and `PSF0` through `PSF3`) where each subtype represents the quality of the energy and direction reconstruction, respectively. The "0" quartile contains the lowest quality reconstruction, while "3" contains the best reconstruction quality events. The usage of a specific event class and type is defined according to the scientific purpose of the analysis. For standard extra galactic point source analysis, *Fermi*-LAT collaboration recommends[§] the use of `SOURCE` class events, and `BACK` and `FRONT` events combined.

[99]: Abdo et al. (2009), "The on-orbit calibration of the Fermi Large Area Telescope"

5.3 *Swift* analysis

Lastly, we briefly discuss the data reduction and event reconstruction for the XRT and UVOT instruments on board the *Swift* detector [102]. A detailed and complete description, as well as a user guide, of the data

[‡] A description of the event classes and types can be found at `https://fermi.gsfc.nasa.gov/ssc/data/analysis/documentation/Cicerone/Cicerone_Data/LAT_DP.html`

[§] `https://fermi.gsfc.nasa.gov/ssc/data/analysis/documentation/Cicerone/Cicerone_Data_Exploration/Data_preparation.html`

Figure 5.8: Window timing mode event grades. Taken from [128].

reduction and event reconstruction software can be found in the *Swift-XRT data reduction guide*[128] and the *Swift UVOT software guide*[129].

[128]: Capalbi et al. (2005), *The SWIFT XRT Data Reduction Guide*
[129]: Immler et al. (2008), *The Swift-UVOT software guide*

All *Swift* data is processed in the *Swift* Data Center (SDC) at GFSC and are archived in the High Energy Astrophysics Science Archive Research Center (HEASARC) and also at the UK *Swift* Science Data Center (UKSSDC) at the University of Leicester. Data are processed using the FITS Tools (FTOOLS)[130] software and are publicly available as FITS files.

[130]: Blackburn (1995), "FTOOLS"

5.3.1 XRT data reduction and event reconstruction

The XRT instrument operates in different observation modes, according to the source target X-ray rate and schedule. The modes are image (IM), photodiode (PD), windowed timing (WT) and photon counting (PC) mode. The only two modes used in this thesis are WT and PC modes and will be discussed in further detail. IM mode was designed to rapidly obtain the position of newly observed GRBs by integrating the charge in each CCD pixel with exposures of 0.1 to 0.25 s. The IM mode does not offer spectral measurements, and is suitable for sources at 25 mCrab to 45 Crab strength. PD is the follow-up mode to IM, providing high energy and time resolution, but no imaging capabilities, suitable for sources up to 60 Crab. A typical HBL observation with XRT will be either in WT mode or PC mode because of the typical X-ray strength of Blazars.

Windowed timing data

In this mode, 10 CCD rows are compressed into a single row, and a block of the 200 central columns is read, covering only 8 arcmin of the FoV, and only 1-D spatial information is available. Events are flagged

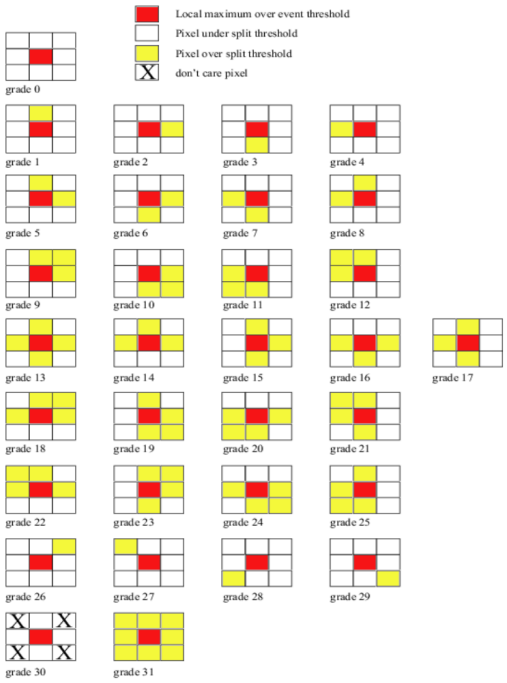

Figure 5.9: Photon counting mode event grades. Taken from [128].

as good (grades 0, 1 and 2) or bad (from 3 to 15) during reconstruction according to the classification shown in Figure 5.8. The grades take into account the position of the local of maximum charge created in a CCD pixel and whether its neighbouring pixels' charges are under or below a previously set threshold. The arrival times, energy, and 1-D position of the events are recorded. The WT mode is suited to sources with fluxes below 5000 mCrab and provides a time resolution of 1.8 ms (as per the original detector publication [102])[¶].

Photon counting mode

In the PC mode, the charge in the whole CCD is registered every 2.5 seconds, therefore providing a lower time resolution than in the WT mode. The 2-D spatial information is preserved. Events are reconstructed by searching 3x3 matrices in the image that have the central pixel as the local maximum, with its charge falling within the threshold. If a 3x3 matrix corresponds to this criteria, the outer ring of a 5x5 matrix centred on the same local maximum pixel is tested. If any of the pixels in the outer ring exceeds the threshold, the event is discarded, and in doing so most of the cosmic rays are eliminated. A grade is assigned to each surviving event, according to Figure 5.9, where events with a grade between 0 and 12 are marked as good events, and grades 13 and above are considered bad events. Bad events are usually discarded during the analysis. Then the energy of the events, the arrival time, and the 2-D position are recorded.

[¶] In Table 2.1 of the *Swift-XRT data reduction guide* (available online at `https://www.swift.ac.uk/analysis/xrt/files/xrt_swguide_v1_2.pdf`), it is stated that the operation fluxes of WT mode are between 1 and 600 mCrab.

The PC mode is suited to sources with fluxes below 1m Crab (as per the original detector publication [102]).

Pipeline

The analysis pipeline for XRT data produces a list of Good Time Intervals (GTIs), which are the periods where good data can be obtained. Events that fall within a GTI are selected for analysis. The analysis produces clean and calibrated events, images, spectra and light curves, in which mode-specific conditions are taken into account. The `xrtpipeline`[‖] is a pipeline created with all the different FTOOLS used for XRT's data reduction and event reconstruction.

5.3.2 UVOT data reduction and event reconstruction

Photons arriving at the detector are directed onto the detector system. On-board processing determines the position of the original photon through a centroid detection algorithm. Then, the energy of the event is reconstructed on board using filter information and gain corrections from previously estimated calibrations (such as linearity and dynamic range of the detector's response). For in-flight calibration, four off-axis flood-LEDs are used to provide flat fielding measurements. The energy, position, and time of the event are down-linked for further processing using ground systems. UVOT ground processing produces two science data modes: *image* and *event*. As suggested by the names, calibrated 2-D images and event lists with energy, direction, and time stamps are provided as FITS files. In this thesis, we make use of the events lists, mostly concerned with the energy of the events and time stamps. Similarly to `xrtpipeline`, a FTOOLS-based UVOT pipeline is provided publicly at HEASARC.

[‖] Available for download in `https://heasarc.gsfc.nasa.gov/docs/software/lheasoft/download.html`

Statistical methods 6

Having determined then the number of signal events, we can then build a count spectrum (as well as a background spectrum): the number of events as a function of energy, or, per energy bin. From the counts and background spectrum, one can determine the number of excess events that are above the background level as a function of energy. By taking into account the total area and time of data collection, we can finally determine the flux of photons that are being measured from our particular source or region of interest.

The statistical methods described in this chapter are the foundation for the results obtained in this thesis. This chapter mainly covers maximum likelihood techniques for significance estimation, data fitting, and uncertainty estimation. These are not the only methods available in the literature, and others will be discussed in later chapters of the thesis, such as the Monte Carlo Markov chain method [131] of parameter sampling.

[131]: Sammut (2010), "Markov chain Monte Carlo"

6.1 Statistical nature of light detection

A photon has a finite probability of arriving at a detector and being measured. Each photon is an individual, discrete event, and its probability is independent of other processes.

In an experiment, after a certain time t, a total number of n photons is detected. Noting that n is a random variable with expectation equal to ν, the probability density function (pdf) $f(n)$ is then described as a *Poissonian distribution* [132], which has the form

[132]: Cowan (1998), *Statistical data analysis*

$$f(n) \equiv f(n|\nu) = \frac{\nu^n e^{-\nu}}{n!}, \tag{6.1}$$

where the notation $f(n|\nu)$ is the conditional probability of f of n given ν.

In the continuum limit ($n \to x$), the expectation value of x, $E[x]$ and variance $V[x]$, is given by:

$$E[x] = \int_{-\infty}^{\infty} x f(x) dx = \int_{-\infty}^{\infty} x \frac{\nu^x e^{-\nu}}{x!} dx = \nu, \tag{6.2}$$

$$V[x] = E[(x - E[x])^2] = \int_{-\infty}^{\infty} (x-\nu)^2 f(x) dx = \int_{-\infty}^{\infty} (x-\nu)^2 \frac{\nu^x e^{-\nu}}{x!} dx = \nu. \tag{6.3}$$

Therefore, a Poisson distribution of a random variable x can be fully described by its mean value v, which is also its variance. If the experiment is repeated N times, probability rules that in order to obtain a total number of counts $n_{tot} = \sum_{i=0}^{N} n_i$, the probability $\mathscr{P}(n_{tot})$ is

$$\mathscr{P}(n_{tot}) = p(n_1)p(n_2)p(n_3)(n_N) \equiv \prod_{i=0}^{N} p(n_i) = \prod_{i=0}^{N} f(n_i|v_i), \tag{6.4}$$

where $p(n_i)$ is the probability of measuring n_i counts between $[n_i, n_i + 1]$, i.e., $p(n_i) = f(n_i|v_i)$.

6.1.1 The likelihood ratio test and the significance of a detection

In most measurements, we have to account for the presence of a background.

Let us assume that we observe a portion of the sky with area A, for a given time t_{on} where a source is expected to be present (also known as the ON region). After a time t_{on}, the number of measured events is N_{on}. To estimate the number of background events, we observe a portion of the sky for a given time t_{off}, also with area A, but where no source is expected to be present (known as the OFF region). After t_{off}, a total of N_{off} is measured. An example of such an experiment is given in Figure 6.1. Knowing the ratio between the on and off time $\alpha = t_{on}/t_{off}$, one could estimate the expected number of background events $\hat{N}_{off}$ that are measured from the ON region as

$$\hat{N}_B = \alpha N_{off}. \tag{6.5}$$

Therefore, in order to estimate signal events N_S, one has

$$N_S = N_{on} - \hat{N}_B = N_{on} - \alpha N_{off}. \tag{6.6}$$

However, due to the statistical nature of these events, some fraction of the calculated number of signal events N_S (also known as excess events) may be due to random fluctuations at the background level. One has to determine how statistically reliable the estimate of N_S is. The method proposed by Li and Ma [133] (hereafter referred to as Li&Ma) involves the use of the likelihood ratio test [134]. This test calculates the ratio of two likelihoods of a certain set of parameters Θ that produce a distribution of random variables X, $L(\Theta|X) = f(X|\Theta)$. Wilk's theorem [135] states that for a large number of samples of the random variable, the likelihood ratio (or the natural log of the likelihood ratio multiplied by a factor of -2) tends asymptotically to a χ^2 (chi-square) distribution. The standard

[133]: Li et al. (1983), "Analysis methods for results in gamma-ray astronomy."

[134]: Neyman et al. (1933), "IX. On the problem of the most efficient tests of statistical hypotheses"

[135]: Wilks (1938), "The large-sample distribution of the likelihood ratio for testing composite hypotheses"

deviation (or the number of standard deviations, commonly referred to as sigmas [σs]) of this distribution indicates the significance of this excess measurement.

In Li&Ma, in order to compose the likelihood ratio, the authors assume two hypotheses for the experiment mentioned above. The first, the null hypothesis, is where there are no signal events in the ON region, that is, all N_{on} and N_{off} events are due to background. Then the expectation value of N_S is zero or $\langle N_S \rangle = 0$. The second hypothesis, or the alternative hypothesis, is the one where the expectations of signal and background events are maximum, i.e.,

$$\langle N_S \rangle = N_{on} - \alpha N_{off}, \tag{6.7}$$

$$\langle N_B \rangle = \alpha N_{off}. \tag{6.8}$$

In the case that our null hypothesis is true, the expectation value for our background events yields

$$\langle N_B \rangle = \frac{\alpha}{1+\alpha}\left(N_{on} + N_{off}\right). \tag{6.9}$$

With that, we can construct our likelihood ratio λ as

$$\lambda = \frac{\text{Likelihood of null hypothesis}}{\text{Likelihood of alternative hypothesis}} = \\ = \frac{p\left[N_{on}, N_{off} | \langle N_S \rangle = 0, \langle N_B \rangle = \frac{\alpha}{1+\alpha}\left(N_{on} + N_{off}\right)\right]}{p\left[N_{on}, N_{off} | \langle N_S \rangle = N_{on} - \alpha N_{off}, \langle N_B \rangle = \alpha N_{off}\right]} \tag{6.10}$$

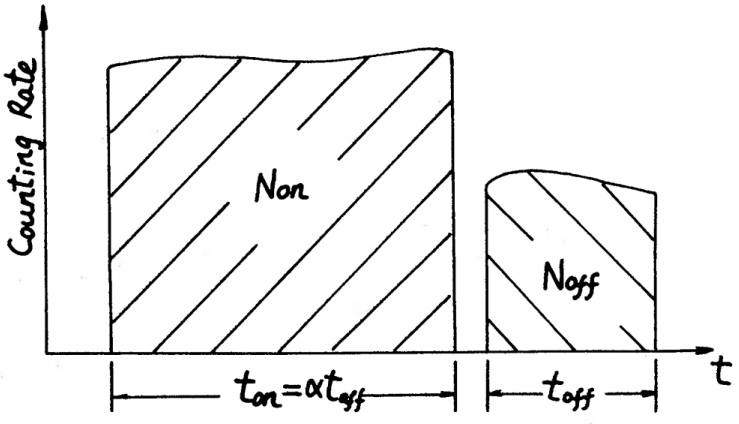

Figure 6.1: Famous illustration from the Li&Ma reference. The figure depicts the counting rates obtained at the ON region after t_{on} interval, and the rates obtained at the OFF region after $t_{off} = t_{on}/\alpha$ interval. N_{on} and N_{off} are the total number of events measured at these regions. Taken from [133].

With the assumption that both N_{on} and N_{off} are random variables that follow a Poissonian distribution (Equation 6.1), and taking the natural log of λ, and multiplying by a factor -2, one has the following:

$$S = \sqrt{-2 \ln \lambda} = \\ = \sqrt{2}\left\{N_{on} \ln\left[\frac{1+\alpha}{\alpha}\left(\frac{N_{on}}{N_{on}+N_{off}}\right)\right] + N_{off} \ln\left[(1+\alpha)\left(\frac{N_{off}}{N_{on}+N_{off}}\right)\right]\right\}^{1/2} \tag{6.11}$$

Equation 6.11 is the famous Eq. 17 in Li&Ma. This equation will quantify how significant a measurement of a pair N_{on} and N_{off} is by a number S of standard deviations, or sigmas. In astronomy, a nominal value of 5σ is the standard for claiming the detection of a new source.

6.1.2 Test statistics

We now discuss some statistics concepts related to energy binned data with known and unknown background.

Poissonian distributed data with known background

Let us assume that n counts were measured in an experiment, distributed over a number m of energy bins such that $n = \sum_{i=0}^{m} n_i$. Equation 6.4 tells us that the likelihood of observing such events is given by, assuming that n are Poissonian distributed:

$$L(n|n) = \prod_{i=0}^{m} L(n_i|n_i) = \\ = \prod_{i=0}^{m} f(n_i|n_i) = \prod_{i=0}^{m} \frac{n_i^{n_i} e^{-n_i}}{n_i!} \tag{6.12}$$

Now, let us assume that our hypothesis predicts a number of signal and background counts, μ_S and μ_B, respectively, as a function of energy. Therefore, in the i-th energy bin, the expected number of signal and background events are $\mu_{S,i}$ and $\mu_{B,i}$. Then, the likelihood of observing n events given the expectation values μ_S and μ_B, is:

$$L(\mu_S, \mu_B|n) = \prod_{i=0}^{m} f(n_i|\mu_{S,i} + \mu_{B,i}) = \\ = \prod_{i=0}^{m} \frac{\left(\mu_{S,i} + \mu_{B,i}\right)^{n_i} e^{-\left(\mu_{S,i}+\mu_{B,i}\right)}}{n_i!} \quad (6.13)$$

Omitting the product in Equation 6.13, we can maximise the log of Equation 6.13 as a function of μ_S and μ_B to find

$$\frac{\partial \log L}{\partial \mu_S} = \frac{\partial \log L}{\partial \mu_B} = 0 \implies \hat{\mu_S} + \hat{\mu_B} = n. \quad (6.14)$$

where $\hat{\mu_S}$ and $\hat{\mu_B}$ are any pair (μ_S, μ_B) that obeys the condition in Equation 6.14, therefore maximising the likelihood $L(n|\mu_S, \mu_B)$ (and also its log). These are called Maximum Likelihood Estimators (MLE) [132]. In order to test how well our hypothesis fits the observed data, we will again invoke the likelihood ratio test (Equation 6.10). We want to test our hypothesis (the expectation values μ_S, μ_B), using Equation 6.13 against our "true" hypothesis, Equation 6.12. The likelihood ratio $\lambda(C)$ will then be

[132]: Cowan (1998), *Statistical data analysis*

$$\lambda(C) = \frac{L(n|\mu_S, \mu_B)}{L(n|n)}. \quad (6.15)$$

By taking the natural log of Equation 6.15 and multiplying it by -2, we have

$$C = -2\log\lambda(C) = \frac{\log\left[L(n|\mu_S, \mu_B)\right]}{\log\left[L(n|n)\right]} = \\ = 2 \times \left[\mu_S + \mu_B - n \times \log(\mu_S + \mu_B) - log n - n\right]. \quad (6.16)$$

Equation 6.16 is known as **Cash statistics** or **C-stat** [136]. It is used when the expectation μ_B for the background is known (i.e., there is a model for the background). Equation 6.16 when calculated for a set (n, μ_S, μ_B) yields a value called **Test Statistic** (TS), a statistical metric. From Wilk's Theorem, the value $\sqrt{C} = \sqrt{-2\log\lambda(C)} = \sqrt{TS}$ is the number of standard deviations based on which we can evaluate our hypothesis for the values of (μ_S, μ_B). The larger the TS value, the better our model fits the observed data.

[136]: Cash (1979), "Parameter estimation in astronomy through application of the likelihood ratio."

Poissonian distributed data with unknown background

In Subsection 6.1.2, we derived a statistic metric for the case where the expectation for the background is known (e.g., through simulations or an analytical model). However, in astrophysics, it is common for the

background to be unknown. In such cases, the lack of knowledge of the background can be accounted for by measuring it, in a way similar to that presented in Subsection 6.1.1. At least two measurements are performed: one of the ON regions (the region where a source is expected to be present) and another (or several others) of an OFF region (containing no sources).

If $t_{on/off}$ and $A_{on/off}$ are the time and areas of the ON/OFF regions, we define the acceptance factor α as

$$\alpha \equiv \frac{t_{on}}{t_{off}} \frac{A_{on}}{A_{off}}. \tag{6.17}$$

After a time t_{on}, n_{on} counts are measured from the ON region, and after a time t_{off}, n_{off} counts are measured from the OFF region. Still under the assumption that n_{on} and n_{off} are random variables, *Poissonianly* distributed over m energy bins, we have

$$\begin{aligned} L(n_{on}, n_{off}|n_{on}, n_{off}) &= \prod_{i=0}^{m} L(n_{i,on}, n_{i,off}|n_{i,on}, n_{i,off}) = \\ &= \prod_{i=0}^{m} f(n_{i,on}|n_{i,on}) f(n_{i,off}|n_{i,off}) = \prod_{i=0}^{m} \frac{n_{i,on}^{n_{i,on}} e^{-n_{i,on}}}{n_{i,on}!} \frac{n_{i,off}^{n_{i,off}} e^{-n_{i,off}}}{n_{i,off}!}, \end{aligned} \tag{6.18}$$

where $n_{i,on/off}$ is the number of counts in the i-th energy bin.

Once again, we assume that the expectation values for the number of signal and background counts are μ_S and μ_B. Therefore, the likelihood of μ_S and μ_B and α, given n_{on} and n_{off} will be

$$\begin{aligned} L(\mu_S, \mu_B, \alpha|n_{on}, n_{off}) &= \prod_{i=0}^{m} L(\mu_{i,S}, \mu_{i,B}, \alpha|n_{i,on}, n_{i,off}) = \\ &= \prod_{i=0}^{m} f(\mu_{i,S} + \mu_{i,B}|n_{i,on}) f(\mu_{i,B}/\alpha|n_{i,off}) = \\ &= \prod_{i=0}^{m} \frac{(\mu_{i,S} + \mu_{i,B})^{n_{i,on}} e^{-(\mu_{i,S}+\mu_{i,B})}}{n_{i,on}!} \frac{(\mu_{i,B}/\alpha)^{n_{i,off}} e^{-(\mu_{i,B}/\alpha)}}{n_{i,off}!}. \end{aligned} \tag{6.19}$$

In the case where both μ_S and μ_B are known and are free parameters, we find

$$\begin{cases} \frac{\partial \log L}{\partial \mu_S} = 0 \implies \hat{\mu_S} = n_{on} - \alpha n_{off}, \\ \frac{\partial \log L}{\partial \mu_B} = 0 \implies \hat{\mu_B} = n_{off}, \end{cases} \tag{6.20}$$

where $\hat{\mu_S}$ and $\hat{\mu_B}$ are the MLE of Equation 6.19. But since we do not know the expectation for the background, it is useful to write it as a function of our known values ($\mu_S, \alpha, n_{on}, n_{off}$). By minimising $L(\mu_S, \mu_B, \alpha | n_{on}, n_{off})$ with respect to μ_B, we have

$$\frac{\partial \log L}{\partial \mu_B} = \frac{\alpha n_o n}{\mu_S + \alpha \mu_B} + \frac{n_{off}}{\mu_B} - (\alpha + 1) = 0 \implies$$
$$\implies \mu_B = \frac{b + \sqrt{b^2 + 4(\alpha + 1)\alpha n_{off} \mu_S}}{2\alpha(\alpha + 1)}, \quad (6.21)$$

where

$$b = \alpha(n_{on} + n_{off}) - (\alpha + 1)\mu_S \quad (6.22)$$

Now the likelihood in Equation 6.19 no longer depends on μ_B - $L(\mu_S, \mu_B, \alpha | n_{on}, n_{off}) = L(\mu_S, \alpha | n_{on}, n_{off})$. Now we construct the likelihood ratio $\lambda(W)$, with Equation 6.19 and Equation 6.18. $\lambda(W)$ is defined as

$$\lambda(W) = \frac{L(\mu_S, \alpha | n_{on}, n_{off})}{L(n_{on}, n_{off} | n_{on}, n_{off})}, \quad (6.23)$$

so we can define the **W-statistics** or **W-stat** as

$$W = \sqrt{-2 \log \lambda(W)} =$$
$$= 2\{ \mu_S + (1 + \alpha)\mu_B -$$
$$- n_{on}[\ 1 - \log(\mu_S + \alpha\mu_B) - log(n_{on})\ ] -$$
$$- n_{off}[\ 1 - \log(\mu_B) - \log(n_{off})\ ]\ \}. \quad (6.24)$$

Gaussian distributed data

In some cases, a measurement can be treated as a random Gaussian variable centred around a given value with a given variance, e.g. flux points instead of counts with error bars. In that case, the likelihood follows a Gaussian distribution. Let us define a set of m independent Gaussian random variables y_i, where $i = 1, 2, ..., m$, $y_i = M(x_i)$, and M is the measurement at given x_i. Each measurement has a variance σ_i associated with it. Now, let us assume that for each y_i value there is a true (predicted) value, $\mu_i = T(x_i)$, where T is the theoretical model which we are trying to compare to our data. Therefore, the pdf $f(\mathbf{y}|\mu, \sigma)$ is

$$f(\mathbf{y}|\mu,\sigma) = \prod_{i=1}^{m} \frac{1}{\sqrt{2\pi\sigma_i^2}} \exp\left[\frac{-(y_i-\mu_i)^2}{2\sigma_i^2}\right] \tag{6.25}$$

where $\mathbf{y} = y_1, ..., y_m$, $\mu = \mu_1, ..., \mu_m$, $\sigma = \sigma_1, ..., \sigma_m$. When the true value μ_i depends on unknown parameters $\theta = \{\theta_1, ..., \theta_k\}$, so that $\mu_i = \mu_i(x_i, \theta)$, the logarithmic likelihood $L(\theta)$ is

$$\log L(\theta) = -\frac{1}{2} f(\mathbf{y}|\mu,\sigma) = -\frac{1}{2} \sum_{i=1}^{m} \frac{[y_i - \mu_i(x_i,\theta)]^2}{\sigma_i^2}, \tag{6.26}$$

where, in order to find the parameters that maximise $\log L(\theta)$, one just needs to minimise

$$\chi^2(\theta) = \sum_{i=1}^{m} \frac{[y_i - \mu_i(x_i,\theta)]^2}{\sigma_i^2}. \tag{6.27}$$

6.2 Flux and spectral reconstruction

In all three cases mentioned above (C-stat, W-stat, or Gaussian), an expectation value is assumed for the number of signal events. The metrics given in Equation 6.16, Equation 6.24, and Equation 6.27 are used to determine the likelihood of such expectation given the observed data. An important observable in astrophysics is the differential observed flux of photons: the amount of photons per solid angle per time per energy that a source is emitting in a given period. If $\Phi = dn/d\Omega dt dE$ is the differential flux of a given source, then the number n of counts measured during the time period $[t_{min}, t_{max}]$ can be written as

$$n = \int\int\int_{t_{min}}^{t_{max}} \Phi(E,\hat{\kappa},t) dE d\hat{\kappa}\, dt, \tag{6.28}$$

where $\hat{\kappa}$ is the photon's 2-dimensional direction of arrival.

To make a realistic prediction of the expected number of signal events, one has to account for the physical limitations of the detector. Due to the intrinsic statistical nature of the events and the numerical limitations of the reconstruction algorithms used in the processing of the measured data, we define the probability $p(E, \hat{\kappa}, E_{rec}, \hat{\kappa_{rec}})$. $p(E, \hat{\kappa}, E_{rec}, \hat{\kappa_{rec}})$ is the probability of measuring a photon with energy E and arrival direction $\hat{\kappa}$ and reconstructing its energy to E_{rec} and arrival direction to $\hat{\kappa_{rec}}$. The probability $p(E, \hat{\kappa}, E_{rec}, \hat{\kappa_{rec}})$ can be factored into three different terms [137]:

[137]: D'Amico (2022), "Statistical tools for imaging atmospheric Cherenkov telescopes"

$$p(E, \hat{\kappa}, E_{rec}, \hat{\kappa_{rec}}) = p(E_{rec}|E) \times p(\hat{\kappa_{rec}}|E, \hat{\kappa}) \times p(E, \hat{\kappa}). \tag{6.29}$$

The term $p(E_{rec}|E)$ is used to estimate the **energy dispersion** of the instrument and is determined by a **migration matrix**. The probability $p(\hat{\kappa_{rec}}|E, \hat{\kappa})$ is known as the **Point Spread Function** (PSF). The *a priori* probability is $p(E, \hat{\kappa})$ is known as **effective area**. These quantities, the migration matrix, the PSF, and the effective area, are known as **Instrument Response Functions** (IRFs). Every detector combined with the algorithm (or software) used in the processing of the collected data has a set of IRF attached to it. The IRFs are usually determined from Monte Carlo (MC) simulations: the emission, propagation, and detection of both the signal and background events are simulated and then subjected to the reconstruction algorithms, thus estimating these probabilities in the form of IRFs. In the context of estimating the IRFs of a detector, it is standard to define the energy variable above E as the true energy values used in the MC simulations, E_{true}.

The energy migration matrix $M(E_{rec}|E_{true})$ is a two-dimensional histogram of n bins of E_{true} versus m bins of E_{rec}. The $PSF(\hat{\kappa_{rec}}|E_{true}, \hat{\kappa})$ is energy dependent and is determined by the 68% containment radius of the reconstructed positions of the arrival directions of the events, in a certain energy range. The effective area is simply the detector's total area of collection multiplied by the fraction of simulated events that survive analysis selection cuts (see next section). The effective area $A(E_{true})$ can be written as

$$A(E_{true}) = A_T \left(\frac{\text{number of events after selection cuts with at} E_{true}}{\text{total number of events simulated at } E_{true}} \right), \tag{6.30}$$

where A_T is the total area in which the events were simulated. Knowing the IRFs of a detector, one can write the number of expected signal events (as well as background events if the background model is known) as

$$\mu_S = \int_{t_{min}}^{t_{max}} dt \int_{\Omega} d\,\hat{\kappa} \int_0^{\infty} dE_{true} \int dE_{rec} \\ \Phi(E_{true}, \hat{\kappa}, t) \times M(E_{rec}|E_{true}) \times PSF(\hat{\kappa_{rec}}|E_{true}, \hat{\kappa}) \times A(E_{true}). \tag{6.31}$$

Therefore, for any source spectrum $\Phi(E_{true}, \hat{\kappa}, t, \theta)$ that depends on a set of parameters $\theta = \theta_1, \theta_2, ..., \theta_n$, one can calculate the expectation values μ_S with Equation 6.31 and compare them to the observed data using Equation 6.16, Equation 6.24 and Equation 6.27. Notice that we can use Equation 6.31 to calculate the expectation value for any given energy bin $[E_{i,rec}, E_{i,rec} + \Delta E_{rec}]$.

This fitting process is known as *forward folding* [137]. The forward folding process is widely used in the process of fitting spectral models to observed data. The set of IRFs of a given detector is generally a non-invertible

[137]: D'Amico (2022), "Statistical tools for imaging atmospheric Cherenkov telescopes"

matrix, and with forward folding we are able to avoid these inversions and calculate the TS of spectral models to a given data at the event level.

6.2.1 Spectral analysis

We have determined the expectation values for the number of signal events in Equation 6.31 as a function of the assumed spectral shape $\Phi(E, \hat{\kappa}, t)$ and the IRF of the detector. For convenience, let us now assume that the spectrum Φ is in steady state, i.e. it does not depend on the elapsed time t, and is also isotropic (which is justified in our case since we will be performing a point source analysis), which means that we can simply integrate the temporal and spatial dependence in Equation 6.31 with a constant PSF. In this case, $\Phi \equiv \Phi(E)$. If we now assume a functional form for $\Phi(E)$ that depends on a set of independent parameters $\theta = \{\theta_1, \theta_2, ..., \theta_n\}$, the likelihood of the observed data given our expectation will be a function of θ:

$$\mu_S \to \mu_S(\theta_1, \theta_2, ..., \theta_n) \implies \begin{cases} C \to C(n, \theta_1, \theta_2, ..., \theta_n), \\ W \to W(n_{on}, n_{off}, \alpha, \theta_1, \theta_2, ..., \theta_n), \\ \chi^2 \to \chi^2(n, \theta_1, \theta_2, ..., \theta_n). \end{cases}$$

As mentioned above, the set of parameters $\hat{\theta} = \{\hat{\theta}_1, \hat{\theta}_2, ..., \hat{\theta}_n\}$ that maximise the likelihood is given by

$$\frac{\partial log L(\theta_i)}{\partial \theta_i}\Big|_{\hat{\theta}_i} = 0. \tag{6.32}$$

Having determined the set of the "best-fit" parameters $\hat{\theta}$, we can define the quantity TS_{max}

$$log L(\hat{\theta}_i) \equiv TS_{i,max}, \tag{6.33}$$

which is the value of TS when calculating the logarithmic likelihood at $\hat{\theta}$. We will introduce the sets $\hat{\theta}_{min} = \{\hat{\theta}_{1,min}, \hat{\theta}_{2,min}, ..., \hat{\theta}_{n,min}\}$ and $\hat{\theta}_{max} = \{\hat{\theta}_{1,max}, \hat{\theta}_{2,max}, ..., \hat{\theta}_{n,max}\}$, such that

$$TS_{i,max} - log L\left(\hat{\theta}_{i,min}\right) = 1, \tag{6.34}$$

$$log L\left(\hat{\theta}_{i,max}\right) - TS_{i,max} = 1. \tag{6.35}$$

The values $\hat{\theta}_{i,\mathrm{min}}$ and $\hat{\theta}_{i,\mathrm{max}}$ are the lower and upper bounds of the value of $\hat{\theta}_i$ such that the variation of TS is 1. In this way, we can define the

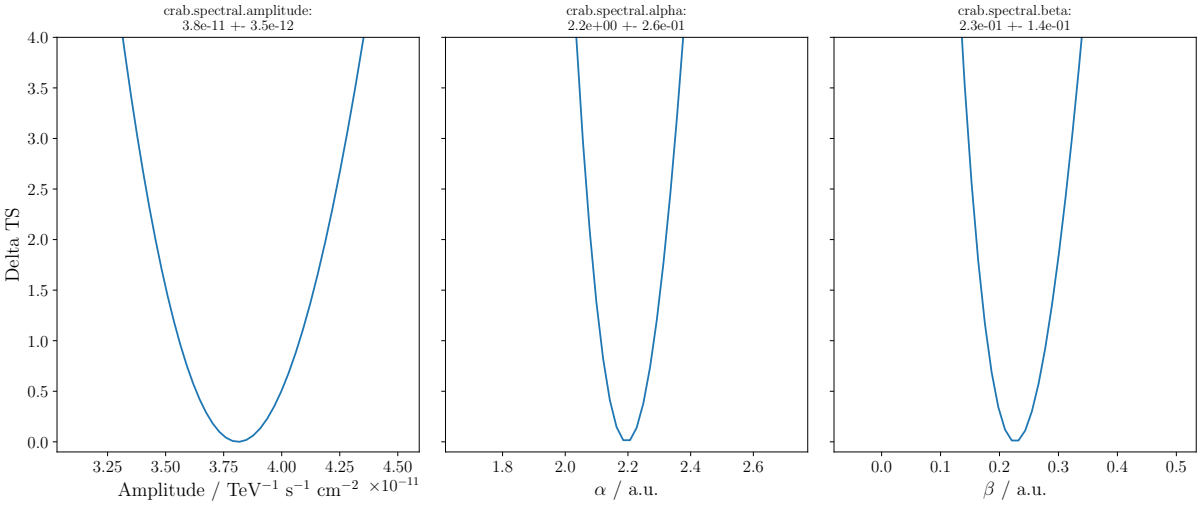

Figure 6.2: Likelihood profile of log-parabola parameters fitted to the Crab Nebula data. The Delta TS (y-axis) is calculated as the variation relative to the minimum value as a function of the parameter value. Adapted from `https://docs.gammapy.org/dev/tutorials/api/fitting.html`.

1-standard-deviation interval as the asymmetrical uncertainty values for the best-fit parameters as

$$\hat{\theta}_i \rightarrow \hat{\theta}_i \pm^{\hat{\theta}_{i,max}-\hat{\theta}_i}_{\hat{\theta}_i-\hat{\theta}_{i,min}} . \tag{6.36}$$

In Figure 6.2, we show an example of this method applied to the Crab Nebula data. In this example, we assume a logarithmic parabolic spectrum

$$\Phi(E) = \Phi_0 \left(\frac{E}{E_0}\right)^{-\alpha-\beta log\left(\frac{E}{E_0}\right)} , \tag{6.37}$$

where Φ_0 is the normalisation of the spectrum at the reference energy E_0 and α and β are the spectral index of the power law and the curvature, respectively. In this case, Φ_0, α and β are free parameters, and E_0 is fixed to 1 TeV. Figure 6.2 shows the likelihood profiles for each parameter and the nominal fit values with the corresponding uncertainty values.

Once the best-fit parameters of the model are defined, we can calculate the flux of a source in a given energy range, i.e., the integral flux over the whole sensitive energy range of a detector or in an energy bin for flux points estimation. The details of the flux point estimation will be discussed in Chapter 7.

Below are provided some useful quantities that are related to/derived from the photon spectrum:

Useful definitions

Counts spectrum The number of counts (photon counts) as a function of energy. Defined as $\frac{dN}{dE}$, given in erg^{-1}.

Photon spectrum Photon flux as a function of energy. Defined as $\frac{dN}{dEdAdt}$, given in $\mathrm{erg}^{-1}\mathrm{cm}^{-2}\mathrm{s}^{-1}$.

Energy Spectrum or Spectral Energy Distribution (SED) Photon energy flux as a function of energy. Defined as $E^2\frac{dN}{dEdAdt}$, given in $\mathrm{erg\ cm}^{-2}\mathrm{s}^{-1}$.

Integral flux Photon flux integrated over an energy range. Defined as $\int \frac{dN}{dEdAdt}dE$, given in $\mathrm{cm}^{-2}\mathrm{s}^{-1}$.

Integral energy flux Photon energy flux, integrated over a energy range. Defined as $\int E\frac{dN}{dEdAdt}dE$, given in $\mathrm{erg\ cm}^{-2}\mathrm{s}^{-1}$.

Lightcurve The integral flux or the integral energy flux as a function of time. The time bins usually have a length of a day, a week, a month, etc.

Data analysis application to 1ES 1218+304 and 1ES 0229+200 data

Data analysis and lightcurves | 7

In Subsection 2.2.2 and Subsection 2.3.1 we discussed variability aspects and the different spectral aspects of EHBLs. Given the availability of long-term data on 1ES 1218+304 and 1ES 0229+200, in this chapter, we will present an extensive study on the spectral and flux variability via lightcurves. We describe the analysis methods applied to the data from each instrument and the results obtained for each source.

7.1 VERITAS data analysis

We performed the data reconstruction using the package `Eventdisplay` [108]. The complete method is described in Section 5.1 and its subsections. After the low-level reconstruction has been finished, we are ready to produce high-level products such as spectra, lightcurves, and significance maps, which will be discussed in this chapter. All observations are taken at an 0.5° offset of the source's position, where the offset can be to the north, south, east, or west of the source. These are called *wobble* observations in VERITAS. *Wobble* observations are used to measure background events that are equidistant from the pointing position, while at the same time measuring source events. We will discuss the application of *wobble* observations later in this section. All observations were taken at *nominal high voltage* (NHV) as opposed to *reduced high voltage* (RHV). RHVs observations are taken at nights where the rates of the night sky background (NSB)* lights are not suitable for NHV observations. The high voltage gain applied to the PMTs is set to a reduced value to avoid saturation, at the cost of reduced trigger rates (i.e. [138]). It should be noted that we only selected NHV observations that were taken during good weather conditions and without identified instrumental problems.

[138]: Archambault et al. (2017), "Gamma-ray observations under bright moonlight with VERITAS"

7.1.1 Background estimation

In the absence of a background description, one has to rely on methods to estimate the background rates in the source's FoV. In IACTs, the two most common methods used are the *reflected* and *ring* background regions. The complete description of these methods is provided in [139]. We show a schematic illustration in Figure 7.1 of the different geometries of each method. Counts from *off*-source regions (OFF region) are used to estimate background rates. The assumption here is that the background events are

[139]: Berge et al. (2007), "Background modelling in very-high-energy ɣ-ray astronomy"

* Diffuse light emission from stars, city lights, moon light, etc.

isotropically distributed within the FoV. We provide a brief description of the OFF regions used in each method:

Ring background A ring is placed around the expected source position, concentric to the source region in sky coordinates. The acceptance parameter $\alpha = \Omega_{on}/\Omega_{off}$, that is, the ratio between the solid angle of the ON region Ω_{on} and the solid angle of the OFF region Ω_{off} is typically set to ~ 1.7 [139]. One of the caveats in this approach is that the instruments acceptance can vary depending on the offset to the pointing position, therefore, one has to account for that during ring-background estimations.

Reflected-region background The OFF regions are circles placed in a ring around the pointing position. The offset in which the OFF regions are placed is the same as the ON region offset. In addition, the OFF regions have the same size and shape as the ON region, so that α is simply the number of ON regions N_{ON} divided by the number of OFF regions N_{OFF}, $\alpha = N_{ON}/N_{OFF}$.

7.1.2 High-level analysis

Source's spectra and lightcurves are calculated with the python package `gammapy` [140]. The analysis in `gammapy` is structured as follows:

[140]: Donath et al. (2023), "Gammapy"

1. Observations are selected from a *data store* - a virtual location containing the event lists and the required IRFs for the analysis, as FITS files, which also contains observation metadata, such as date, observing duration, pointing information, etc. The selected observations must have been taken at least within 2° of the target source.
2. Time cuts are applied to the selected observations to remove short intervals of compromised data.
3. We define the geometry of our region of interest (ROI): a 150-bin x 150-bin area centred on the target source, with a bin size of 0.05°.
4. In order to prevent an overestimation of background rates, any bright star (lower than 7 magnitude) within 1.75° of the target and/or any known gamma-ray source within the ROI is masked out, i.e. no event from these regions is accounted for.
5. A reflected-region background estimation is performed using 1 ON and 6 OFF regions, with radii equal to $\sqrt{0.008}$ degrees (the size of VERITAS PSF). The regions are placed equidistantly of the pointing direction, at 0.5° offset.
6. The on and off counts are extracted, and from each observation a *dataset* is created containing the list of on and off events, migration matrix and effective areas of each observation[†], as shown in Figure

[†] A set of IRFs is previously simulated for different zenith angles, season of the year (summer on winter) and set of cuts (soft, moderate or hard).

7.2.

7. To avoid poorly reconstructed events with large biases, we set an energy threshold based on the estimated energy dispersion: the safe energy range is set to be where $(E_{true} - E_{rec})/E_{true}$ is lower than 20%.
8. We then follow the process described in Section 6.2. We used W-stats (Equation 6.24) to find the best-fit parameters of our assumed spectral model.
9. In order to calculate the flux of photons in a given range (which can be either in an energy bin to calculate flux points or the integral flux to produce a lightcurve), the step above is repeated over the desired energy range, keeping only the normalisation parameter of the model as a free parameter while fixing the other parameters.

In the above steps, the PSF is not taken into account during the forward folding process because we perform a point-source analysis, meaning that the extension of our source is smaller than our angular resolution, and therefore all counts are considered to have come from the same direction at this stage of the analysis. This means that the expected number of signal events μ_S, from Equation 6.31, becomes

$$\mu_S = \int_{t_{min}}^{t_{max}} dt \int_0^{\infty} dE_{true} \int dE_{rec} \Phi(E_{true}, \hat{\kappa}, t) \times M(E_{rec}|E_{true}) \times A(E_{true}).$$

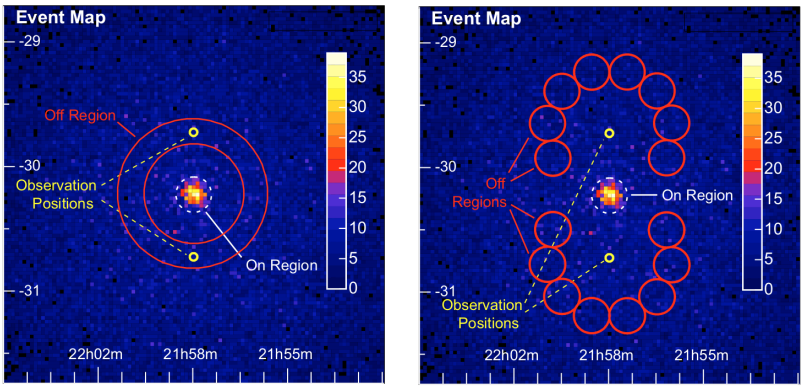

Figure 7.1: Background estimation methods, *ring background* (left) and *reflected regions* (right). These methods of background estimation are described in Subsection 7.1.1. Taken from [139].

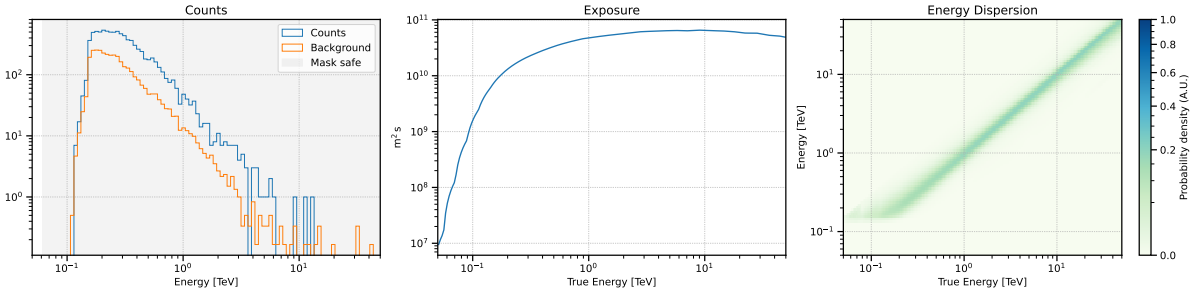

Figure 7.2: Dataset with IRFs, created with a *reflected region analysis* in `gammapy`, from 1ES 1218+304 data. Background counts are the off counts normalised by the ratio between the number of ON regions and OFF regions $\alpha = 1/6$.

7.2 *Fermi*-LAT data analysis

The low-level reconstruction of *Fermi*-LAT data is described in Section 5.2. The data are queried from the LAT data server[‡]. All available photon data within 15° of 1ES 1218+304 and 1ES 0229+200 positions are downloaded, covering the same period as the VERITAS observations. Data analysis is handled by the package `fermipy` [141]. `fermipy` provides a python framework for data selection, spectral and spatial model fitting, SED and light curve extraction, etc., based on Fermi's `Science Tools` [§].

[141]: Wood et al. (2017), "Fermipy"

7.2.1 Quality cuts

Quality cuts are applied to the available data. The cuts are shown in Table 7.1. The first cut applied is based on the classes and types of events (as described in Subsection 5.2.2). The chosen class and type will define which events are accepted and also which set of IRFs will be used later in the analysis. Mode and data quality cuts are used in the determination of good time intervals (GTIs). Lastly, a cut on the zenith angle is applied to reduce the background contamination originating from Earth's limb.

7.2.2 High-level analysis

With the event types and classes defined, we now define the ROI of our analysis. We center our ROI at the target position of the source and

Table 7.1: *Fermi*-LAT data quality cuts. For consistency, we keep the notation used in `fermpiy`'s documentation.

Cut	Description	Selection
Event class	`P8R2_SOURCE_V6` IRFs	`evclass` : 128
Event type	Back AND front converting events	`evtype` : 3
Data quality	Data taken has not been affected by external factors	`DATA_QUAL`> 0
Mode	Data taking	`LAT_CONFIG`== 1
Angle	Maximum zenith angle allowed, in degrees	`zmax` : 90

[‡] `https://fermi.gsfc.nasa.gov/cgi-bin/ssc/LAT/LATDataQuery.cgi`
[§] `https://fermi.gsfc.nasa.gov/ssc/data/analysis/documentation/`

Table 7.2: Selection criteria used for this analysis in addition to the quality cuts. These criteria will be used for all different steps in the analysis of the *Fermi*-LAT data, unless stated otherwise.

Parameter	Description	Selection
`roiwidth`	The ROI's side size in degrees	10 °
`binsz`	The spatial bin size used in the ROI	0.1 °
`binsperdec`	The number of energy bins per decade in energy	8
`emin`	The minimum energy taken into account during the analysis	100 MeV
`emax`	The maximum energy taken into account during the analysis	300 GeV
`tmin`	The minimum Mission Elapsed Time (MET) considered in seconds	MET 252 460 802 seconds (2009, January 1st)
`tmax`	The maximum Mission Elapsed Time (MET) considered in seconds	MET 662 601 605 seconds (2021, December 12th)

define the ROI geometry with the parameters described in Table 7.2. The values in Table 7.2 are standard values used in the analysis of point-like sources data. Events that fall within a GTI and within the minimum and maximum times of our ROI model are selected. Events are then grouped into spatial and energy bins (and time bins if defined) according to the ROI model. These are known as *counts* cubes.

Fermi-LAT does not have a fixed pointing direction during operation, therefore the livetime and exposure are calculated per each bin, as explained in the *Cicerone* documentation[¶].

The livetime is defined as the time that the LAT observed a given position on the sky at a given inclination angle. These livetimes define what are known as *livetime* cubes. The livetime cubes are then used to calculate the total response of the instrument over the entire ROI, written as $\varepsilon(E_{true}, \hat{\kappa})$, defined as follows:

$$\varepsilon(E_{true}, \hat{\kappa}) = \int_{\text{ROI}} dE_{rec} d\hat{\kappa}_{rec} dt \varepsilon(E_{rec}, \hat{\kappa}_{rec}; E_{true}, \hat{\kappa}, t), \tag{7.1}$$

where $\varepsilon(E_{rec}, \hat{\kappa}_{rec}; E_{true}, \hat{\kappa}, t)$ is the spatial/energy dependent response for a time t. For the reasons described in Section 6.2, the response function $\varepsilon(E_{true}, \hat{\kappa})$ will then be used to calculate the predicted number of photons from a given source, assuming a certain source intensity (again, Equation 6.31). Therefore, in this case we have that the expectation for the number of signal photons from a given source with photon intensity $\Phi(E_{true}, \hat{\kappa})$ is

$$\mu_S = \int dE_{true} d\hat{\kappa} \Phi(E_{true}, \hat{\kappa}) \times \varepsilon(E_{true}, \hat{\kappa}_{true}).$$

[¶] `https://fermi.gsfc.nasa.gov/ssc/data/analysis/documentation/Cicerone/Cicerone_-Data_Exploration/livetime_and_exposure.html`

[142]: Abdollahi et al. (2020), "Fermi large area telescope fourth source catalog"

The last ingredient of our analysis is the background estimation. A galactic interstellar emission model (`gll_iem_v07.fits`) is provided by the LAT Collaboration [142]. An isotropic diffuse gamma-ray emission model is also included. The isotropic diffuse emission model is provided for each event class and event type combination (in our case, we use `iso_P8R3_SOURCE_V3_v1.txt`). Both models are described in the 4FGL reference and through their online documentation [‖]. Therefore, the background expectation in the ROI, μ_B, is defined both spatially and in energy. Since our background expectation is known, we can use Equation 6.16 to compare the observed number of counts with the expected number (source + background) in each energy, space, and time bin. Beyond the target source, all known gamma-ray sources within the ROI are taken into account. We use a fit procedure where we allow the parameters of the sources' spectral models to float. `fermipy` utilises an optimization process to take the spectral model parameters closer to the global minima. In the first fit iteration, the spectral model of each source in the ROI is fitted a number of times. Sources with $TS < 2$ after optimisation are removed from the ROI to speed up the computation time. Sources within 2° distances from our target model, and sources with $TS > 10$ have their spectral model parameters freed after optimisation. Finally, in the next iteration, we perform a second fit to find the best models for the sources in the ROI.

SED and flux calculation

Once the fit to the full ROI is done and the best model is found, in order to calculate the photon flux of the target in a given energy range (an energy bin for the SED calculation or the integral flux in the whole energy range for a light curve calculation, for instance), the source target model is replaced by a power law with spectral index $\Gamma = 2$ and normalisation parameter N_0. The fit is done once again, but keeping only the normalisation parameter N_0 as a free parameter, and fixing everything else, namely the spectral index of the target's model Γ and all the other sources' models in the ROI. Having found the best-fit value for N_0, the flux and SED can then be calculated according to the definitions in Subsection 6.2.1.

7.3 *Swift*-XRT data analysis

7.3.1 Data selection

In Section 5.3 and Subsection 5.3.1, we provide a brief description of the raw data processing and reduction to the event lists necessary to perform the high-level analysis in this section. Data are downloaded

[‖] `https://fermi.gsfc.nasa.gov/ssc/data/analysis/software/aux/4fgl/Galactic_Diffuse_Emission_Model_for_the_4FGL_Catalog_Analysis.pdf`

from HEASARC and quality cuts are applied during data reduction. First, we only select pointing observation runs, i.e., runs where the telescope has already settled after slewing to the source. Runs are also selected on the basis of the observation modes: Only WT and PC runs are used. To generate the event lists, the events are filtered according to their grade and observation mode. Only events with a grade between 0 and 12 are selected for PC mode (Figure 5.9), and between 0 and 2 for WT mode (Figure 5.8). The pointing direction of the runs must be at an angular distance that is at least larger than 45° to the Sun and 30° to the Moon. The last criteria are the angular distances between the run pointing and the Earth's limb (must be greater than 45°) and the day-night twilight line (must be greater than 120°).

7.3.2 High-level analysis

We first define the ON and OFF regions from which the counts will be extracted. The ON region is a circular region with a radius of 20 pixels ($\approx$ 47 arcseconds), centred at the source location. The OFF region will be defined as an annular region also centred on the source location: for PC mode, the OFF region inner and outer radii are set in order to have the same area as the ON region, being at least larger than 20 pixels. For WT mode runs, the inner and outer radii are set to 80 and 120 pixels, respectively, to ensure that the OFF region always contains at least 40 pixels. This is necessary to ensure that there will always be a patch of dark sky (i.e., absent of X-ray sources) in the beginning or the end of an WT observation. Having defined the ON and OFF regions, we use `xselect` to extract the counts spectra from these regions.

One caveat regarding the analysis of PC mode runs is the presence of pile-up effects in the central pixel of the image. Photon pile-up occurs when the charge measurements of two or more photons overlap in the central image pixel. Pile-up effects are not expected to occur for count rates below 0.5 counts/second. To correct for pile-up effects, a simple estimation of the counts rate of the ON region is performed. For runs with a rate higher than 0.5 counts/second, an innermost circular region of 6 arcseconds is excluded from the ON region. The OFF region radii are corrected to match the new ON region area, and the counts are once again extracted. If the rates are still higher than 0.5 counts/second, the process is repeated, increasing the exclusion region radius by another 6 arcseconds.

Having extracted the source (ON) and background (OFF) counts spectra, we can now perform the spectral analysis of our data. For that, we use the ancillary response files (ARFs) created during the data processing and response matrix files (RMFs) from the instrument's calibration. ARFs

contain an instrument response matrix with corrections for vignetting and corrections to the PSF that are caused by missing data.

The counts are binned into energy bins with at least 20 counts, which allows us to treat the data as Gaussian distributed (due to the Central Limit Theorem) statistics, assuming that the counts obbey Poissonian statistics. We can then use a chi-squared metric to test the models (Equation 6.27).

Spectrum and absorption

In the X-ray energy range, photons can be absorbed in interactions with atomic matter, primarily hydrogen, while they travel through space. To account for this effect, we define the observed counts spectrum dN/dE as

$$\frac{dN}{dE} = \left(\frac{dN}{dE}\right)_{emitted} e^{-n_H \sigma(E)}, \tag{7.2}$$

where $\left(\frac{dN}{dE}\right)_{emitted}$ is the intrinsic photon spectrum emitted at the source and is attenuated according to the density of the hydrogen column in the direction of the source n_H and the photoeletric cross section $\sigma(E)$. The hydrogen column densities are calculated using *Swift*'s collaboration tool**, based on [143]. The SED and flux (lightcurves) calculations are performed as described in Subsection 6.2.1.

[143]: Willingale et al. (2013), "Calibration of X-ray absorption in our galaxy"

7.4 *Swift*-UVOT data analysis

We now present the results of the analysis of the data taken by the Swift-UVOT detector in the optical/ultraviolet range. As described in Subsection 5.3.2, cleaned and calibrated event list files and images are created. We then extract light curves and count spectra for each available filter from the position of our source. Provided the photometric calibration data of the telescope [144], the count rates can be converted into fluxes for each filter. The resulting data in erg cm^{-2} s^{-1} Å^{-1} are corrected for by the central wavelength value of each filter in Å so that our results can be presented in units of energy flux erg cm^{-2} s^{-1}. The wavelengths are listed in Table 4.1.

[144]: Poole et al. (2007), "Photometric calibration of the Swift ultraviolet/optical telescope"

7.5 Analysis results

In the next sections, we present spectra and lightcurves obtained from VERITAS, *Fermi*-LAT, *Swift*-XRT and *Swift*-UVOT high-level analysis.

** https://www.swift.ac.uk/analysis/nhtot/

Our goal is to study the time evolution of the MWL emission from our target sources. Several studies on 1ES 1218+304 and 1ES 0229+200 place them as prototypical EHBL objects (e.g. [38, 43, 45]), but for the first time we have access to more than 10 years of MWL data. Studies of the broadband SED of EHBL objects with no detected variability within the time range used are now possible. Furthermore, studies on IGMF strength with EHBLs depend on the minimum variability time observed for the source [145, 146], and, in particular, 1ES 0229+200 is one of the standard sources to measure IGMF strength (e.g. [52, 147]).

7.6 1ES 1218+304 data

7.6.1 VERITAS

The Blazar 1ES 1218+304 catalogued in the *Einstein Slew* survey (ES) in 1991 [148], was identified as a BL Lac object in 1979 [149]. It is located at RA $12^{h}21^{m}26.3^{s}$, Dec 30°21′26.3" [44], at a redshift $z = 0.182$ [150]. A spectral index $\Gamma \sim 3$ is reported (e.g. [40, 151]) for a spectrum described using a power law $\propto E^{-\Gamma}$ in the VHE range, with a variable flux of 6% - 20% Crab [44][152].

Table 7.3 summarises the sample of VHE data taken by the VERITAS collaboration used in this thesis. In Figure 7.3 we show VERITAS' cumulative significance of 1ES 1218+304 as a function of time; the monthly binned light curve; and the integrated spectral index and amplitude of the season in Figure 7.4. A power-law fit to each observing season yields an average spectral index per season of $\overline{\Gamma} \simeq 3.6$ with a standard deviation of ~ 0.5, using 1 TeV as reference energy. No variability in the spectral index is observed for the two highest flux months around 58500 and 58800 MJD, but rather an increase in the total number excess events as shown by the increase in amplitude in the bottom panel of Figure 7.4.

7.6.2 *Fermi*-LAT

In *Fermi*-LAT fourth source catalogue data release 4 (4FGL-DR4) [153], 1ES 1218+304 is associated with the source 4FGL J1221.3+3010, with a detection significance of $\approx 90.5\sigma$. For the time period that matches the

[38]: Costamante et al. (2018), "The NuSTAR view on hard-TeV BL Lacs"
[43]: Aliu et al. (2014), "A three-year multi-wavelength study of the very-high-energy gamma-ray blazar 1ES 0229+200"
[45]: Archambault et al. (2014), "Test of models of the cosmic infrared background with the multiwavelength of the blazar 1ES 1218+30.4 in 2009"
[145]: Finke et al. (2015), "Constraints on the intergalactic magnetic field with gamma-ray observations of blazars"
[146]: Dermer et al. (2011), "Time delay of cascade radiation for TeV blazars and the measurement of the intergalactic magnetic field"
[52]: Ackermann et al. (2018), "The Search for Spatial Extension in High-latitude Sources Detected by the Fermi Large Area Telescope"
[147]: Acciari et al. (2023), "A lower bound on intergalactic magnetic fields from time variability of 1ES 0229+200 from MAGIC and Fermi/LAT observations"
[148]: Elvis et al. (1992), "The Einstein slew survey"
[149]: Wilson et al. (1979), "On the identification of the high-latitude X-ray source 2A 1219 + 305"
[44]: Acciari et al. (2009), "VERITAS observations of the BL Lac object 1ES 1218+304"
[150]: Bade et al. (1998), "The Hamburg/RASS catalogue of optical identifications"
[40]: Albert et al. (2006), "Discovery of very high energy gamma rays from 1ES 1218+30.4"
[151]: Benbow (2011), "Highlights of the VERITAS blazar observation program"
[152]: Acciari et al. (2010), "Discovery of variability in the very high energy γ-ray emission of 1ES 1218+304 with VERITAS"
[153]: Ballet et al. (2023), *Fermi large area telescope fourth source catalog data release 4 (4FGL-DR4)*

Table 7.3: Summary table of 1ES 1218+304 observations taken by VERITAS in which data are used in this thesis. The accumulated significance is calculated using Equation 6.11

Observation period	December 2008 to February 2021
Number of runs	477
Total exposure	~ 175 hours
Acumulated significance (σ)	~ 68

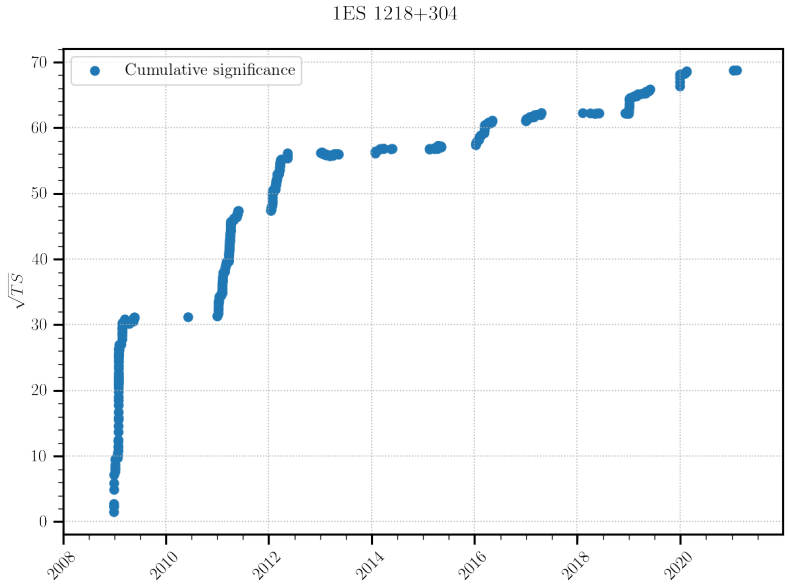

Figure 7.3: VERITAS cumulative significance on 1ES 1218+304 from 2008 to 2021

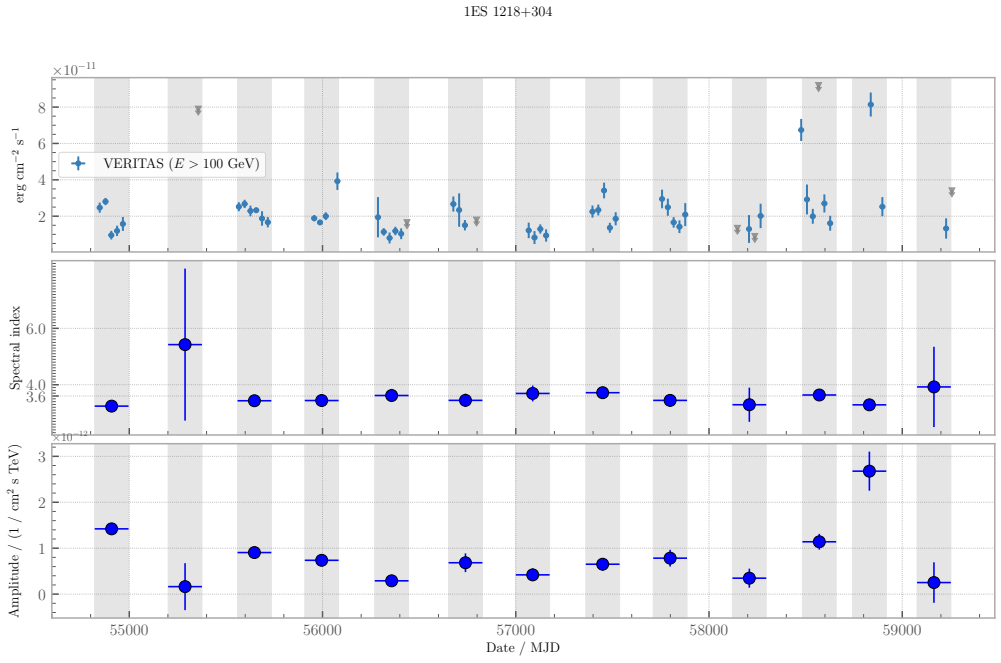

Figure 7.4: 1ES 1218+304 VERITAS lightcurve (top) and spectral parameters (middle and bottom) per observing season. On the top pad is presented VERITAS energy flux lightcurve, for energies greater than 100 GeV, in bins of 1 month. The grey arrows on the top pad are upper limits (TS < 4). The middle and bottom pad are the spectral indices and normalization respectively, derived from a power-law spectrum in energy fitted to the data comprehended in that period. In the middle pad, the average spectral index value ($\overline{\Gamma} \simeq 3.6$) was added as an extra dashed line to the grid. The grey areas represent VERITAS observing seasons.

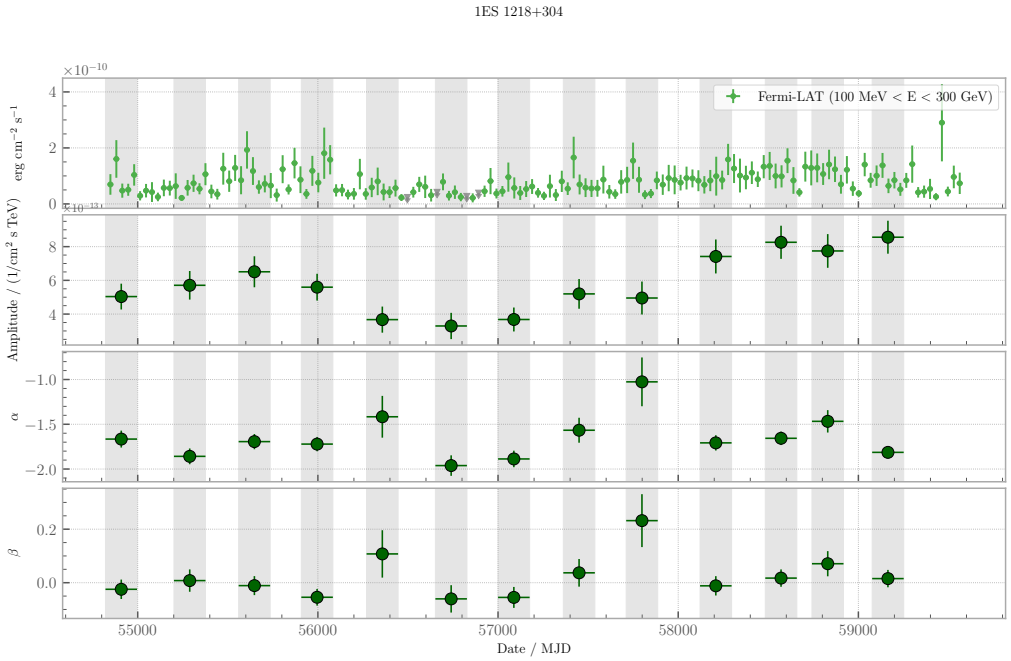

Figure 7.5: 1ES 1218+304 *Fermi*-LAT lightcurve (top) and spectral parameters (second, third and fourth rows) per observing season. On the top pad is presented *Fermi*-LAT the observed energy flux lightcurve, for energies greater between 100 MeV and 300 GeV, in bins of 1 month. The grey arrows on the top pad are upper limits (TS < 4). The second, third and fourth rows are the normalization, spectral indices and curvature factor respectively, derived from a log-parabola spectrum in energy fitted to the data comprehended in that period. The grey areas represent VERITAS observing seasons.

VERITAS observations, we calculate a significance for 1ES 1218+304 of $\approx 83\sigma$ in the 100 MeV to 300 GeV energy range.

4FGL-DR4 reports a log-parabolic spectral model for the photon distribution $\phi \propto (E/E_0)^{-\alpha-\beta log(E/E_0)}$, where the reference energy E_0 is set to 2509.47 MeV, and the spectral index and curvature parameter are $\alpha = 1.6762 \pm 0.0295$ and $\beta = 0.0256 \pm 0.0097$, respectively. The monthly light curve of 1ES 1218+304 is shown in Figure 7.5, calculated between 100 MeV and 300 GeV. We also present the best-fit parameters from the log-parabola spectrum of the integrated data within VERITAS' visibility period of the object (see also Figure 7.4). The average spectral index calculated is $\overline{\alpha} \simeq -1.6$, with a standard deviation of ~ 0.2, while the average curvature parameter is $\overline{\beta} \simeq 0.02$ with a standard deviation of ≈ 0.07.

7.6.3 *Swift*-XRT

We show the light curve of 1ES 1218+304 in the 0.3 to 10 keV energy range in Figure 7.6. The light curve is daily binned and the significance of all the calculated fluxes exceeds the upper limit threshold of $TS > 4$, given the high statistics available in this energy range. The first observation used in this was taken on 8 March 2006, and the last one on 5 June 2020. We fit a log-parabola model to the data. The average spectral index observed is $\overline{\alpha} \simeq 2.0 \pm 0.2$, and the average curvature parameter observed

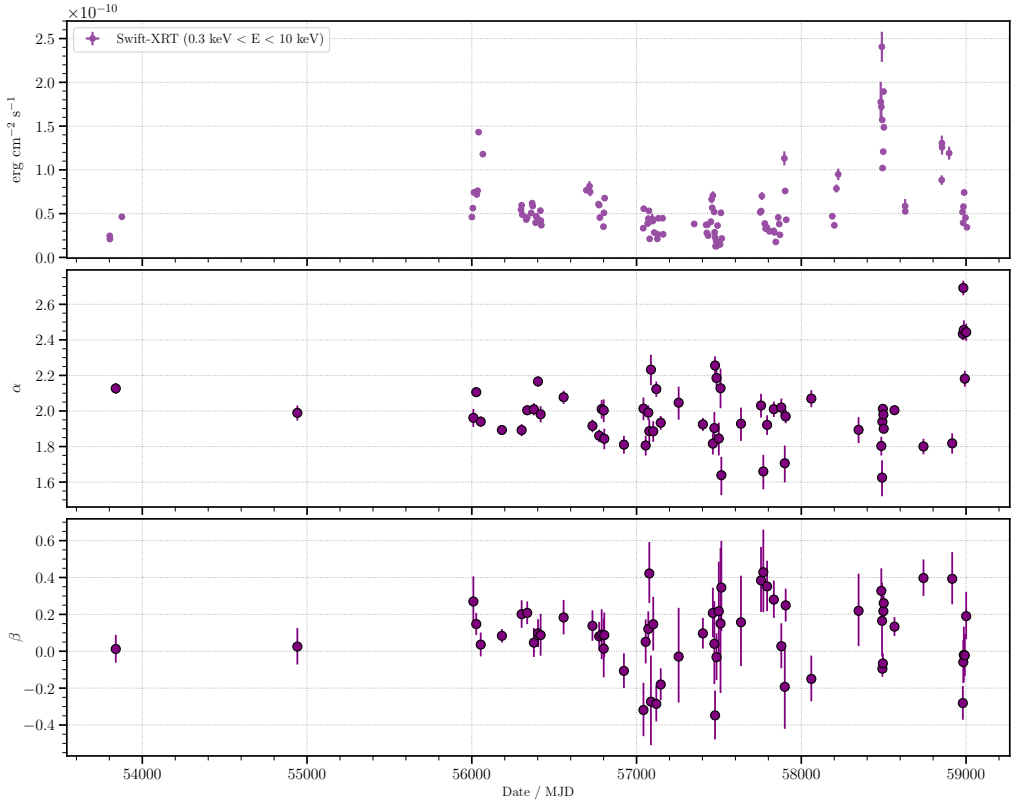

Figure 7.6: 1ES 1218+304 XRT lightcurve (top) and spectral parameters (middle and bottom) per observing season. On the top pad is presented XRT energy flux lightcurve, for energies between 0.3 KeV and 10 KeV, with one observation per bin. The middle and bottom pad are the spectral indices and curvature parameters respectively, derived from a log-parabola spectrum in energy fitted to the data comprehended in that period.

is $\overline{\beta} \simeq 0.09 \pm 0.18$. From Figure 7.6 and Figure 7.4, we observe that the highest energy flux detected in X-rays by XRT coincides temporally with the highest monthly energy flux between in the VERITAS data, around MJD 58500. The same cannot be said for the monthly high flux observed around MJD 58800 in the VHE energy range, where the X-ray counterpart does not present an increased energy flux state around the same period.

7.6.4 *Swift*-UVOT

In Figure 7.7, we show the light curve for each filter. UVOT's observations are taken simultaneously to XRT's observations. It is possible to notice increased UV/optical activity around MJD 58500 and 58900, the first time also corresponding to an increase in X-ray and VHE activity, while the second does not appear to have an X-ray or gamma-ray counterpart.

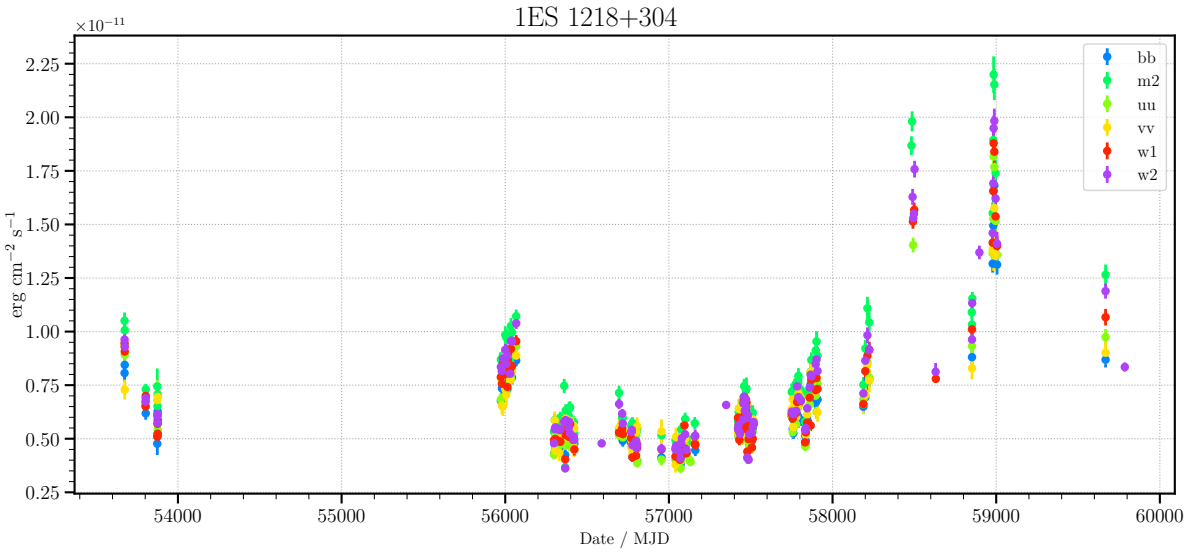

Figure 7.7: 1ES 1218+304 optical/UV lightcurve. Energy flux of photons with wavelengths corresponding to UVOT's *v*, *b*, *u*, *w1*, *m2*, *w2* filters. The wavelengths are listed in Table 4.1.

7.7 1ES 0229+200 data

7.7.1 VERITAS

The EHBL 1ES 0229+200 was first catalogued in 1991 in the *Einstein Slew* survey [148], and was further identified as an BL Lac object in 1993 [154] and as an HBL in 1995 [155]. Is at a redshift $z = 0.1396$ [156], located at RA $2^{h}32^{m}53.2^{s}$, Dec 20°16′21" [39]. It has a reported spectral index of 2.50 ± 0.19 (stat) ± 0.10 (syst) in the discovery publication [39] and 2.44 ± 0.11 reported by VERITAS [43]. Despite its relatively hard spectrum, it is also a faint source, which can be seen from both VERITAS' cumulative significance in Figure 7.8 and its light curve in Figure 7.9. In 12 years of observations, with a sharp increase in significance in the initial period of observations, it remains in a low state, as indicated by the number of upper limits ($TS < 4$) in the lightcurve. In Table 7.4 we present the VERITAS observation statistics. The cumulative significance obtained within the described period is around 10.8 σ. The average spectral index per season is $\overline{\Gamma} \simeq 3.2$ with a standard deviation of ~ 0.7.

[154]: Schachter et al. (1993), "Ten new BL Lacertae objects discovered by an efficient X-ray/radio/optical technique"

[155]: Giommi et al. (1995), "Radio to X-ray energy distribution of BL Lacertae objects."

[156]: Woo et al. (2005), "Black hole masses and host galaxy evolution of radio-loud active galactic nuclei"

[39]: Aharonian, F. et al. (2007), "New constraints on the mid-IR EBL from the HESS discovery of VHE gamma rays from 1ES0229+200"

Table 7.4: Summary table of 1ES 0229+200 observations taken by VERITAS in which data are used in this thesis. The accumulated significance is calculated using Equation 6.11

Observation period	October 2009 to January 2021
Number of runs	451
Total exposure	~ 161 hours
Acumulated significance (σ)	~ 10.8

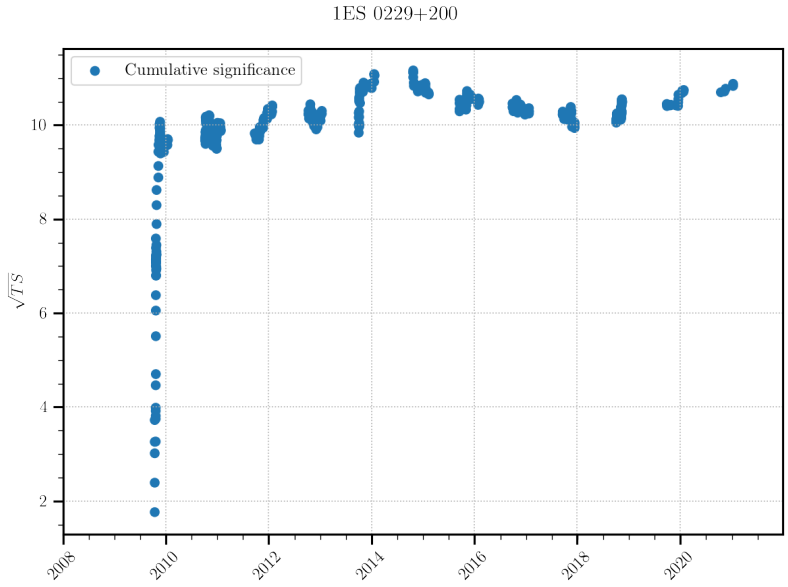

Figure 7.8: VERITAS cumulative significance on 1ES 0229+200 from 2009 to 2021

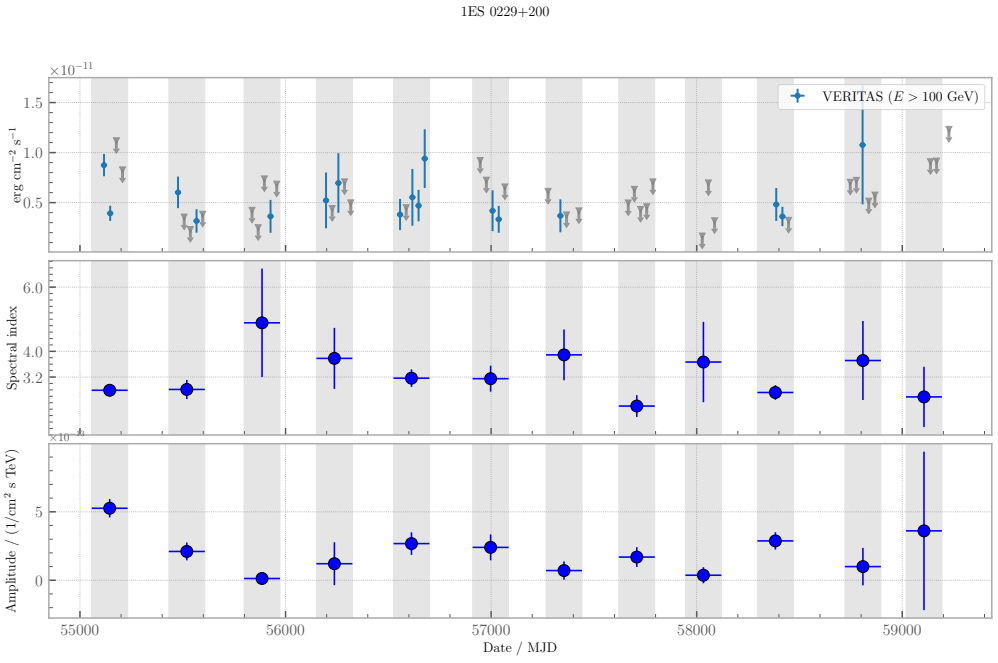

Figure 7.9: 1ES 0229+200 VERITAS lightcurve (top) and spectral parameters (middle and bottom) per observing season. On the top pad is presented VERITAS energy flux lightcurve, for energies greater than 100 GeV, in bins of 1 month. The grey arrows on the top pad are upper limits (TS < 4). The middle and bottom pad are the spectral indices and normalization respectively, derived from a power-law spectrum in energy fitted to the data comprehended in that period. In the middle pad, the average spectral index value ($\overline{\Gamma} \simeq 3.2$) was added as an extra dashed line to the grid. The grey areas represent VERITAS observing seasons.

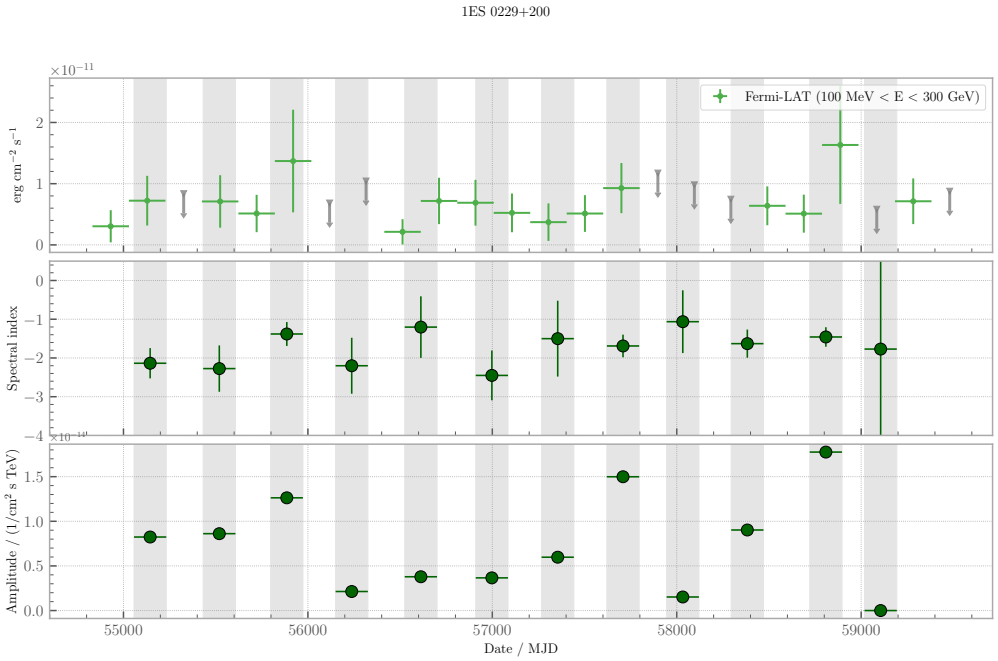

Figure 7.10: 1ES 0229+200 *Fermi*-LAT lightcurve (top) and spectral parameters (middle and bottom) per observing season. On the top pad is presented *Fermi*-LAT the observed energy flux lightcurve, for energies greater between 100 MeV and 300 GeV, in bins of 6 months. The grey arrows on the top pad are upper limits (TS < 4). The second and third the amplitude and spectral indices and curvature factor respectively, derived from a power-law spectrum in energy fitted to the data comprehended in that period. The grey areas represent VERITAS observing seasons.

7.7.2 *Fermi*-LAT

Listed as 4FGL J0232.8+2018 in the 4FGL-DR4 catalogue, *Fermi*-LAT has accumulated $\approx 15.2\sigma$ of detection significance on 1ES 0229+200 with its 12 years of data. The catalogue reports a power law spectrum type $\phi \propto (E/E_0)^{-\Gamma}$, with $\Gamma = 1.7518 \pm 0.0798$, and an energy flux of $(3.8699 \pm 0.4561) \times 10^{-12}$ erg/cm^2/s between 1 and 100 GeV. In this work, our estimated detection significance is $TS = 172.43$ ($\approx 13\sigma$), which is considerably less significant than 1ES 1218+304. This behaviour agrees with our estimated energy flux of $(5.2 \pm 0.9) \times 10^{-12}$ erg/cm^2/s, which is one order of magnitude lower than the energy flux of 1ES 1218+304.

In Figure 7.10 we show a 6-month binned light curve 1ES 0229+200. The grey arrows in Figure 7.10 show upper limits, with TS < 4. An increased integration time of six months is needed to counterbalance the decreased statistics due to the source strength in this band.

7.7.3 *Swift*-XRT

In Figure 7.11, we present 1ES 0229+200's energy flux and spectral parameter lightcurves. The observations dates span from the first one on the 8th of August 2008 up to the last one on the 14th of August 2021.

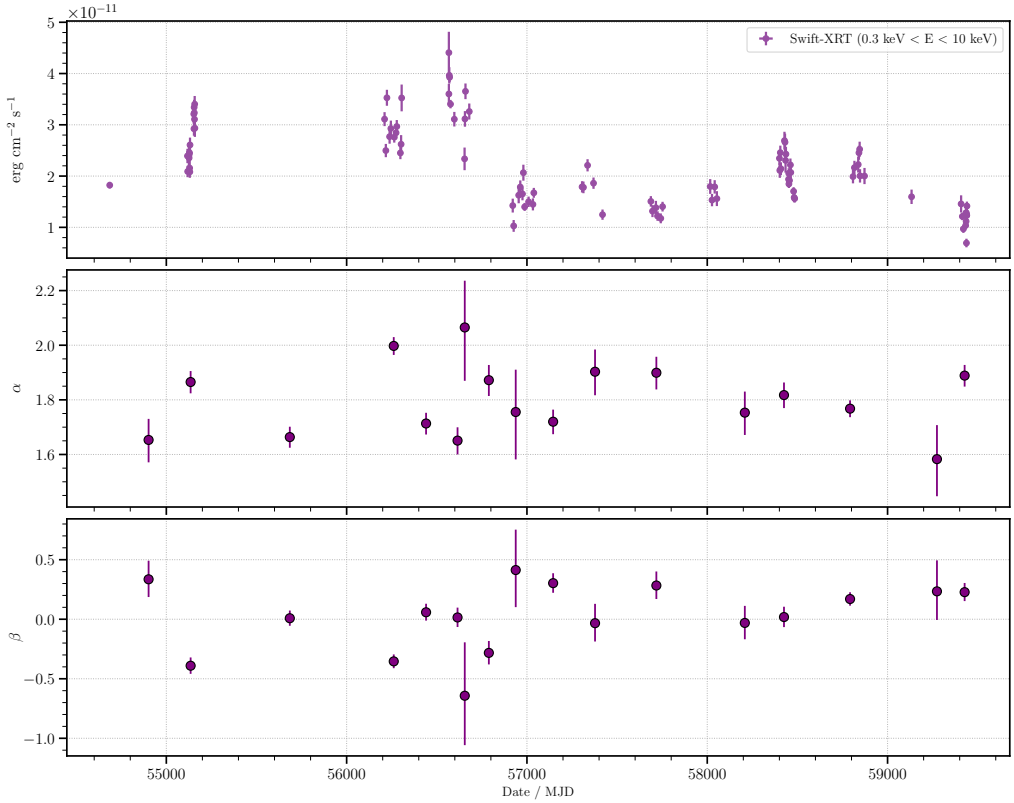

Figure 7.11: 1ES 0229+200 XRT lightcurve (top) and spectral parameters (middle and bottom) per observing season. On the top pad is presented XRT energy flux lightcurve, for energies between 0.3 KeV and 10 KeV, with one observation per bin. The middle and bottom pad are the spectral indices and curvature parameters respectively, derived from a log-parabola spectrum in energy fitted to the data comprehended in that period.

A log-parabola model is fitted to the data, and the average spectral index and curvature parameter observed over time are $\overline{\alpha} \simeq 1.8 \pm 0.1$ and $\overline{\beta} \simeq 0.02 \pm 0.28$, respectively.

7.7.4 *Swift*-UVOT

In Figure 7.12 we present the UV/optical light curves, obtained with *Swift*-UVOT. Taking a closer look at Figure 7.12, one can notice that the V and B bands maintain their energy flux levels around 5×10^{-12} erg cm^{-2} s^{-1} and 3×10^{-12} erg cm^{-2} s^{-1}, respectively, throughout most of the observation period, except observations after MJD 59400. For the shorter wavelengths $W1$ and $W2$, variations are larger, for some periods, around 1 one order of magnitude in erg cm^{-2} s^{-1}. This is evidence of contamination by thermal emission from the host galaxy, mostly in the optical range.

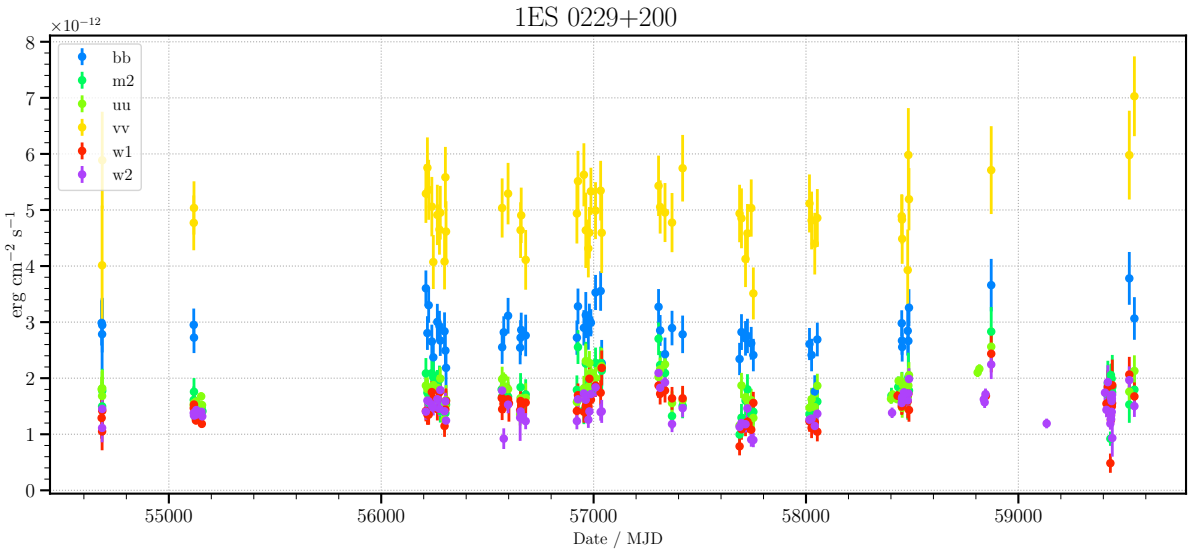

Figure 7.12: 1ES 0229+200 optical/UV lightcurve. Energy flux of photons with wavelengths corresponding to UVOT's *v*, *b*, *u*, *w*1, *m*2, *w*2 filters. The wavelengths are listed in Table 4.1

7.8 Summary

This chapter was used to introduce the particular elements of the high-level analysis of each instrument and the lightcurves as products. The MWL SEDs will be discussed in further chapters, where we will discuss in more detail the spectral analysis of the presented data and the subsequent emission modelling.

Temporal analysis and SED extraction

8

As seen in the light curves presented in Chapter 7, the energy flux of a source can vary with time. The change in the observed energy flux of a source can be due to a variation in the spectral index of the spectral energy distribution and/or to a variation in the general normalisation of the spectrum (e.g., bottom pad in Figure 7.4 or middle pad in Figure 7.6). The SSC model described in Subsection 3.4.1 has one main assumption: all non-thermal radiation is being produced by the interactions of the same distribution of particles (electrons and positrons) and are also emitted from the same region. This begs the question: Is emission across different frequencies in the SED temporally correlated? However, our biggest limitation is that, due to the lack of statistics (especially in the HE and VHE bands), we require long integration periods to obtain significant source detections. To understand the interplay of long integration times, the temporal correlation between energy bands, and to try to determine the flux states of the sources, we will use a Bayesian block algorithm [157].

8.1 Bayesian blocks

The Bayesian Blocks method consists of analysing time-series data and detecting statistically significant variations. The method consists of dividing the data into blocks of constant rates, resulting in a piecewise constant representation of the time-series data. The use of Bayesian blocks to find significant change points in time series is particularly useful to study data sparsely distributed in time, addressing issues such as data gaps and exposure variations [158].

8.1.1 The algorithm

We will introduce the algorithm used to calculate the edges of the blocks, based on [158]. Let us introduce the quantities N_{blocks}, the total number of blocks, and N_{cp}, the number of change points detected. N_{blocks} cannot be larger than the number N of data cells - the data points sorted in time -, and is greater than zero, therefore $0 \leq N_{blocks} \leq N$. The number N_{cp} must be $N_{cp} = N_{blocks} + 1$, where the beginning of the second block and the end of the last block are considered change points. The number of blocks and, therefore, the number of change points can only be evaluated relative to a certain *prior probability*. We parameterize the prior probability for a given number of N_{blocks} as

[158]: Scargle et al. (2013), "Studies in astronomical time series analysis. VI. Bayesian block representations"

$$P(N_{blocks}) = \frac{1-\gamma}{1-\gamma^{N+1}}\gamma^{N_{blocks}}, \tag{8.1}$$

with γ as the only parameter. For convenience, we take the natural log of γ, and name it the `ncp_prior` parameter, i.e., `ncp_prior`$= \ln\gamma$.

The likelihood of measuring a random block k containing N_k data cells, which in our case are energy fluxes points, which will be treated as having Gaussian-distributed errors, is given by

$$L^{(k)} = \prod_n L_n = \frac{(2\pi)^{-N_k/2}}{\prod_m \sigma_m} e^{-\frac{1}{2}\sum_n\left(\frac{x_n-\lambda}{\sigma_n}\right)^2}, \tag{8.2}$$

where x_n and σ_n are data points and errors and λ is the constant rate of the Bayesian block. Maximum likelihood is obtained from Equation 8.2 when $\lambda = \lambda_{max} = -b_k/2a_k$, with

$$a_k = \frac{1}{2}\sum_n \frac{1}{\sigma_n^2}, \tag{8.3}$$

$$b_k = -\sum_n \frac{x_n}{\sigma_n^2}. \tag{8.4}$$

Combining Equations 8.2, 8.3 and 8.4, one gets to the so-called fitness function ([158], Eq. 41):

$$\log L_{max}^{(k)} = \frac{b_k^2}{4a_k}. \tag{8.5}$$

The algorithm recursively calculates the maximum likelihood using Equation 8.5 and adds one data cell each time, up to the last. At each iteration, the likelihood value is compared with `ncp_prior`. The algorithm will output, for each iteration, the data cell in which the difference between the calculated likelihood and `ncp_prior` was maximum. This indicates a change point that is statistically significant compared to the prior probability given a certain threshold. This threshold is the *false positive rate*, or the probability of detecting a change point when there is no signal present. In our case, we set the allowed probability p_0 of a false positive at $p_0 \approx 0.0026$ (or 3σ), less than 3 times out of 10000. We can then define the edges of our blocks over time.

8.1.2 Prior calculation

In [158], a recipe is provided to fix the prior probability of N_{blocks}, or, in other words, to find the value of γ.

In order to do it, we follow these steps:

1. We generate a noise sample by simulating 150 light curves (for each wavelength) for 20 different values of `ncp_prior`, ranging from 0.2 to 4 .
2. Afterwards, we sample light curves from a normal distribution, centred around the calculated average energy flux, and with standard deviation derived from the errors of the data points in the original light curve.
3. Using each of the `ncp_prior` values, we apply the Bayesian blocks algorithm and counted the number of times a block was detected using our sample of 150 fake light curves.
4. Finally, γ is obtained for each value of `ncp_prior` by calculating the ratio of block detections per total number of fake samples, and stored to be used later in the analysis of the original data as calibration files.

8.2 Bayesian blocks results

We will now present the results of the application of the Bayesian block algorithm to the MWL lightcurves of 1ES 1218+304 and 1ES 0229+200 presented in Section 7.6 and Section 7.7. Upper limits are not taken into account during the calculation of the Bayesian blocks.

We show in Figure 8.1 and Figure 8.2 the light curves and the Bayesian blocks. The solid lines represent the average energy flux in a block, and the shaded area is one standard deviation from the average. The edges of the blocks are listed in Tables A.1 and A.2.

The algorithm for the Bayesian blocks detection is implemented in the python package `astropy`* [159]. Furthermore, a discussion on the lightcurve bin size selection and false positive rate threshold is presented in chapter A of the appendix.

[159]: Collaboration et al. (2022), "The Astropy Project"

The general trend observed for both EHBLs is that, defining variability as observing or not changing points in the Bayesian blocks, we can see the most variability in the X-ray band, relative to the VHE and HE gamma rays.

The Bayesian blocks algorithm was not applied to the optical/ultraviolet light curves built from UVOT data because of the presence of contamination from thermal emission from the host galaxy (e.g., [38]). More details of the emission of the host galaxy are provided in Chapter 9.

[38]: Costamante et al. (2018), "The NuSTAR view on hard-TeV BL Lacs"

* More information can be found on `astropy`'s documentation at `https://docs.astropy.org/en/stable/api/astropy.stats.bayesian_blocks.html`

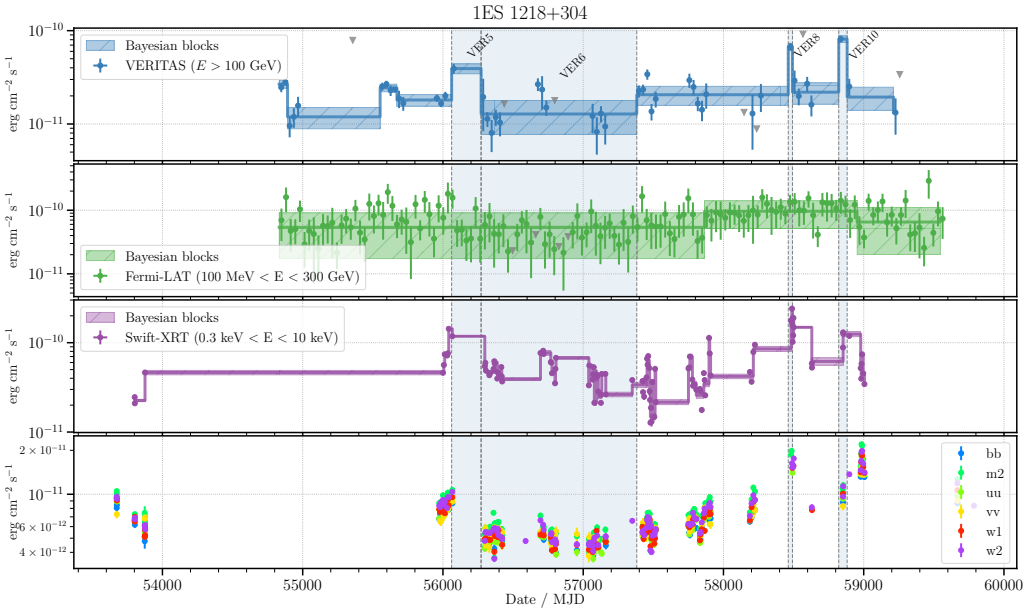

Figure 8.1: 1ES 1218+304 MWL light curve and Bayesian blocks, for monthly binned VERITAS data (first row), monthly binned *Fermi*-LAT data (second row), and observation-binned for XRT (third row) and UVOT (fourth row) data. The grey arrows are the calculated upper limits for bins with TS < 4. The solid lines and shaded area represent the block's average energy flux and 1σ standard deviation region. Four time intervals are highlighted: *VER5*, *VER6*, *VER8* and *VER10*. The time intervals are listed in Table 8.1.

8.2.1 1ES 1218+304

VERITAS

The variability in the VHE gamma-ray emission becomes evident from the results of the Bayesian blocks. In Figure 8.1, we highlight the blocks that will be used in later steps in the analysis: an intermediate state, identified as *VER5*, followed by the lowest state of the source, marked as *VER6*. In addition, we identify the two sudden changes, the flaring states - the shortest and brightest states - are also detected and marked as *VER8* and *VER10* respectively.

Fermi-LAT

Two change points are detected in the 1ES 1218+304 light curve. The increased activity in the HE gamma-ray seen after the first change point at approximately MJD 57900, encompasses the two flaring states observed in VHE energies.

Swift-XRT

Most of the variability is observed in the X-ray band, with periods of increased X-ray activity coinciding with periods of increased VHE activ-

ity.

8.2.2 1ES 0229+200

VERITAS

A single point change was detected: the very first observations taken with VERITAS point toward an excited VHE state during that period, marked as *VER1* in the figure. The apparent non-variability could be due to the lack of statistics since the presence of many upper limits prohibits a good representation of the variability in this band.

Fermi-LAT

No change points are detected in LAT's lightcurve, a simillar behaviour as observed in the VHE energy band. Again, this can be attributed due to the lack of statistics.

8.2.3 *Swift*-XRT

Regarding the variability of 1ES 0229+200 in the X-ray energy band, we identified the highest energy flux state as *XRT5*, and we are interested in analysing the evolution before and during this high state, for which we have also identified the block *XRT4*. The lowest X-ray state of 1ES 0229+200 is identified as the block *XRT12*. These blocks are highlighted in Figure 8.2.

8.2.4 VHE's spectral variability per block

An indicator of the extremeness of an HBL object is a hard intrinsic[1] VHE spectrum, with a spectral index $\Gamma_{VHE} < 2$. An spectral index of $\Gamma_{VHE} \sim 1.5$ implies that the distributions of the charged particles that produced the emission would have spectral indices $\alpha < 2$, where $dN/d\gamma \propto \gamma^{-\alpha}$, with N and γ being the number and Lorentz factor of those particles. In such cases, that would mean that the most energetic particles carry most of the energy of the system, which is not expected [30].

In Figures 8.3 and 8.4, we plot the model parameters from a power-law spectrum, fitted to each VHE block. We plot the observed and EBL-deabsorbed values derived from each block, in addition to the observed results from [45] and [43]. The de-absorbed values (intrinsic) are obtained by fitting the data using a power-law spectrum multiplied by an energy dependent absorption factor (as discussed in Section 3.5), using the EBL model from [73], and extracting the best-fit spectral index.

1: Intrinsic here refers to the spectral index of the spectrum emitted at the source, before EBL absorption effects

[30]: Biteau et al. (2020), "Progress in unveiling extreme particle acceleration in persistent astrophysical jets"

[45]: Archambault et al. (2014), "Test of models of the cosmic infrared background with the multiwavelength of the blazar 1ES 1218+30.4 in 2009"

[43]: Aliu et al. (2014), "A three-year multi-wavelength study of the very-high-energy gamma-ray blazar 1ES 0229+200"

[73]: Domínguez et al. (2011), "Extragalactic background light inferred from AEGIS galaxy-SED-type fractions"

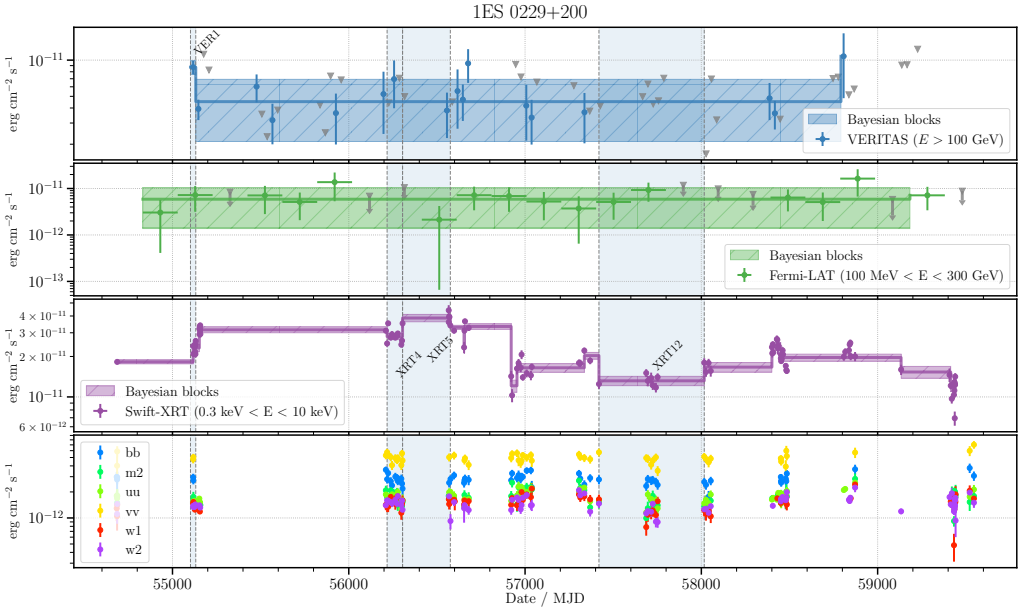

Figure 8.2: 1ES 0229+200 MWL light curve and Bayesian blocks, for monthly binned VERITAS data (first row), monthly binned *Fermi*-LAT data (second row), and observation-binned for XRT (third row) and UVOT (fourth row) data. The grey arrows are the calculated upper limits for bins with TS < 4. The solid lines and shaded area represent the block's average energy flux and 1σ standard deviation region. Four time intervals are highlighted: *VER1*, *XRT4*, *XRT5* and *XRT12*. The time intervals are listed in Table 8.1.

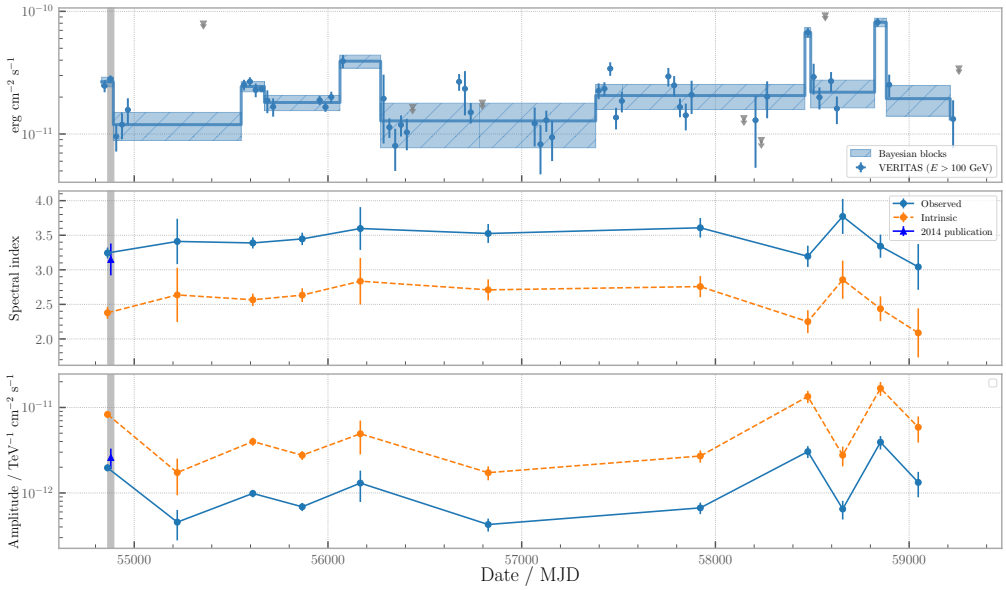

Figure 8.3: 1ES 1218+304 intrinsic and observed spectral index and amplitude per block. VERITAS lightcurve is presented in monthly bins (top). The grey arrows are the calculated upper limits for bins with TS < 4. The solid lines and shaded area represent the block's average energy flux and 1σ standard deviation region. The middle and bottom pad are the spectral indices and normalization respectively, derived from a power-law spectrum in energy fitted to the data comprehended in that period. Solid blue lines in the middle and bottom pad are the observed spectral indices and normalization, while the dashed orange lines are the EBL de-absorbed values (the EBL model used is given in [73]). For comparison, we also plot the results obtained in the 2014 publication ([45]), where the shaded grey area is the time interval used in that work and the dark blue triangles are the observed values from a power-law fit to the data in that period.

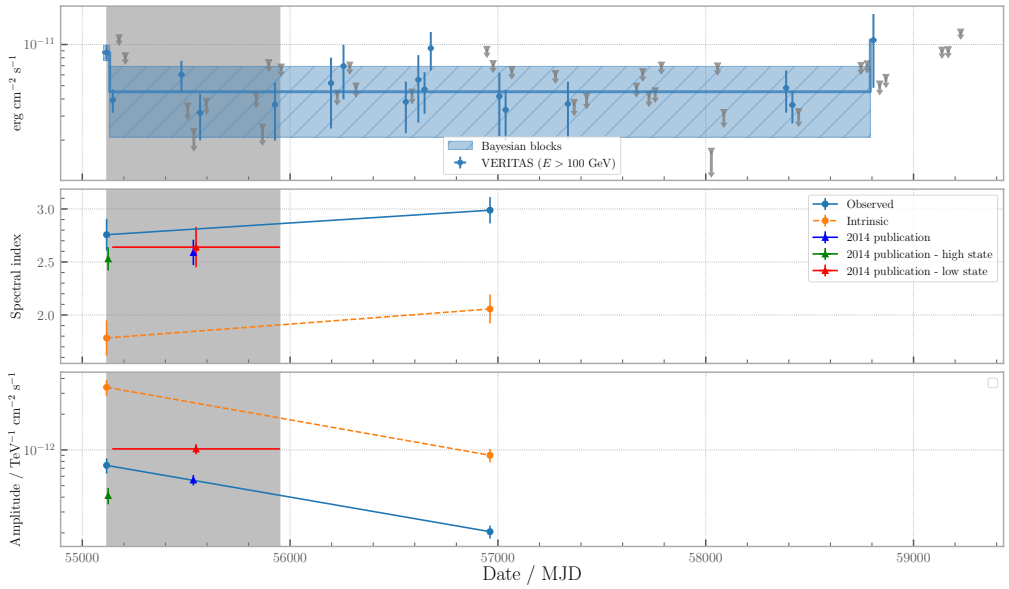

Figure 8.4: 1ES 0229+200 intrinsic and observed spectral index and amplitude per block. VERITAS lightcurve is presented in monthly bins (top). The grey arrows are the calculated upper limits for bins with TS < 4. The solid lines and shaded area represent the block's average energy flux and 1σ standard deviation region. The middle and bottom pad are the spectral indices and normalization respectively, derived from a power-law spectrum in energy fitted to the data comprehended in that period. Solid blue lines in the middle and bottom pad are the observed spectral indices and normalization, while the dashed orange lines are the EBL de-absorbed values (the EBL model used is given in [73]). For comparison, we also plot the results obtained in the 2014 publication ([43]), where the shaded grey area is the data period used in that work. The dark blue triangle with no x error bar is the quoted value from a power-law fit to the whole data from that period. The green (high state) and red triangles (low state) are the values from a power-law fit to the data comprehended between their x error range.

1ES 1218+304

Looking first at Figure 8.3 spectral indices per block, in fact, in fact none of the periods the intrinsic spectral index crosses the threshold of 2. Interestingly, the hardest spectra are observed during the two flaring states of blocks *VER8* and *VER10*, with intrinsic spectral indices of $\approx 2.2 \pm 0.2$ and $\approx 2.4 \pm 0.2$, respectively. Notice that the last data point is ignored since for that block the number of observations was too small to have a statistically sound analysis.

1ES 0229+200

For 1ES 0229+200, the intrinsic spectral indices are $\approx 1.7 \pm 0.1$ and $\approx 2.0 \pm 0.1$ for the first and second blocks, respectively. The value observed for the first block is less than 2 within 1σ confidence, while the second is consistent with 2 within the 1σ confidence band. 1ES 0229+200 has historically presented hard VHE spectra (e.g. [39, 43, 147]); therefore, these results come as no surprise.

[39]: Aharonian, F. et al. (2007), "New constraints on the mid-IR EBL from the HESS discovery of VHE gamma rays from 1ES0229+200"
[43]: Aliu et al. (2014), "A three-year multi-wavelength study of the very-high-energy gamma-ray blazar 1ES 0229+200"
[147]: Acciari et al. (2023), "A lower bound on intergalactic magnetic fields from time variability of 1ES 0229+200 from MAGIC and Fermi/LAT observations"

8.2.5 Time period selection for modelling

In this work, to analyse the data available in a time-sensitive manner, we want to define different data periods to be analysed, building the broadband SED from such period, and modelling the emission, minimising the presence of spectral and flux variability. Ideally, after our Bayesian block analysis, every overlap between blocks across the energy bands (as is, e.g., with 1218's *VER8*) could be used. Or in other words, we would want to use the same time interval in all energy bands, therefore, making sure that there is no variability detected by the Bayesian blocks algorithm with 3σ confidence. In this way, when fitting the data from these periods with an SSC model, we would obtain the time evolution of the model parameter space as a function of time. We are, however, limited by two factors:

1. The lack of statistics in short periods of VHE and HE bands force us to use large integration windows to obtain a significant source detection in all bands in low states;
2. The SED modeling is computationally intense, so increasing the amount of data that needs to be processed, significantly increases the real time required to finish the analysis;

To compensate for these factors, we selected periods of data that represent different source states, such as low, intermediate, and high X-ray or gamma-ray energy fluxes and combinations thereof. When selecting these periods, we also took into account integration windows size as large as to provide enough statistics for a proper analysis of the data, and where the observed spectral variability is not large. As criteria for spectral variability,

As highlighted in Figure 8.1 and Figure 8.2, the selection of the time intervals is based on the blocks:

* *VER5, VER6, VER8* and *VER10* for 1ES 1218+304, in which the X-ray data comprised by *VER6* edges is stacked.
    - The short integration times defined by *VER8* and *VER10* in 1218's case were inadequate for having enough statistics with *Fermi*-LAT's data. Therefore, we chose the integration times for 1ES 1218+304 *Fermi*'s data to match the edges of the second Bayesian block in the HE band.
* *VER1, XRT4, XRT5* and *XRT12*
    - For 1ES 0229+200, that was the case for *XRT4*, and *XRT5* periods, where both VERITAS and *Fermi*-LAT data were low in statistics.
    - The integration time of both *Fermi*-LAT and VERITAS data to match the beginning of the fourth, and the end of the fifth

Table 8.1: Table of integration periods

1ES 1218+304

Integration periods in MJD			
Swift-XRT	*Fermi*-LAT	VERITAS	Notes
56062.00 to 56273.00			*VER5*
56272.00 to 57383.00			*VER6*
58462.00 to 58492.00	57864.00 to 58953.00	58462.00 to 58492.00	*VER8*; Increased *Fermi* integration time
58822.00 to 58882.00		58822.00 to 58882.00	*VER10*; Increased *Fermi* integration time

1ES 0229+200

Integration periods in MJD			
Swift-XRT	*Fermi*-LAT	VERITAS	Notes
55102.00 to 55132.00	54831.00 to 55133.00	55102.00 to 55132.00	*VER1*; Increased *Fermi* integration time
56217.41 to 56305.11	55132.00 to 57420.00		*XRT4*; Increased *Fermi* and VERITAS integration time
56305.11 to 56576.03			*XRT5*; Increased *Fermi* and VERITAS integration time
57419.00 to 58017.00			*XRT12*

VERITAS observation seasons, to be used together with *XRT4*, and *XRT5* X-ray data.

The final times used for the emission modelling study are summarised in Table 8.1:

8.3 Spectral analysis of the selected periods

In this section, we will look at some properties that can be extracted directly from the data. We combine spectral measurements from the available gamma-ray and X-ray data. In that way, we can start characterising the synchrotron and IC peaks in the broadband SED before diving deeper into complex radiative models.

8.3.1 HE and VHE joint analysis

We performed a joint analysis of the available gamma-ray data in the HE/VHE range. For that, we fit a log-parabola function and EBL absorption to the *Fermi*-LAT and VERITAS datasets using `gammapy`. The log-parabola function is better suited for this task given its curved shape, since we are most interested in describing the shape of the IC peak. The EBL model used is given in [73]. The likelihood of the model given the data is calculated as a W-stat likelihood (Equation 6.24) distribution for

[73]: Domínguez et al. (2011), "Extragalactic background light inferred from AEGIS galaxy-SED-type fractions"

Table 8.2: List of SED properties. [1] the block name, referring to the names in Table 8.1; [2] frequency of the synchrotron peak in Hz; [3] synchrotron peak νF_ν, in erg cm^{-2} s^{-1}; [4] frequency of the IC peak in TeV; [5] IC peak νF_ν, in erg cm^{-2} s^{-1}; [6] EBL de-absorbed VHE spectral index

1ES 1218+304

Block [1]	$10^{16} \times \nu^{\rm sync}_{\rm peak}$ [2]	$10^{11} \times \nu F^{\rm sync}_{\nu,\rm peak}$ [3]	$10^{26} \times \nu^{\rm IC}_{\rm peak}$ [4]	$10^{11} \times \nu F^{\rm IC}_{\nu,\rm peak}$ [5]	Γ_{VHE} [6]
VER5	220	3.6	4.1	2.3	2.6 ± 0.3
VER6	60	1.7	0.1	0.8	2.4 ± 0.2
VER8	80	5.1	> 24	17	1.9 ± 0.3
VER10	70	4.0	> 24	36	2.1 ± 0.2

1ES 0229+200

Block [1]	$10^{16} \times \nu^{\rm sync}_{\rm peak}$ [2]	$10^{11} \times \nu F^{\rm sync}_{\nu,\rm peak}$ [3]	$10^{26} \times \nu^{\rm IC}_{\rm peak}$ [4]	$10^{11} \times \nu F^{\rm IC}_{\nu,\rm peak}$ [5]	Γ_{VHE} [6]
VER1	> 240	6.1	15.2	0.74	1.8 ± 0.2
XRT4	> 240	1.8	0.7	0.18	2.2 ± 0.2
XRT5	210	1.4	0.7	0.18	2.2 ± 0.2
XRT12	50	0.4	27.0	0.10	1.2 ± 0.4

VERITAS data, since we rely on reflected regions to estimate the background (see Subsection 7.1.1). Cash statistics are used to calculate the likelihood (Equation 6.16) of the *Fermi*-LAT data, given that we use the background models provided by the *Fermi* collaboration (see Subsection 7.2.2). The log-parabola distribution is defined as follows:

$$\frac{dN}{dE} = N_0 \left(\frac{E}{E_0}\right)^{-\alpha-\beta\ln\left(\frac{E}{E_0}\right)}, \tag{8.6}$$

where N_0 is the normalisation parameter, α the spectral index, β is the attenuation factor (responsible for the function's curvature), and E_0 is the reference energy fixed to 1 TeV.

The results of the joint fits are presented in Figure 8.5 and Figure 8.6 for 1ES 1218+304 and 1ES 0229+200 data, respectively. The intrinsic model obtained from the joint fits can be used to estimate the energy in which the maximum of the SED occurs in the gamma-ray range and the value of the maximum. These are useful quantities when it comes to the classification of BL Lac objects. In Table 8.2 these values are presented, along with the intrinsic spectral index obtained from the analysis of the VERITAS data alone.

8.3.2 Synchrotron peak frequency of EHBLs

The standard BL Lac classification has HBLs as objects that show synchrotron peak frequencies $\nu^{\rm sync}_{\rm peak} > 10^{15}$ Hz. EHBLs, on the other hand,

typically present $\nu^{\rm sync}_{\rm peak} \sim 10^{17}$ Hz, as is the case for 1ES 1218+304 and 1ES 0229+200 (e.g., [38]). EHBLs are also expected to have a hard intrinsic TeV spectral index of $\Gamma_{VHE} < 2$ (e.g. [30]). In [160] (FF19 from now on), combine these empirical observations to study the population of EHBL candidates. In FF19, the authors argue that EHBLs may not be a homogeneous population. They collect published data on several EHBL candidates: the frequency of their synchrotron peaks ($\nu^{\rm sync}_{\rm peak}$), their synchrotron peak luminosities ($\nu L\nu^{\rm sync}_{\rm peak}$), and their intrinsic VHE spectral indices. The authors then define a VHE gamma-ray slope S as

[38]: Costamante et al. (2018), "The NuSTAR view on hard-TeV BL Lacs"
[160]: Foffano et al. (2019), "A new hard X-ray-selected sample of extreme high-energy peaked BL Lac objects and their TeV gamma-ray properties"

$$S = 2 - \Gamma_{VHE}, \tag{8.7}$$

where Γ_{VHE} is the intrinsic TeV spectral index. Therefore, $S = 0$ acts as a threshold for hard and non-hard spectral indices.

Then, the authors proceed to find evidence (see FF19's Figures 4 and 5) that EHBLs can be further subdivided into two subcategories: 'HBL-like' EHBLs, with IC peak energy between 0.1 TeV and 1 TeV, and 'hard-TeV' EHBLs where the IC peaks at energies above 10 TeV.

In this section, we reproduce the FF19 investigation using our gamma-ray and X-ray data:

* We find 1ES 1218+304 and 1ES 0229+200 synchrotron and IC energy peaks, and their respective luminosities, using data from the proposed intervals listed in Table 8.1
* We fit log-parabola spectrum to the X-ray and gamma-ray data from these periods
* We estimate the peaks energies and luminosities from the fits results
    - For the gamma-ray data, the fits were performed and discussed in Section 8.3
* We performed the fits using the available *Swift*-XRT data

The X-ray results are shown in Figure 8.7 for 1ES 1218+304, and in Figure 8.8 for 1ES 0229+200. All results are listed in Table 8.2. We reproduce FF19 Figures 4 and 5, plotting the distribution of synchrotron/IC peak frequencies as a function of the TeV slopes. Our findings are shown in Figure 8.9 and Figure 8.10. We notice from our investigation that 1ES 1218+304 and 1ES 0229+200 are not strictly confined to a single possible population, but instead show a transit between states and present a dynamic VHE spectrum hardness. The results of our investigation only reinforce our initial motivation, which is to try to understand how the broadband EHBL emission evolves with time.

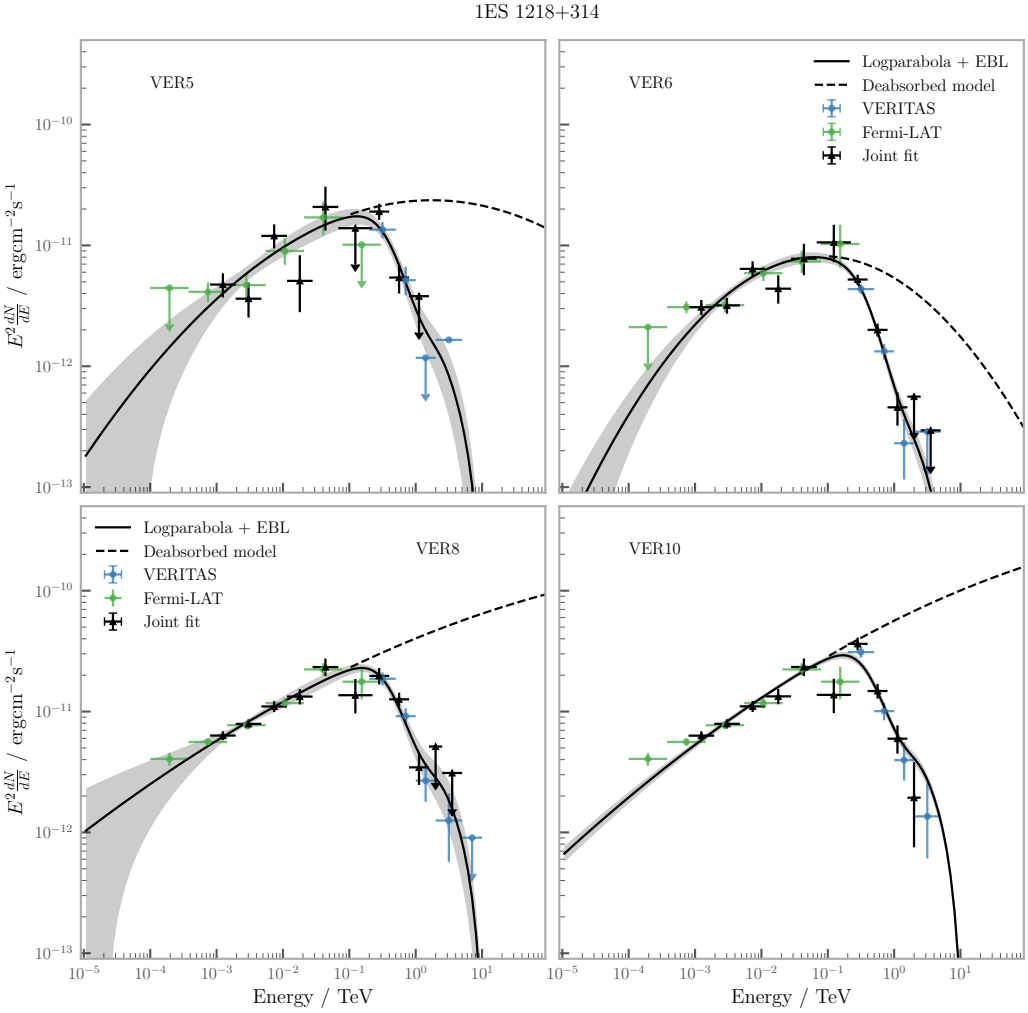

Figure 8.5: 1ES 1218+304 joint *Fermi*-LAT and VERITAS analysis. In green, the flux points obtained from the analysis of *Fermi*-LAT data only, using `fermipy`. In blue, the flux points obtained from the analysis of VERITAS data only, using `gammapy`. The black solid line, dashed line and flux points are the best fit observed model, intrinsic model and estimated flux points from the joint analysis with `gammapy`. The shaded grey area is the 1σ standard deviation region from the fit. Top left: *VER5*. Top right: *VER6*. Bottom left: *VER8*. Bottom right: *VER10*.

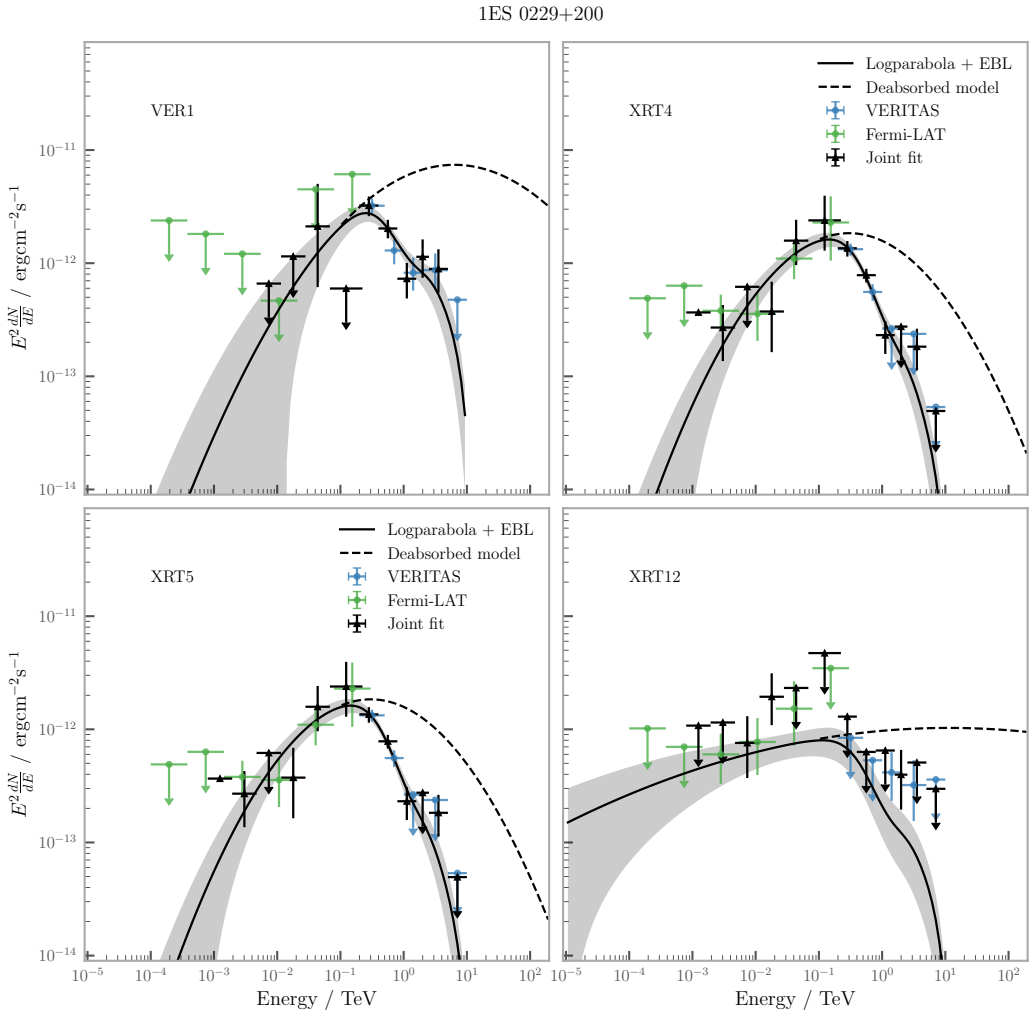

Figure 8.6: 1ES 0229+200 joint *Fermi*-LAT and VERITAS analysis. In green, the flux points obtained from the analysis of *Fermi*-LAT data only, using `fermipy`. In blue, the flux points obtained from the analysis of VERITAS data only, using `gammapy`. The black solid line, dashed line and flux points are the best fit observed model, intrinsic model and estimated flux points from the joint analysis with `gammapy`. The shaded grey area is the 1σ standard deviation region from the fit. Top left: *VER1*. Top right: *XRT4*. Bottom left: *XRT5*. Bottom right: *XRT12*.

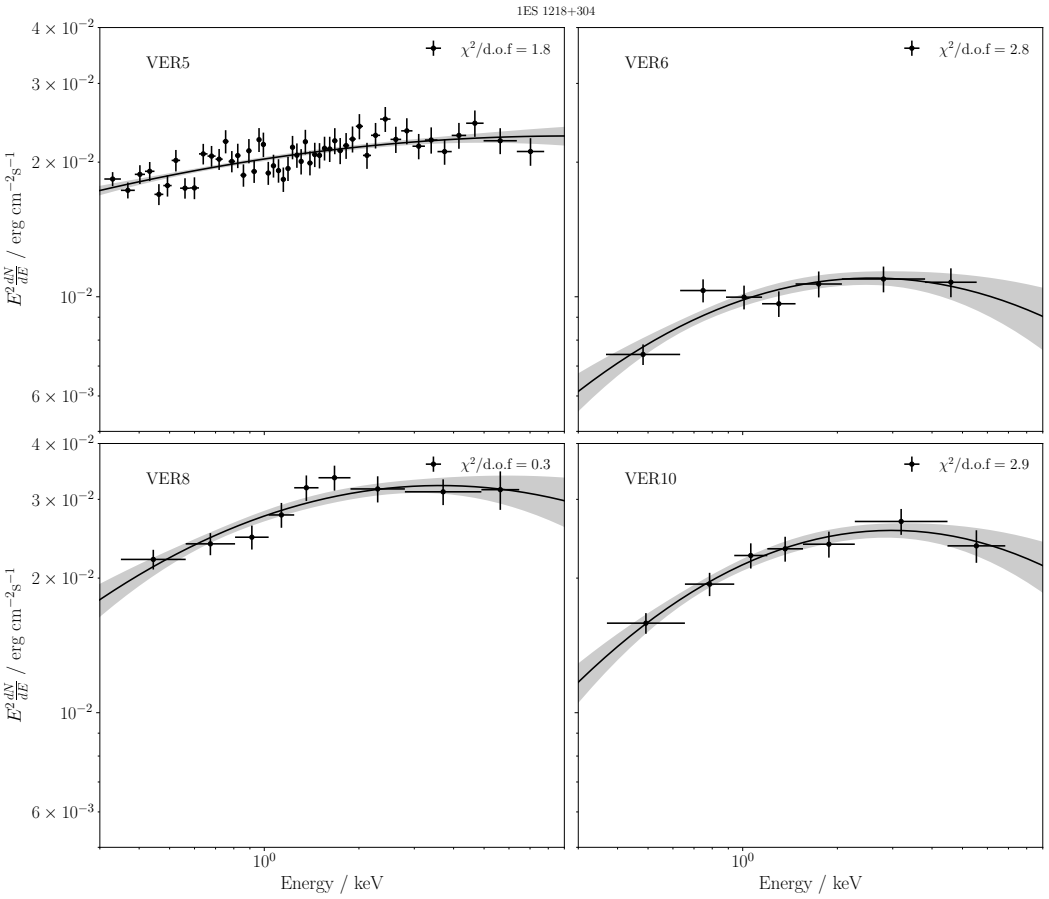

Figure 8.7: 1ES 1218+304 a chi-square fit of a log-parabola model to the XRT flux points for each period. Black points are energy flux data per energy bin. The solid black line is the best-fit model, with the 1σ standard deviation region as the grey shaded area. The periods are denoted by the blocks name, on the top left of each pad. On the top right, the χ^2/d.o.f. of the fit is shown.

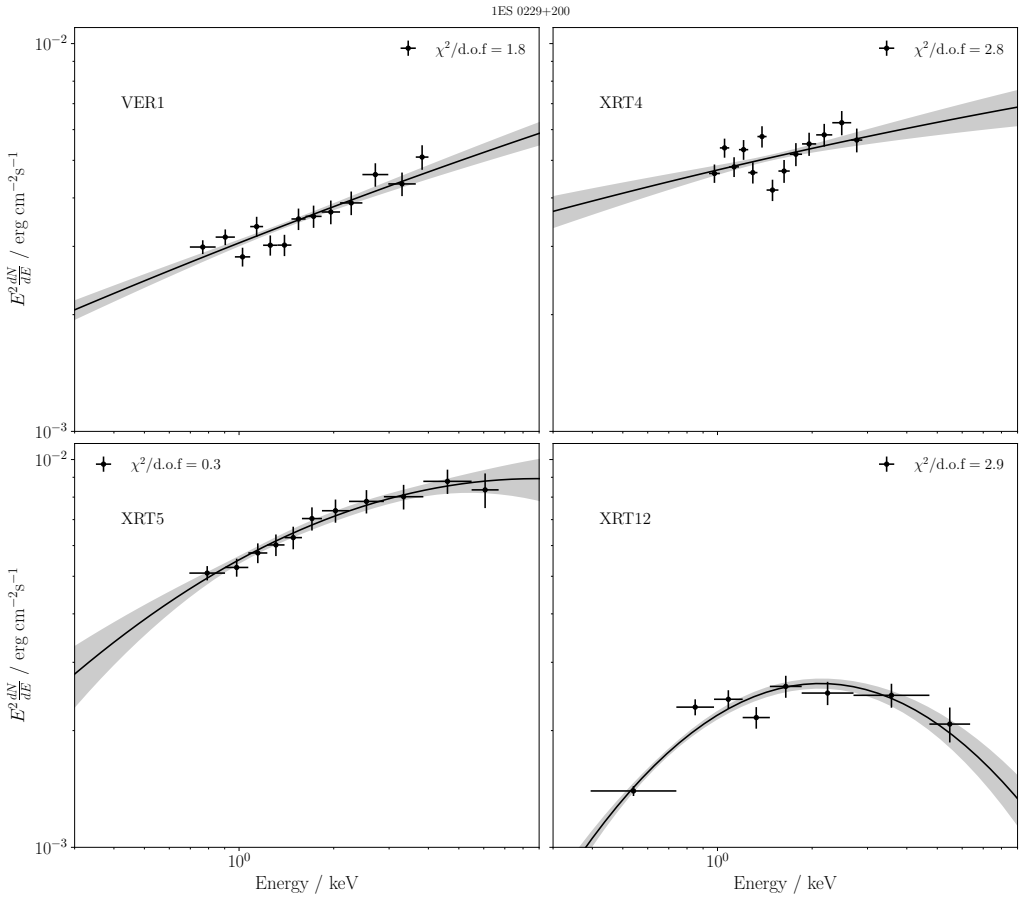

Figure 8.8: 1ES 0229+200 a chi-square fit of a log-parabola model to the XRT flux points for each period. Black points are energy flux data per energy bin. The solid black line is the best-fit model, with the 1σ standard deviation region as the grey shaded area. The periods are denoted by the blocks name, on the top left of each pad. On the top right, the χ^2/d.o.f. of the fit is shown.

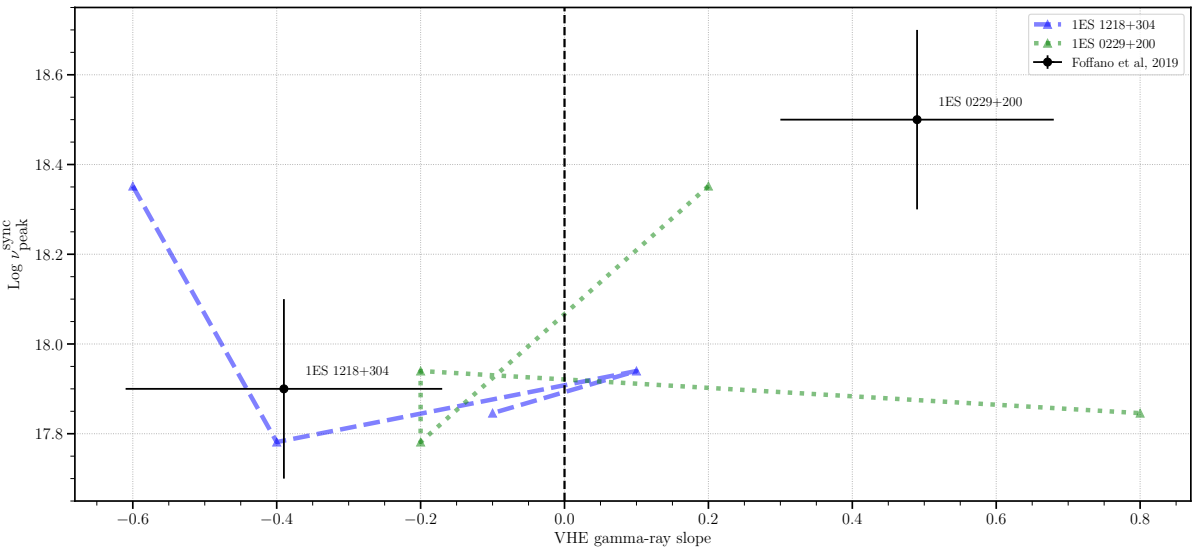

Figure 8.9: Synchrotron peak position (log of the frequency, in Hz) with respect to the VHE gamma-ray slope (from Equation 8.7). The dashed blue and dotted green lines *y* axis values are taken from Table 8.2 and converted to the apropriate quantities and units. The black points are extracted from FF19 (Figure 4 in [160]).

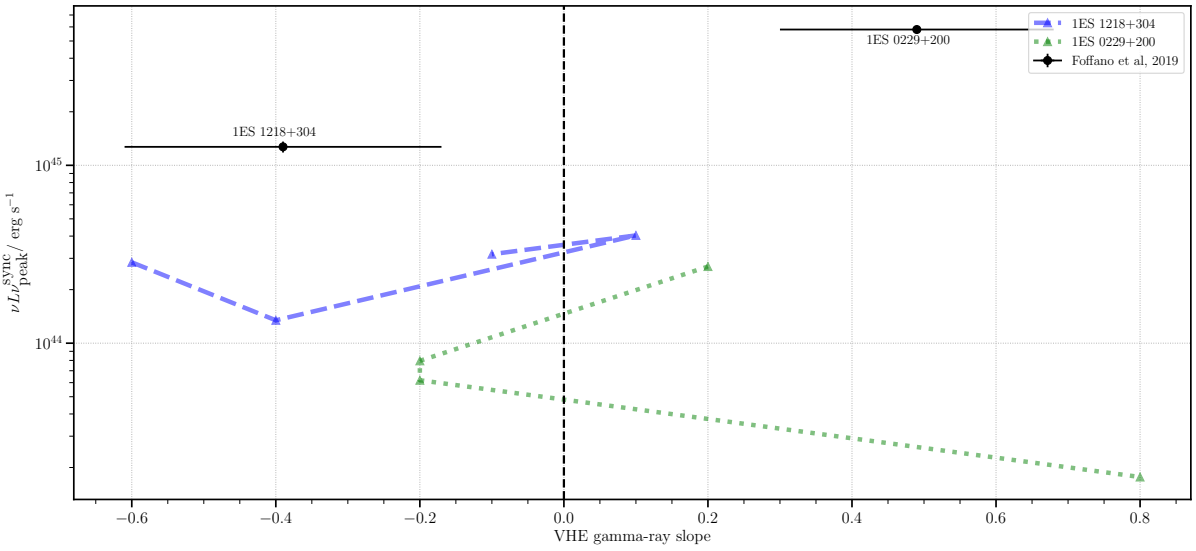

Figure 8.10: Synchrotron peak luminosity with respect to the VHE gamma-ray slope (from Equation 8.7). The dashed blue and dotted green lines *y* axis values are taken from Table 8.2 and converted to the apropriate quantities and units. The black points are extracted from FF19 (Figure 5 in [160]).

9 Emission modelling

We will now model the light emission from the selected periods of time using a one-zone leptonic synchrotron self-Compton (SSC) model, described in Subsection 3.4.1.

9.1 Model description

We use the SSC model described in [70]. We made use of `agnpy`*, a `python` package for the modeling of the radiative processes in jetted AGNs [161] (see Chapter 3). The SSC emission is calculated using `agnpy`, which numerically calculates equations 3.36 and 3.54 and outputs the broadband SED, for a given set of input parameters. The SSC model consists of a population of electrons $N_e(\gamma)$ distributed in Lorentz factor γ as a broken power law, parametrised as:

$$N_e(\gamma) = K\left[\left(\frac{\gamma}{\gamma_b}\right)^{-p_1} H(\gamma; \gamma_{min}, \gamma_b) + \left(\frac{\gamma}{\gamma_b}\right)^{-p_2} H(\gamma; \gamma_b, \gamma_{max}),\right] \tag{9.1}$$

where K is the spectral normalisation, γ_{min}, γ_b and γ_{max} are the minimum, break and maximum values of γ; p_1 and p_2 are the spectral indices before and after the break and $H(\gamma; \gamma_1, \gamma_2)$ is the Heaviside function. K,γ_{min}, γ_b, γ_{max}, p_1 and p_2 are kept as free parameters. From Equation 3.36, we have the Doppler factor δ_D, the magnetic field B as free parameters. The luminosity d_L is obtained from the source's redshift z. Lastly, from Equation 3.54, the size of the emission region R_B is also a parameter of the model. However, we can constrain the value of R_B with a simple estimation: the minimum variability timescale is constrained to the ballistic diffusion of photons inside the volume defined by a sphere of radius R_B. The photons travel at the speed of light c, and taking into account relativistic effects, we find that the minimum variability timescale observed $t_{v,\min}$ is

$$t_{v,\min} \geq \frac{(1+z)R_B}{\delta_D c}.$$

The term $(1+z)$ accounts for the cosmological expansion of the universe [13]. We can constrain the size of the emission region to

$$R_B = \frac{c\delta_D t_{v,\min}}{1+z}. \tag{9.2}$$

[70]: Finke et al. (2008), "Synchrotron self-Compton analysis of TeV X-ray-selected BL Lacertae objects"

[161]: Nigro et al. (2022), "agnpy"

[13]: Dermer et al. (2009), *High energy radiation from black holes: gamma rays, cosmic rays, and neutrinos*

* `https://agnpy.readthedocs.io/en/latest/index.html`

The minimum variability time $t_{v,\mathrm{min}}$ is obtained from the data.

In summary, we are left with a set of 8 free parameters:

$$\Theta = \{K, \gamma_{min}, \gamma_b, \gamma_{max}, p_1, p_2, \delta_D, B\}. \tag{9.3}$$

9.1.1 Host galaxy emission

[162]: Silva et al. (1998), "Modeling the effects of dust on galactic spectral energy distributions from the ultraviolet to the millimeter band"

For the host galaxy thermal emission, we opted to use the template model for giant elliptical galaxies provided in [162]. In Figure 9.1 we plot the energy flux data in the UV/optical band for the different 1ES 0229+200 blocks, and the host galaxy emission as a function of the galaxy age. We can conclude from Figure 9.1 and in particular from Figure 9.2 that the emission from a 13 Gyr galaxy appears to be the only one that is not ruled out by our optical/UV SED data. Therefore, for the host galaxy emission, we use the template model of a 13 Gyr giant elliptical galaxy in the next steps of the analysis.

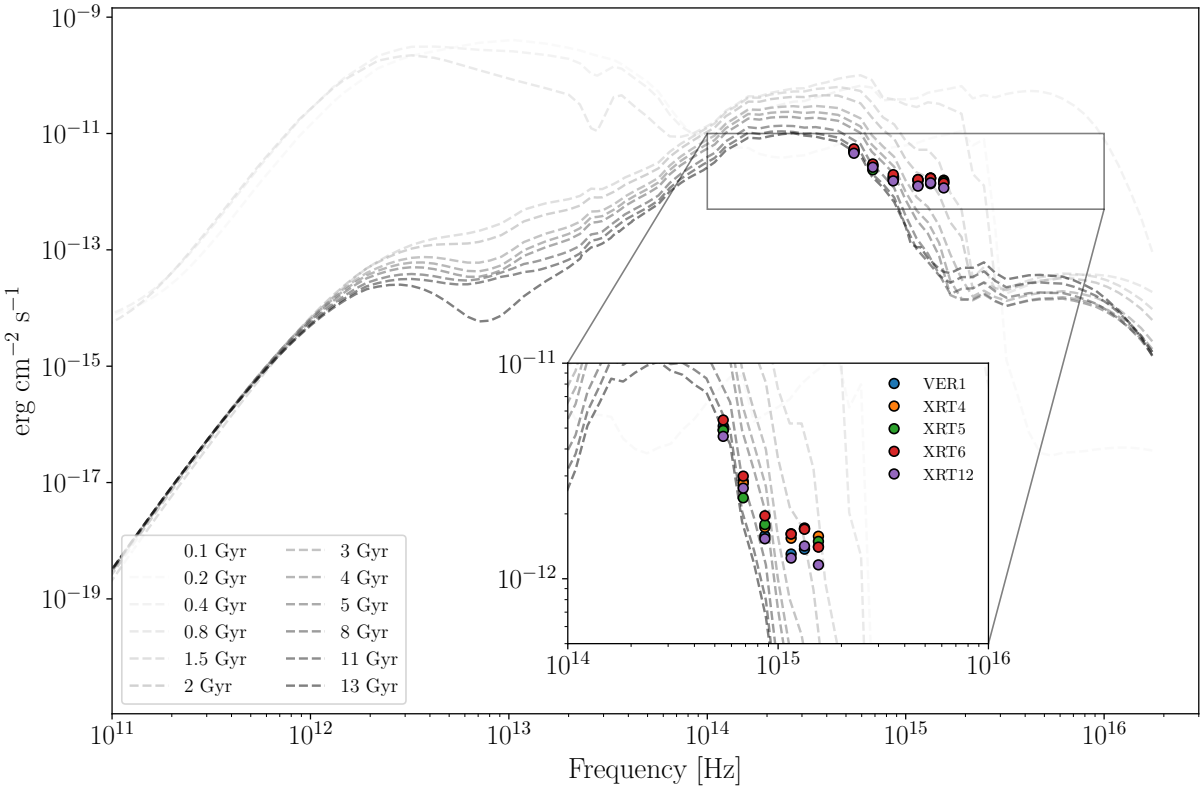

Figure 9.1: Host galaxy emission templates from [162] as a function of frequency, plotted for different galaxy ages as dashed grey lines. The optical/UV SEDs for the four time intervals defined for 1ES 0229+200 in Chapter 8 are plotted for comparison. The inset shows a zoom at frequencies 10^{14} Hz $< \nu < 10^{16}$ Hz.

9.1.2 EBL absorption

[73]: Domínguez et al. (2011), "Extragalactic background light inferred from AEGIS galaxy-SED-type fractions"

To account for EBL absorption, we use `Dominguez+11` [73] EBL model.

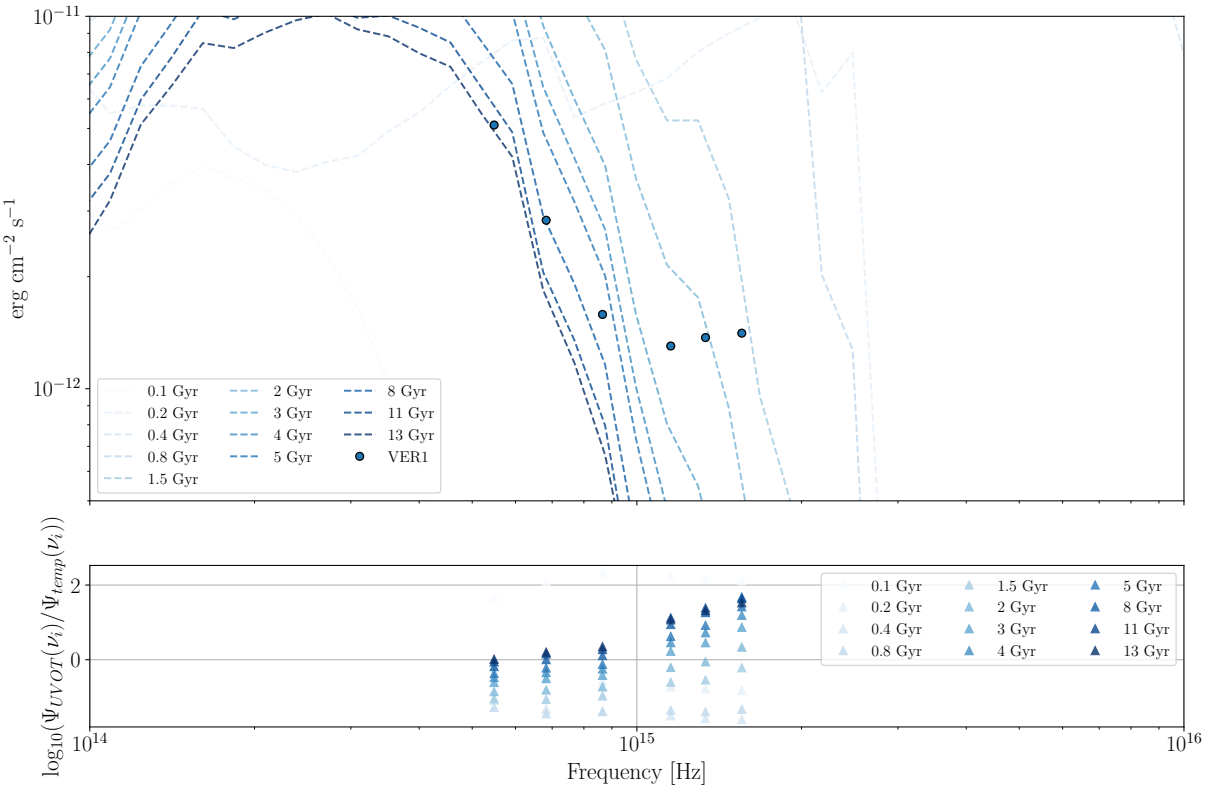

Figure 9.2: Host galaxy emission templates from [162] as a function of frequency, plotted for different galaxy ages as dashed blue lines (top) and the logarithmic difference between 1ES 0229+200 optical/UV SED data for the period *VER1* and the template models (bottom).

The calculated SSC + host galaxy SED is exponentially attenuated according to the optical depth of the EBL, as described in Equation 3.65.

9.2 Fitting procedure

[163]: Goodman et al. (2010), "Ensemble samplers with affine invariance"

The adopted fitting procedure makes use of a Markov chain Monte Carlo (MCMC) ensemble sampler[163]. This method uses a number $N_{walkers}$ of walkers to sample a probability distribution of the parameter space. The walkers will sample a predefined number of realisations N_{steps}, where in each step the current state of each walker is used to make a decision to move to a different location in the phase space. In this way, the walkers do not sample independently of each other, allowing a better sampling efficiency [163]. Given a dataset $X = \{x_1, ..., x_n\}$, the likelihood $L(\Theta|X)$ of Θ parameters given X dataset is the criteria used by the walker, therefore, predicting the model's *a posteriori* likelihood given the data. For a more formal description, consider that $Y_k(t)$ is the position of the k-th walker in step t, where $k = 0, ..., N_{walkers}$ and $t = 0, ..., N_{steps}$. For each step t, the walker $Y_k(t)$ represents a set of parameters of the model such that

$$Y_k(t) : \{K, \gamma_{min}, \gamma_b, \gamma_{max}, p_1, p_2, \delta_D, B\}_t^k. \tag{9.4}$$

Therefore, the values of the parameters Y_k for each step t form a **trace** (or chain) of all the corresponding model parameters, as shown in Figure 9.3 sampled from the likelihood distribution. In this way, we can control by changing the total number of walkers and steps how large the samples will be. More steps/walkers will produce better likelihood samplings, but will also increase the computational costs required for the analysis. For our results, we use a total number of steps $N_{steps} = 2500$ and walkers $N_{walkers} = 20$. The beginning of the trace is usually "burnt-in", to avoid large variations. These variations are usually due to the initial likelihoods being too far from the minimum likelihood. A certain burn-in number (in Figure 9.3, 1000 steps) is chosen such that the traces have sufficient steps to stabilise around a minimum. The burnt-in steps are not taken into account in the final sample.

Figure 9.4 shows an example of a **corner plot**, where one can visualise the distributions of parameters and correlations between them. Figure 9.4 we plot the distributions and correlation of the subset of parameters $\{\delta_D, B\}$, obtained from the sampling of block *VER5* data. From the traces, after burn-in, one has access to the parameter distributions and correlations. From the sample distributions, we can obtain the 16th, 50th and 84th percentiles as the lower 1σ standard deviation boundary, the median, and upper 1σ standard deviation boundary, or, in other words, the best-fit values and asymmetric errors.

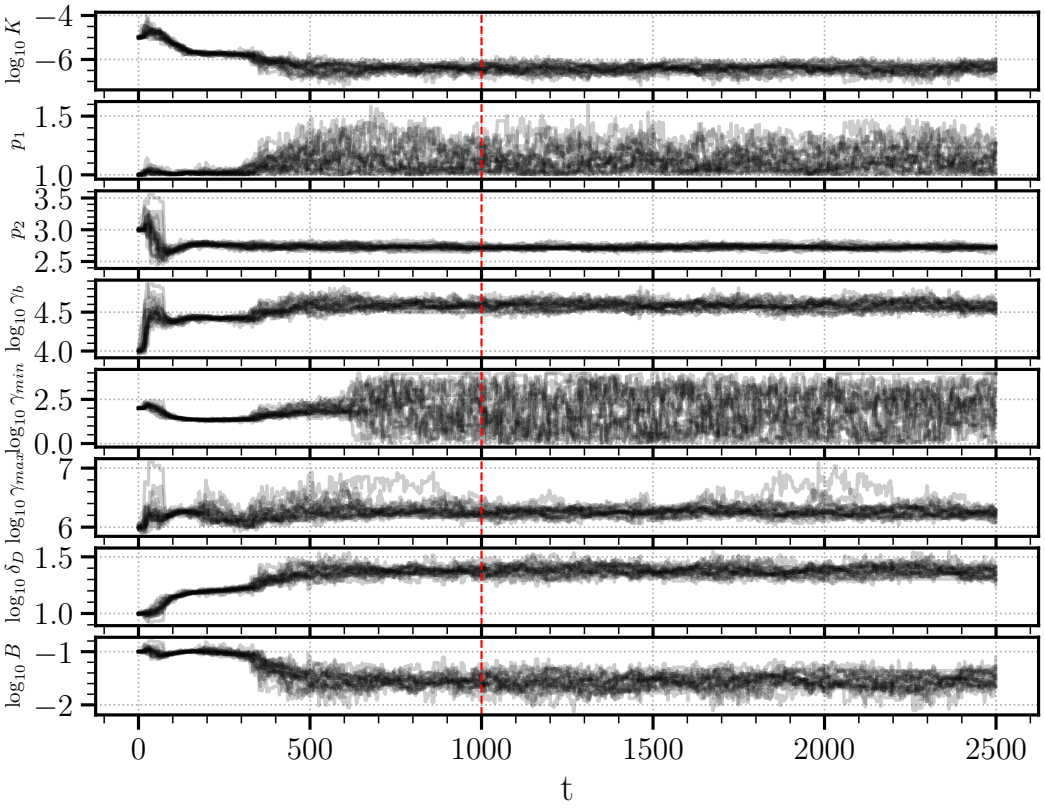

Figure 9.3: Trace plot of the MCMC sampling from *VER5* data using an SSC model. In each pad are plotted the traces of all walkers for each SSC model parametr. The red dashed line corresponds to $n_{burn} = 1000$.

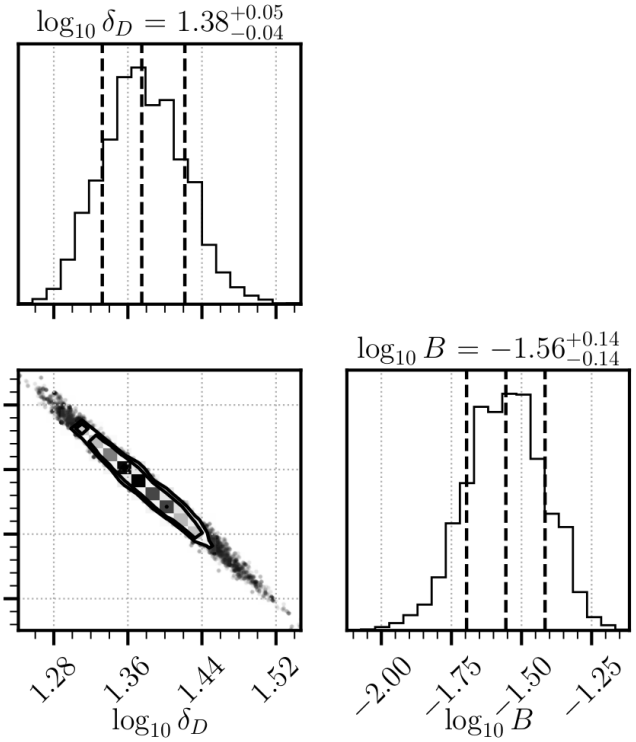

Figure 9.4: Corner plot example from *VER5* with the distributions of $\log_{10} \delta_D$ and $\log_{10} B$, and the 2-D correlation between these quantities.

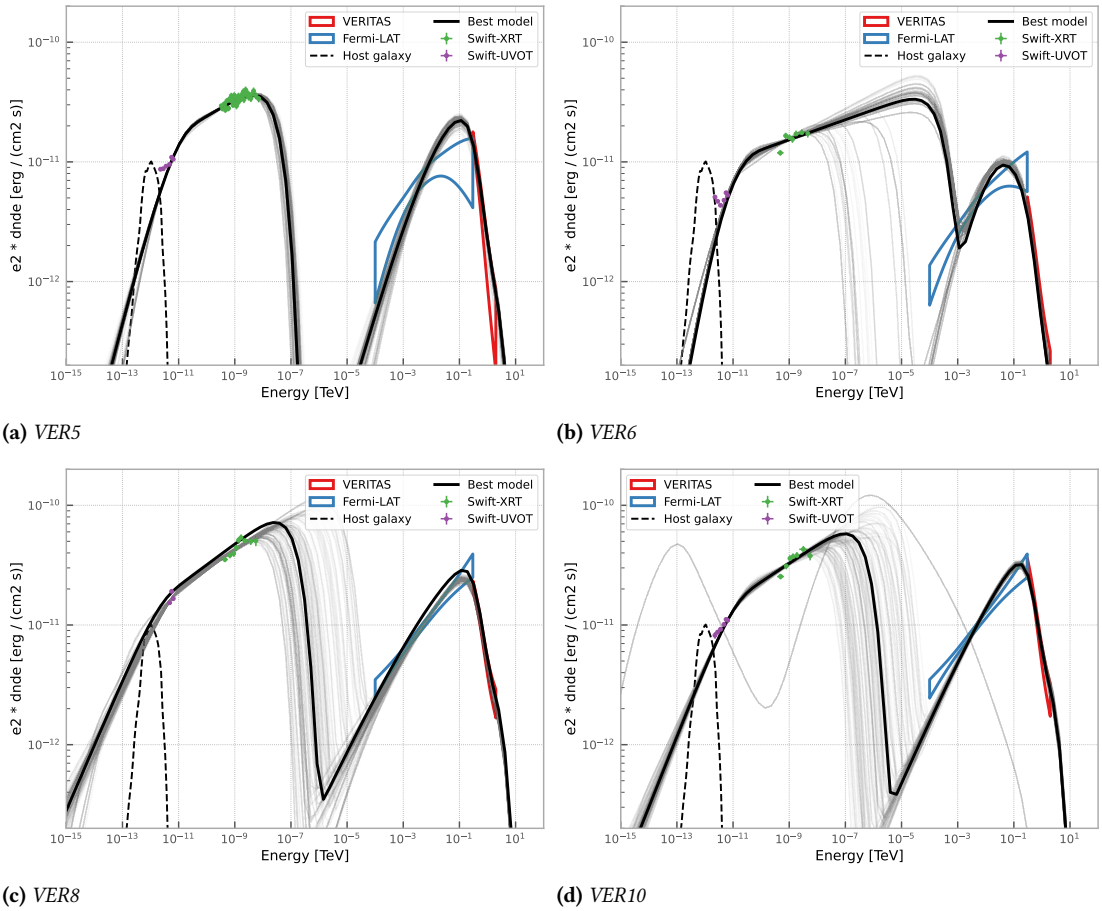

(a) *VER5* **(b)** *VER6*

(c) *VER8* **(d)** *VER10*

Figure 9.5: SEDs and MCMC preliminary fit results per block (black solid line) and the datasets (green and purple data points; the blue and red line regions) used in this analysis. The grey lines represent the last 25 steps of the 20 walkers.

9.2.1 Datasets and likelihood calculation

We use the package `gammapy` to calculate the likelihood used as a criteria during the MCMC sampling. In `gammapy`, we create datasets containing *Swift*-UVOT, *Swift*-XRT, *Fermi*-LAT , and VERITAS datasets. See Section 7.1, Subsection 7.2.2 and Subsection 7.3.2 for information on how these datasets are constructed. However, there is one difference regarding how XRT and UVOT data are treated: data are read in `gammapy` as flux points instead of event lists and IRFs due to software incompatibilities, which were beyond the scope of this thesis. Once the data are combined into a single dataset, we can perform a joint likelihood estimation, where the logarithm of the likelihoods of each individual dataset is summed.

The logarithmic likelihood is calculated for each instrument data as follows (see Chapter 6):

VERITAS W-stat likelihood, from Equation 6.24
***Fermi*-LAT** C-stat likelihood, from Equation 6.16
XRT and UVOT data Chi-squared likelihood, from Equation 6.26, with x_i and σ_i are flux points and standard deviation respectively

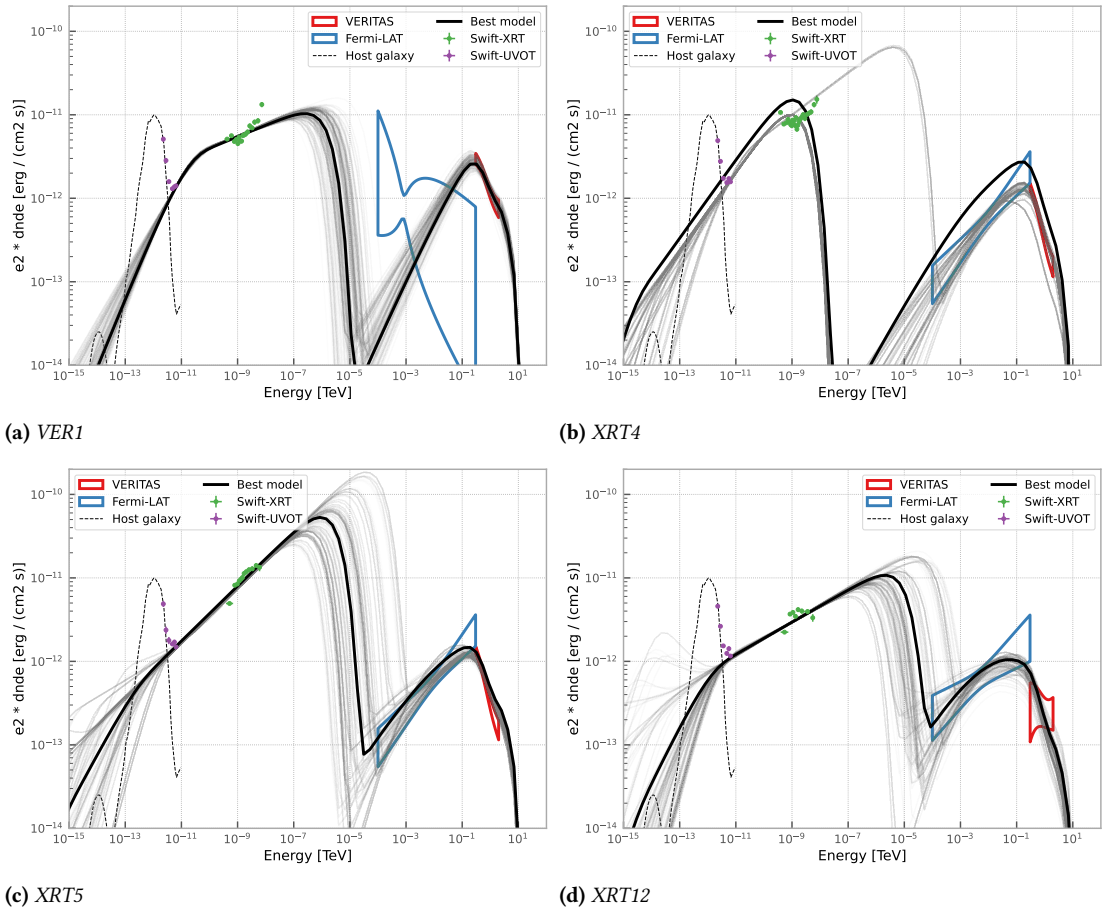

(a) *VER1* **(b)** *XRT4*

(c) *XRT5* **(d)** *XRT12*

Figure 9.6: SEDs and MCMC preliminary fit results per block (black solid line) and the datasets (green and purple data points; the blue and red line regions) used in this analysis. The grey lines represent the last 25 steps of the 20 walkers.

In Figures 9.5 and 9.6, we show the results of the MCMC sampling and the datasets used, per block. The time intervals of the blocks are listed in Table 8.1. In Figure 9.5 and Figure 9.6, we plot XRT's and UVOT's SED points, the 1-sigma region derived from the individual fits of *Fermi*-LAT and VERITAS data, and the host galaxy template SED. The last 25 steps of the 20 walkers are plotted as grey lines, alongside a preliminary best model curve - that is, the model resulting from the median parameter values (0.5 quantile) - in black, with a burn-in of **1000** steps. The samples shown are EBL absorbed. The complete corner plots with the parameter distributions and correlations, as well as the trace plots, used to extract the best model values and for further analysis are presented in Chapter B of the appendix.

Analysis caveats

Regarding the MCMC sampling results, it is clear from Figure 9.5 and Figure 9.6 that the data used in this study do not sufficiently constrain the entire parameter space, as seen in the large degeneracy in the location of the synchrotron peak energy. The grey lines in Figure 9.5 and Figure 9.6

show the scale of deviation from the median values during the MCMC sample. The poor constrains to the location of the synchrotron peak energy can skew some parameter distributions during the sampling, which can over- or underestimate parameter median values used to construct the best model SED representation. This results in an apparent best model that can completely overshoot the data. In addition, the IC peak description seems to be dominated by the more precisely measured VERITAS data, which can cause the apparent poor agreement with the best-fit spectrum model (power law) derived solely from *Fermi*-LAT's data. A low number of burnt-in steps can also bias the estimation of the parameter quantile values. It is also worth mentioning that, as observed from the traces plots in B.1 and B.2, that some parameters can offer little to no constraining power, as is the case for the minimum Lorentz factor of the electrons $\gamma_{\rm min}$, which is in turn reflected on the very large errors shown in Table 9.1.

9.3 Modeling results

After visual assessment of the individual block traces, burn-in values are determined to exclude the large and rapid variations observed especially in the first steps, therefore, after the walkers have converged to a value on average. The set the burn-in values for each block of data are shown as the red dashed lines in the trace plots in B.1 and B.2. The best-fit parameter values are extracted from the MCMC samples of each block. The best-fit results are shown in Table 9.1. The quoted values are the median of the MCMC sample distributions, and the asymmetric errors are calculated as the absolute difference between the median and the 16th and 84th percentiles as negative and positive errors, respectively. *The values in Table 9.1 are* ***not*** *the ones used to generate the best model curve in Figures 9.5 and 9.6.*

In Figure 9.7 and Figure 9.7, we show the evolution of the SSC parameters per block. We want to highlight the following:

* For both sources, on all of the blocks of data, we obtain median values of $\gamma_{min} \gg 1$ (by at least one order of magnitude). However, comparing the median values with the upper and lower limits obtained, we observe that γ_{min} is poorly constrained by the data. In fact, this means that the lower limits of γ_{min} are consistent with ~ 1.
* Although we estimate extremely large values for the equipartition parameter k_{eq} - especially in 1ES 1218+304 flaring states *VER8* and *VER10*, and the elevated state in 1ES 0229+200 *VER1* - that does not appear to be the general trend in the different blocks. The best counterexamples are the results obtained for the sources' most quiet states, *VER6* for 1ES 1218+304 and *XRT12* for 1ES 0229+200, where we obtained 2 and 11 respectively.

Table 9.1: SSC model best-fit parameters used to draw the models in Figures 9.9 and 9.10. The quoted values are the medians of the MCMC samples, and the asymmetric errors are the 16th and 84th percentile values respectively. Note: the values listed here are **not** the ones used to generate the best model curve in Figures 9.5 and 9.6.

1ES 1218+304

Block	$10^6 \times K$ / cm^{-3}	p_1	p_2	$10^4 \times \gamma_b$	γ_{min}	$10^7 \times \gamma_{max}$	δ_D	B / mG	k_{eq}
VER5	$0.4^{+0.2}_{-0.1}$	$1.11^{+0.10}_{-0.08}$	$2.72^{+0.03}_{-0.03}$	$3.8^{+0.5}_{-0.4}$	71^{+1100}_{-67}	$0.18^{+0.04}_{-0.03}$	23^{+2}_{-2}	30^{+10}_{-7}	40
VER6	3^{+1}_{-1}	$1.2^{+0.7}_{-0.2}$	$2.83^{+0.04}_{-0.05}$	$2.7^{+0.2}_{-0.3}$	8700^{+900}	8^{+1}_{-8}	$10.9^{+1.9}_{-0.8}$	200^{+50}_{-70}	2
VER8	$0.010^{+0.072}_{-0.008}$	$1.9^{+0.1}_{-0.4}$	$2.65^{+0.03}_{-0.02}$	6^{+3}_{-3}	52^{+620}_{-49}	$1.3^{+3.9}_{-0.6}$	87^{+9}_{-12}	$0.7^{+0.4}_{-0.2}$	1×10^4
VER10	$0.009^{+0.01}_{-0.005}$	$1.82^{+0.07}_{-0.08}$	$2.69^{+0.03}_{-0.03}$	$1.2^{+0.4}_{-0.3}$	24^{+140}_{-21}	2^{+4}_{-1}	57^{+13}_{-9}	$1^{+1}_{-0.6}$	9×10^3

1ES 0229+200

Block	$10^6 \times K$ / cm^{-3}	p_1	p_2	$10^4 \times \gamma_b$	γ_{min}	$10^7 \times \gamma_{max}$	δ_D	B / mG	k_{eq}
VER1	$0.001^{+0.003}_{-0.001}$	$1.3^{+0.2}_{-0.2}$	$2.72^{+0.02}_{-0.02}$	28^{+10}_{-8}	70^{+2000}_{-70}	6^{+2}_{-2}	49^{+10}_{-10}	$0.5^{+0.7}_{-0.3}$	3×10^4
XRT4	11^{+90}_{-9}	$2.2^{+0.2}_{-0.5}$	$2.05^{+0.02}_{-0.01}$	$0.2^{+0.4}_{-0.2}$	1331^{+5000}_{-1000}	$0.089^{+0.030}_{-0.009}$	30^{+7}_{-3}	7^{+3}_{-4}	150
XRT5	1^{+100}_{-1}	$1.7^{+0.9}_{-0.5}$	$2.3^{+0.01}_{-0.01}$	$1.0^{+2}_{-0.9}$	283^{+7000}_{-280}	3^{+4}_{-1}	24^{+10}_{-10}	10^{+80}	80
XRT12	5^{+20}_{-4}	$1.6^{+1.0}_{-0.4}$	$2.6^{+0.02}_{-0.02}$	$1.3^{+0.9}_{-0.5}$	416^{+8000}_{-400}	3^{+5}_{-2}	12^{+10}_{-3}	70^{+100}_{-60}	11

* We can extend the conclusion of the last point to the Doppler factor values δ_D, which are aligned with the behaviour of k_{eq}, where we have values ranging from 10 to 25 for the blocks *VER5* and *VER6* for 1ES 1218+304, *XRT5* and *XRT12* for 1ES 0229+200.

These elements provide arguments in favour of a non-persistent extreme behaviour of 1ES 1218+304 and 1ES 0229+200.

Lastly, we present the SSC SEDs evaluated from the nominal values of the parameters in Table 9.1 in Figure 9.9 and Figure 9.10. The peak frequencies and energy density fluxes values are highlighted by the dot-dashed lines.

For comparison, we list the energies of the synchrotron and IC peaks together with the energy density fluxes at the peak in Table 9.2 derived from the full SSC model fit. Compared with the peak energies and luminosities derived from the joint HE/VHE empirical fit (Subsection 8.3.1) listed in Table 9.2, it is possible to observe once again the lack of energy coverage to constrain the synchrotron peak energy and, consequently, its luminosity, illustrated by the very large values of $\nu^{\rm sync}_{\rm peak}$ and the large spread of the grey curves from Figure 9.5 and Figure 9.6. It becomes clear from Table 8.2 and Table 9.2 that additional data are required to properly constrain synchrotron emission in this model.

However, since the MCMC samples from the SSC model are estimated from the joint likelihood from the whole broadband dataset, we will take these results at face value to discuss the synchrotron/Compton dominance. The ratio between the luminosities of the synchrotron peak and of the IC peak, $R = \nu F^{\rm sync}_{\nu,\rm peak} / \nu F^{\rm IC}_{\nu,\rm peak}$, is calculated from Table 9.2. We will call R the dominance parameter, and we will use it to assess which process

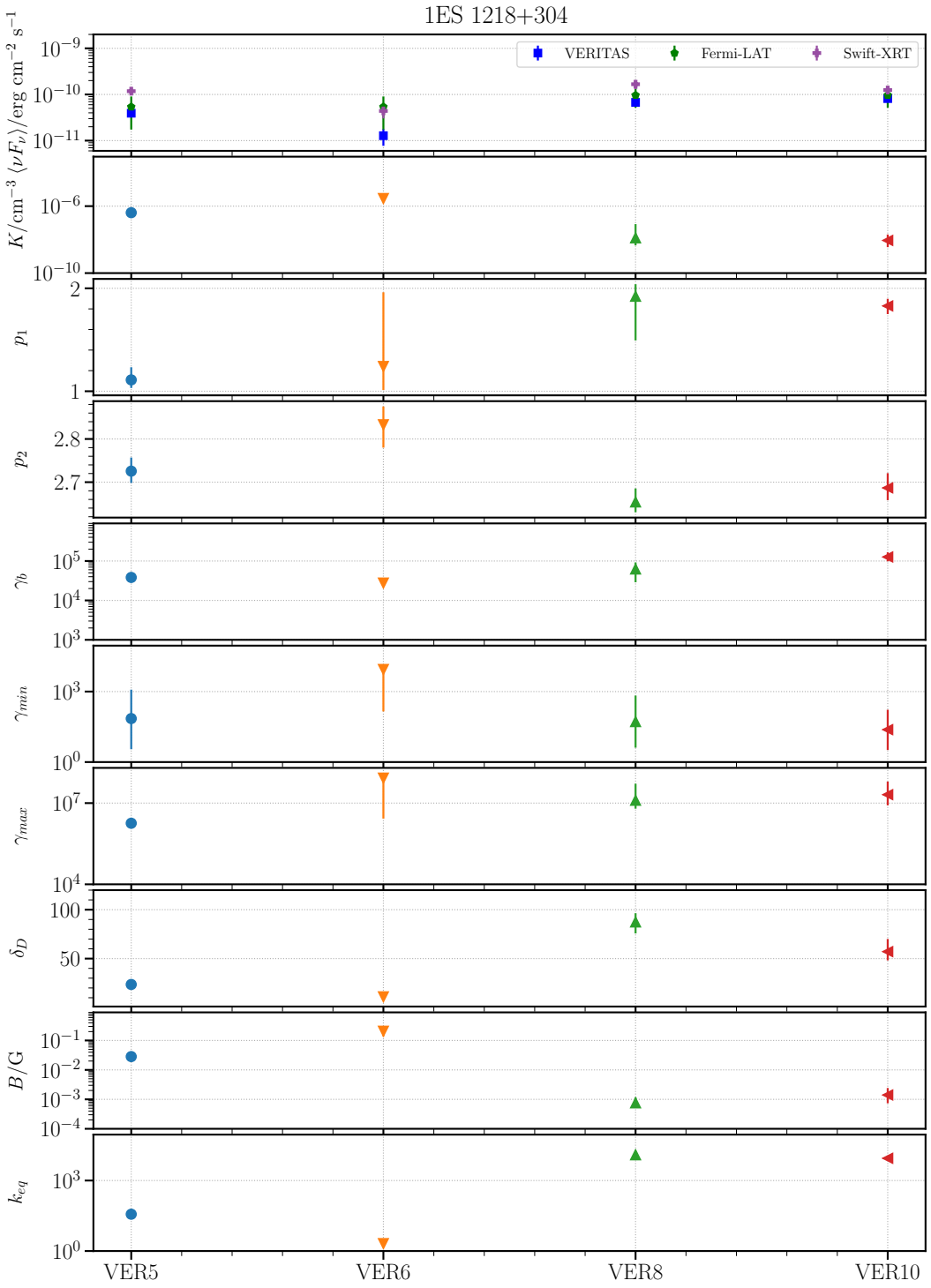

Figure 9.7: 1ES 1218+304 SSC parameters evolution. On the top panel are shown the average fluxes per block, per instrument.

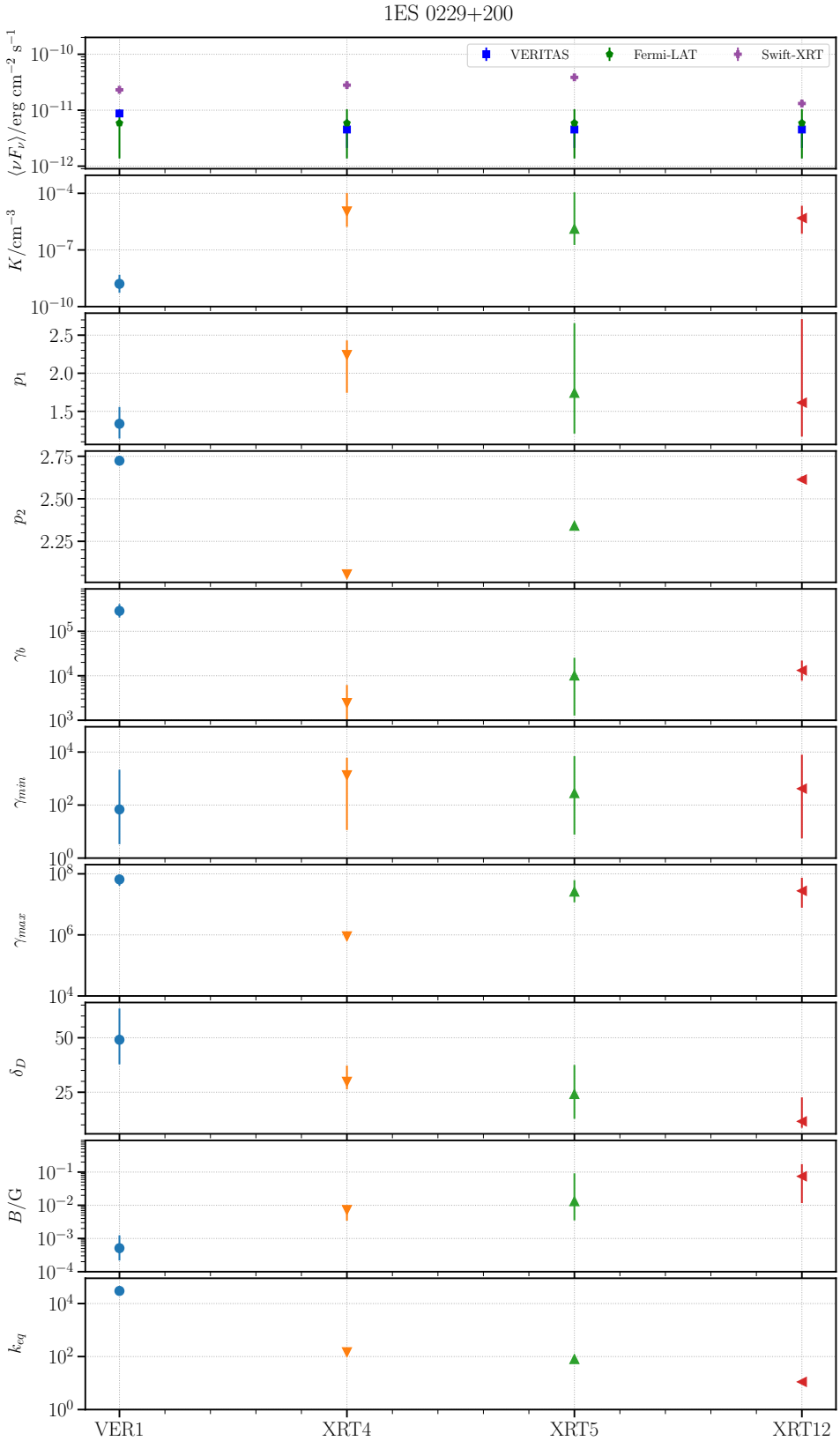

Figure 9.8: 1ES 0229+200 SSC parameters evolution. On the top panel are shown the average fluxes per block, per instrument.

Table 9.2: List of SED properties derived from the SSC modeling. [1] the block name, referring to the names in Table 8.1; [2] frequency of the synchrotron peak in Hz; [3] synchrotron peak νF_ν, in erg cm^{-2} s^{-1}; [4] frequency of the IC peak in TeV; [5] IC peak νF_ν, in erg cm^{-2} s^{-1}

1ES 1218+304

Block [1]	$10^{16} \times \nu^{\rm sync}_{\rm peak}$ [2]	$10^{11} \times \nu F^{\rm sync}_{\nu,\rm peak}$ [3]	$10^{26} \times \nu^{\rm IC}_{\rm peak}$ [4]	$10^{11} \times \nu F^{\rm IC}_{\nu,\rm peak}$ [5]
VER5	106	3.5	0.4	2.3
VER6	> 240	3.3	0.09	0.9
VER8	> 240	7.2	3.8	4.0
VER10	> 240	5.7	2.9	5.1

1ES 0229+200

Block [1]	$10^{16} \times \nu^{\rm sync}_{\rm peak}$ [2]	$10^{11} \times \nu F^{\rm sync}_{\nu,\rm peak}$ [3]	$10^{26} \times \nu^{\rm IC}_{\rm peak}$ [4]	$10^{11} \times \nu F^{\rm IC}_{\nu,\rm peak}$ [5]
VER1	> 240	1.0	6.7	0.66
XRT4	19	0.9	0.7	0.4
XRT5	> 240	5.3	15	0.26
XRT12	> 240	1.0	0.1	0.10

dominates the emission. From Table 9.2 and Figures 9.9 and 9.10, we conclude:

1ES 1218+304 shows a weak synchrotron dominance The estimated values of the dominance parameter are $R \approx [1.5, 3.6, 1.8, 1.1]$. The greatest synchrotron dominance in emission occurs during *VER6*, which is indeed the quietest VHE state, as seen from the average block flux of ~ 1.3 erg cm^{-2} s^{-1}(top pannel in Figure 9.7) and lowest peak energy $E^{\rm IC}_{\rm peak} = 40$ GeV. For the other time intervals, $R \sim 1$ and 1 to 2 orders of magnitude lower magnetizations.

1ES 0229+200 is heavily synchrotron dominated 1ES 0229+200 dominance parameter are $R \approx [1.5, 5, 20, 10]$. The lowest observed value of R corresponds to the single elevated state in VHE data, *VER1*. During the other time intervals, where the synchrotron emission is very pronounced, we do observe really high magnetization levels, with magnetic field intensities $B \gg 1$ mG.

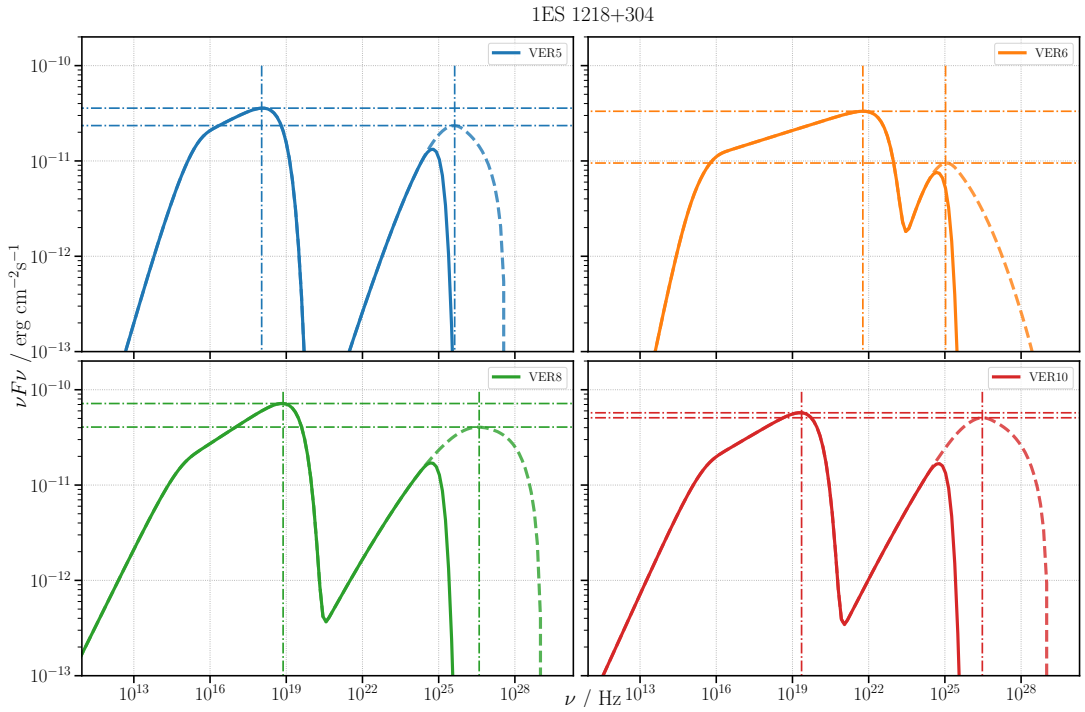

Figure 9.9: 1ES 1218+304 SSC broadband SEDs per block. The solid line represents the observed SSC emission. The dashed line represents the EBL de-absorbed emission. We use `Dominguez+11` [73] EBL model. The positions of the energy peaks and their luminosities are highlighted with dot-dashed lines.

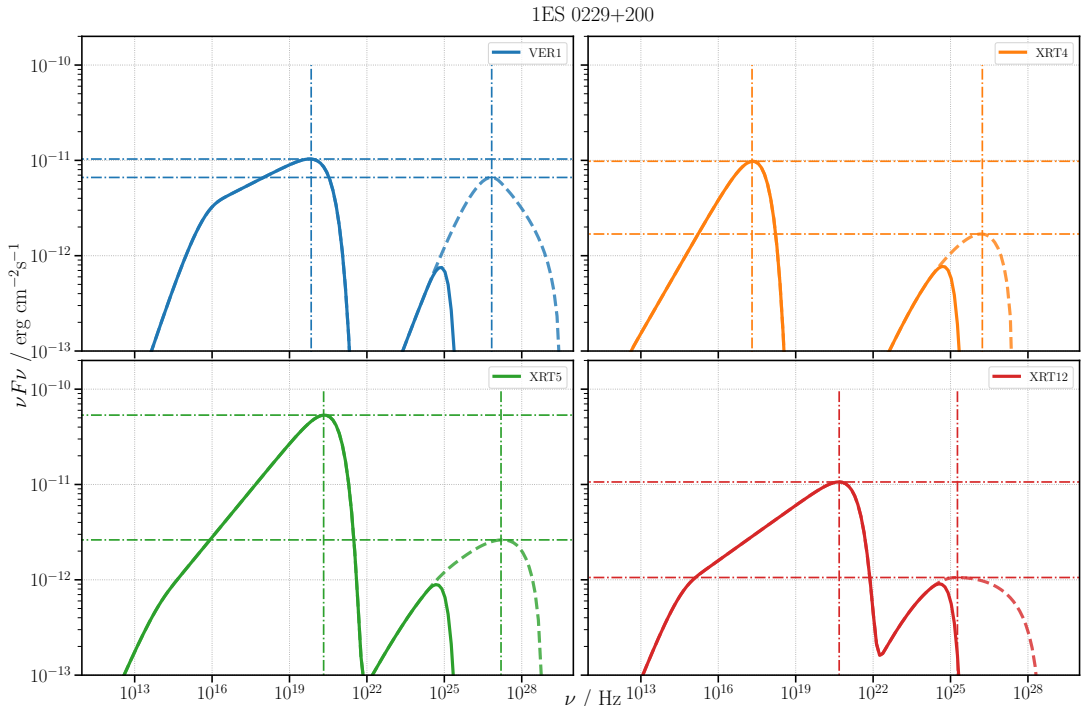

Figure 9.10: 1ES 0229+200 SSC broadband SEDs per block. The solid line represents the observed SSC emission. The dashed line represents the EBL de-absorbed emission. We use `Dominguez+11` [73] EBL model. The positions of the energy peaks and their luminosities are highlighted with dot-dashed lines.

10 Discussion and conclusions

In the recent history of gamma-ray astronomy, the HBL objects 1ES 1218+304 and 1ES 0229+200 were always described as prototypical extreme HBL objects. Measurements on both sources have reported a hard intrinsic spectrum, with a TeV (0.1 - 10 TeV) spectral index $\Gamma < 2$ and inverse Compton peak energies $E^{\rm IC}_{\rm peak} > 10$ (e.g. [38, 39, 44]). One of the recent questions around the HBL/EHBL classification arises from sources that appear to change behaviours with time [30], which is the case, for instance, for the HBL object Mrk 501, with a "harder when brighter" behaviour [164].

In this thesis, we also address the issue of long-term data from EHBL candidates. The last VERITAS publications on 1ES 1218+304 [45] and 1ES 0229+200 [43] only had access to small data samples, relative to ours. With over 10 years of MWL data, where variability is present at the VHE band or in other energy ranges, we aimed to understand whether those previous snapshots are indicative of the behaviour over a longer baseline.

In this work, we collected the MWL data available at the time and produced a long-term study on the behaviour of these sources. The main goal was to rely on novel, statistically sound, analysis techniques in order to identify:

* Long-term light curves stability,
* Possible source states,
* Whether these sources persistently showed extreme behaviour,
* Whether a single zone, leptonic SSC model could describe the time resolved SEDs from our EHBL candidates

First, we analysed gamma-ray data from the VERITAS collaboration in the VHE range, and the public data from the *Fermi*-LAT detector in the HE range. We also analysed archival optical/ultraviolet and X-ray data from the *Swift*-UVOT and *Swift*-XRT detectors. The estimated light curves from the MWL data were used in a Bayesian blocks analysis in order to identify different flux states of the sources. We produced an extensive spectral study, where, in addition to reporting seasonal spectral indices on the X-ray, HE and VHE ranges, we produced a deep investigation on the sources states based on a Bayesian block detection algorithm [158]. Once these states have been identified and the periods of data have been selected, we used a one-zone leptonic SSC model to describe the broadband SED from each period. To do it, we used an MCMC sampling technique to explore the parameter space.

[158]: Scargle et al. (2013), "Studies in astronomical time series analysis. VI. Bayesian block representations"

In this chapter, we discuss the conclusions of our findings.

10.1 The VHE spectrum hardness and peak energy

[59]: Blandford et al. (1978), "Particle acceleration by astrophysical shocks."
[30]: Biteau et al. (2020), "Progress in unveiling extreme particle acceleration in persistent astrophysical jets"

In a shock acceleration scenario, the interaction between acceleration and cooling timescales leads the spectrum of accelerated particles to $dN/d\gamma \propto \gamma^{-p}$, where $p \simeq 2$ [59], which in turn would lead to a TeV intrinsic spectral index of $\Gamma_{VHE} \simeq 2$ [30]. In Table 8.2 we list the values of the intrinsic spectral indices fitted to VERITAS data only, in the TeV range. The only period of time observed with an intrinsic spectral index $\Gamma_{VHE} < 2$ is the quietest state of 1ES 0229+200, *XRT12*, with $\Gamma_{VHE} = 1.2 \pm 0.4$. For all the other periods that were analysed, the value of $\Gamma_{VHE} \gtrsim 2$, as expected from a shock acceleration scenario. Other acceleration scenarios such as shear acceleration [60] or magnetic reconnection [19], could explain deviations from the expectation of $p \simeq 2$. However, the lack of gamma-ray statistics observed from 1ES 0229+200 light curves (Figure 8.2) during *XRT12* hinders the strength of any hypothesis that can be made.

[60]: Rieger et al. (2004), "Shear acceleration in relativistic astrophysical jets"
[19]: Guo et al. (2016), "Efficient production of high-energy nonthermal particles during magnetic reconnection in a magnetically dominated ion-electron plasma"

The combination of a hard spectrum with a peak emission above 1 TeV would imply in large minimum Lorentz factors of the electrons ($\sim 10^4$ - 10^5) [30]. In Table 8.2, are also listed the IC peak energies, as estimated from a fit using a log-parabola model to the joint *Fermi*-LAT and VERITAS data from each selected period.

When comparing the results in Table 8.2, with those obtained from the SSC modelling of the same data periods in Table 9.2, we observe a large discrepancy: In the log-parabola fit, we estimate values of $E^{\rm IC}_{\rm peak} > 1$ TeV in the blocks *VER5*, *VER8*, and *VER10* for 1ES 1218+304, and *VER1* and *XRT12* for 1ES 0229+200, being as large as 10 TeV in both sources. However, IC peak energies from the physical SSC models are lower than for the log-parabola fit in all cases, with the exception of *XRT5*, which in the SSC modelling shows $E^{\rm IC}_{\rm peak} \simeq 6.5$. This indicates that the VERITAS data dominates the fits derived with the MCMC method, due to better precision when compared to *Fermi*'s data.

Taking the maximum IC emission from the SSC models at face values, we observed peak IC energies in both sources $E^{\rm IC}_{\rm peak} > 1$ TeV, during 1ES 1218+304 flaring states, *VER8* and *VER10*, *VER1* and *XRT5* from 1ES 0229+200.

10.2 The X-ray band and synchrotron peak

An 1 keV peak synchrotron emission puts EHBLs well beyond the standard HBL classification. A log-parabola model provides a good description of the XRT data points in most cases, except for cases of very hard X-ray spectra, which is the case for 1ES 0229+200 *VER1* and *VER4* states. In [160], recalling FF19, the authors showed evidence for a possible extension to the blazar sequence ([10, 11]), where EHBLs may appear as two different populations, based on the frequency and luminosity of the synchrotron peak relative to the *TeV slope*, $S = 2 - \Gamma_{VHE}$. We reproduced the analysis in FF19, and showed our results in Subsection 8.3.2. We observed a transition between the two populations stated in FF19 in both of our sources, with 1ES 1218+304 staying predominantly in a soft, less extreme state, only crossing over during its first flare (*VER8*), while 1ES 0229+200 is observed to transit equally between states.

[160]: Foffano et al. (2019), "A new hard X-ray-selected sample of extreme high-energy peaked BL Lac objects and their TeV gamma-ray properties"

[10]: Ghisellini et al. (2017), "The Fermi blazar sequence"

[11]: Fossati et al. (1998), "A unifying view of the spectral energy distributions of blazars"

We also observed a large discrepancy between the values found with a simple log-parabola fit of the synchrotron peak, when compared to the values obtained with the SSC model, but that is due to the lack of additional data covering the X-ray range of 10 - 150 keV. The most straightforward solution to this issue is to include data from hard X-ray instruments, such as the Burst Alert Telescope (BAT) [101], which will be done in a future work.

[101]: Barthelmy et al. (2005), "The burst alert telescope (BAT) on the SWIFT Midex mission"

10.3 Broadband SED modelling

We apply a MCMC sampling technique to sample the posteriori likelihood distribution of the parameters of an one-zone leptonic SSC model, when describing MWL data from our EHBLs. We tried to avoid mixing of different source states, which can happen when using very large data integration periods. We rely on a Bayesian blocks algorithm to detect

1ES 1218+304			
	γ_{min}	δ_D	k_{eq}
VER5	71^{+1100}_{-67}	23^{+2}_{-2}	40
VER6	8700^{+900}	$10.9^{+1.9}_{-0.8}$	2
VER8	52^{+620}_{-49}	87^{+9}_{-12}	1×10^4
VER10	24^{+140}_{-21}	57^{+13}_{-9}	9×10^3
Archambault et al. (2014) [45]	~ 1	38	3×10^{-3}
Costamante et al. (2018) [38]	100	50	4.5×10^3

Table 10.1: Minimum Lorentz factors, Doppler factors and equipartition parameters from this work and the literature.

Table 10.2: 1ES 0229+200 min. Lorentz, Doppler factor and equipartition parameter from the literature.

	1ES 0229+200		
	γ_{min}	δ_D	k_{eq}
VER1	70^{+2000}_{-70}	49^{+10}_{-10}	3×10^4
XRT4	1331^{+5000}_{-1000}	30^{+7}_{-3}	150
XRT5	283^{+7000}_{-280}	24^{+10}_{-10}	80
XRT12	416^{+8000}_{-400}	12^{+10}_{-3}	11
Tavechio et al. (2009) [32]			
Model 1	10^4	50	$\sim 1.09 \times 10^8$
Model 2	8.5×10^5	30	$\sim 7.43 \times 10^{-1}$
Model 3	5×10^5	50	$\sim 2.24 \times 10^{-1}$
Aliu et al. (2014) [43]	10^4	53-100	2×10^4 - 10^5
Costamante et al. (2018) - Model *a* [38]	100	50	1.7×10^5
Costamante et al. (2018) - Model *b* [38]	2×10^4	50	2.0×10^4

changes in the lightcurves built from *Swift*-XRT, *Fermi*-LAT and VERITAS data. These changes define blocks of constant energy flux with a confidence level of 3σ. We observed that despite a large degeneracy in the position, we obtained a good sampling of the *a posteriori* likelihood distributions of the parameters of the SSC model.

We summarise in Table 10.1 and Table 10.2 the values found in this work and in the literature for γ_{min}, δ_D and k_{eq}.

In contrast to the present literature, the description of the model of the different periods of data **does not always require conditions heavily out of equipartition** ($k_{eq} \gg 1$).

We do observe large Doppler factors during some periods of data from both sources. The Doppler factors ($\gtrsim 50$) in 1ES 1218+304 flaring states *VER8* and *VER10*, are 87 and 57 respectively. During 1ES 1218+304 non-flaring periods, *VER5* and *VER6*, lower Doppler factors are observed, of 23 and 10.9 respectively.

1ES 0229+200 shows its largest Doppler factor of ~ 50 during its only period of elevated VHE emission, *VER1*.

A strong anticorrelation is always observed between Doppler factors and magnetic field strength from the corner plots in Figures B.1 and B.2. Assuming a steady jet viewing angle, increased Doppler factors imply larger bulk Lorentz factors of the acceleration region. At the same time, the number of leptons, as seen by the normalisation parameter K, shows a positive correlation with the magnetisation level. Together, these facts could suggest a decrease in the accretion rate during elevated VHE emission periods, which is consistent with the scenario proposed in [165, 166], due to the increased transference of angular momentum to the black

[165]: D'Elia et al. (2001), "The Connection between BL Lacs and Flat-Spectrum Radio Quasars"
[166]: Cavaliere et al. (1999), "The Evolution of the BL Lacertae Objects"

hole by the accretede particles.

With respect to the minimum Lorentz factor of the accelerated particles, large values of $\gamma_{min} \gg 1$ are also observed. However, the values of γ_{min} in both sources, for all time periods, are found to be consistent with 1 with $\sim 1\sigma$ confidence, as derived from the MCMC samples. From these results, we can expect that with the current energy coverage provided by the data, γ_{min} does not provide good constraining power.

10.3.1 The necessity of better time-resolved SED data

In this thesis, we showed a considerable discrepancy between our modelling of the broadband 1ES 1218+304 and 1ES 0229+200 SEDs, to the ones available in the literature, as highlighted in Table 10.1 and Table 10.2. Our approach was to select periods where flux and spectral variability is not observed in the different energy ranges. This is done in an attempt to minimise the use of large integration windows of data. This approach is most likely responsible for the observed discrepancies between the results shown here and the literature, and could change the current paradigm on EHBLs as a source class. The main downside is the reduced statistics available for short windows of time. More studies are required for a better understanding of the so-called extreme behaviour in a low-statistics regime (in the available gamma ray data), as is the case of 1ES 0229+200, for instance.

One hopeful perspective is the finalisation of the next generation IACT array, the Cherenkov Telescope Array (CTA)[106]. The sensitivity of CTA in the *Alpha* configuration is estimated to improve the sensitivity of current-generation IACTs in at least one order of magnitude [107].

[106]: Acharya et al. (2013), "Introducing the CTA concept"

[107]: Zanin et al. (2021), "CTA – the World's largest ground-based gamma-ray observatory"

10.4 Summary and outlook

We faced the challenging task of analysing and modelling long-term MWL data of two EHBL objects, 1ES 1218+304 and 1ES 0229+200, where we found evidence of **nonpersistent extreme behaviour** of these sources. With this work, we tried to establish a standard framework for the analysis and modelling of variable sources. Any further analysis on the extreme behaviour of HBLs should factor in the temporal dependence of the models and the data.

The inclusion of multi-instrument data, such as current VHE gamma-ray data from the H.E.S.S. and MAGIC collaborations, and also in other wavelengths such as *Swift*-BAT is highly incentivized, as it is necessary to improve the statistics in the VHE gamma-ray range, and to improve energy coverage.

Appendix

A

Bayesian blocks

In this chapter, we present a brief discussion on the effects of the lightcurve time binning and false-positive rates set for Bayesian block detection, and the complete results of the Bayesian block detection in Tables A.1 and A.2.

A.1 1ES 1218+304

With the Bayesian blocks detected from the 1ES 1218+304 VERITAS lightcurve, we calculated the distribution of *energy flux density*, shown in Figure A.1. The energy flux density per block is the ratio between the energy flux of the block and the block length.

With regard to the different time bins, the impact on the energy flux density is easily observed from the left panel in Figure A.1, the most impact being in the extreme cases of the weekly and 6-monthly bins.

With regard to the different false positive rates, increasing the threshold starting from 3σ will not cause any difference in the number of detected change points.

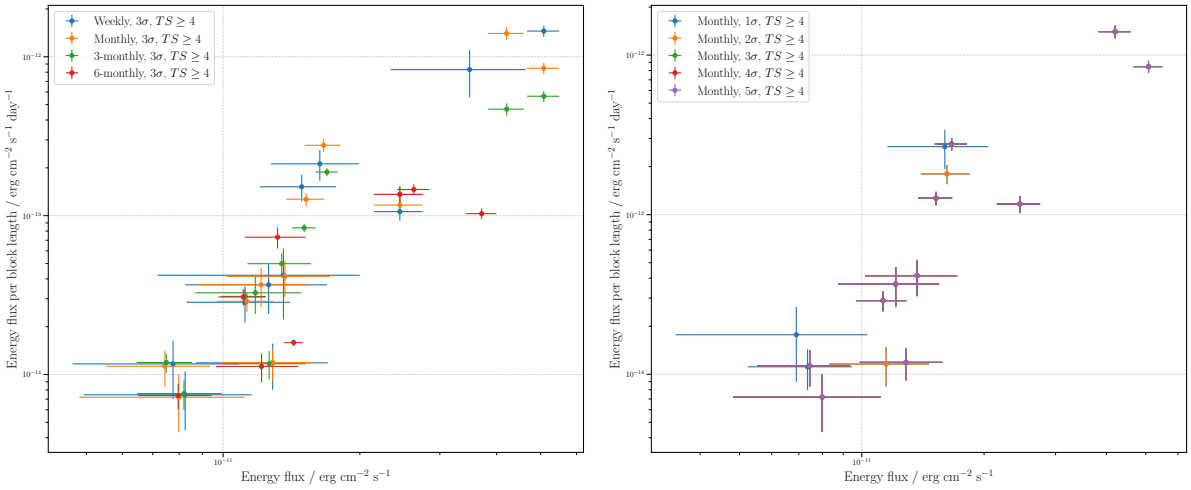

Figure A.1: Energy flux per block length for different time bins (left) and Bayesian block detection confidence level (right)

Table A.1: 1ES 1218+304 Bayesian block edges, average energy flux of the block and standard deviation, with a false positive rate threshold of 3σ. We used the monthly binned VERITAS, monthly binned *Fermi*-LAT and binned per observation *Swift*-XRT lightcurves.

Block edges / MJD	Average energy flux / $10^{11} \times \mathrm{erg cm^{-2} s^{-1}}$	Standard deviation / $10^{11} \times \mathrm{erg cm^{-2} s^{-1}}$
	VERITAS	
54832.000766018515	2.666	0.242
54892.000766018515	1.193	0.307
55552.000766018515	2.440	0.234
55672.000766018515	1.807	0.256
56062.000766018515	3.924	0.479
56272.000766018515	1.279	0.507
57382.000766018515	2.059	0.475
58462.000766018515	6.740	0.607
58492.000766018515	2.192	0.560
58822.000766018515	8.139	0.660
58882.000766018515	1.943	0.542
59212.000766018515	1.325	0.558
	Fermi-LAT	
54831.99476851852	5.394	3.656
57864.80034625772	9.624	4.456
58952.65452088156	6.523	4.503
59546.029525221835	7.360	3.815
	Swift-XRT	
53802.11644396406	2.255	0.072
53875.79061344373	4.628	0.271
56006.29110391572	5.627	0.184
56012.75684119454	7.377	0.210
56041.23115067291	14.308	0.264
56066.87802668577	11.796	0.124
56298.4624066444	5.704	0.169
56306.480767029665	4.699	0.154
56366.31743992196	6.012	0.184
56387.27981551794	4.385	0.141
56416.19595351113	5.339	0.160
56419.20023712074	3.904	0.134
56695.428193919004	7.718	0.460
56769.25194651218	6.027	0.186
56777.182422689235	4.552	0.149
56799.243996753095	3.513	0.140
56802.18201130763	5.087	0.172

Block edges / MJD	Average energy flux / $10^{11} \times \mathrm{erg cm^{-2} s^{-1}}$	Standard deviation / $10^{11} \times \mathrm{erg cm^{-2} s^{-1}}$
56806.18147456323	6.770	0.208
57040.41167931146	3.331	0.143
57043.41578109429	5.562	0.188
57067.36820963676	4.144	0.161
57075.420869862566	5.311	0.215
57079.41431027546	2.124	0.124
57095.28182461415	4.214	0.446
57107.36150705077	2.489	0.132
57132.31784572912	4.471	0.162
57161.19067519856	2.636	0.164
57349.8084737719	3.376	0.238
57455.36818979964	6.374	0.423
57470.86674498277	5.204	0.315
57473.776644010184	2.637	0.140
57479.29920306989	1.479	0.109
57491.34098672177	3.636	0.235
57507.21242523696	1.480	0.115
57512.26872031638	5.095	0.340
57517.250918158905	2.158	0.133
57750.49149848258	5.221	0.345
57760.4561997349	7.007	0.437
57778.391716925	3.494	0.215
57806.36778435511	2.578	0.179
57860.179205716864	3.451	0.247
57897.18024359911	11.316	0.803
57902.03100778146	7.587	0.177
57908.27948744692	4.203	0.259
58213.1638760359	8.530	0.561
58482.15283703031	17.408	1.881
58489.0629149122	24.053	1.719
58491.163458176095	15.706	0.207
58493.15123057014	10.205	0.160
58497.15439718083	12.078	0.162
58499.12948728668	18.940	0.215
58501.18815823958	14.858	0.203
58629.96145609821	6.173	0.573
58853.19176375043	12.485	0.819
58978.48127310091	5.188	0.115
58982.46325104621	3.953	0.095
58984.27797560886	5.797	0.189
58988.65246475755	7.416	0.212
58996.41618770344	4.538	0.129
59005.24473350234	3.441	0.159
59005.24473350234	3.441	0.159

A.2 1ES 0229+200

We repeat the conclusions from the previous section for 1ES 0229+200 Bayesian blocks. The main difference is that, regardless of the false positive rate threshold and time binning used, there are always two blocks detected in the 1ES 0229+200 VERITAS lightcurve (1 change point detection), as observed in Figure A.2.

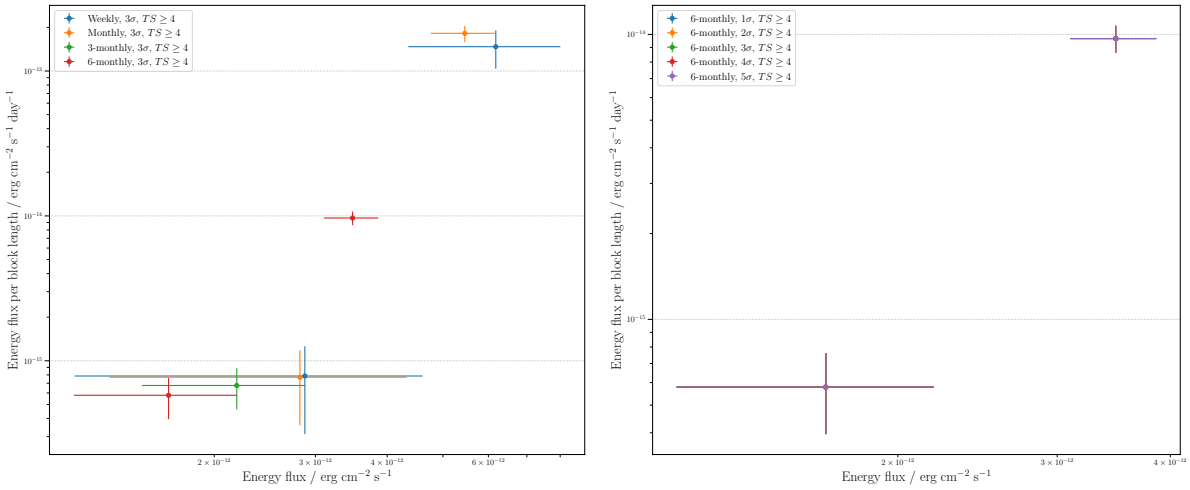

Figure A.2: Energy flux per block length for different time bins (left) and Bayesian block detection confidence level (right)

Table A.2: 1ES 0229+200 Bayesian block edges, average energy flux of the block and standard deviation, with a false positive rate threshold of 3σ. We used the monthly binned VERITAS, monthly binned *Fermi*-LAT and binned per observation *Swift*-XRT lightcurves.

Block edges / MJD	Average energy flux / $10^{12} \times \mathrm{erg cm^{-2} s^{-1}}$	Standard deviation / $10^{12} \times \mathrm{erg cm^{-2} s^{-1}}$
	VERITAS	
55102.000766018515	8.745	1.115
55132.000766018515	4.517	2.410
58792.000766018515	10.762	5.937
	Fermi-LAT	
54831.99476851852	5.883	4.511
59183.41146701388	7.128	3.733
	Swift-XRT	
54685.99274540583	18.226	0.638
55117.29970304767	23.152	1.466
55152.243554871144	31.555	1.585
56217.4167364049	28.050	1.389
56305.11306869923	38.639	2.478
56576.03380905808	32.957	1.161
56654.12175287057	23.354	2.208
56656.11133597016	33.427	1.536
56921.30022592487	12.099	1.255
56954.21315073105	16.476	1.205
57336.2111969181	20.291	1.146
57419.12359401362	13.178	1.061
58016.39545404795	16.662	1.354
58400.30530259944	23.813	1.621
58450.83223047982	19.650	1.202
59133.1476155265	15.325	1.545
59414.674073209535	11.696	0.741
59440.0909688404	14.154	0.869

B

MCMC corner and trace plots

B.1 1ES 1218+304

1ES 1218+304 complete traces and corner plots from each block. The numbers of burnt-in runs on the traces, used to produce the corner plots, are 1000, 1500, 1000, and 1200 in Figures B.1, B.2, B.3, and B.4, respectively.

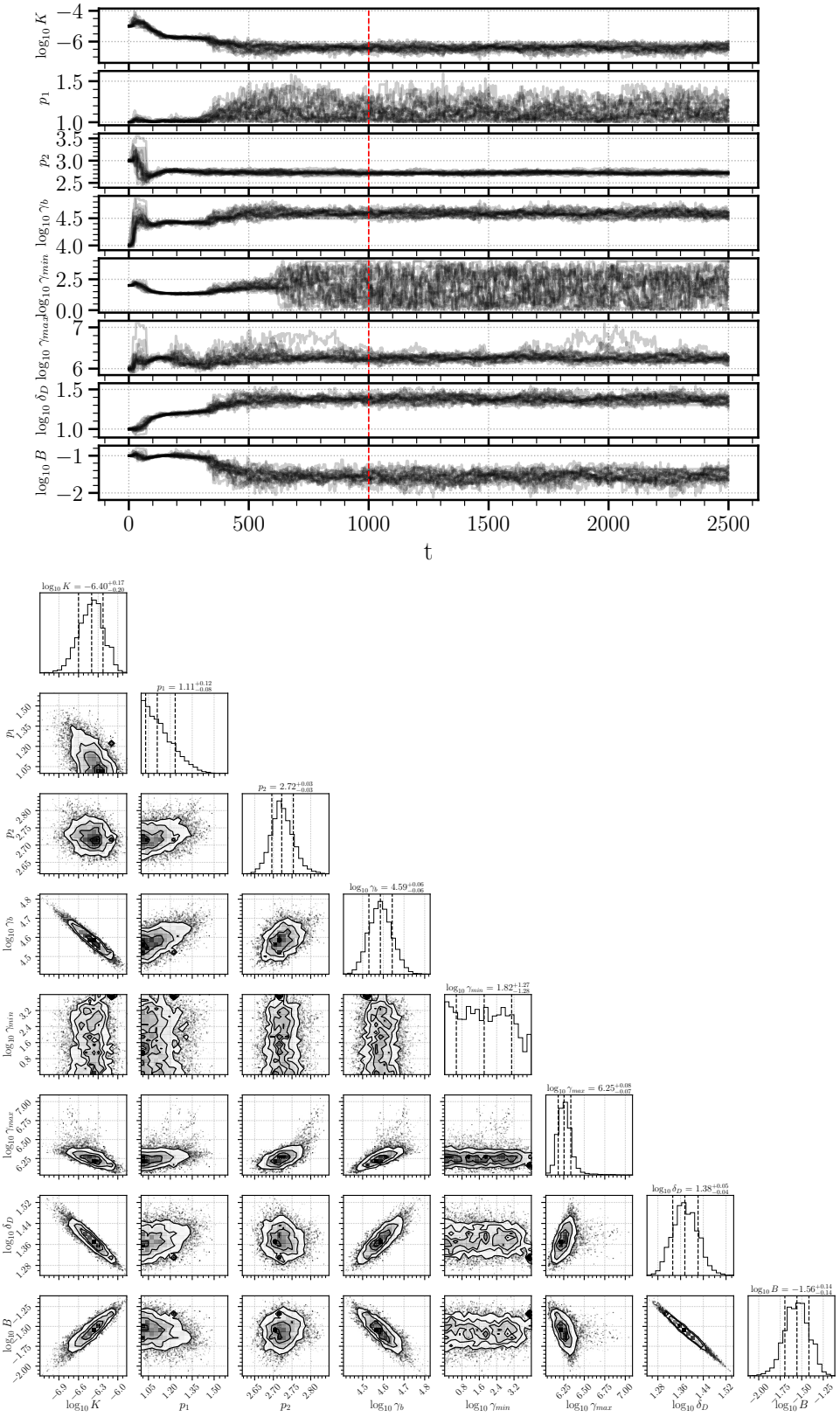

Figure B.1: *VER5* MCMC trace (top) and corner plot (bottom)

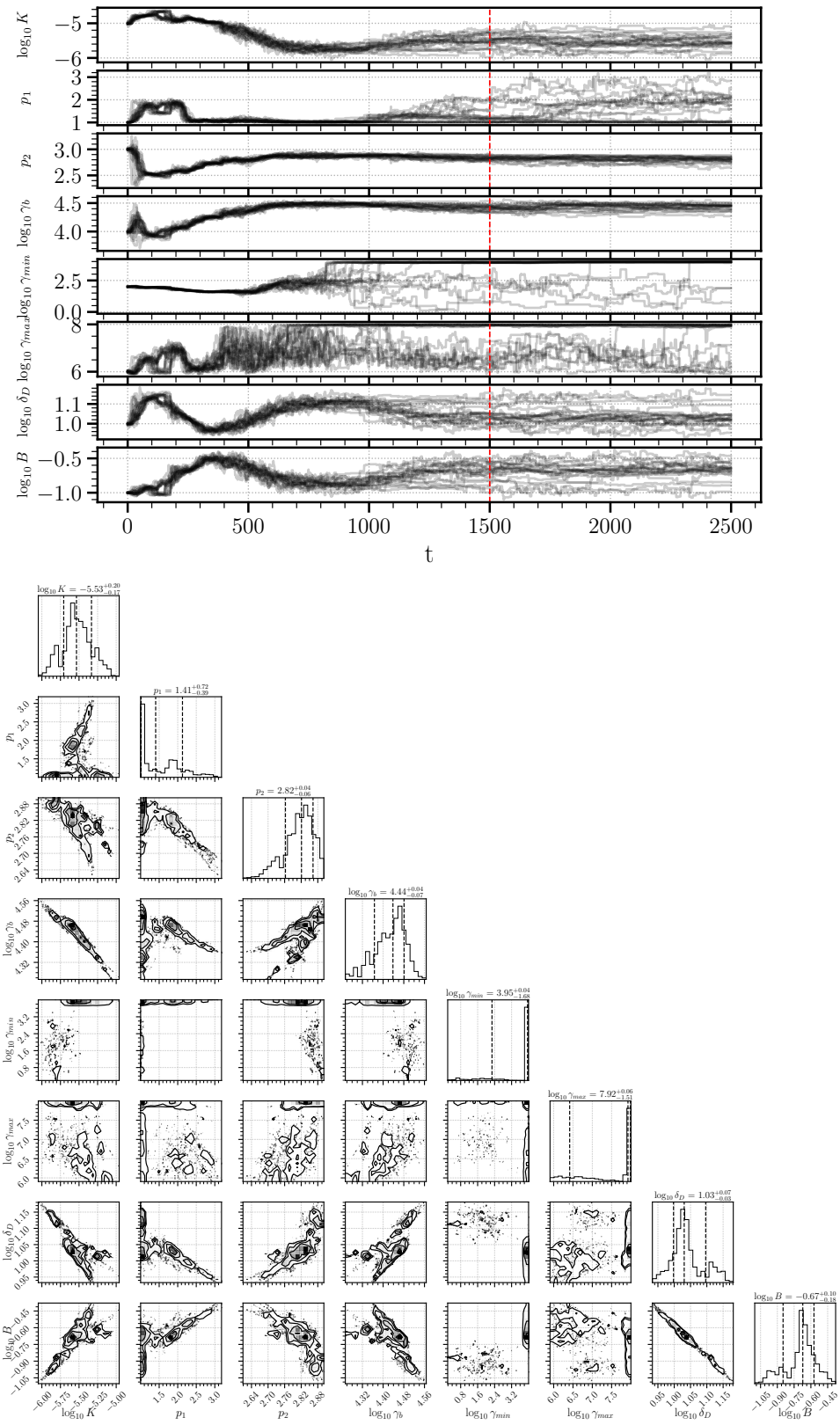

Figure B.2: *VER6* MCMC trace (top) and corner plot (bottom)

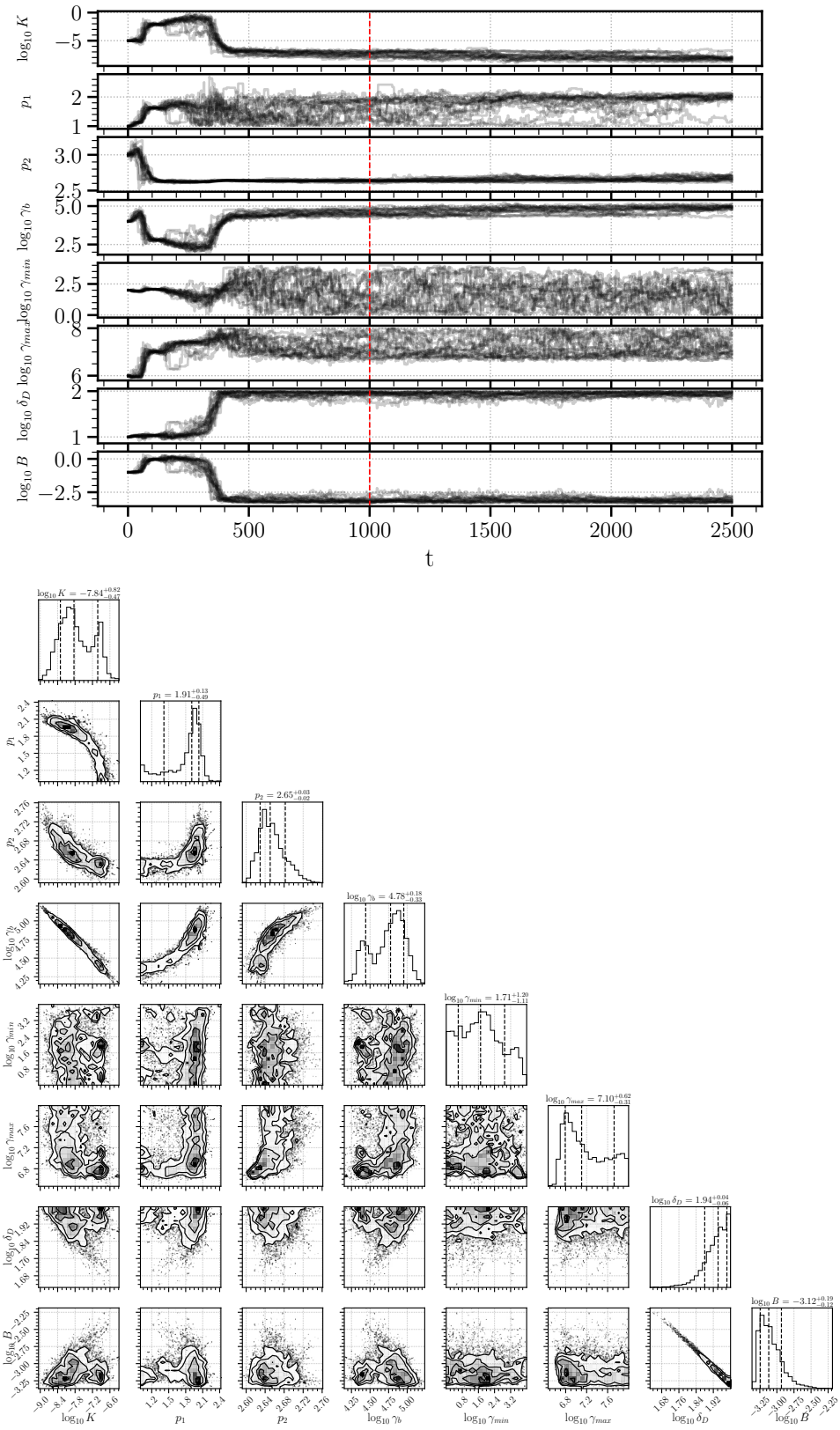

Figure B.3: *VER8* MCMC trace (top) and corner plot (bottom)

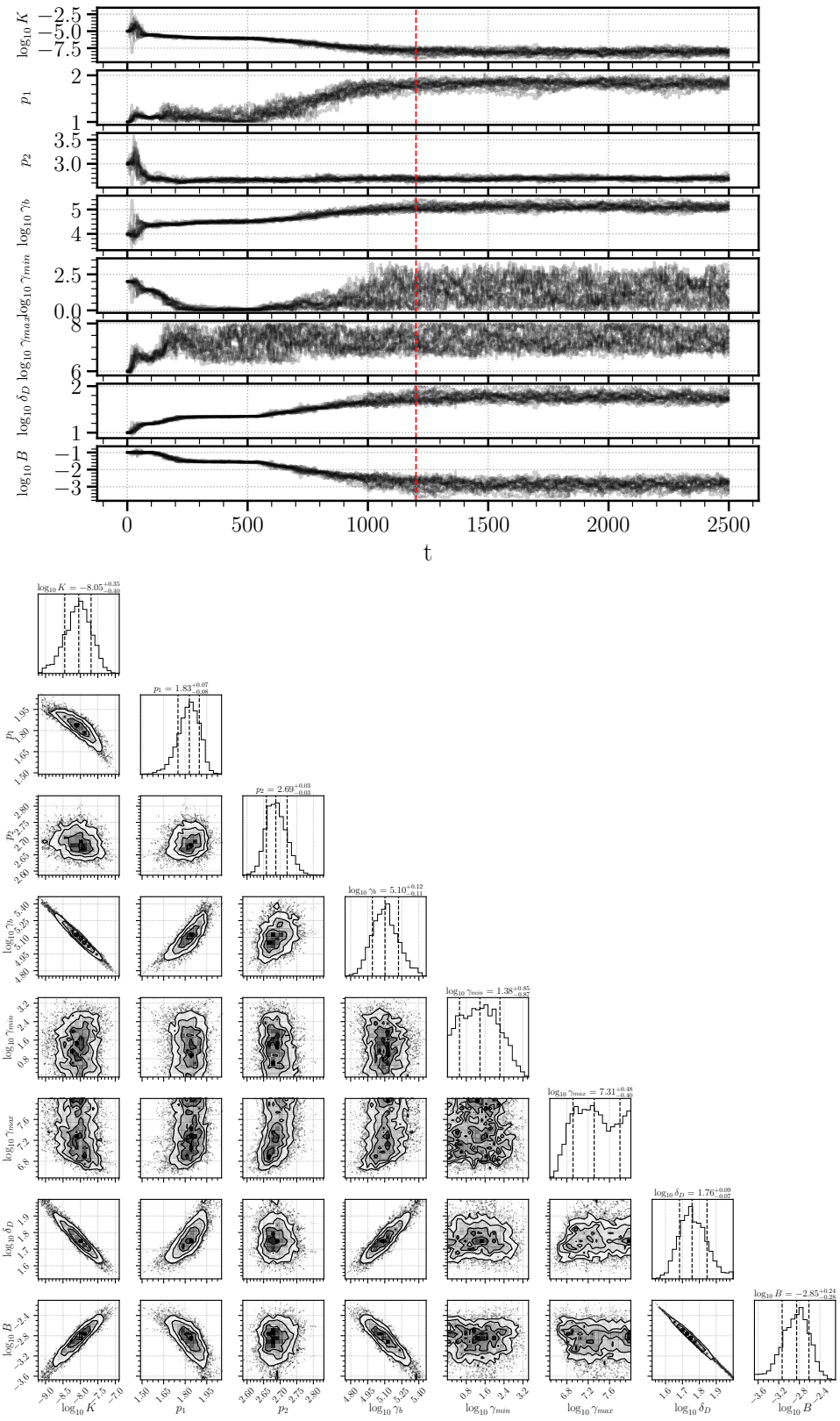

Figure B.4: *VER10* MCMC trace (top) and corner plot (bottom)

B.2 1ES 0229+200

1ES 0229+200 complete traces and corner plots from each block. The numbers of burnt-in runs on the traces, used to produce the corner plots, are 1000, 1500, 1000, and 1000 in Figures B.1, B.2, B.3, and B.4, respectively.

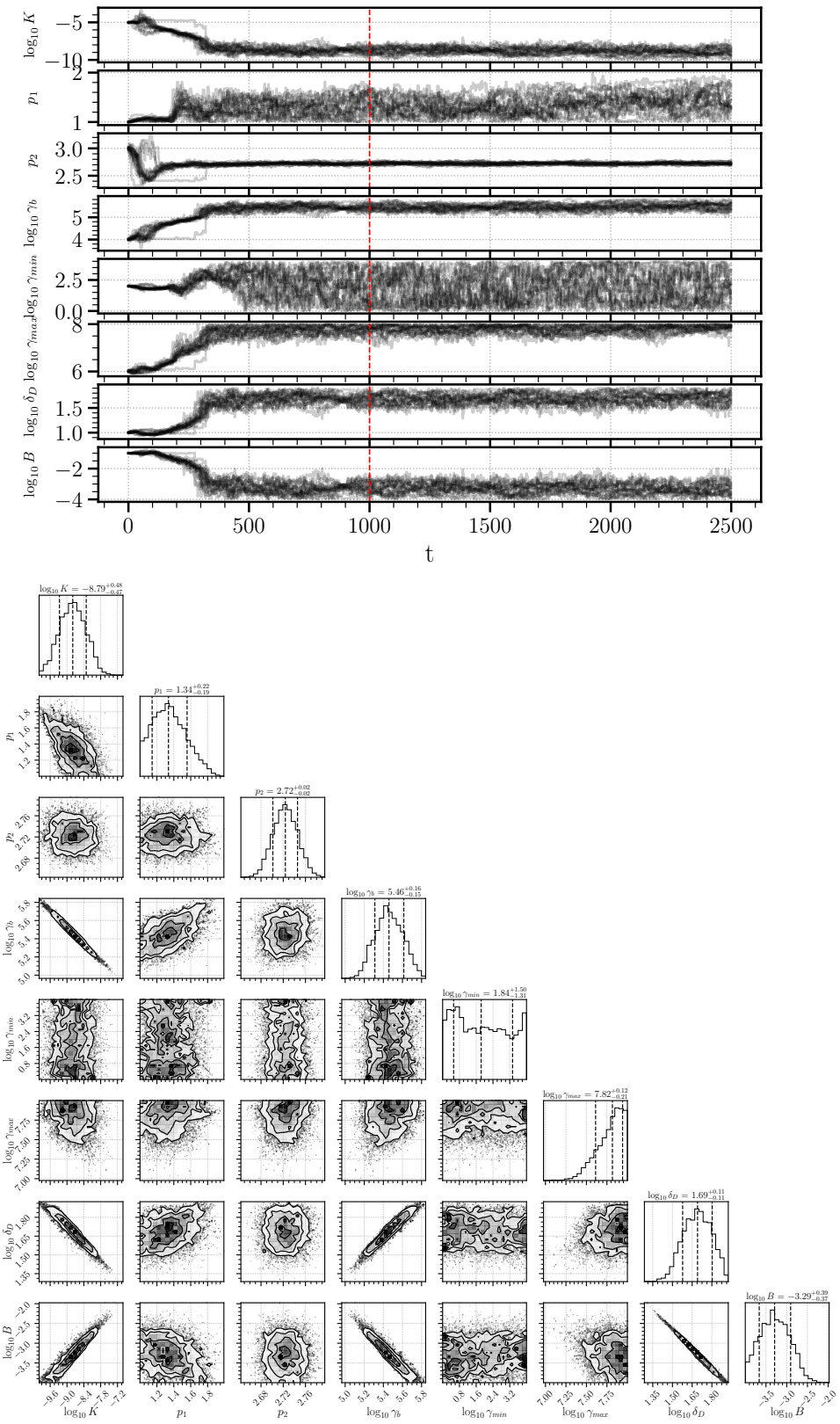

Figure B.5: *VER1* MCMC trace (top) and corner plot (bottom)

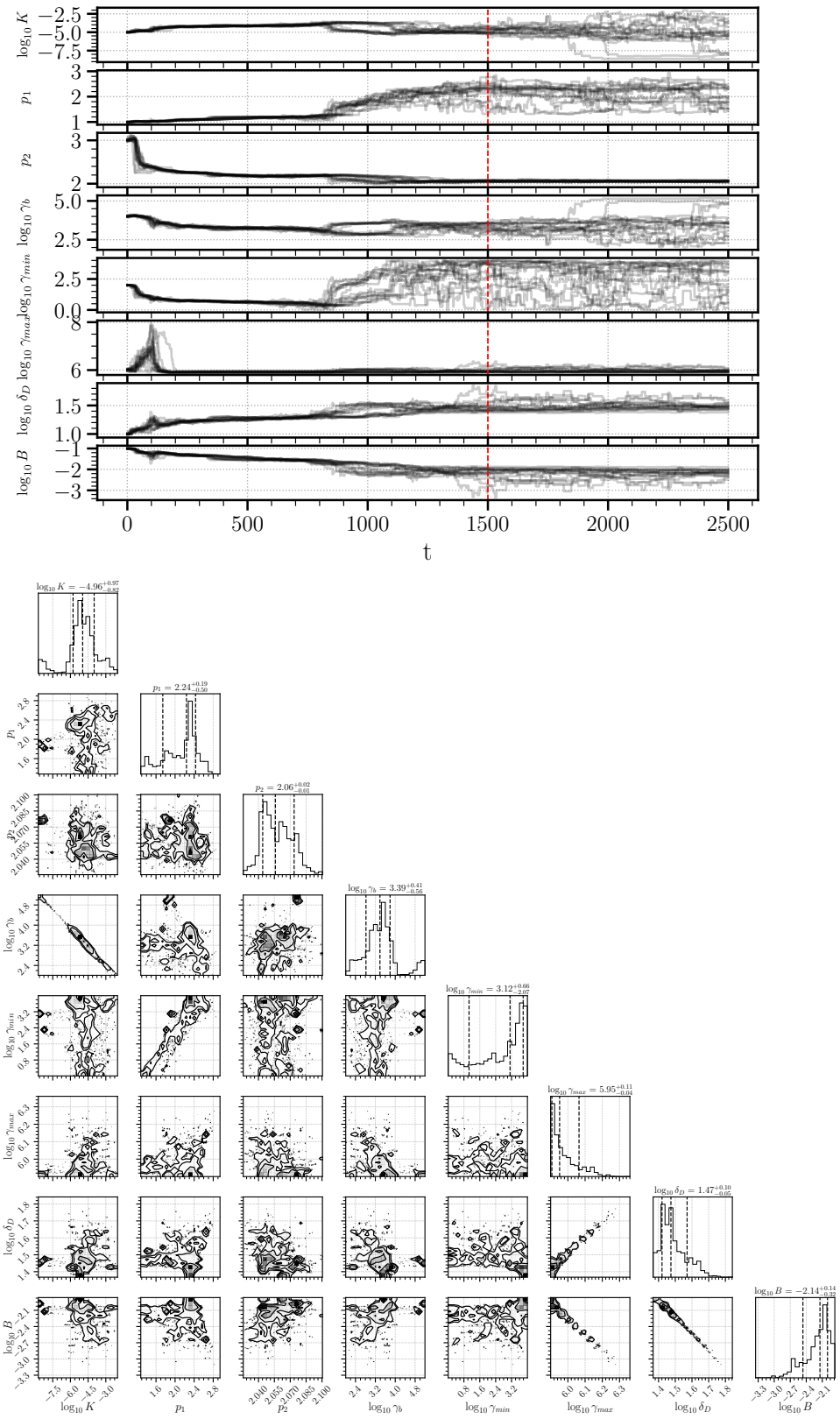

Figure B.6: *XRT4* MCMC trace (top) and corner plot (bottom)

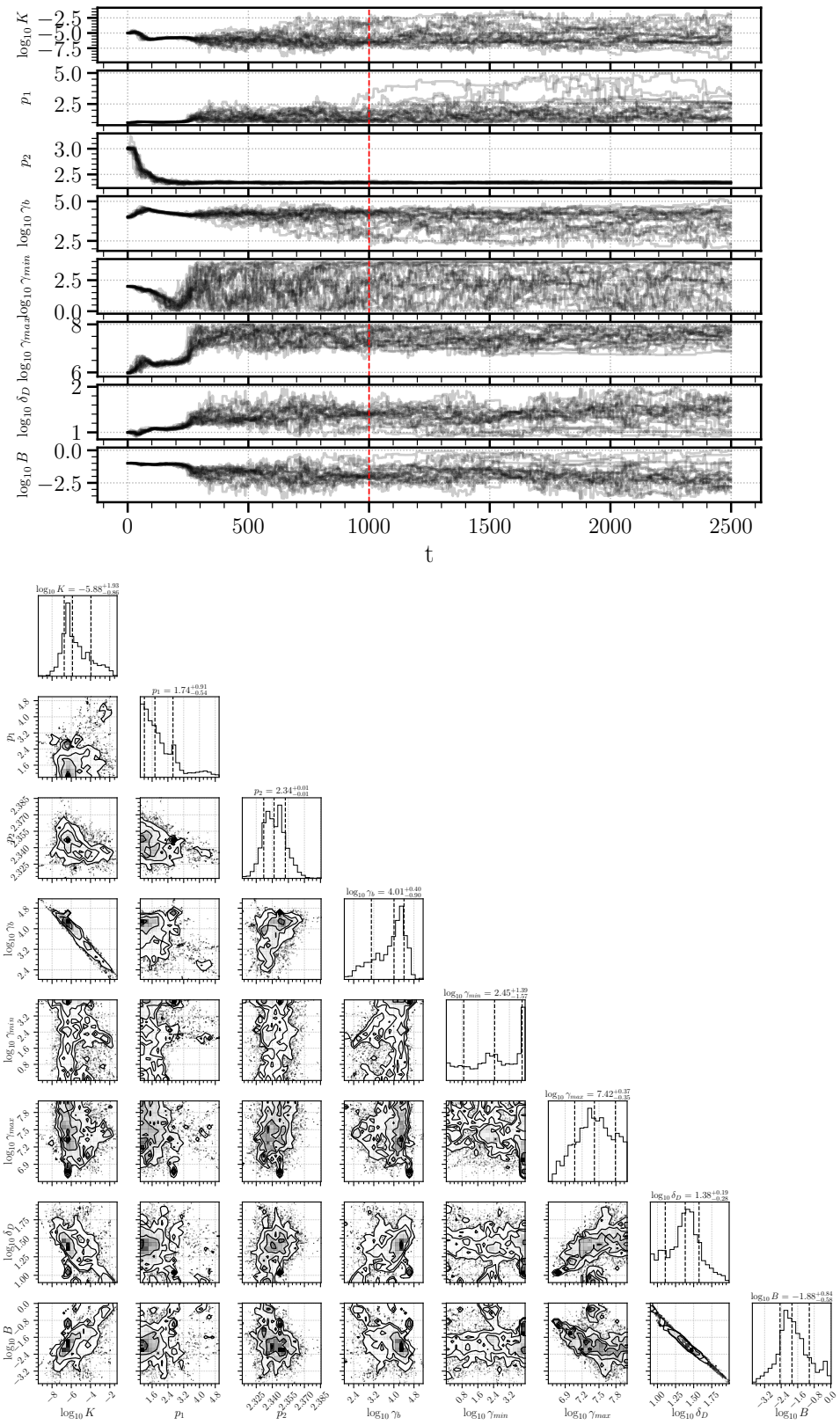

Figure B.7: *XRT5* MCMC trace (top) and corner plot (bottom)

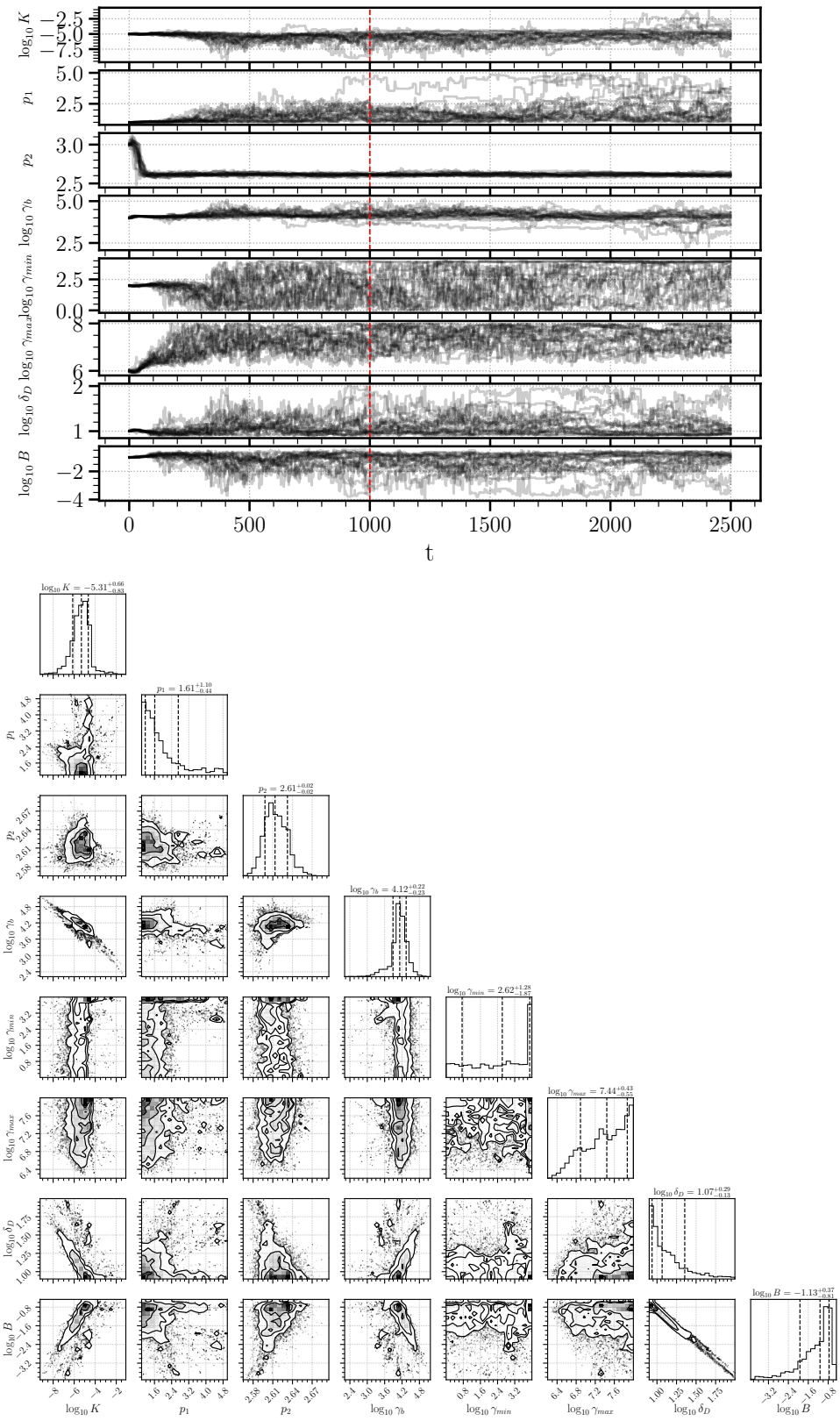

Figure B.8: *XRT12* MCMC trace (top) and corner plot (bottom)

Bibliography

Here are the references in citation order.

[1] Volker Beckmann and Chris R. Shrader. *The AGN phenomenon: open issues*. Feb. 2013. DOI: 10.48550/arXiv.1302.1397. URL: http://arxiv.org/abs/1302.1397 (cited on page 2).

[2] Volker Beckmann and Chris R. Shrader. *Active galactic nuclei*. Aug. 2012 (cited on pages 2, 5).

[3] P. Padovani et al. "Active galactic nuclei: what's in a name?" In: *The Astronomy and Astrophysics Review* 25.1 (Aug. 2017), p. 2. DOI: 10.1007/s00159-017-0102-9 (cited on pages 2, 3, 7).

[4] E. Massaro et al. "Roma-BZCAT: a multifrequency catalogue of blazars." en. In: *Astronomy & Astrophysics* 495.2 (Feb. 2009), pp. 691–696. DOI: 10.1051/0004-6361:200810161 (cited on pages 5, 6).

[5] Jonathan Biteau and Manuel Meyer. "Gamma-ray cosmology and tests of fundamental physics." In: *Galaxies* 10.2 (2022). DOI: 10.3390/galaxies10020039 (cited on pages 6, 12, 13).

[6] P. Giommi et al. "A simplified view of blazars: clearing the fog around long-standing selection effects." In: *Monthly Notices of the Royal Astronomical Society* 420.4 (Mar. 2012), pp. 2899–2911. DOI: 10.1111/j.1365-2966.2011.20044.x (cited on pages 6, 9).

[7] S. P. Wakely and D. Horan. "TeVCat: An online catalog for very high energy gamma-ray astronomy." In: *International Cosmic Ray Conference*. Vol. 3. International Cosmic Ray Conference. Jan. 2008, pp. 1341–1344 (cited on page 6).

[8] M. Ackermann et al. "The third catalog of active galactic nuclei detected by the Fermi large area telescope." en. In: *The Astrophysical Journal* 810.1 (Aug. 2015), p. 14. DOI: 10.1088/0004-637X/810/1/14 (cited on page 6).

[9] W. B. Atwood et al. "The large area telescope on the Fermi gamma-ray space telescope mission." In: *The Astrophysical Journal* 697.2 (May 2009), p. 1071. DOI: 10.1088/0004-637X/697/2/1071 (cited on pages 6, 41).

[10] G. Ghisellini et al. "The Fermi blazar sequence." In: *Monthly Notices of the Royal Astronomical Society* 469.1 (Apr. 2017), pp. 255–266. DOI: 10.1093/mnras/stx806 (cited on pages 7, 8, 127).

[11] G. Fossati et al. "A unifying view of the spectral energy distributions of blazars." In: *Monthly Notices of the Royal Astronomical Society* 299.2 (Sept. 1998), pp. 433–448. DOI: 10.1046/j.1365-8711.1998.01828.x (cited on pages 7, 8, 127).

[12] M. Böttcher and C. D. Dermer. "An evolutionary scenario for blazar unification." In: *The Astrophysical Journal* 564.1 (Jan. 2002), p. 86. DOI: 10.1086/324134 (cited on page 8).

[13] Charles D. Dermer and Govind Menon. *High energy radiation from black holes: gamma rays, cosmic rays, and neutrinos*. 2009 (cited on pages 8, 13, 17, 20, 25, 26, 111).

[14] Eileen T. Meyer et al. "From the blazar sequence to the blazar envelope: Revisiting the relativistic jet dichotomy in radio-loud active galactic nuclei." en. In: *The Astrophysical Journal* 740.2 (Oct. 2011), p. 98. DOI: 10.1088/0004-637X/740/2/98 (cited on page 8).

[15] Marie-Helene Ulrich, Laura Maraschi, and C. Megan Urry. "Variability of active galactic nuclei." In: *Annual Review of Astronomy and Astrophysics* 35.1 (1997), pp. 445–502. DOI: 10.1146/annurev.astro.35.1.445 (cited on page 9).

[16] F. Aharonian et al. "An exceptional very high energy gamma-ray flare of PKS 2155–304." In: *The Astrophysical Journal* 664.2 (July 2007), p. L71. DOI: 10.1086/520635 (cited on page 9).

[17] J. Albert et al. "Variable very high energy γ-ray emission from Markarian 501." In: *The Astrophysical Journal* 669.2 (Nov. 2007), p. 862. DOI: 10.1086/521382 (cited on page 9).

[18] M. Böttcher and C. D. Dermer. "Timing signatures of the internal-shock model for blazars." In: *The Astrophysical Journal* 711.1 (Feb. 2010), p. 445. DOI: 10.1088/0004-637X/711/1/445 (cited on page 9).

[19] Fan Guo et al. "Efficient production of high-energy nonthermal particles during magnetic reconnection in a magnetically dominated ion-electron plasma." In: *The Astrophysical Journal Letters* 818.1 (Feb. 2016), p. L9. DOI: 10.3847/2041-8205/818/1/L9 (cited on pages 9, 126).

[20] Boella, G. et al. "BeppoSAX, the wide band mission for X-ray astronomy." In: *Astron. Astrophys. Suppl. Ser.* 122.2 (1997), pp. 299–307. DOI: 10.1051/aas:1997136 (cited on page 9).

[21] Elena Pian et al. "BeppoSAX observations of unprecedented synchrotron activity in the BL Lacertae object Markarian 501." In: *The Astrophysical Journal* 492.1 (Nov. 1997), p. L17. DOI: 10.1086/311083 (cited on page 9).

[22] Costamante, L. et al. "Extreme synchrotron BL Lac objects - Stretching the blazar sequence." In: *A&A* 371.2 (2001), pp. 512–526. DOI: 10.1051/0004-6361:20010412 (cited on page 9).

[23] Costamante, L. and Ghisellini, G. "TeV candidate BL Lac objects." In: *Astronomy & Astrophysics* 384.1 (2002), pp. 56–71. DOI: 10.1051/0004-6361:20011749 (cited on page 9).

[24] T. C. Weekes et al. "VERITAS: the very energetic radiation imaging telescope array system." In: *Astroparticle Physics* 17.2 (2002), pp. 221–243. DOI: https://doi.org/10.1016/S0927-6505(01)00152-9 (cited on pages 9, 36, 49, 50).

[25] Wystan Benbow and H. E. S. S. Collaboration. "The status and performance of H.E.S.S." In: *AIP Conference Proceedings* 745.1 (Feb. 2005), pp. 611–616. DOI: 10.1063/1.1878471 (cited on page 9).

[26] Eckart Lorenz. "Status of the 17 m ∅ MAGIC telescope." In: *New Astronomy Reviews* 48.5 (2004), pp. 339–344. DOI: https://doi.org/10.1016/j.newar.2003.12.059 (cited on page 9).

[27] Chang, Y.-L. et al. "The 3HSP catalogue of extreme and high-synchrotron peaked blazars." In: *Astronomy & Astrophysics* 632 (2019), A77. DOI: 10.1051/0004-6361/201834526 (cited on page 10).

[28] Arsioli, B. et al. "1WHSP: An IR-based sample of 1000 VHE blazar candidates." In: *A&A* 579 (2015), A34. DOI: 10.1051/0004-6361/201424148 (cited on page 10).

[29] Chang, Y.-L. et al. "2WHSP: A multi-frequency selected catalogue of high energy and very high energy blazars and blazar candidates." In: *A&A* 598 (2017), A17. DOI: 10.1051/0004-6361/201629487 (cited on page 10).

[30] J. Biteau et al. "Progress in unveiling extreme particle acceleration in persistent astrophysical jets." In: *Nature Astronomy* 4.2 (Feb. 2020), pp. 124–131. DOI: 10.1038/s41550-019-0988-4 (cited on pages 10, 12, 99, 105, 125, 126).

[31] L. Maraschi, G. Ghisellini, and A. Celotti. "A jet model for the gamma-ray–emitting Blazar 3C 279." In: *The Astrophysical Journal Letters* 397 (Sept. 1992), p. L5. DOI: 10.1086/186531 (cited on page 11).

[32] F. Tavecchio et al. "The hard TeV spectrum of 1ES 0229+200: new clues from Swift." In: *Monthly Notices of the Royal Astronomical Society: Letters* 399.1 (Oct. 2009), pp. L59–L63. DOI: 10.1111/j.1745-3933.2009.00724.x (cited on pages 11, 128).

[33] Charles D. Dermer and Reinhard Schlickeiser. "Model for the high-energy emission from blazars." In: *The Astrophysical Journal* 416 (Oct. 1993), p. 458. DOI: 10.1086/173251 (cited on page 11).

[34] Marek Sikora, Mitchell C. Begelman, and Martin J. Rees. "Comptonization of diffuse ambient radiation by a relativistic jet: The source of gamma rays from blazars?" In: *The Astrophysical Journal* 421 (Jan. 1994), p. 153. DOI: 10.1086/173633 (cited on page 11).

[35] M. Błażejowski et al. "Comptonization of infrared radiation from hot dust by relativistic jets in quasars." In: *The Astrophysical Journal* 545.1 (Dec. 2000), p. 107. DOI: 10.1086/317791 (cited on page 11).

[36] M. Böttcher et al. "Leptonic and hadronic modeling of Fermi-detected blazars." In: *The Astrophysical Journal* 768.1 (Apr. 2013), p. 54. DOI: 10.1088/0004-637X/768/1/54 (cited on page 11).

[37] Anton Prosekin et al. "Time structure of gamma-ray signals generated in line-of-sight interactions of cosmic rays from distant blazars." In: *The Astrophysical Journal* 757.2 (Sept. 2012), p. 183. DOI: 10.1088/0004-637X/757/2/183 (cited on page 11).

[38] L Costamante et al. "The NuSTAR view on hard-TeV BL Lacs." In: *Monthly Notices of the Royal Astronomical Society* 477.3 (May 2018), pp. 4257–4268. DOI: 10.1093/mnras/sty857 (cited on pages 11, 22, 85, 97, 105, 125, 127, 128).

[39] Aharonian, F. et al. "New constraints on the mid-IR EBL from the HESS discovery of VHE gamma rays from 1ES0229+200." In: *Astronomy & Astrophysics* 475.2 (2007), pp. L9–L13. DOI: 10.1051/0004-6361:20078462 (cited on pages 11, 12, 89, 101, 125).

[40] J. Albert et al. "Discovery of very high energy gamma rays from 1ES 1218+30.4." In: *The Astrophysical Journal* 642.2 (Apr. 2006), p. L119. DOI: 10.1086/504845 (cited on pages 11, 85).

[41] Jamie Holder. "VERITAS: Status and highlights." In: *International Cosmic Ray Conference*. Vol. 11. International Cosmic Ray Conference. Jan. 2011, p. 137. DOI: 10.7529/ICRC2011/V12/H11 (cited on pages 12, 37).

[42] J. Holder et al. "The first VERITAS telescope." In: *Astroparticle Physics* 25.6 (2006), pp. 391–401. DOI: https://doi.org/10.1016/j.astropartphys.2006.04.002 (cited on pages 12, 36).

[43] E. Aliu et al. "A three-year multi-wavelength study of the very-high-energy gamma-ray blazar 1ES 0229+200." In: *The Astrophysical Journal* 782.1 (Jan. 2014), p. 13. DOI: 10.1088/0004-637X/782/1/13 (cited on pages 12, 85, 89, 99, 101, 125, 128).

[44] V. A. Acciari et al. "VERITAS observations of the BL Lac object 1ES 1218+304." In: *The Astrophysical Journal* 695.2 (Apr. 2009), p. 1370. DOI: 10.1088/0004-637X/695/2/1370 (cited on pages 12, 85, 125).

[45] S. Archambault et al. "Test of models of the cosmic infrared background with the multiwavelength of the blazar 1ES 1218+30.4 in 2009." In: *The Astrophysical Journal* 788.2 (June 2014), p. 158. DOI: 10.1088/0004-637X/788/2/158 (cited on pages 12, 85, 99, 100, 125, 127).

[46] Elisa Pueschel and Jonathan Biteau. *Cosmology with very-high-energy gamma rays*. 2021. DOI: 10.48550/ARXIV.2112.05952. URL: https://arxiv.org/abs/2112.05952 (cited on page 12).

[47] Robert J. Gould and Gérard P. Schréder. "Opacity of the universe to high-energy photons." In: *Phys. Rev.* 155.5 (Mar. 1967), pp. 1408–1411. DOI: 10.1103/PhysRev.155.1408 (cited on page 12).

[48] Ryley Hill, Kiyoshi W. Masui, and Douglas Scott. "The Spectrum of the Universe." In: *Applied Spectroscopy* 72.5 (2018), pp. 663–688. DOI: 10.1177/0003702818767133 (cited on pages 12, 28).

[49] A. U. Abeysekara et al. “Measurement of the extragalactic background light spectral energy distribution with VERITAS.” In: *The Astrophysical Journal* 885.2 (Nov. 2019), p. 150. DOI: 10.3847/1538-4357/ab4817 (cited on page 13).

[50] Ruth Durrer and Andrii Neronov. “Cosmological magnetic fields: their generation, evolution and observation.” In: *The Astronomy and Astrophysics Review* 21.1 (June 2013), p. 62. DOI: 10.1007/s00159-013-0062-7 (cited on page 13).

[51] J. V. Jelley. “High-Energy ɣ-Ray Absorption in Space by a 3.5°K Microwave Field.” In: *Phys. Rev. Lett.* 16.11 (Mar. 1966), pp. 479–481. DOI: 10.1103/PhysRevLett.16.479 (cited on page 13).

[52] M. Ackermann et al. “The Search for Spatial Extension in High-latitude Sources Detected by the Fermi Large Area Telescope.” en. In: *The Astrophysical Journal Supplement Series* 237.2 (Aug. 2018), p. 32. DOI: 10.3847/1538-4365/aacdf7 (cited on pages 13, 85).

[53] H. Abdalla et al. “Sensitivity of the Cherenkov telescope array for probing cosmology and fundamental physics with gamma-ray propagation.” In: *Journal of Cosmology and Astroparticle Physics* 2021.02 (Feb. 2021), p. 048. DOI: 10.1088/1475-7516/2021/02/048 (cited on page 13).

[54] Rodrigo Guedes Lang, Humberto Martínez-Huerta, and Vitor de Souza. “Improved limits on Lorentz invariance violation from astrophysical gamma-ray sources.” In: *Phys. Rev. D* 99.4 (Feb. 2019), p. 043015. DOI: 10.1103/PhysRevD.99.043015 (cited on page 13).

[55] Alessandro De Angelis, Giorgio Galanti, and Marco Roncadelli. “Relevance of axionlike particles for very-high-energy astrophysics.” In: *Phys. Rev. D* 84.10 (Nov. 2011), p. 105030. DOI: 10.1103/PhysRevD.84.105030 (cited on page 13).

[56] Alessandro Mirizzi, Georg G. Raffelt, and Pasquale D. Serpico. “Signatures of axionlike particles in the spectra of TeV gamma-ray sources.” In: *Phys. Rev. D* 76.2 (July 2007), p. 023001. DOI: 10.1103/PhysRevD.76.023001 (cited on page 13).

[57] Enrico Fermi. “On the origin of the cosmic radiation.” In: *Phys. Rev.* 75.8 (Apr. 1949), pp. 1169–1174. DOI: 10.1103/PhysRev.75.1169 (cited on page 15).

[58] Giovanni Morlino. “High-energy cosmic rays from supernovae.” en. In: *Handbook of Supernovae*. Ed. by Athem W. Alsabti and Paul Murdin. Cham: Springer International Publishing, 2017, pp. 1711–1736. DOI: 10.1007/978-3-319-21846-5_11 (cited on page 15).

[59] R. D. Blandford and J. P. Ostriker. “Particle acceleration by astrophysical shocks.” In: *The Astrophysical Journal Letters* 221 (Apr. 1978), pp. L29–L32. DOI: 10.1086/182658 (cited on pages 15, 126).

[60] Frank M. Rieger and Peter Duffy. “Shear acceleration in relativistic astrophysical jets.” In: *The Astrophysical Journal* 617.1 (Dec. 2004), p. 155. DOI: 10.1086/425167 (cited on pages 16, 126).

[61] Marek Sikora, Mieszko Rutkowski, and Mitchell C. Begelman. “A spine–sheath model for strong-line blazars.” In: *Monthly Notices of the Royal Astronomical Society* 457.2 (Feb. 2016), pp. 1352–1358. DOI: 10.1093/mnras/stw107 (cited on page 16).

[62] A. Shukla and K. Mannheim. “Gamma-ray flares from relativistic magnetic reconnection in the jet of the quasar 3C 279.” In: *Nature Communications* 11.1 (Aug. 2020), p. 4176. DOI: 10.1038/s41467-020-17912-z (cited on page 16).

[63] Claudio Chiuderi, Paola Pietrini, and Guidetta Torricelli Ciamponi. “Extragalactic jets as current-carrying systems. I. Equilibrium and stability.” In: *The Astrophysical Journal* 339 (Apr. 1989), p. 70. DOI: 10.1086/167276 (cited on page 16).

[64] Giannios, D. and Spruit, H. C. "The role of kink instability in Poynting-flux dominated jets." In: *Astronomy & Astrophysics* 450.3 (2006), pp. 887–898. DOI: 10.1051/0004-6361:20054107 (cited on page 16).

[65] Markus Boettcher, Daniel E. Harris, and Henric Krawczynski. *Relativistic jets from active galactic nuclei.* 2012 (cited on pages 20, 25, 29).

[66] George R. Blumenthal and Robert J. Gould. "Bremsstrahlung, synchrotron radiation, and Compton scattering of high-energy electrons traversing dilute gases." In: *Rev. Mod. Phys.* 42.2 (Apr. 1970), pp. 237–270. DOI: 10.1103/RevModPhys.42.237 (cited on page 22).

[67] George B. Rybicki and Alan P. Lightman. *Radiative processes in astrophysics.* 1979 (cited on page 22).

[68] Malcolm S. Longair. *High energy astrophysics.* 3rd ed. Cambridge University Press, 2011 (cited on page 22).

[69] H. M. MacDonald. "Zeroes of the Bessel functions." In: *Proceedings of the London Mathematical Society* s1-30.1 (1898), pp. 165–179. DOI: https://doi.org/10.1112/plms/s1-30.1.165 (cited on page 22).

[70] Justin D. Finke, Charles D. Dermer, and Markus Böttcher. "Synchrotron self-Compton analysis of TeV X-ray-selected BL Lacertae objects." In: *The Astrophysical Journal* 686.1 (Oct. 2008), p. 181. DOI: 10.1086/590900 (cited on pages 23, 27, 111).

[71] Alberto Saldana-Lopez et al. "An observational determination of the evolving extragalactic background light from the multiwavelength HST/CANDELS survey in the Fermi and CTA era." In: *Monthly Notices of the Royal Astronomical Society* 507.4 (Aug. 2021), pp. 5144–5160. DOI: 10.1093/mnras/stab2393 (cited on page 28).

[72] Guilaine Lagache, Jean-Loup Puget, and Hervé Dole. "Dusty infrared galaxies: Sources of the cosmic infrared background." en. In: *Annual Review of Astronomy and Astrophysics* 43.Volume 43, 2005 (Aug. 2005), pp. 727–768. DOI: 10.1146/annurev.astro.43.072103.150606 (cited on page 28).

[73] A. Domínguez et al. "Extragalactic background light inferred from AEGIS galaxy-SED-type fractions." In: *Monthly Notices of the Royal Astronomical Society* 410.4 (Jan. 2011), pp. 2556–2578. DOI: 10.1111/j.1365-2966.2010.17631.x (cited on pages 28, 30, 99–101, 103, 112, 123).

[74] Justin D. Finke, Soebur Razzaque, and Charles D. Dermer. "Modeling the extragalactic background light from starts and dust." In: *The Astrophysical Journal* 712.1 (Feb. 2010), p. 238. DOI: 10.1088/0004-637X/712/1/238 (cited on pages 28–30).

[75] Franceschini, A., Rodighiero, G., and Vaccari, M. "Extragalactic optical-infrared background radiation, its time evolution and the cosmic photon-photon opacity." In: *Astronomy & Astrophysics* 487.3 (2008), pp. 837–852. DOI: 10.1051/0004-6361:200809691 (cited on pages 28, 30).

[76] Robert J. Gould. *Electromagnetic processes.* Vol. 54. Princeton University Press, 2006 (cited on page 29).

[77] Giuseppe Di Sciascio. "Ground-based gamma-ray astronomy: An introduction." In: *Journal of Physics: Conference Series* 1263.1 (June 2019), p. 012003. DOI: 10.1088/1742-6596/1263/1/012003 (cited on page 32).

[78] P. K. F. Grieder. *Extensive air showers: High energy phenomena and astrophysical aspects - A tutorial, reference manual and data book.* 2010 (cited on pages 32, 35, 49).

[79] R. Battiston. "High precision cosmic ray physics with AMS-02 on the International Space Station." en. In: *La Rivista del Nuovo Cimento* 43.7 (July 2020), pp. 319–384. DOI: 10.1007/s40766-020-00007-2 (cited on page 33).

[80] A. U. Abeysekara et al. “Observation of the Crab nebula with the HAWC gamma-ray observatory.” In: *The Astrophysical Journal* 843.1 (June 2017), p. 39. DOI: 10.3847/1538-4357/aa7555 (cited on page 33).

[81] Harm Schoorlemmer. “A next-generation ground-based wide field-of-view gamma-ray observatory in the southern hemisphere.” In: *Proceedings of 36th International Cosmic Ray Conference — PoS(ICRC2019)*. Vol. 358. 2019, p. 785. DOI: 10.22323/1.358.0785 (cited on pages 33, 34).

[82] Zhen Cao et al. “The large high altitude air shower observatory (LHAASO) science book (2021 Edition).” In: *arXiv e-prints* (May 2019), arXiv:1905.02773. DOI: 10.48550/arXiv.1905.02773 (cited on page 34).

[83] J. V. Jelley. “Cerenkov radiation and its applications.” In: *British Journal of Applied Physics* 6.7 (July 1955), p. 227. DOI: 10.1088/0508-3443/6/7/301 (cited on pages 34–36).

[84] Jamie Holder. “Atmospheric Cherenkov gamma-ray telescopes.” In: *arXiv e-prints* (Oct. 2015), arXiv:1510.05675. DOI: 10.48550/arXiv.1510.05675 (cited on pages 35, 36).

[85] Jeremy S. Perkins and Gernot Maier. “VERITAS telescope 1 relocation: Details and improvements.” In: (Dec. 2009) (cited on page 36).

[86] Dave B. Kieda. “The gamma ray detection sensitivity of the upgraded VERITAS observatory.” In: *33rd International Cosmic Ray Conference*. Aug. 2013, p. 0700 (cited on page 37).

[87] Nahee Park. “Performance of the VERITAS experiment.” In: *PoS* ICRC2015 (2016), p. 771. DOI: 10.22323/1.236.0771 (cited on page 37).

[88] John M. Davies and Eugene S. Cotton. “Design of the quartermaster solar furnace.” In: *Solar Energy* 1.2 (1957), pp. 16–22. DOI: https://doi.org/10.1016/0038-092X(57)90116-0 (cited on page 38).

[89] E. Roache et al. “Mirror facets for the VERITAS telescopes.” In: *International Cosmic Ray Conference*. Vol. 3. International Cosmic Ray Conference. Jan. 2008, pp. 1397–1400 (cited on page 38).

[90] A. Nepomuk Otte. “The upgrade of VERITAS with high efficiency photomultipliers.” In: *arXiv e-prints* (Oct. 2011), arXiv:1110.4702. DOI: 10.48550/arXiv.1110.4702 (cited on page 38).

[91] Roland Winston. “Principles of solar concentrators of a novel design.” In: *Solar Energy* 16.2 (1974), pp. 89–95. DOI: https://doi.org/10.1016/0038-092X(74)90004-8 (cited on page 38).

[92] J. Hall et al. “Veritas CFDs.” In: *International Cosmic Ray Conference*. Vol. 5. International Cosmic Ray Conference. July 2003, p. 2851 (cited on page 38).

[93] Benjamin Zitzer and VERITAS Collaboration. “The VERITAS upgraded telescope-level trigger systems: Technical details and performance characterization.” In: *International Cosmic Ray Conference*. Vol. 33. International Cosmic Ray Conference. Jan. 2013, p. 3076. DOI: 10.48550/arXiv.1307.8360 (cited on page 38).

[94] E. Hays and VERITAS Collaboration. “VERITAS data acquisition.” In: *arXiv e-prints* (Oct. 2007), arXiv:0710.2288. DOI: 10.48550/arXiv.0710.2288 (cited on page 38).

[95] P. F. Rebillot et al. “The VERITAS flash ADC electronics system.” In: *International Cosmic Ray Conference*. Vol. 5. International Cosmic Ray Conference. July 2003, p. 2827 (cited on page 38).

[96] Adams, C. B. et al. “The throughput calibration of the VERITAS telescopes.” In: *A&A* 658 (2022), A83. DOI: 10.1051/0004-6361/202142275 (cited on pages 39, 48).

[97] M. Ajello et al. “Fermi farge area telescope performance after 10 years of operation.” en. In: *The Astrophysical Journal Supplement Series* 256.1 (Sept. 2021), p. 12. DOI: 10.3847/1538-4365/ac0ceb (cited on pages 39, 40, 58).

[98] M. Ackermann et al. “The Fermi large area telescope on orbit: Event classification, instrument response functions, and calibration.” en. In: *The Astrophysical Journal Supplement Series* 203.1 (Oct. 2012), p. 4. DOI: 10.1088/0067-0049/203/1/4 (cited on pages 40, 58).

[99] A. A. Abdo et al. “The on-orbit calibration of the Fermi Large Area Telescope.” In: *Astroparticle Physics* 32.3 (Oct. 2009), pp. 193–219. DOI: 10.1016/j.astropartphys.2009.08.002 (cited on pages 41, 59).

[100] N. Gehrels et al. “The Swift gamma-ray burst mission.” In: *The Astrophysical Journal* 611.2 (Aug. 2004), p. 1005. DOI: 10.1086/422091 (cited on page 42).

[101] Scott D. Barthelmy et al. “The burst alert telescope (BAT) on the SWIFT Midex mission.” In: *Space Science Reviews* 120.3 (Oct. 2005), pp. 143–164. DOI: 10.1007/s11214-005-5096-3 (cited on pages 42, 45, 127).

[102] David N. Burrows et al. “The Swift X-Ray Telescope.” In: *Space Science Reviews* 120.3 (Oct. 2005), pp. 165–195. DOI: 10.1007/s11214-005-5097-2 (cited on pages 42, 43, 59, 61, 62).

[103] Peter W. A. Roming et al. “The Swift ultra-violet/optical telescope.” In: *Space Science Reviews* 120.3 (Oct. 2005), pp. 95–142. DOI: 10.1007/s11214-005-5095-4 (cited on pages 42, 44, 45).

[104] Hans Wolter. “Spiegelsysteme streifenden Einfalls als abbildende Optiken für Röntgenstrahlen.” In: *Annalen der Physik* 445.1-2 (1952), pp. 94–114. DOI: https://doi.org/10.1002/andp.19524450108 (cited on pages 42, 43).

[105] Fiona A. Harrison et al. “The nuclear spectroscopic telescope array (NuSTAR) high-energy X-ray mission.” In: *The Astrophysical Journal* 770.2 (May 2013), p. 103. DOI: 10.1088/0004-637X/770/2/103 (cited on page 45).

[106] B. S. Acharya et al. “Introducing the CTA concept.” In: *Astroparticle Physics* 43 (2013), pp. 3–18. DOI: https://doi.org/10.1016/j.astropartphys.2013.01.007 (cited on pages 45, 129).

[107] Roberta Zanin et al. “CTA – the World’s largest ground-based gamma-ray observatory.” In: *PoS* ICRC2021 (2021), p. 005. DOI: 10.22323/1.395.0005 (cited on pages 45, 129).

[108] Gernot Maier and Jamie Holder. “Eventdisplay: An Analysis and Reconstruction Package for Ground-based Gamma-ray Astronomy.” In: 2017 (cited on pages 47, 77).

[109] Gernot Maier et al. *VERITAS-Observatory/EventDisplay_v4: Eventdisplay - version v487e*. Aug. 2022. DOI: 10.5281/zenodo.7025695. URL: https://doi.org/10.5281/zenodo.7025695 (cited on page 47).

[110] Rene Brun and Fons Rademakers. “ROOT — An object oriented data analysis framework.” In: *Nuclear Instruments and Methods in Physics Research Section A: Accelerators, Spectrometers, Detectors and Associated Equipment* 389.1 (1997), pp. 81–86. DOI: https://doi.org/10.1016/S0168-9002(97)00048-X (cited on page 47).

[111] A. M. Hillas. “Cerenkov light images of EAS produced by primary gamma rays and by nuclei.” In: *19th International Cosmic Ray Conference (ICRC19), Volume 3*. Vol. 3. International Cosmic Ray Conference. Aug. 1985, p. 445 (cited on pages 47, 51, 52).

[112] Ralph Bird et al. *V2DL3 - VERITAS (VEGAS and Eventdisplay) to DL3 converter*. Sept. 2023. DOI: 10.5281/zenodo.8306205. URL: https://github.com/VERITAS-Observatory/V2DL3 (cited on page 48).

[113] Cosimo Nigro, Tarek Hassan, and Laura Olivera-Nieto. “Evolution of data formats in very-high-energy gamma-ray astronomy.” en. In: *Universe* 7.10 (Oct. 2021), p. 374. DOI: 10.3390/universe7100374 (cited on page 48).

[114] I. H. Bond, A. M. Hillas, and S. M. Bradbury. "An island method of image cleaning for near threshold events from atmospheric Čerenkov telescopes." In: *Astroparticle Physics* 20.3 (2003), pp. 311–321. DOI: https://doi.org/10.1016/S0927-6505(03)00193-2 (cited on page 50).

[115] Christian Skole. "Search for extremely short transient gamma-ray sources with the VERITAS observatory." PhD Thesis. Humboldt U., Berlin, 2016. DOI: 10.18452/17608 (cited on page 51).

[116] M. Cawley et al. "Application of two dimensional imaging of atmospheric Cerenkov light to very high energy gamma ray astronomy." In: *International Cosmic Ray Conference*. Vol. 1. International Cosmic Ray Conference. Aug. 1983, p. 118 (cited on page 51).

[117] David J. Fegan. "γ/hadron separation at TeV energies." In: *Journal of Physics G: Nuclear and Particle Physics* 23.9 (Sept. 1997), p. 1013. DOI: 10.1088/0954-3899/23/9/004 (cited on pages 51, 52).

[118] W. Hofmann et al. "Comparison of techniques to reconstruct VHE gamma-ray showers from multiple stereoscopic Cherenkov images." In: *Astroparticle Physics* 12.3 (1999), pp. 135–143. DOI: https://doi.org/10.1016/S0927-6505(99)00084-5 (cited on page 52).

[119] F. A. Aharonian et al. "The potential of ground based arrays of imaging atmospheric Cherenkov telescopes. I. Determination of shower parameters." In: *Astroparticle Physics* 6.3 (1997), pp. 343–368. DOI: https://doi.org/10.1016/S0927-6505(96)00069-2 (cited on page 54).

[120] H. Krawczynski et al. "Gamma–hadron separation methods for the VERITAS array of four imaging atmospheric Cherenkov telescopes." In: *Astroparticle Physics* 25.6 (2006), pp. 380–390. DOI: https://doi.org/10.1016/j.astropartphys.2006.03.011 (cited on page 55).

[121] Leo Breiman. *Classification and regression trees*. New York: Routledge, Oct. 2017 (cited on page 56).

[122] Yoav Freund and Robert E Schapire. "A short introduction to boosting." en. In: *Journal of Japanese Society for Artificial Intelligence* 14.5 (Sept. 1999), pp. 771–780 (cited on page 56).

[123] A. Hoecker et al. *TMVA - toolkit for multivariate data analysis*. July 2009. DOI: 10.48550/arXiv.physics/0703039. URL: http://arxiv.org/abs/physics/0703039 (cited on pages 56, 59).

[124] Maria Krause, Elisa Pueschel, and Gernot Maier. "Improved γ/hadron separation for the detection of faint γ-ray sources using boosted decision trees." In: *Astroparticle Physics* 89 (Mar. 2017), pp. 1–9. DOI: 10.1016/j.astropartphys.2017.01.004 (cited on pages 56, 57).

[125] R. J. Hanisch et al. "Definition of the Flexible Image Transport System (FITS)." en. In: *Astronomy & Astrophysics* 376.1 (Sept. 2001), pp. 359–380. DOI: 10.1051/0004-6361:20010923 (cited on page 58).

[126] W. Atwood et al. *Pass 8: Toward the full realization of the Fermi-LAT scientific potential*. Mar. 2013. DOI: 10.48550/arXiv.1303.3514. URL: http://arxiv.org/abs/1303.3514 (cited on page 58).

[127] P. Bruel et al. *Fermi-LAT improved Pass~8 event selection*. Oct. 2018. DOI: 10.48550/arXiv.1810.11394. URL: http://arxiv.org/abs/1810.11394 (cited on page 58).

[128] M Capalbi et al. *The SWIFT XRT Data Reduction Guide*. en. Apr. 2005. URL: https://www.swift.ac.uk/analysis/xrt/files/xrt_swguide_v1_2.pdf (cited on pages 60, 61).

[129] S. Immler et al. *The Swift-UVOT software guide*. Mar. 2008. URL: https://swift.gsfc.nasa.gov/analysis/UVOT_swguide_v2_2.pdf (cited on page 60).

[130] J. K. Blackburn. "FTOOLS: A FITS data processing and analysis software package." In: 77 (Jan. 1995), p. 367 (cited on page 60).

[131] Claude Sammut. "Markov chain Monte Carlo." en. In: *Encyclopedia of Machine Learning*. Ed. by Claude Sammut and Geoffrey I. Webb. Boston, MA: Springer US, 2010, pp. 639–642. DOI: 10.1007/978-0-387-30164-8_511 (cited on page 63).

[132] Glen Cowan. *Statistical data analysis*. Oxford university press, 1998 (cited on pages 63, 67).

[133] T. -P. Li and Y. -Q. Ma. "Analysis methods for results in gamma-ray astronomy." In: *The Astrophysical Journal* 272 (Sept. 1983), pp. 317–324. DOI: 10.1086/161295 (cited on pages 64, 65).

[134] Jerzy Neyman, Egon Sharpe Pearson, and Karl Pearson. "IX. On the problem of the most efficient tests of statistical hypotheses." In: *Philosophical Transactions of the Royal Society of London. Series A, Containing Papers of a Mathematical or Physical Character* 231.694-706 (1933), pp. 289–337. DOI: 10.1098/rsta.1933.0009 (cited on page 64).

[135] S. S. Wilks. "The large-sample distribution of the likelihood ratio for testing composite hypotheses." In: *The Annals of Mathematical Statistics* 9.1 (1938), pp. 60–62. DOI: 10.1214/aoms/1177732360 (cited on page 64).

[136] W. Cash. "Parameter estimation in astronomy through application of the likelihood ratio." In: *The Astrophysical Journal* 228 (Mar. 1979), pp. 939–947. DOI: 10.1086/156922 (cited on page 67).

[137] Giacomo D'Amico. "Statistical tools for imaging atmospheric Cherenkov telescopes." In: *Universe* 8.2 (2022). DOI: 10.3390/universe8020090 (cited on pages 70, 71).

[138] S. Archambault et al. "Gamma-ray observations under bright moonlight with VERITAS." In: *Astroparticle Physics* 91 (May 2017), pp. 34–43. DOI: 10.1016/j.astropartphys.2017.03.001 (cited on page 77).

[139] D. Berge, S. Funk, and J. Hinton. "Background modelling in very-high-energy ϒ-ray astronomy." en. In: *Astronomy & Astrophysics* 466.3 (May 2007), pp. 1219–1229. DOI: 10.1051/0004-6361:20066674 (cited on pages 77–79).

[140] Axel Donath et al. "Gammapy: A Python package for gamma-ray astronomy." en. In: *Astronomy & Astrophysics* 678 (Oct. 2023), A157. DOI: 10.1051/0004-6361/202346488 (cited on page 78).

[141] M. Wood et al. "Fermipy: An open-source Python package for analysis of Fermi-LAT Data." In: 301 (July 2017), p. 824. DOI: 10.22323/1.301.0824 (cited on page 80).

[142] S. Abdollahi et al. "Fermi large area telescope fourth source catalog." en. In: *The Astrophysical Journal Supplement Series* 247.1 (Mar. 2020), p. 33. DOI: 10.3847/1538-4365/ab6bcb (cited on page 82).

[143] R. Willingale et al. "Calibration of X-ray absorption in our galaxy." In: *Monthly Notices of the Royal Astronomical Society* 431.1 (May 2013), pp. 394–404. DOI: 10.1093/mnras/stt175 (cited on page 84).

[144] T. S. Poole et al. "Photometric calibration of the Swift ultraviolet/optical telescope." In: *Monthly Notices of the Royal Astronomical Society* 383.2 (Dec. 2007), pp. 627–645. DOI: 10.1111/j.1365-2966.2007.12563.x (cited on page 84).

[145] Justin D. Finke et al. "Constraints on the intergalactic magnetic field with gamma-ray observations of blazars." en. In: *The Astrophysical Journal* 814.1 (Nov. 2015), p. 20. DOI: 10.1088/0004-637X/814/1/20 (cited on page 85).

[146] Charles D. Dermer et al. "Time delay of cascade radiation for TeV blazars and the measurement of the intergalactic magnetic field." en. In: *The Astrophysical Journal* 733.2 (June 2011), p. L21. DOI: 10.1088/2041-8205/733/2/L21 (cited on page 85).

[147] V. A. Acciari et al. "A lower bound on intergalactic magnetic fields from time variability of 1ES 0229+200 from MAGIC and Fermi/LAT observations." en. In: *Astronomy & Astrophysics* 670 (Feb. 2023), A145. DOI: 10.1051/0004-6361/202244126 (cited on pages 85, 101).

[148] Martin Elvis et al. "The Einstein slew survey." en. In: *The Astrophysical Journal Supplement Series* 80 (May 1992), p. 257. DOI: 10.1086/191665 (cited on pages 85, 89).

[149] A. S. Wilson et al. “On the identification of the high-latitude X-ray source 2A 1219 + 305.” In: *Monthly Notices of the Royal Astronomical Society* 187.2 (June 1979), pp. 109–115. DOI: 10.1093/mnras/187.2.109 (cited on page 85).

[150] N. Bade et al. “The Hamburg/RASS catalogue of optical identifications.” en. In: *Astronomy and Astrophysics Supplement Series* 127.2 (Jan. 1998), pp. 145–152. DOI: 10.1051/aas:1998339 (cited on page 85).

[151] Wystan Benbow. “Highlights of the VERITAS blazar observation program.” In: 8 (Jan. 2011), p. 47. DOI: 10.7529/ICRC2011/V08/0746 (cited on page 85).

[152] V. A. Acciari et al. “Discovery of variability in the very high energy γ-ray emission of 1ES 1218+304 with VERITAS.” In: *The Astrophysical Journal* 709 (Feb. 2010), pp. L163–L167. DOI: 10.1088/2041-8205/709/2/L163 (cited on page 85).

[153] J. Ballet et al. *Fermi large area telescope fourth source catalog data release 4 (4FGL-DR4)*. Nov. 2023. DOI: 10.48550/arXiv.2307.12546. URL: http://arxiv.org/abs/2307.12546 (cited on page 85).

[154] Jonathan F. Schachter et al. “Ten new BL Lacertae objects discovered by an efficient X-ray/radio/optical technique.” In: *The Astrophysical Journal* 412 (Aug. 1993), p. 541. DOI: 10.1086/172942 (cited on page 89).

[155] P. Giommi, S. G. Ansari, and A. Micol. “Radio to X-ray energy distribution of BL Lacertae objects.” In: *Astronomy and Astrophysics Supplement Series* 109 (Feb. 1995), pp. 267–291 (cited on page 89).

[156] Jong-Hak Woo et al. “Black hole masses and host galaxy evolution of radio-loud active galactic nuclei.” In: *The Astrophysical Journal* 631 (Oct. 2005), pp. 762–772. DOI: 10.1086/432681 (cited on page 89).

[157] Jeffrey D. Scargle. “Studies in astronomical time series analysis. V. Bayesian blocks, a new method to analyze structure in photon counting data*.” en. In: *The Astrophysical Journal* 504.1 (Sept. 1998), p. 405. DOI: 10.1086/306064 (cited on page 95).

[158] Jeffrey D. Scargle et al. “Studies in astronomical time series analysis. VI. Bayesian block representations.” en. In: *The Astrophysical Journal* 764.2 (Feb. 2013), p. 167. DOI: 10.1088/0004-637X/764/2/167 (cited on pages 95, 96, 125).

[159] The Astropy Collaboration et al. “The Astropy project: Sustaining and growing a community-oriented open-source project and the latest major release (v5.0) of the core package*.” en. In: *The Astrophysical Journal* 935.2 (Aug. 2022), p. 167. DOI: 10.3847/1538-4357/ac7c74 (cited on page 97).

[160] L Foffano et al. “A new hard X-ray-selected sample of extreme high-energy peaked BL Lac objects and their TeV gamma-ray properties.” In: *Monthly Notices of the Royal Astronomical Society* 486.2 (June 2019), pp. 1741–1762. DOI: 10.1093/mnras/stz812 (cited on pages 105, 110, 127).

[161] C. Nigro et al. “agnpy: An open-source python package modelling the radiative processes of jetted active galactic nuclei.” en. In: *Astronomy & Astrophysics* 660 (Apr. 2022), A18. DOI: 10.1051/0004-6361/202142000 (cited on page 111).

[162] Laura Silva et al. “Modeling the effects of dust on galactic spectral energy distributions from the ultraviolet to the millimeter band.” en. In: *The Astrophysical Journal* 509.1 (Dec. 1998), p. 103. DOI: 10.1086/306476 (cited on pages 112, 113).

[163] Jonathan Goodman and Jonathan Weare. “Ensemble samplers with affine invariance.” In: *Communications in Applied Mathematics and Computational Science* 5.1 (Jan. 2010), pp. 65–80. DOI: 10.2140/camcos.2010.5.65 (cited on page 114).

[164] M. L. Ahnen et al. “Extreme HBL behavior of Markarian 501 during 2012.” en. In: *Astronomy & Astrophysics* 620 (Dec. 2018), A181. DOI: 10.1051/0004-6361/201833704 (cited on page 125).

[165] V. D'Elia and A. Cavaliere. "The Connection between BL Lacs and Flat-Spectrum Radio Quasars." In: 227 (Jan. 2001), p. 252 (cited on page 128).

[166] A. Cavaliere and D. Malquori. "The Evolution of the BL Lacertae Objects." en. In: *The Astrophysical Journal* 516.1 (Mar. 1999), p. L9. DOI: 10.1086/311984 (cited on page 128).